ALLOSTERIC INTERACTIONS IN COORDINATION CAGES

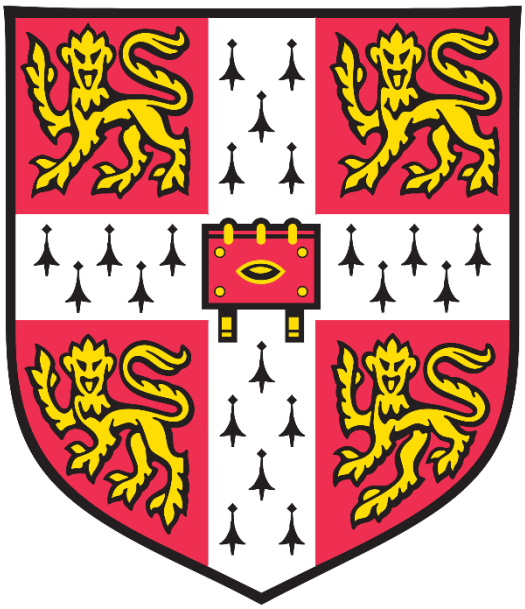

Felix John Rizzuto

Trinity College

April 2018

A dissertation submitted to the University of Cambridge as part of the

Doctor of Philosophy

DECLARATION

I hereby declare that this dissertation, entitled *Allosteric interactions in coordination cages*, is the result of work that I have undertaken in the University Chemical Laboratory at the University of Cambridge between November 2014 and April 2018. Except where stated to the contrary, this dissertation is my own work; credit for results obtained from collaboration with other parties is referenced to directly in the text. Figures that have been reproduced or adapted from other sources are indicated as such in their corresponding caption references. Aspects of the results presented herein have been published in peer-reviewed journals; original publications are referenced in the main text and a list of publications is included. This dissertation has not been, nor is currently being, submitted for any other degree, diploma or other academic qualification at this or any other university. It does not exceed 60,000 words in length.

Felix J. Rizzuto

ABSTRACT

Biomolecular receptors can catalyse reactions, alter their geometry, and inhibit their activity in response to molecules binding around their periphery. Synthetic receptors that can mimic this allosteric binding behaviour extend the potential applications of host-guest chemistry to programmable molecular systems. Modulating the degree and magnitude of interaction between components within these systems enables the design of chemical behaviour akin to biological complexity.

With a view to developing artificial guest-binding regulation systems, a series of metal-organic cages capable of both the peripheral and internal encapsulation of guests are presented: octahedra capable of accommodating two guests in different locations simultaneously; cuboctahedral receptors that bind fullerenes with all-or-nothing positive cooperativity and assemble supramolecular entities internally; a heteroleptic triangular prism capable of recognising steroids and enantiopure natural products; and a tetrahedron that binds fullerene clusters. Each of these architectures employs one or more binding site to either: a) template specific products; b) regulate the cooperativity of binding of large anionic guests; c) assemble coordination complexes and interlocked species inside their cavities; d) alter their morphology in well-defined ways; or e) form assemblies with new electronic and electrochemical functionality. In all cases, chemical systems that respond to multiple stimuli simultaneously are explored, and new applications for bringing multiple species into proximity are detailed. The allosteric binding motifs described herein can be extended to sort reaction mixtures, generate specific isomeric forms, stabilise labile species and promote tuneable modes of intermolecular cooperativity.

PUBLICATIONS AND COPYRIGHT INFORMATION

Parts of this dissertation have been published in the following peer-reviewed journals:

[1] F. J. Rizzuto, W.-Y. Wu, T. K. Ronson, J. R. Nitschke, *Angew. Chem. Int. Ed.*, **2016**, *55*, 7958-7962 (inside front cover, *Angew. Chem. Int. Ed.*, **2016**, *55*, 7866).

[2] F. J. Rizzuto, J. R. Nitschke, *Nat. Chem.*, **2017**, *9*, 903-908.

[3] F. J. Rizzuto*, D. M. Wood*, T. K. Ronson, J. R. Nitschke, *J. Am. Chem. Soc.*, **2017**, *139*, 11008-11011.

Any work included in this dissertation that has been published has been reproduced herein with permission. Additional work that was carried out during the course of this PhD project, but not included in this dissertation, has been published in the following peer-reviewed journals:

[4] F. J. Rizzuto, C. Hua, B. Chan, T. B. Faust, A. Rawal, C. F. Leong, J. M. Hook, C. J. Kepert, D. M. D'Alessandro, *Phys. Chem. Chem. Phys.*, **2015**, *17*, 11252-11259.

[5] W. J. Ramsay*, F. J. Rizzuto*, T. K. Ronson, K. Caprice, J. R. Nitschke, *J. Am. Chem. Soc.*, **2016**, *138*, 7264-7267.

[6] J. L. Greenfield, F. J. Rizzuto, I. Goldberga, J. R. Nitschke, *Angew. Chem. Int. Ed.*, **2017**, *56*, 7541-7545.

[7] A. Plajer, K. Bold, F. J. Rizzuto, R. Garcia-Rodriguez, T. K. Ronson, D. S. Wright, *Dalton Trans*., **2017**, *46*, 12775-12779.

[8] C. Hua, F. J. Rizzuto, X. Zhang, F. Tuna, D. Collison, D. M. D'Alessandro, *New. J. Chem.*, **2017**, *41*, 108-114.

[9] F. J. Rizzuto, M. Kieffer, J. R. Nitschke, *Chem. Sci.,* **2018**, *9*, 1925-1930.

[10] A. Plajer, R. Garcia-Rodriguez, F. J. Rizzuto and D. Wright, *Chem. Eur. J.*, **2018**, *24*, 2013-2019.

[11] A. Plajer, A. Colebatch, F. J. Rizzuto, P. Prohm, A. D. Bond, R. Garcia-Rodriguez and D. Wright, *Angew. Chem. Int. Ed.* **2018**, DOI:10.1002/anie.201802350.

[12] A. Plajer, H.-C. Niu, F. J. Rizzuto, D. Wright, **2018**, *Dalton Trans.*, **2018**, accepted.

*denotes joint first author

ACKNOWLEDGEMENTS

I cannot thank my supervisor, Prof Jonathan Nitschke, enough for his constant support and insight; not only have you allowed me to pursue my own designs without question, but you've actively sought to help me achieve them. While your ideas were often crazy (there really is no better word for it), the scope through which you view science has taught me much. I am forever grateful for your help and advice.

Unerring thanks also go to Dr Andrew Bond, Dr Paul Skelton, Dr Asha Boodhun and the entire NMR facility team – when an instrument crashed, you were always there to help. To the entirety of Lab 354: thanks for keeping me sane and enduring my inappropriateness; I've enjoyed laughing and complaining with and about all of you. The importance of lab atmosphere to the sanity of a PhD student is highly undervalued, so props to the people who kept my mania at bay: you know who you are. If any one of you ever read this, hit me up for a drink any time: just don't talk about the roof leaking. My thanks likewise go to all previous members of the Nitschke group: cheers for leaving behind your ligands for me to pillage.

Attention must be paid to Dr Wenyuan Wu and Dr Dan Wood, who set precedent for the results in Chapters 3 and 7, respectively, and Dr Tanya Ronson who was always available to address my crystallographic issues. Thanks to Derrick and Anna for running some special NMR experiments for me too. To my various Diamond partners in crime – Will, Marion and John – you all made what should have been a miserable experience entertaining (although I count my blessings that I never have to do a 2-9 am shift ever again).

To my collaborators – Alex, Angela, Dan, Dom, Jake, John, Marion, Patrick, Tanya, Will (I'm sure I'm forgetting someone…) – you are some of the best scientists I have had the pleasure of working with. You have all made me a better researcher, a better scientist and a far more thoughtful conversationalist than I could have ever dreamed possible. To say I wish you all the best in all you do would be a severe understatement.

On a more formal note, thanks to Cambridge Australia Scholarships and Trinity College for giving me money. The last three and a bit years would not have happened without your financial support.

To the Nitschke group at large: communication is the greatest skill you can possible learn during your time here. When arguing with a fool, make sure they aren't doing the same thing. Obstinacy is a useful tactic only when you're right; sincere thanks to everyone who showed me I wasn't always.

ABBREVIATIONS AND SYMBOLS

BPh_4^-	tetraphenylborate
COSY	correlation spectroscopy
Cp	cyclopentadienyl
CV	cyclic voltammetry/voltammogram
DOSY	Diffusion Ordered Spectroscopy
equiv/eq	equivalents
ESI	Electrospray Ionisation
fac	facial
Fc/Fc^+	ferrocene redox couple
HMBC	heteronuclear multiple bond coherence
HOMO	highest occupied molecular orbital
HSQC	heteronuclear multiple quantum coherence
LUMO	lowest unoccupied molecular orbital
mer	meridional
MS	mass spectrometry
M_xL_y	a metal complex with *x* number of metals (M) and *y* number of ligands (L)
NIR	near-infrared
NMR	Nuclear Magnetic Resonance
NOE	Nuclear Overhauser effect
NOESY	Nuclear Overhauser effect correlation spectroscopy
NTf_2^-	triflimide; bis(trifluoromethanesulfonyl)imide
OTf^-	triflate; trifluoromethanesulfonate
PCBM	[6,6]-phenyl C_{61} butyric acid methyl ester
ROESY	Rotating-frame nuclear Overhauser effect correlation spectroscopy
RT	room temperature
SCXRD	Single Crystal X-ray Diffraction
UV-Vis	Ultraviolet-visible
δ	chemical shift

TABLE OF CONTENTS

Chapter 1

Introduction

1.1 Long-range communication and biological allostery

The transmission of chemical information between interacting and dynamic components is the hallmark of biological efficacy. In response to the receipt of molecular payloads, receptors can convey and propagate information to other cellular constituents. As the number of signals between components builds, a communication cascade occurs throughout the cell, acting to regulate the activities of individual components. When these transmission highways intertwine, networks of overlapping and merging communication channels are generated to output event-specific responses. In this way, biology pre-coordinates its reaction to even the slightest change in environmental conditions. From a single binding event, a response is actuated to alleviate or regulate a specific situation.[1,2]

Signal transduction networks such as these are the ultimate biological tool employed for the regulation of cellular activity and underscore the importance of long-range communication in living systems. Allostery, where the binding of one molecule affects the binding of another molecule at a distal receptor site, is an integral part of these cascade processes (Figure 1.1).[3,4] Binding processes like allostery rely heavily on molecular cooperation and organisation, both between receptor and substrate, and between binding substrates. Engineering these interactions in abiological systems is not trivial – structural rearrangement, association strength and guest displacement must be tempered to complement multiple binding events and promote cooperation between species.

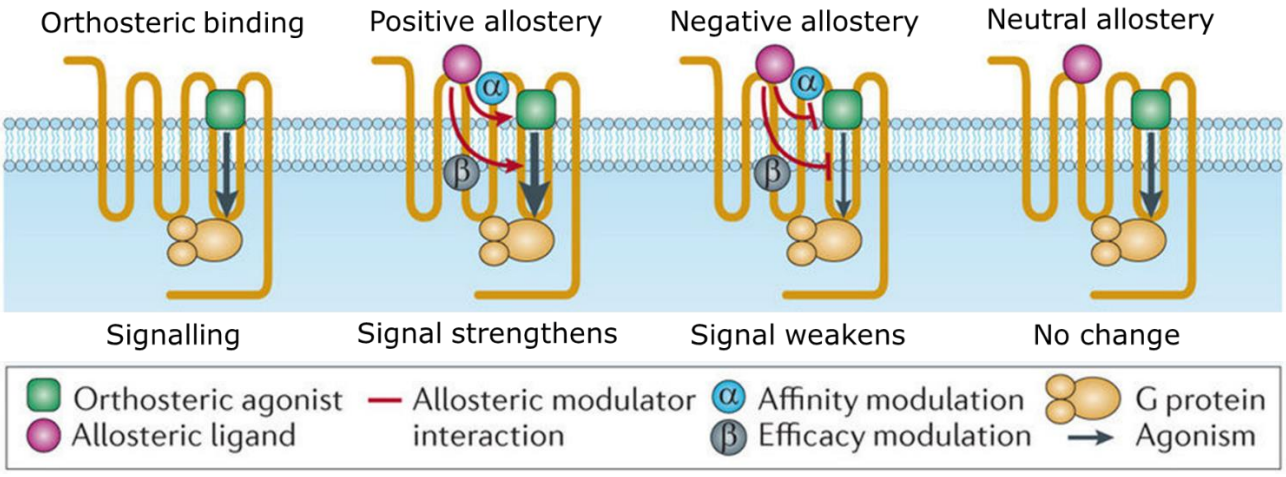

Figure 1.1 | A model for allosteric regulation in a lipid bilayer. **a**, Orthosteric agonists bind to a receptor, resulting in downstream signalling through the bilayer. **b**, Positive allosteric modulators bind to a different site and enhance the affinity (cooperativity factor-α) and/or efficacy (modulation factor-β) of the orthosteric agonist. **c**, Negative allosteric modulators decrease the affinity and/or efficacy of the orthosteric agonist and **d**, some allosteric ligands have no effect on the affinity and/or efficacy mediated by the orthosteric agonist. Figure adapted from reference 5.

In synthetic chemical hosts, installing multiple binding sites, each of which can recognise specific molecular targets, on a single structure relies on comprehending the forces behind molecular

recognition. Typically, these interactions are intermolecular: reversible bonds, wide-ranging in terms of strength (although typically weaker than covalent bonding) and often complementary, promoting equilibration under thermodynamic control. Supramolecular chemistry makes use of these intermolecular interactions to generate synthetic receptors capable of binding selectivity and regulation.[6-9]

1.2 Host-guest chemistry in coordination cages

The preconditions for guest binding in supramolecular hosts are varied and wide-ranging.[10] Generally, hosts are designed to frame a space that can store small molecule payloads. Several classes of hosts – ranging from small organic ion transporters to macromolecular aggregates – have been identified as promising candidates for studying molecular recognition phenomena.[11] Among them, metallosupramolecular complexes provide unique advantages. Owing to the symmetries imposed by different ligand configurations and metal coordination spheres, these assemblies are geometrically tailorable; subtle and facile alterations of either metal or organic components have led to diverse structural outputs with equally diverse cavity geometries (Figure 1.2).[12] The bespoke nature of these assemblies has enabled variety of shape, size and rigidity by applying simple geometric rules of symmetry and vector complementarity between organic and inorganic components.

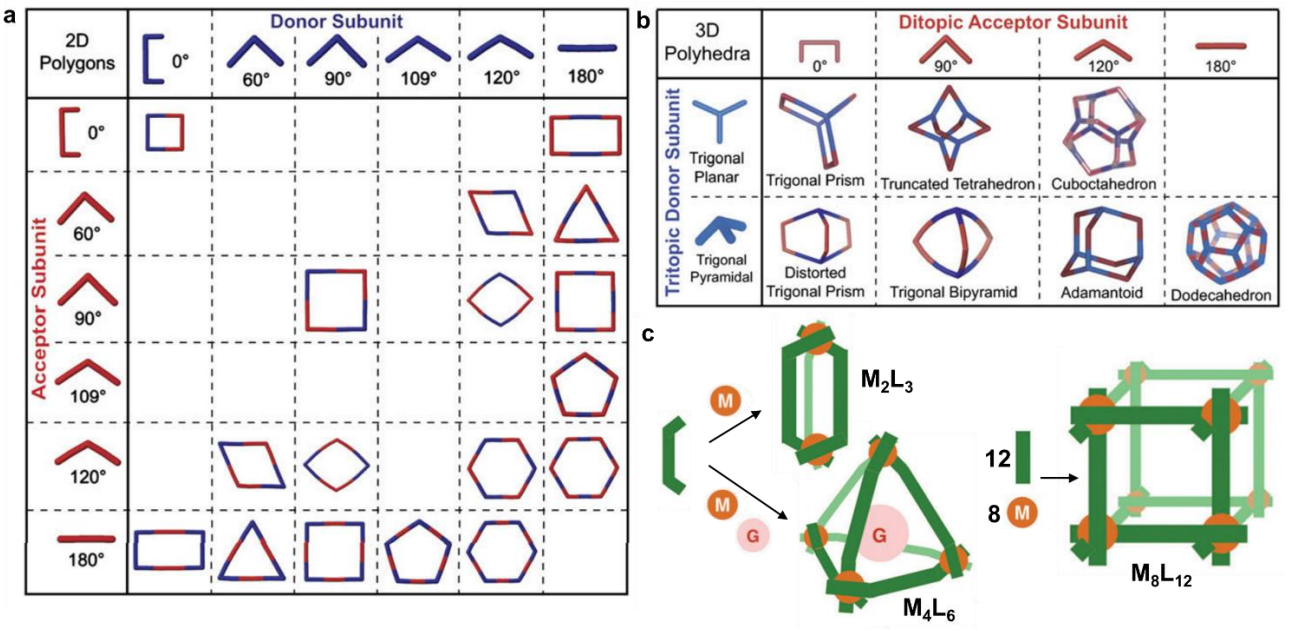

Figure 1.2 | Metal-organic architectures can be formed from units with geometric complementarity. **a**, Convex, two-dimensional polygons form from ditopic substituents. **b**, Three-dimensional shapes form from the combination of ditopic and tritopic units. **c**, Specific examples of 3D assembly, where the bite angle of ligands (green) and metal ions (M, orange) determine the metal:ligand stoichiometries of resulting cages that can encapsulate guests (G). Figures adapted from references 13 and 14.

The ease with which the cavities of these capsular supramolecular complexes can be tailored has led to diverse host-guest chemistry; by tuning the geometry and size of these cavities, cages can be designed to bind specific molecular targets. Rules governing the specificity and strength of molecular binding events are nevertheless complex. To combat serendipity, a series of methods to improve guest association have been implemented, ranging from simple electrostatic complementary to holistic scaffold design and cavity engineering.

1.3 Strategies for the central encapsulation of guests

The encapsulation of guests inside a cavity is a thermodynamic process: it can be driven by entropic and/or enthalpic forces. In the former instance, expulsion of solvent from the central cavity drives binding; in the latter, the cooperative intermolecular interactions established between the host and guest upon binding provide an enthalpically-favourable driving force. Several strategies have been employed to take advantage of these interactions, many employing the inherent properties of metal-organic complexes (electrostatics, organic electronics, etc.) or more nuanced properties such as structural adaptation and unsaturated metal sites. As an overarching rule, some form of size complementarity between host and guest molecule is conducive to successful guest binding events, but even this prerequisite can be superseded by the judicious choice of assembling components.

1.3.1 General guidelines: size and shape complementarity

The 55% rule states that the optimal binding affinity is achieved when *ca.* 55% of the available cavity is occupied by the guest: higher guest occupancy volumes restrict the motion of the guest in the host, decreasing entropy; when occupancy percentages are lower than 55%, strong distance-dependent intermolecular interactions holding the guest in place weaken, decreasing the enthalpic contribution to binding.[15] If strong intermolecular forces between host and guest are present, up to 70% of the cavity can be occupied.

Promoting a good size and shape match between the volume of the cavity and the volume of the guest is thus critical to optimise binding interactions. Hunter, Ward *et al.* investigated this trend in water-soluble cubic cage **1.1**, wherein binding strength tailed off past a cavity occupation of *ca.* 50% (Figure 1.3).[16] A linear relationship between the free energy associated with binding and the surface area of the guest was uncovered for guests of different size; shape differences, however, showed no correlation. In a separate report, Ward *et al.* observed that the rate of exchange of guests was

dependant on the size and shape of the ligand employed during assembly: rigid ligands showed slower rates of exchange on the NMR timescale than did flexible ligands.[17]

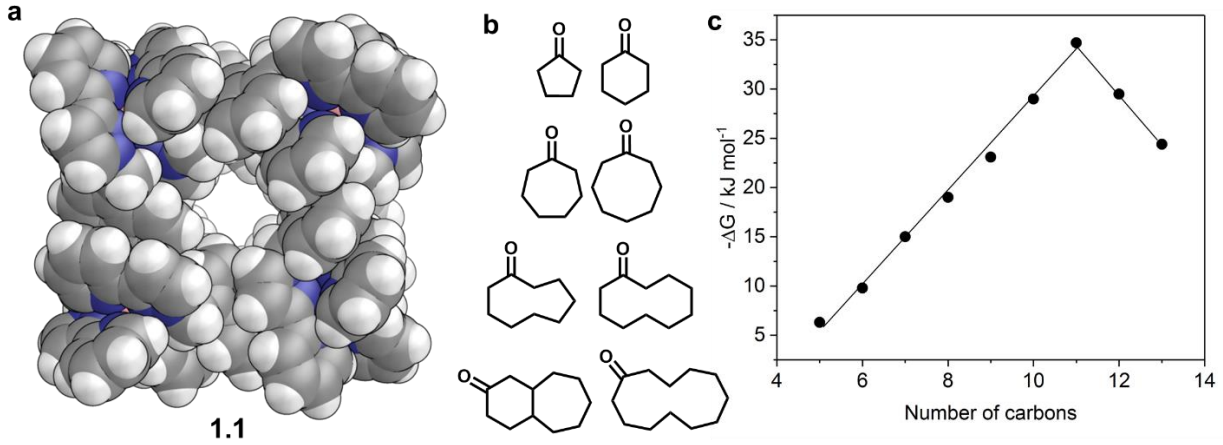

Figure 1.3 | a, Crystal structure of water-soluble cage $Co^{II}_8L_{12}$ **1.1**. **b**, Cyclic guests of different chain lengths that can be bound within **1.1**. **c,** Plot of the binding free energy *vs.* the number of carbon atoms for the guest series shown in **b** (Co^{II} – pink, C – grey, N – blue, H – white).

With a view towards demonstrating the importance of cavity size changed upon host-guest dynamics, Clever *et al.* reported that the strength of guest binding was morphology-dependent: the affinity of $B_{12}F_{12}^{2-}$ for $Pd^{II}_2L_4$ cage **1.2** was observed to increase by two orders of magnitude upon cavity contraction (Figure 1.4).[18] Light was employed as the stimulus to effect this morphology change, wherein ligand $\mathbf{L^{1.2}}$ switches between open and closed forms upon light irradiation. A snugger fit for the guest was created in the open state of the ligand, improving its association.

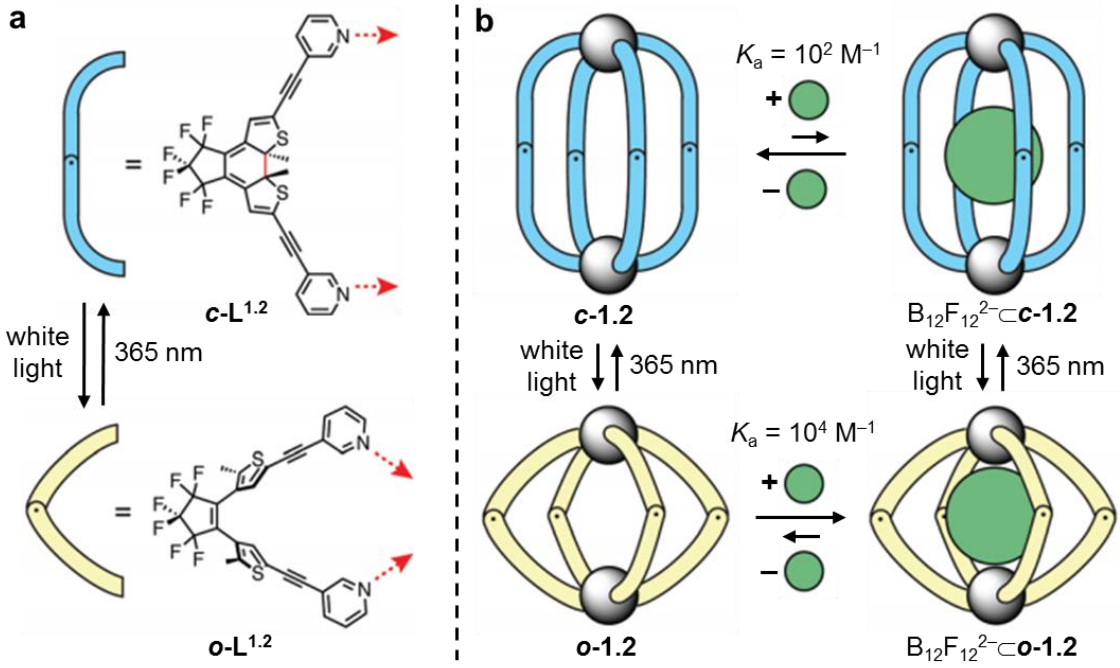

Figure 1.4 | **a**, Light absorption drives the interconversion between an 'open' (*o*) flexible state and a rigid 'closed' (*c*) state in $\mathbf{L^{1.2}}$. **b**, $Pd^{II}_2L_4$ cage **1.2** contains photochromic units that enable cavity contraction or expansion, thereby creating a tighter or looser fit for a $B_{12}F_{12}^{2-}$ anion (depicted as a green circle), respectively, depending on the wavelength of light irradiation. Figure adapted from references 18 and 19.

Changing the nature of the space surrounding the cavity can also lead to more efficient guest binding. When appended with interior-directing coronene groups, fullerenes can be bound in $Pd^{II}_{12}L_{24}$ cage **1.3**, which has a diameter of 4.6 nm (Figure 1.5).[20] In this instance, the electron-rich substituents connected to the cage scaffold create an interior nanophase that promotes π-interactions with the guest, driving its association with the interior space of the cage. No binding interaction is observed when ligands are unsubstituted.

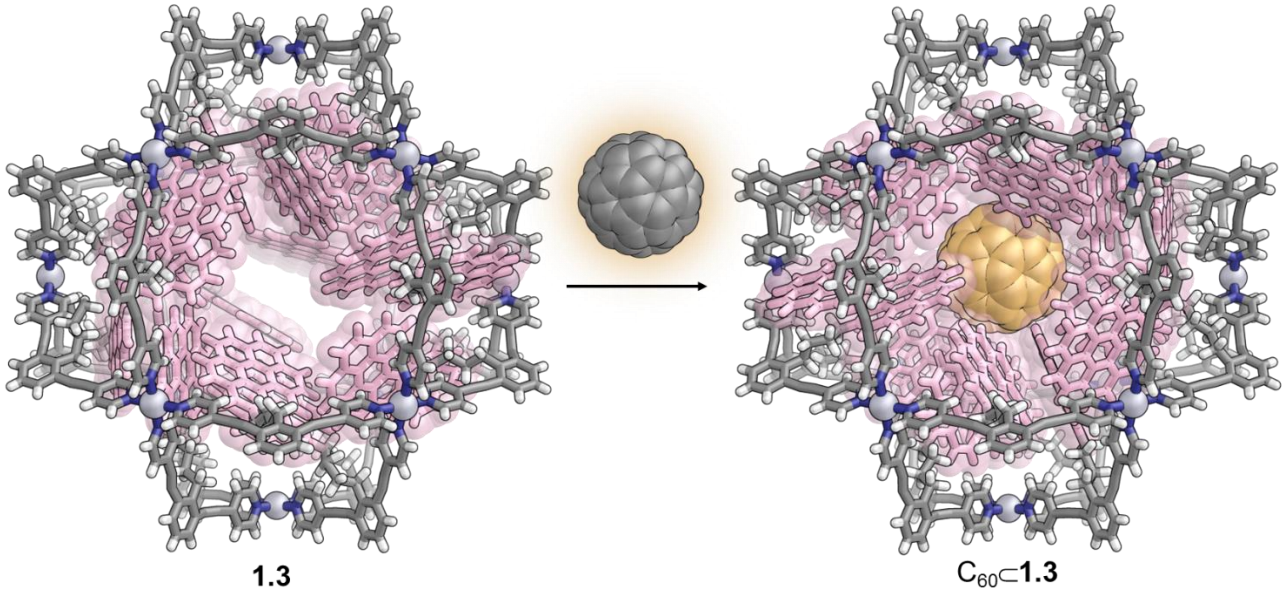

Figure 1.5 | Appending cuboctahedral $Pd^{II}_{12}L_{24}$ cage **1.3** with interior-directing coronene units creates a 'nanophase' within the cage that can be used to bind C_{60} (Pd^{II} – light grey, coronene adduct – pink, C_{60} – orange).

1.3.2 Maximising entropy increase – the hydrophobic effect

A binding event wherein two molecules combine to form a single entity is entropically disfavoured. Usually, an entropic cost is paid by an enthalpic gain; however, not all systems experience entropic penalties upon guest binding. The simplest way to achieve entropic favourability upon guest encapsulation is to engineer systems wherein favourable interactions between the solvent and host are absent. Expulsion of solvent from the cavity upon guest binding increases both the number of degrees of freedom of the solvent and the number of intermolecular interactions in which these molecules can participate (*i.e.*, with bulk solvent). The entropic loss of bringing two entities together is thus compensated for by the entropic gain of solvent reorganisation.[21]

Water-soluble hosts that contain large hydrophobic regions enclosing the cavity have been the most successful cages at implementing this strategy. When no guests were present, the water molecules in $Pd^{II}_4L_4$ cage **1.4** were packed in a hydrogen-bonded array, reflective of the arrangement in I_c-type ice (Figure 1.6a).[22] Displacement of multiple water molecules from the cavity upon binding other guests improved the degrees of freedom of the water, contributing entropically to the free energy

of guest binding. These observations were reinforced by quantitative studies by Raymond *et al.*, detailing that binding guests in water within $Ga^{III}_4L_6$ cage **1.5** was an entropically driven process – the solvent reorganisation energy associated with the displacement of water from the cavity was reported to drive binding (Figure 1.6b).[23,24] Similar effects have been observed in other polar solvents – where solvent displacement drives an entropically favourable binding process.[18]

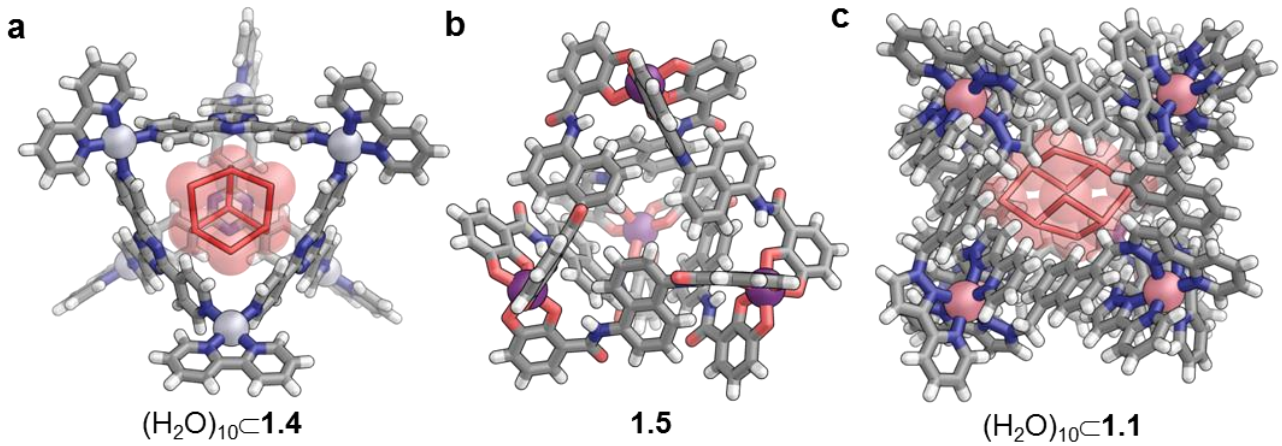

Figure 1.6 | Cages displaying different contributions to the hydrophobic effect. **a**, Water molecules with specific interactions within $Pd^{II}_4L_4$ cage **1.4** are expelled, increasing entropy upon binding. **b**, Guest binding in $Ga^{III}_4L_6$ cage **1.5** is also driven by solvent displacement from the cavity. **c**, Water molecules with non-specific interactions within **1.1** are released, leading to enthalpy increase upon hydrogen bonding with the solvent. The water molecules in **a** are hydrogen-bonded, resembling I_c-type ice, while the water molecules in **c** are disordered in two configurations (only one shown); only half of the encapsulated water molecules in **1.1** participate in hydrogen bonding. Close contacts between H_2O molecules are connected in red in **a** and **c** (Ga^{II} – purple, O – red).

A notable caveat to this rule is that the hydrophobic effect can be enthalpy-based: Ward *et al.* reported that water molecules bound in high-energy configurations (with non-specific or frustrated hydrogen bonds) within **1.1** could be expelled from the cavity to generate enthalpically-favourable hydrogen bonds with the bulk solvent (Figure 1.6c).[25] This highlights an important aspect of the hydrophobic effect: the enthalpic penalty associated with guest desolvation is countervailed by the release of solvent molecules from the cavity, which form new interactions outside the guest-binding environment. High-energy water displacement has likewise been shown to be a driving force for binding in organic hosts.[26]

If the host is flexible or capable of multiple conformations, the restriction imposed on the scaffold upon guest binding also reduces the number of degree of freedom of the host. This often warrants the use of rigid components in the construction of cage topologies, which decrease the number of degrees of freedom the cage can adopt, thereby minimising any unfavourable entropy changes relating to the conformational restriction of the complex upon guest binding. A notable caveat to this rule is where some structural plasticity enables a cage to adapt its morphology to bind a wider range of guests.[27]

1.3.3 Electrostatic interactions

With few exceptions, the central commonality between all metal-organic architectures is that they have charge associated with the metal ions holding them together; typically, metal ions frame the corners of these complexes, defining the polygonal geometry. Positively-charged species are thus able to attract and bind negatively-charged guests. Oftentimes, poor matches between cavity size and guest volume can be overcome by electrostatic attraction alone. Several large cages can bind small anions: *pseudo*-icosahedron **1.6**, with a void of 2800 Å^3, can bind a single molecule of $B_{12}F_{12}^{2-}$, which occupies *ca.* 10% of the cavity;[28] octahedron **1.7** binds a single molecule of tetraphenylborate (BPh_4^-, K_a = 10^5 M^{-1}) within its *ca.* 1600 Å^3 cavity (Figure 1.7).[29] Both of these cages have large aperture windows, allowing for the facile ingress and egress of guests. Coulombic attraction between host and guest is favourable enough to overcome size mismatch, resulting in binding in both cases.

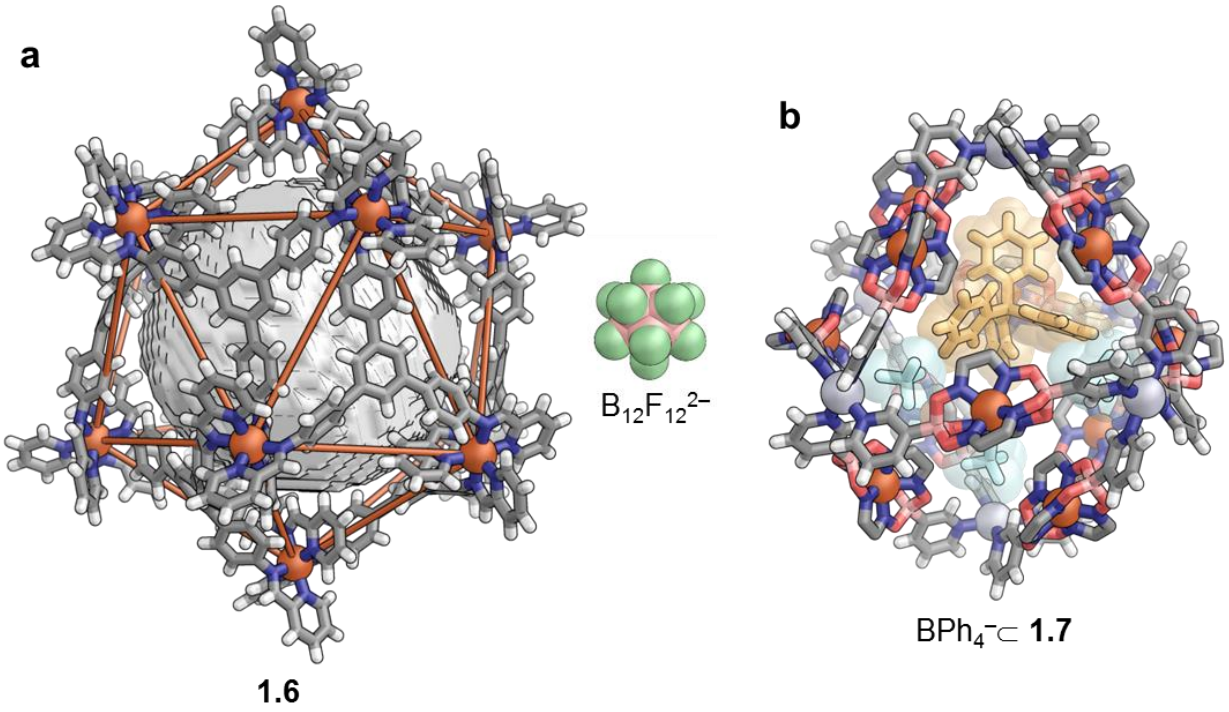

Figure 1.7 | **a**, $Fe^{II}_{12}L_{12}$ cage **1.6** is capable of binding $B_{12}F_{12}^{2-}$ (cavity is highlighted as a grey sphere, metal ion connectivity shown as orange lines). **b**, $Pd^{II}_6L_{12}$ cage **1.7** binds tetraphenylborate (BPh_4^-, orange), despite a poor cavity size match. There is enough space still available within this capsule to bind three molecules of BF_4^- (cyan) in the solid state (methyl groups on the ligand have been omitted for clarity) (Fe^{II} – dark orange, F – green, B – pink).

Recent investigations by Flood *et al.* have shown that the strength of guest binding, driven by electrostatics, can be screened by the solvent employed;[30] a direct correlation between the dielectric constant of the solvents and the anion binding affinity was identified in an organic host. Studies on the guest binding properties of **1.8** by Lusby *et al.* have echoed this finding in metal-organic cages, simultaneously deducing that altering the strength of the ion-pairing interactions between positively-charged hosts and their anions can lead to significant changes in the association constants of neutral guests (Figure 1.8).[31] Weakening the strength of the host ion pair led to an increase in the binding

strength of the guest, suggesting that the anion employed (and the strength of association of that anion to the cage) could be tailored to express specific binding efficiencies. Employing counteranions that were unable to fill the cavities of these cages was also observed to improve binding.

a

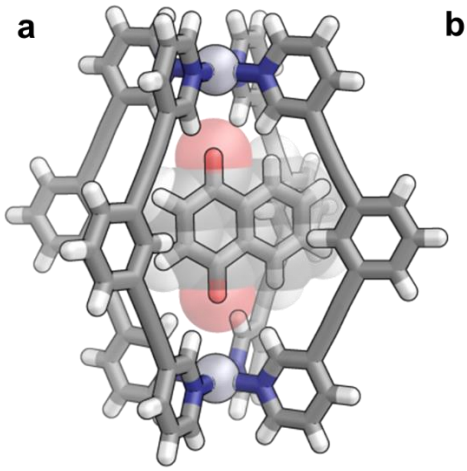

naphthoquinone⊂**1.8**

b

Entry	X	Solvent	K_a [M^{-1}]	ΔG [kJ mol^{-1}]
1	OTf	CD_3CN	210	13.2
2	OTf	CD_3OD	26	8.1
3	OTf	[D_8]THF	290	14.1
4	OTf	CD_2Cl_2	1800	18.7
5	OTf	CD_3NO_2	2000	18.8
6	BF_4	CD_3NO_2	6500	21.7
7	PF_6	CD_3NO_2	13000	23.5
8	SbF_6	CD_3NO_2	22000	24.8
9	BArF	CD_3NO_2	50000	26.8
10	BArF	CD_3OD	530	15.5
11	BArF	CD_3CN	1600	18.3
12	BArF	CD_2Cl_2	350000[b]	31.1

[a] Determined by ^{1}H NMR titration, errors are estimated to be $<10\%$.
[b] Competitive ^{1}H NMR titration

Figure 1.8 | **a**, $Pd^{II}_2L_4$ cage **1.8** binding naphthoquinone. **b**, Table displaying the association constants (K_a) of naphthoquinone with **1.8**, upon changing the counterion (X) or solvent. Figures adapted from reference 31.

While electrostatic attraction works favourably for charged guests and hosts, studies by Sallé *et al.* have shown that neutral guests bind stronger in neutral cages.[32] The study compared $Pd^{II}_4L_2^{8+}$ cage **1.9** against its neutral $Pd^0_4L_2$ congener **1.10**: while the polycationic cage bound polycyclic aromatic guests with low affinities ($K_a < 10^2$ M^{-1}), the neutral congener bound guests with association constants up to three orders of magnitude greater ($K_{a(\text{coronene})} = 10^5$ M^{-1}) (Figure 1.9). Electrochemical manipulations on guest molecules have also shown that the redox state (*i.e.* charge) of a guest can modulate its uptake and release from a supramolecular architecture.[33,34]

a

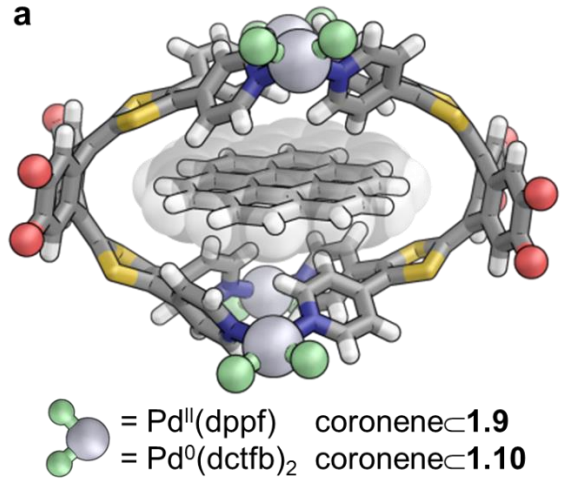

= Pd^{II}(dppf) coronene⊂**1.9**
= Pd^0(dctfb)$_2$ coronene⊂**1.10**

b

Guest	$M_4L_2^{8+}$	M_4L_2
Coronene	63	2.6×10^4
Perylene	96	4.0×10^3
Triphenylene	14	2.8×10^2
Pyrene	[a]	1.7×10^2

[a] No binding could be detected under these conditions.

Figure 1.9 | **a**, Isostructural Pd_4L_2 complexes **1.9** and **1.10** both encapsulate one molecule of coronene internally (dppf = 1,1'-bis(diphenylphosphino)ferrocene, dctfb = 3,5-dichloro-2,4,6-trifluorobenzene). **b**, These cages show different binding affinities (K_a, M^{-1}) for neutral guests, depending on the charge of the assembly (**1.9** has a 8+ charge, **1.10** is neutral) (S – yellow, red balls – ether chains). Figures adapted from reference 32.

1.3.4 Maximising surface area

Closing off the faces of polyhedral cages is the most common method of engineering internal guest binding. This process takes advantage of the favourable enthalpic interactions generated between host and guest molecules upon encapsulation. Bulky aromatic units – porphyrins and polyphenyl moieties – installed on ligand backbones are clear literature favourites. The advantages of employing these moieties are twofold: 1) π-π interactions between aromatic units reinforce structural rigidity, often promoting novel architectures; and 2) electron-rich moieties complement the electronic properties of electron-deficient guests, promoting their binding internally.

Yoshizawa *et al.* have employed this strategy extensively, generating a wealth of architectures tiled with anthracene panels (Figure 1.10).[14] Several of these capsules are capable of binding electron-deficient molecules, planar and spherical aromatic compounds (hosts **1.11–1.13**), as well as structurally more complex and asymmetric guests like dyes and fluorophores (host **1.12**). Guest binding in these instances is usually aided by the hydrophobic effect in water, but it is reinforced by the large π-surface surrounding the encapsulated guest, and the CH-π interactions that are established between host and guest.[35]

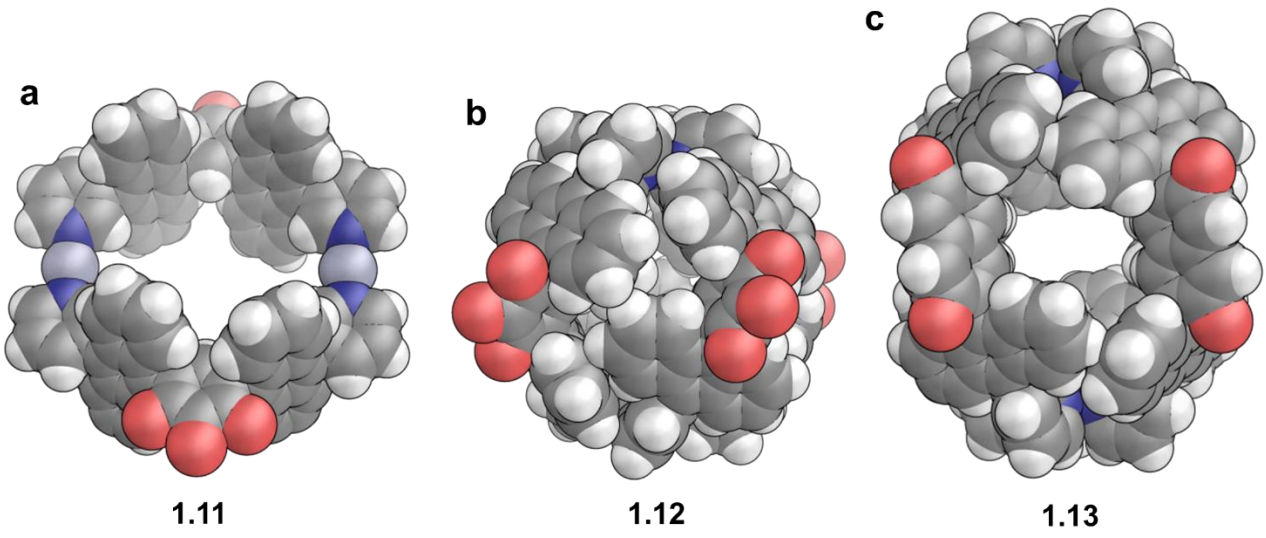

Figure 1.10 | A series of anthracene-panelled architectures developed by Yoshizawa *et al.* **a**, $Hg^{II}L_2$ macrocycle **1.11**, where anthracene units are spaced by a phenyl ring. **b**, $Pd^{II}_2L_4$ capsule **1.12**, employing the same ligand as that used to generate **1.11**. **c**, $Pd^{II}_2L_4$ capsule **1.13**, where anthracene rings are spaced by a naphthalene unit (red balls = ether chains).

The Nitschke group recently demonstrated the advantage of closing off the faces of supramolecular architectures in two comparative studies. The first involved contrasting the guest binding characteristics of cage **1.14**, with a single phenylene ring bridging chelating moieties, with cage **1.15**, where this phenylene ring was replaced by a bulky anthracene unit (Figure 1.11).[36] While the void of **1.15** (4200 $Å^3$) is larger than **1.14** (*ca.* 1000 $Å^3$), only **1.15** is capable of binding anionic guests, which never occupy more that 11% of the cavity.

The second study involved a comprehensive comparison of nine edge-panelled tetrahedra, with the systematic replacement of connector moieties (hosts **1.16–1.23**, Figure 1.12).[37] The observed hierarchy of guest binding within these structures suggested that tetrahedra with open faces were less adept at binding small molecule payloads than those with closed-off faces – offset ligands were consistently better at binding neutral guests than their linear derivatives.

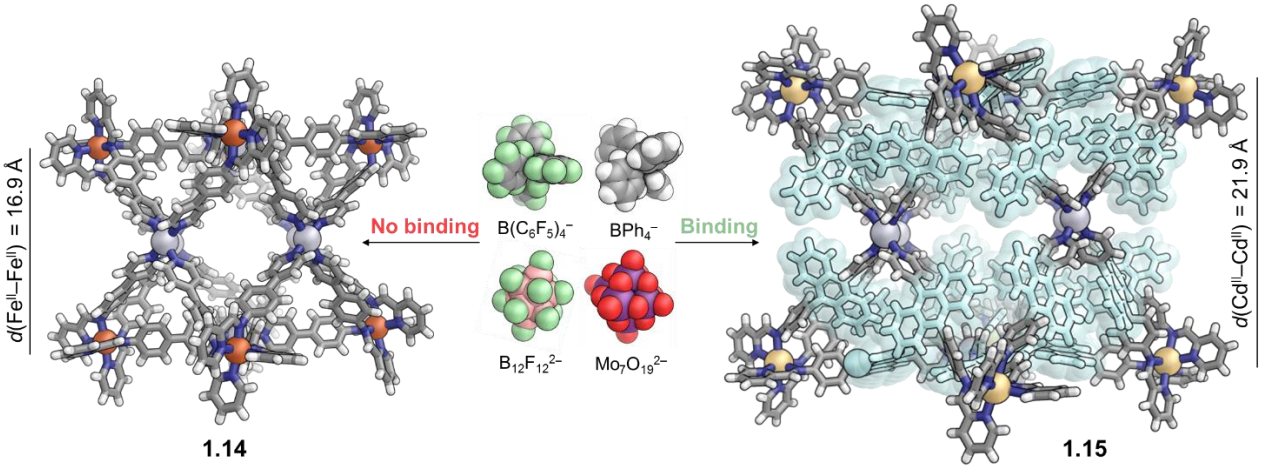

Figure 1.11 | While small structures with small aromatic spacers (**1.14**) are unable to bind guests, adding a bulky anthracene spacer (highlighted in blue) enables the encapsulation of a range of anionic species within **1.15**. Never occupying more than 11% of the cavity, guests are effectively imprisoned by the large aromatic components, which act to close off the faces of the structure and facilitate guest confinement (Cd^{II} – pale yellow).

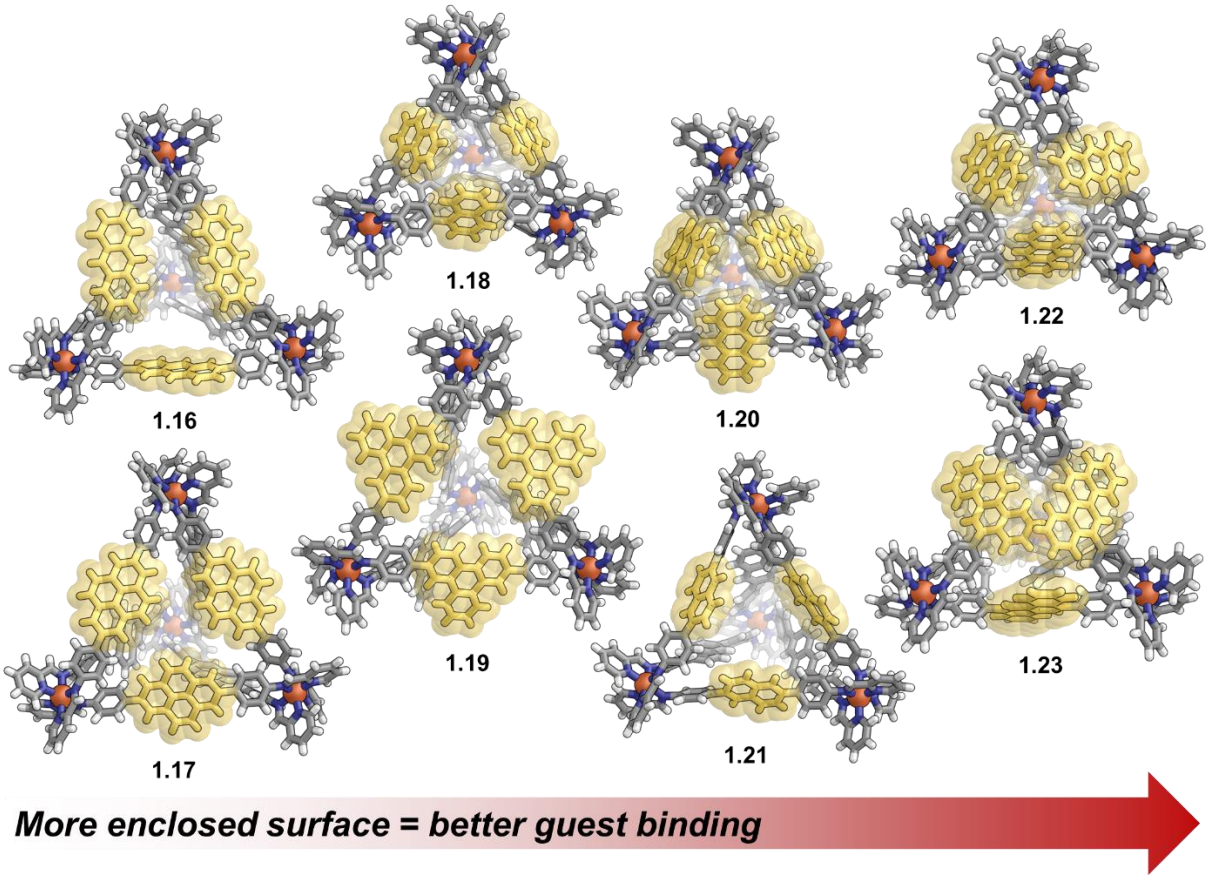

Figure 1.12 | The bulk of the aromatic unit (highlighted in yellow) installed on the ligands of tetrahedral $Fe^{II}_4L_6$ structures **1.16–1.23** were observed to tune the host-guest chemistry of the capsules. Increased steric size or ligand offset resulted in greater enclosure of the cavity, and an enhanced diversity of host-guest chemistry. Guest binding properties improved moving from **1.16** to **1.23**.

1.3.5 Unsaturated metal sites

Metallosupramolecular entities with vacant coordination sites are rare. Oftentimes, these sites are pre-installed within the ligand, enabling coordination processes to occur at the face of an architecture. When a single guest binds to multiple metal sites, guest binding is aided by the chelate effect, often leading to high association constants ($K_a > 10^{20}$ M^{-1}). Anderson *et al.* have used this approach to template the formation of metallomacrocycles installed with metalloporphyrin units.[38-40] Employing porphyrins that can bind one or more axial components enables diversity of macrocycle size and morphology: a fourfold-symmetric porphyrin template generated 4-mer macrocycle **1.24**;[41] using two sixfold-symmetric templates, 12-mer 'caterpillar-track' **1.25** was synthesised[42] (Figure 1.13). Similar metal-directed guest-binding using metalloporphyrins has been employed by de Bruin *et al.* to bind guests capable of size-selective catalysis.[43,44] The reverse situation has also been reported – cages with unsaturated coordination sites can promote the post-synthetic binding of metal ions.[45]

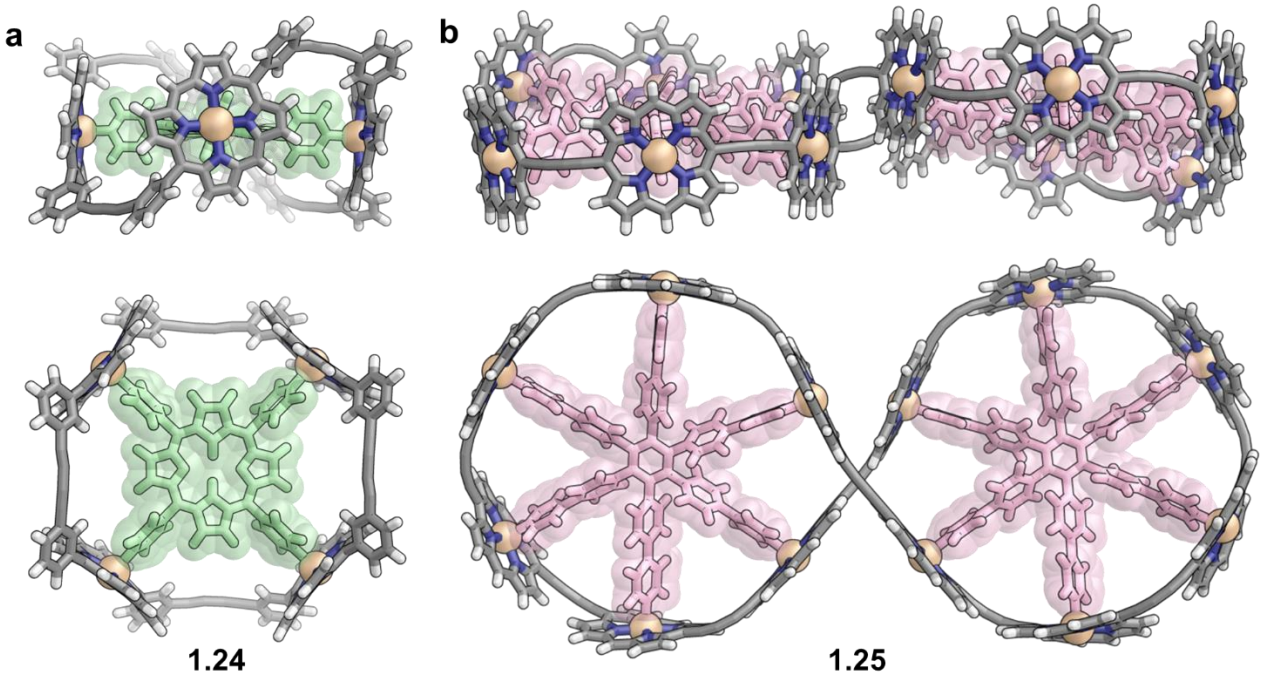

Figure 1.13 | Two views, rotated 90° with respect to each other, of two different macrocycles templated by polypyridyl guests, which coordinate to the Zn^{II} ion of porphyrin subunits. **a**, A 4-mer structure **1.24** templated by a fourfold-symmetric unit (highlighted in green). **b**, A 12-mer 'caterpillar-track' macrocycle **1.25**, templated by two sixfold-symmetric units (highlighted in pink) (Zn^{II} – pale yellow).

When a coordination sphere is saturated, vacant *d*- or *f*-orbitals can provide a site for guest stabilisation. This is particularly common in architectures with square planar nodes: either the metal is coordinatively unsaturated (as with square planar Co^{II} or Cu^{II}), or the d_{z2} orbital is unoccupied (as with square planar Pd^{II}), promoting σ-donation from the guest to metal ion. Metal-guest interactions were first described by Amouri *et al.* in a series of dimetallic structures templated by BF_4^- (Figure 1.14a&b).[46-48] Direct $M^{II}\cdots F$ interactions between host and guest could be identified in complexes

1.26 and **1.27**, which are each composed of unsaturated transition metals. Hooley *et al.* observed a similar interaction between $Pd^{II}_2L_4$ cage **1.8** and *p*-dicyanobenzene guests with polarisable nitrile functionalities (Figure 1.14c).[49] Short contacts between the Pd^{II} ions of the host and nitrogen atom of the guest were observed. The association constant was observed to scale with the solvent employed – polar solvents out-competed the guest.

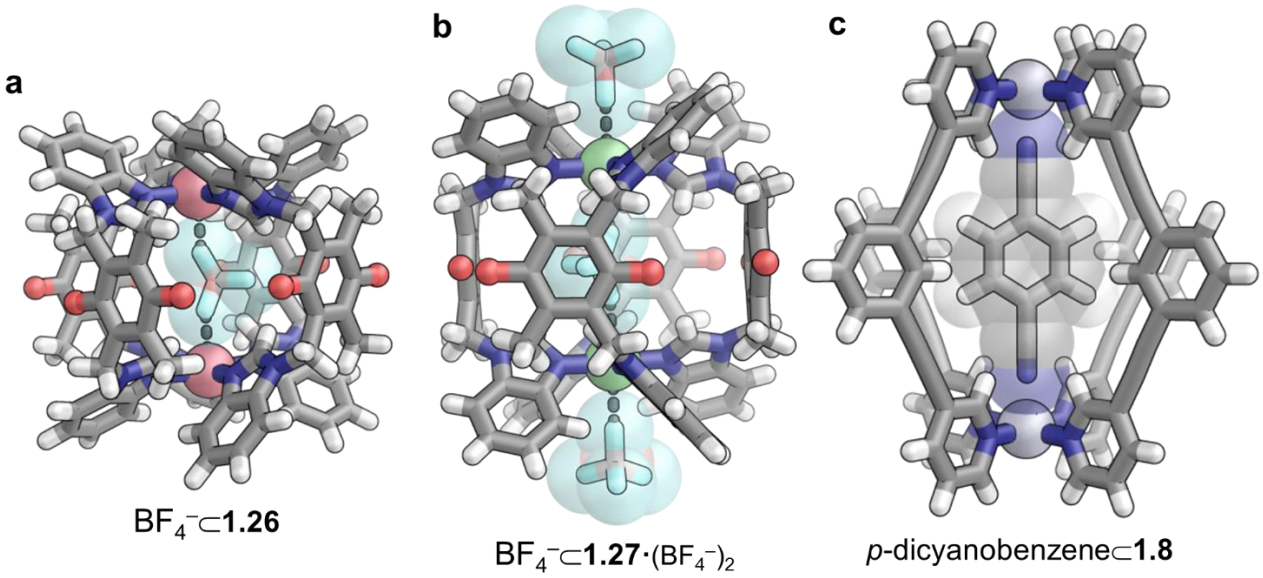

Figure 1.14 | a, $Co^{II}_2L_4$ capsule **1.26** and **b**, $Cu^{II}_2L_4$ capsule **1.27**, both of which have coordinatively unsaturated metal sites at their axial positions; BF_4^- templates these structures and binds directly to the metal ions within (short contacts between guest and metal ion are shown with black dashed lines, Co^{II} – pink, Cu^{II} – green, OMe moieties – red balls). External binding interactions between Cu^{II} and BF_4^- anions were also observed in **1.27**. **c**, *p*-Dicyanobenzene binds between the two Pd^{II} centres of **1.8**.[46,47,49]

1.4 Strategies for binding multiple guest simultaneously

When the principles listed above are applied to more complex systems of interacting molecules, guests can bind at more than one location concurrently. Allosteric communication often results, wherein guest binding affinity is altered as a result of interaction at two or more different regions synchronously. Coordination cages can be engineered to bind multiple species in multiple locations: these can be well-defined pockets in a single molecule, or anomalous external interactions with the cage. Many of the preconditions for this type of chemistry rely on the strategies detailed for single binding events. A key difference, however, is that more than one type of area or surface must be capable of interacting with guests. This ensures that guests bind to different sites of the cage with different strengths, or else engender small structural alterations that affect the size of a distal binding pocket. As such, strategies for engendering cooperativity between guests largely rely on imbuing structures with distinct regions – surfaces, voids or moieties – that are able to interact differentially with guests.

1.4.1 Engineered framework size and electronics

Coordination cages binding unexpected guest sizes or stoichiometries are often branded serendipitous; however, rules governing the binding of multiple guests in large hosts are evident. Cage **1.4** provides an ideal yardstick. Housing a cavity of *ca.* 500 Å^3, **1.4** is able to bind a single, two or four guests simultaneously (Figure 1.15a&b).[50] In each case, the maximum number of guests that can fit inside **1.4** without significant structural perturbation is observed. Here, guest binding is driven jointly by the hydrophobic effect and an electron deficient host, which work cooperatively to increase entropy (solvent displacement from the cavity) and complement the electronic properties of guests (enthalpic gains). Half of the shell of **1.4** is composed of open apertures; the thermodynamic contributions to binding are significant enough to promote guest uptake, as opposed to quick ingress/egress of guests. The same strategy was employed by Würthner *et al.*, in which the encapsulation of two fullerenes was observed in host **1.28** framed by long perylene bisimide units (Figure 1.15c). Theoretically, this host provides a poor fit for two C_{60} guests; binding was promoted by the electronic complementarity between the extended π-surface of the host and the electron-deficient guests.[51]

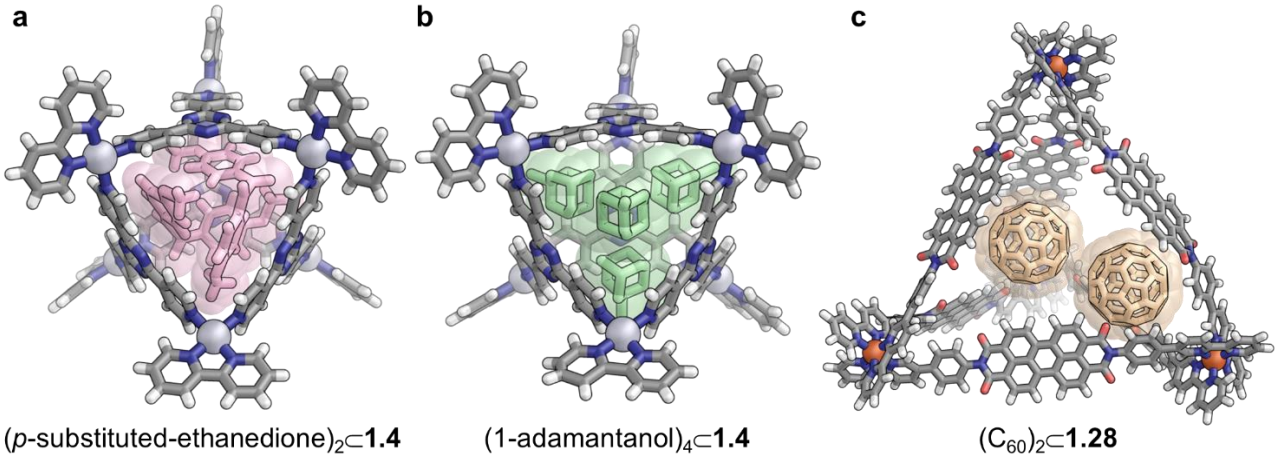

Figure 1.15 | Cage **1.4** is able to bind **a**, two or **b**, four molecules, depending on the size of the guest (guests highlighted in pink and green, respectively). **c**, Two molecules of C_{60} (highlighted in orange) can be bound within tetrahedron **1.28**, owing to the electron deficient environment surrounding the cavity.[50,51]

1.4.1.1 Overcoming Coulombic repulsion

Similar strategies can be applied to overcome the electrostatic repulsion experienced by two anions binding in proximity within a cavity.[52] In the simplest instance, proper cavity size can overcome the repulsion between guests – Sallé e*t al.* reported a synthetic host capable of binding two molecules of dianionic $B_{12}F_{12}^{2-}$, which sit in perfectly-sized pockets at either end of **1.29** (Figure 1.16a).[53] Comprehensive studies by Chifodes, Dunbar *et al.* have shown that tetramer **1.30** (synthesised in the presence of a BF_4^- template) can be converted to pentameric metallocycle **1.31**

upon recognising two SbF_6^- anions (Figure 1.16b).[54] The co-encapsulation of these two anions is due to directional anion-π bonds formed between the anionic fluorine and π-rich tetrazine units, with anion-tetrazine contacts *ca.* 0.4 Å shorter than the sum of the van der Waals radii (3.17 Å).

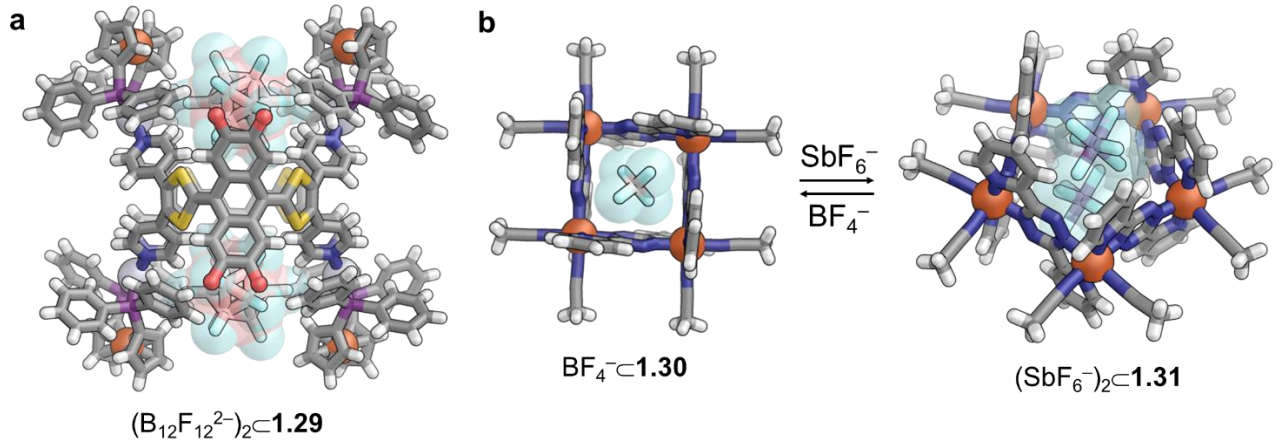

Figure 1.16 | **a**, $Pd^{II}_4L_2$ cage **1.29** binds two $B_{12}F_{12}^{2-}$ anions in two distinct regions.[53] **b**, The addition of SbF_6^- to $Fe^{II}_4L_4$ macrocycle $BF_4^-\subset$**1.30** leads to rearrangement to a larger pentameric metallocycle **1.31**, which binds two molecules of SbF_6^- internally (purple – P in **a**, and Sb in **b**).[54]

Lusby *et al.* reported that multiple anions could be bound within **1.32** by the joint electrostatic complementarity between host (positively-charged) and guest (negatively-charged), and favourable CH–X hydrogen bonds, which were hypothesised to overcome electrostatic repulsion *between* guests (Figure 1.17a&b).[55] The anticooperative encapsulation of two detergent molecules within **1.33** was described by Hardie, Fisher *et al.* – favourable interactions between the alkyl chains of the guest and the aromatic surface of the host, along with electrostatic interactions between host and guest, led to adsorption of two guests to the interior surface of the host (Figure 1.17c).[56]

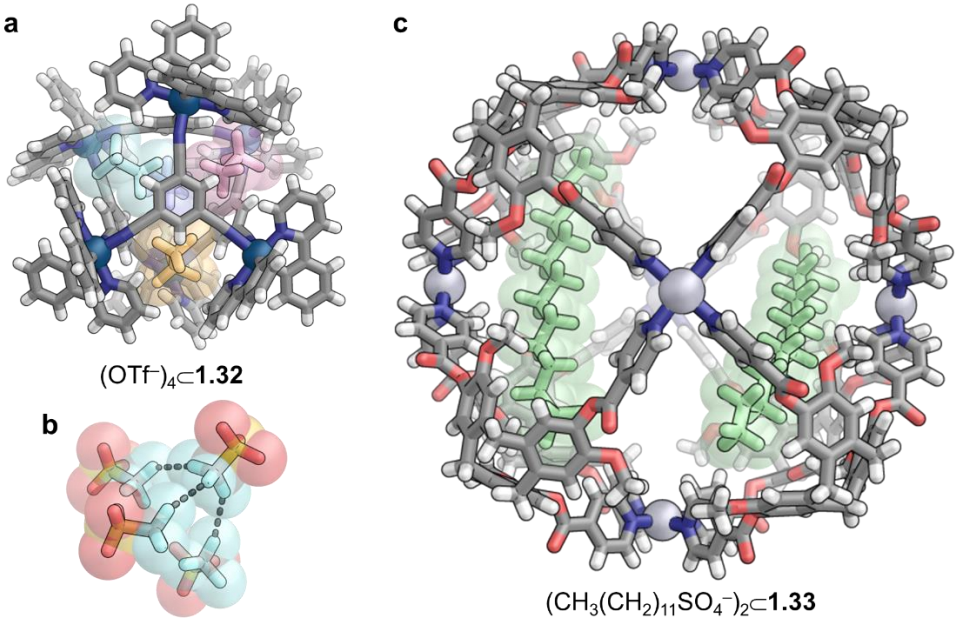

Figure 1.17 | **a**, $Ir^{II}_4L_4$ octahedron **1.32** binds four molecules of OTf^-, each highlighted with a different colour.[55] **b**, Close-up of the four OTf^- molecules bound in **1.32**, with short contacts (<3.0 Å) shown with black dashed lines (Ir^{II} – dark teal). **c**, Two detergent molecules (highlighted in green) can be bound within the voluminous cavity of $Pd^{II}_6L_8$ stellated octahedron **1.33**.[56]

1.4.2 Intermolecular interactions between guests

Initial studies into generating heterotropic guest configurations within hosts revolved around a single geometrical hypothesis: that a cavity too small for an *AA* homotropic guest pair but too large for a *BB* homotropic guest pair would trap the *AB* heterotropic guest pair selectively. Engineering heterotropic guest binding relies on multiple guests being stabilised internally by non-covalent forces, often involving hydrogen bonding and/or van der Waals interactions. The groups of Rebek and Fujita have both used this method to stabilise heterotropic guest configurations and oftentimes transform them.[57-59] In heteroleptic host **1.34**, Fujita *et al.* reported the internal encapsulation of base pair units, held together by hydrogen bonds, in an aqueous environment (Figure 1.18).[60] The hydrogen bonds between two nucleotides are usually too weak to exist in water; they are stabilised by encapsulation within the host, where water is no longer available for hydrogen-bonding with either base. Subsequent studies showed that the formation of single Watson-Crick GC base pairs was preferred over mismatched base pairs with weaker hydrogen-bonding substituents.[61]

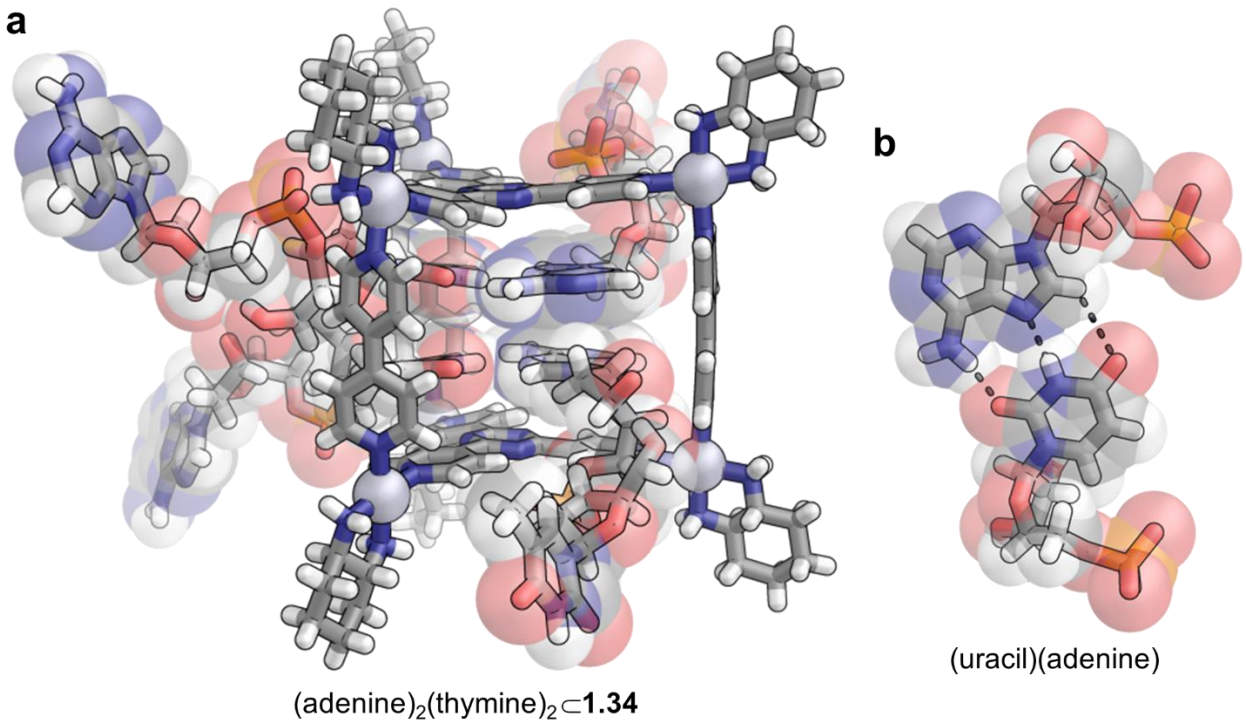

Figure 1.18 | Hydrogen bonds between nucleobase guests are stabilised in the cavity of heteroleptic $Pd^{II}_6L_2L'_3$ architecture **1.34**. **b**, An example of the complementary hydrogen bonding promoted by enclathration in a smaller heteroleptic species.[60]

Intermolecular charge transfer interactions between guests have likewise been observed upon binding in supramolecular hosts. These typically apply to heterotropic guest combinations, requiring both an electron-deficient and electron-rich guest capable of orbital overlap. Yoshizawa *et al.* demonstrated this concept in the co-encapsulation of electron-rich polyaromatics with electron-deficient boron-dipyrromethene (BODPY) dyes in **1.12**.[62] The electronic properties of the aromatic

co-guest employed were observed to tune the fluorescence wavelength of the system upon co-encapsulation – the system could be tuned on a scale from green to orange (Figure 1.19a).

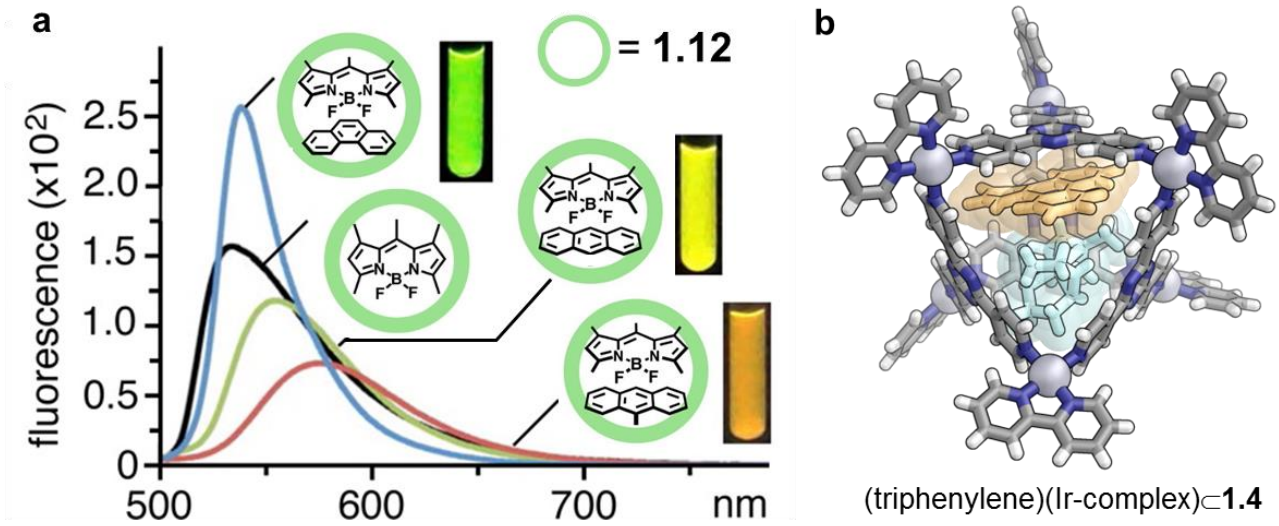

Figure 1.19 | Capsule **1.12** encapsulates two guests simultaneously, tuning the emission wavelength of the system. **b**, Two electronically-complementary guests (highlighted in orange and teal) can be encapsulated within **1.4**, leading to charge transfer between guests.[63] Figure **a** is adapted from reference 62.

Ir- and Rh-Cp-containing metal complexes can only be encapsulated in **1.4** in the presence of a co-encapsulating aromatic guest; individually, neither guest is bound (Figure 1.19b).[63] The charge transfer bands in the UV-Vis spectra of these host-guest complexes were observed to shift with the oxidation potential of the encapsulated electron-poor unit. These studies suggest that orbital overlap and electron delocalisation between guests are driving forces in the formation of hetero- rather than homo-tropic guest adducts.

1.4.3 Segregation of space

Two guests can bind in two separate spaces concurrently. Engineering this cavity division in synthetic systems is not trivial: traditional self-assembly protocols generate architectures with distinct faces or edges; the cavity is generated as a *consequence* of this process, usually as a single, continuous space. Bridging this cavity typically involves one of two strategies: 1) installing more than two parallel coordination sites on linear ligands; or 2) generating interdigitated architectures.

1.4.3.1 Multi-topic axial struts

Ligands containing more than two parallel coordination vectors enable coordination processes at both the terminal and central positions of a ligand simultaneously.[64] Lehn *et al.* first introduced this concept by generating cylindrical heteroleptic structures like **1.35**, where linear polypyridyl ligands act as axial supports for the perpendicular coordination of up to four parallel hexachelate struts

(Figure 1.20a).[65] All three cavities generated by this assembly were capable of binding small anions. The number of cavities in the resulting architecture was directly related to the number of available coordination sites on the axial ligand; the number of guests encapsulated could thus be tuned by altering the height of the cylinder.

This concept has since been adapted by the groups of Bosnich and later Crowley to co-encapsulate different molecular guests in different cavities. The technique relies on tailoring segments between each coordinating moiety within the ligand, so as to engineer multiple cavities with different interior-directing functional groups. For instance, molecular rectangle **1.36**, held together by 4,4'-bipyridine struts, contains two binding sites for small platinum complexes (Figure 1.20b).[66,67] These guests bind with positive homotropic cooperativity, where $K_1 = (1.5 \pm 0.2) \times 10^3\ M^{-1}$ and $K_2 = (5.2 \pm 0.4) \times 10^3\ M^{-1}$.

In subsequent studies, it was observed that switching from a pyridyl ring to a phenyl ring strengthened the association of triflate over cisplatin. Cage **1.37**, constructed from a ligand with both pyridyl and phenylene moieties (oriented perpendicular to the length of the cage), could thus preferentially co-encapsulate triflate in the middle cavity and cisplatin in the surrounding cavities (Figure 1.20c).[68] In this instance, placing N-donors throughout the ligand backbone that were unable to coordinate to metal ions allowed distinct cavities, each with different electronics, to form.

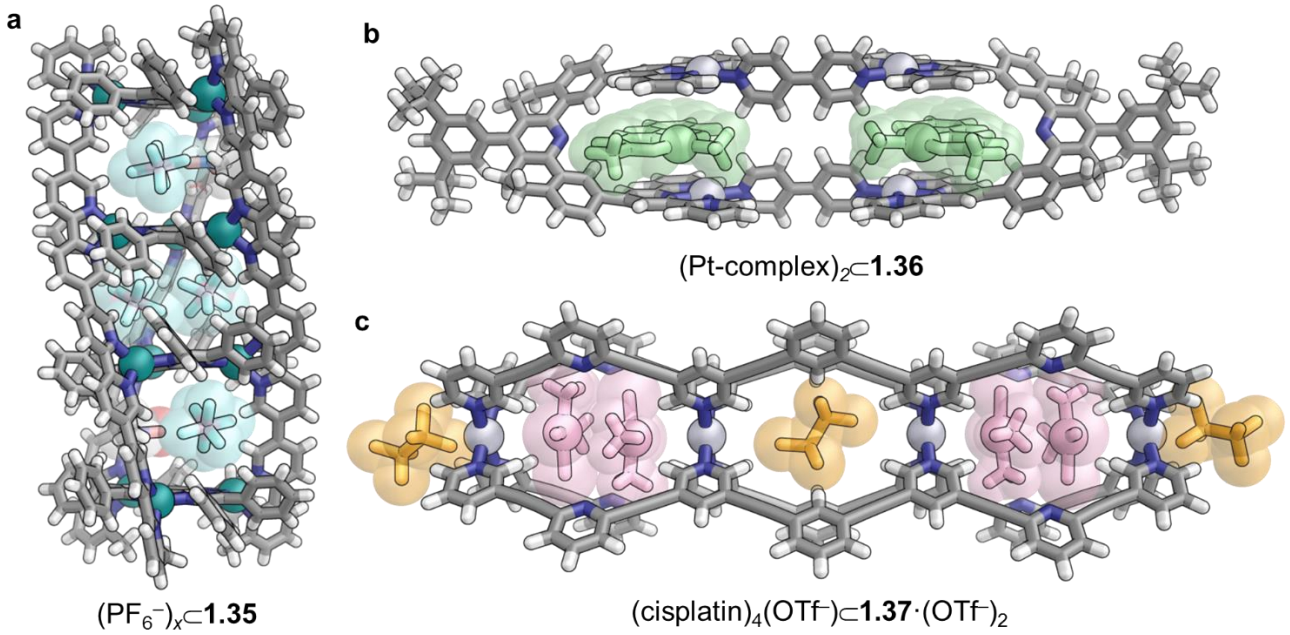

Figure 1.20 | Three structures displaying different approaches to cavity segregation, based on axial struts and ligand laddering. **a**, Heteroleptic $Cu^{I}_{12}L_3L'_4$ ladder-like complex **1.35**, made from three struts and four steps, generates three distinct cavity spaces that each bind BF_4^- (blue) (Cu^I – dark teal).[65] **b**, 4,4'-Bipyridine segregates the cavity of **1.36** into two regions that are each ideal for binding neutral Pt complexes (green).[67] **c**, In $Pd^{II}_4L_4$ tube **1.37**, sites with centrally-directing pyridyl functionalities each bind two cisplatin molecules (pink), while those with phenyl functionalities house a single triflate guest (orange), which also undergoes non-specific interactions at either end.[68]

Yoshizawa *et al.* recently extended this methodology to bind different guests in different stoichiometries in different cavities.[69] While 'molecular peanut' **1.38** is able to accommodate two fullerenes in separated cavities, a unique 1:1:2 host:guest:guest' complex results when diamantane and phenanthrene are introduced simultaneously (Figure 1.21). Molecular modelling studies suggested that this binding configuration was promoted by the changes in the volume of the second cavity upon binding a molecule in the first: binding of diamantane in Cavity 1 increased the volume of Cavity 2 by 6%; binding two molecules of phenanthrene in Cavity 2 decreased the volume of Cavity 1 by 4%. In both cases, the complementary guest was thus favoured over the homotropic guest pairing.

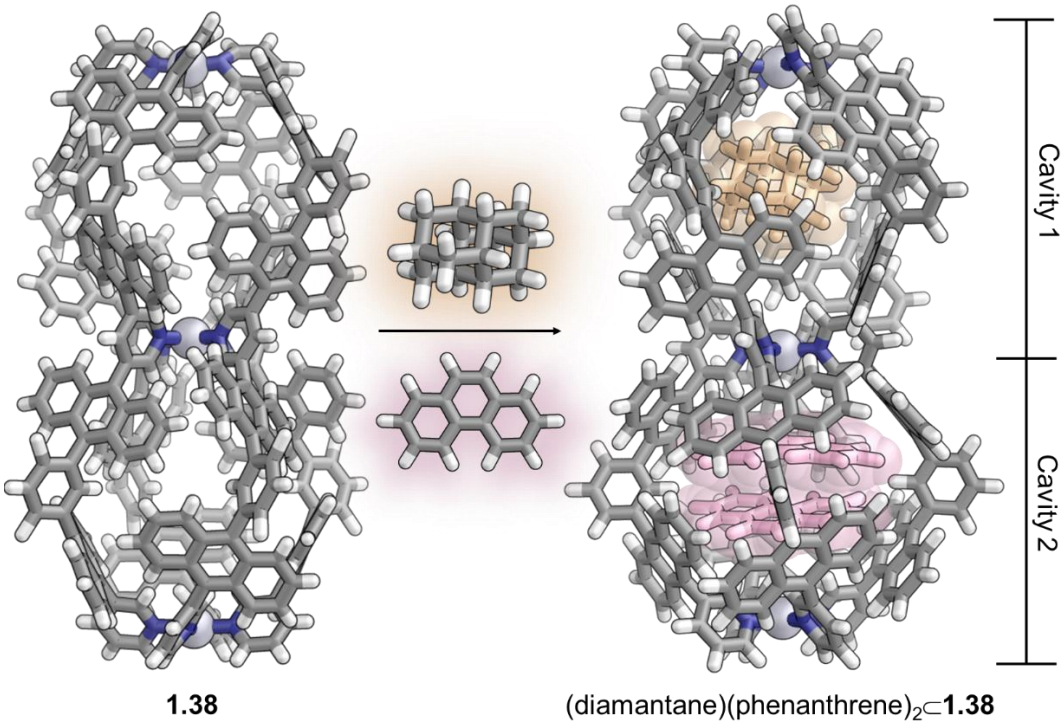

Figure 1.21 | Binding guests within $Pd^{II}_3L_4$ architecutre **1.38** leads to small contractions and expansions in respective cavities, leading to a unique quaternary host-guest adduct comprising both phenanthrene (pink) and diamanatane (orange).[69]

1.4.3.2 Interlocked cages

Interlocked architectures, by geometrical necessity, generate a minimum of three separate cavities – two voids located in the separate cages and one generated by the space between them. As with most multi-cavity structures, these assemblies tend to be cylindrical in morphology, elongated along one axis.

Fujita *et al.* have explored this space with respect to generating interlocked heteroleptic cages from combinations of two- and three-fold symmetric ligands (Figure 1.22). The first example of this structure type was composed of two interlocked heteroleptic M_3LL' cages; however, the favourable π-interactions between ligands resulted in a compressed, void-less assembly.[70] The extrapolation of

this approach to employing axial ligands of different lengths enabled up to five pyrene molecules to be bound in three different cavities. Altering the length of the axial ligand altered the size of the middle cavity, and thus the number of molecules that could be bound (Figure 1.22a&b). Importantly, the two terminal cavities generated by this process were only ever observed to bind single molecules: altering the ligand length only changed the number of molecules that could be bound in the middle cavity. These multi-cavity interlocked structures were furthermore only observed when pyrene was present during synthesis.

Clever *et al.* and others have generated a series of catenated cages based on M_2L_4 structure-types with banana-shaped ligands (Figure 1.22c&d).[71] Depending on the angle of the ligand bend, along with the substituents located at the centre of the ligands, these assemblies can bind two or three guests in different cavities. Subtle changes in the ligand or template can lead to significant changes in the cavity size of the central, as compared to the peripheral, guest binding sites. Allosteric regulation of anion binding often results.

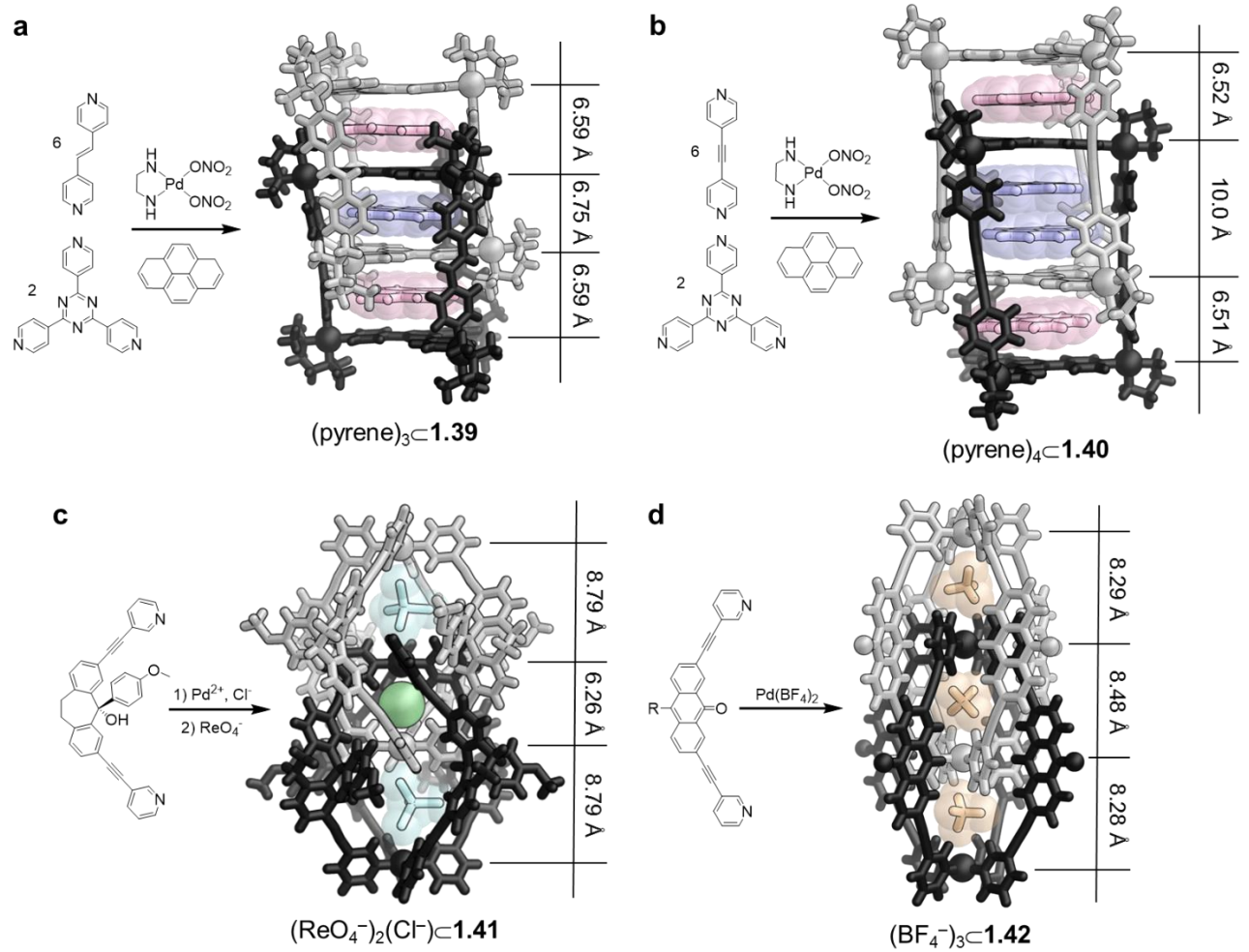

Figure 1.22 | Interlocked architectures for multiple guest binding events, where three separate cavities are generated by self-assembly. Structures **a**, **1.39** and **b**, **1.40** each bind different stoichiometries of pyrene (pink and blue guest), depending on the length of the twofold-symmetric ligand.[72] Similarly, structures **c**, **1.41** and **d**, **1.42** bind different guests depending on the angle of the ligand (ReO_4^- – teal, Cl^- – green, BF_4^- – orange). The presence of templating units (such as Cl^- in **c**) leads to contraction of the middle cavity, enabling access to heterotropic guest combinations.[73] The two interdigitated cages are shown in black and grey for each structure.

Jeong *et al.* synthesised folded metallocycle **1.43** capable of binding two guests in symmetrical cavities, based on segregating the intermolecular forces installed on the ligand[74] (Figure 1.23). The bent geometry of **1.43** directs its pre-installed hydrogen bond donors into the separated cavities, enabling small molecules with hydrogen bond accepting units to be bound. Minimal cooperativity changes were observed upon changing the length of alkynyl chain over which ligands cross – the segregation of donating units alone drives association, irrespective of the cavity size.

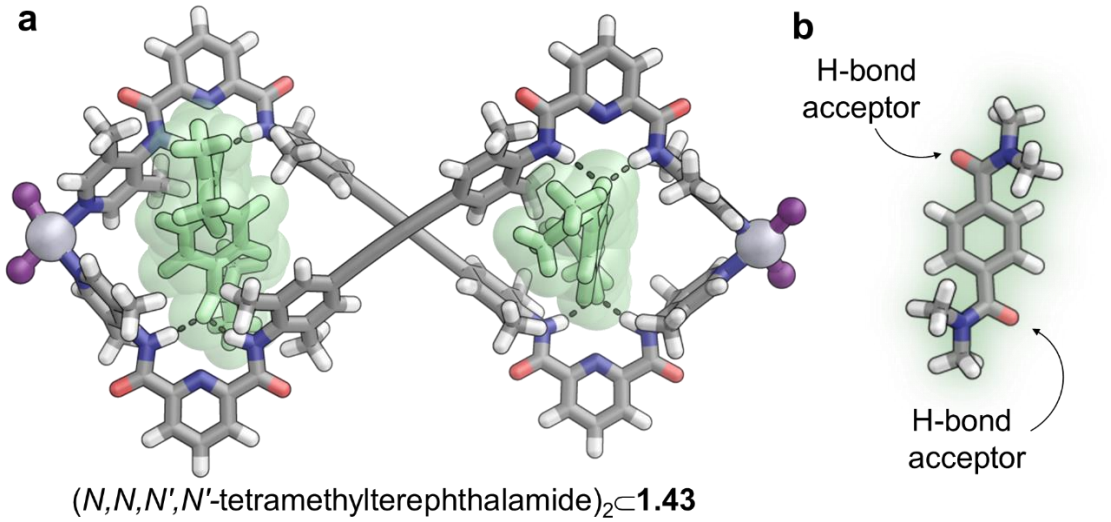

Figure 1.23 | **a**, $Pd^{II}_2L_2$ folded metallocycle **1.43** binds two molecules of *N*,*N*,*N*′,*N*′-tetramethylterephthalamide (green) in two separate pockets, owing to the segregated nature of the NH donors present on each ligand. **b**, Schematic of the guest showing the binding sites that complement the NH donors of **1.43**.[74]

Multi-cavity architectures solve an enduring problem associated with large hollow assemblies, wherein large void volumes prevent site-specific interactions between molecules. They also enable an unprecedented mode of tunability of the number and shape of these cavities, by simply changing the number of coordination sites within an axial ligand, and the spacing between these sites. They are, however, currently exclusive to specific geometries, cylindrical architectures in particular. Other interlocked cage topologies have been reported, but the heavy overlap of ligands within these structures renders them unsuitable for guest binding.[75]

1.4.4 Structural adaptation

Formal biological allostery relies on small configurational changes altering the size or shape of binding pockets: one binding event causes a (often small) structural change in the receptor, leading to an improvement or weakening of secondary binding events at a distant site. Supramolecular complexes that can adapt their morphology or cavity size in response to one guest binding event are thus attractive for tailoring the space available for a second guest. Clever *et al.* have realised this concept in a series of catenated cages, taking advantage of three unique cavities created by two joined cages.[76] Synthesised with three BF_4^- anions occupying its pockets, **1.42** can alter its respective cavity

sizes upon the introduction of two halide guests (Br^- or Cl^-): the top and bottom cavities contract to accommodate the anions, while the central cavity, still holding a BF_4^- anion, enlarges (Figure 1.24). The resulting expansion of the central cavity weakens the affinity for BF_4^-, enabling the replacement of this anion for a neutral benzene molecule.

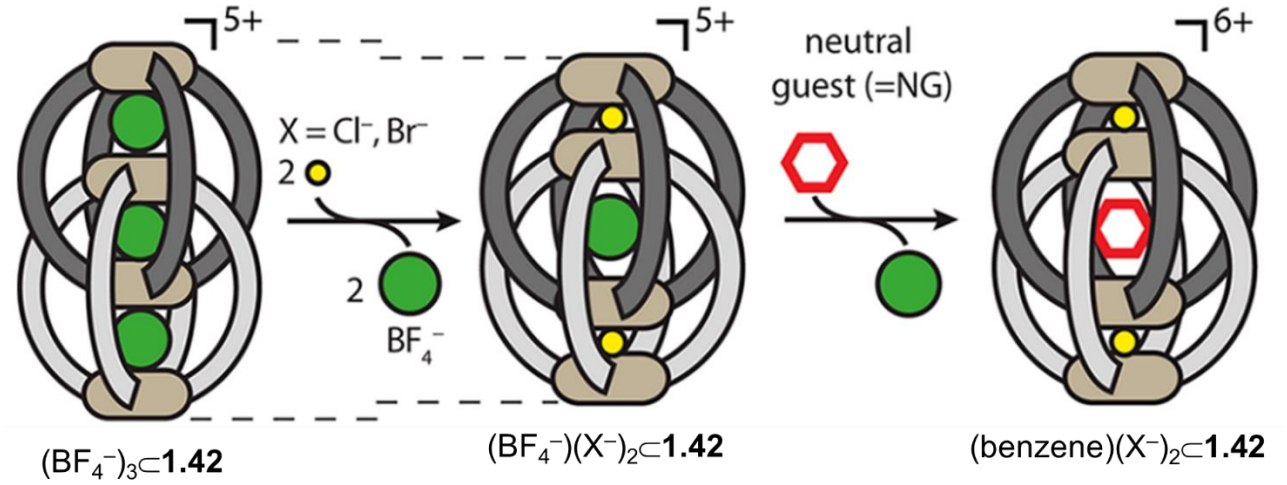

Figure 1.24 | Schematic representation of how halide binding in the outer pockets of **1.42** triggers the uptake of a neutral guest molecule in the central pocket. Figure adapted from reference 76.

Severin *et al.* have also reported a capsule that can bind two guests concurrently: assembly **1.44** expands upon recognising two coronene or two perylene molecules, altering from a void-less structure to one with a cavity of *ca.* 500 $Å^3$ (Figure 1.25).[77] Here, the binding of guests promotes a re-organisation of the binding configuration reinforcing **1.44**, wherein the carboxylic acid functionalities on the naphthalene ligand change from an approximate horizontal to vertical arrangement upon guest recognition. This mechanism for cavity expansion takes advantage of flexible connections between the metal atoms and the ligand, enabling reorganisation processes reminiscent of the 'conformational selection' and 'induced fit' mechanisms observed in some biological receptors.

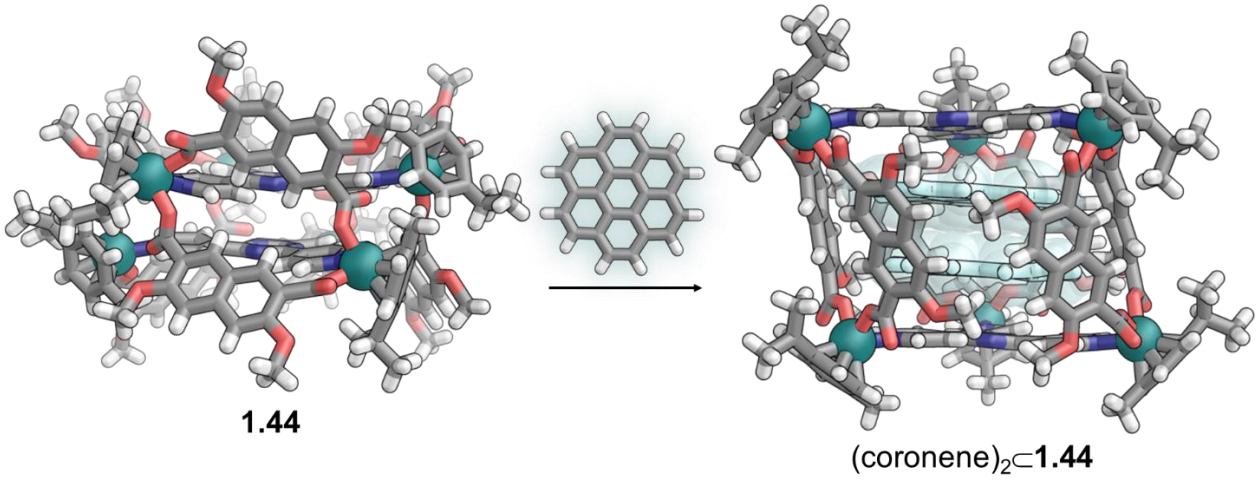

Figure 1.25 | The addition of coronene (blue) to heteroleptic $Ru^{II}L_2L'_6$ architecture **1.44** results in restructuring of the equatorial ligands, leading to cavity expansion and binding of two guests internally (Ru^{II} – dark teal).[77]

1.4.5 Through-cage communication

Nitschke *et al.* have taken advantage of two distinct binding sites around the periphery of cubic capsule **1.45** to regulate the binding activity of anions bound internally.[78,79] This method relies on the formation of distinct binding environments around the periphery of the capsule, providing ideal regions for the association of different guests: neutral planar phosphines were observed to associate with a face of the cube; anionic BPh_4^- associated with a cleft formed by adjacent faces; and $Mo_2O_7^{2-}$ bound to the internal Mo^{II} sites (Figure 1.26). Binding at either peripheral location of **1.45** universally decreased the affinity of a subsequently internally-binding $Mo_2O_7^{2-}$ anion, providing a system of allosteric inhibition.

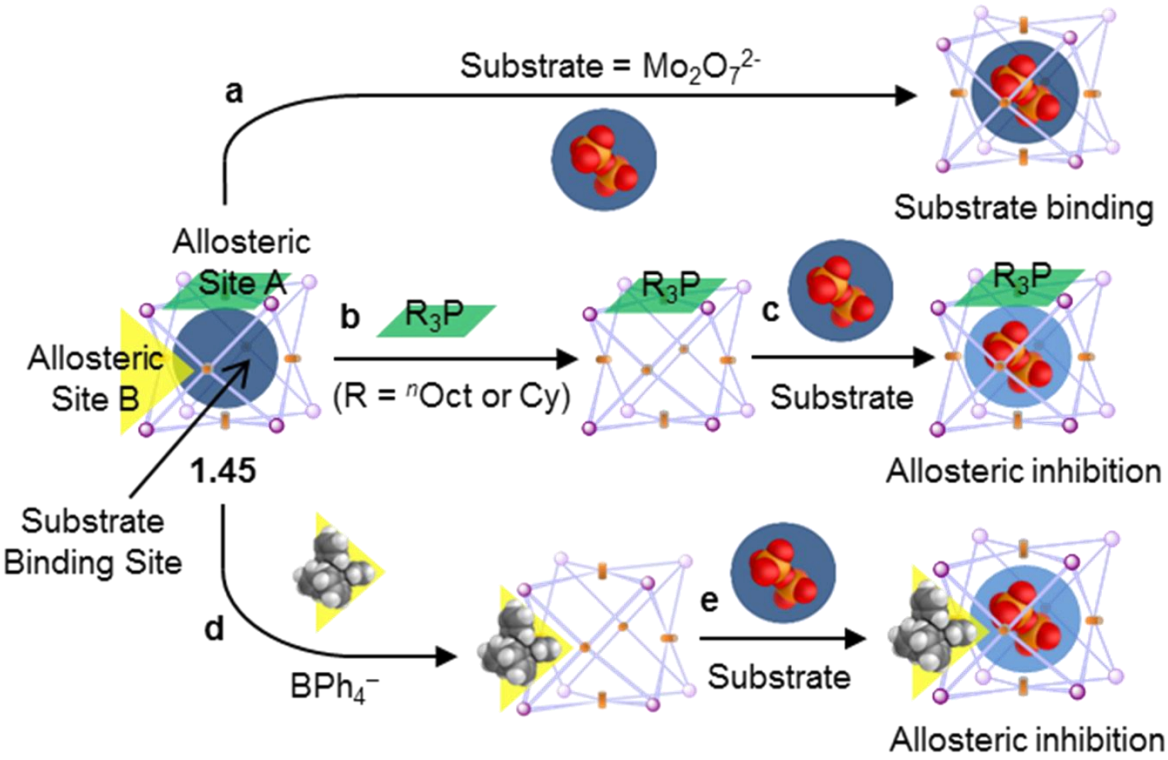

Figure 1.26 | **a,** The dimolybdate anion ($Mo_2O_7^{2-}$) was found to bind internally to **1.45** with high affinity, but when **b**, tricyclohexylphosphine (PCy_3) or tri-*n*-octylphosphine ($^nOct_3P$) coordinated to an exterior face (allosteric site A) or **d**, BPh_4^- associated with the edge (allosteric site B), the binding affinity of $Mo_2O_7^{2-}$ was found to decrease substantially (**c** and **e**, respectively). Figure adapted from reference 79.

Raymond *et al.* explored this concept more generally in water-soluble host **1.5**, detailing that the exterior binding of guests was an enthalpic process, whereas internal encapsulation had been shown to be entropically driven.[24] Recently, these findings were extrapolated to multiple external binding events around the periphery of **1.5**, reinforcing their conclusions: that the locale of binding determined the thermodynamic driving force (Figure 1.27).[80] Entropy drove internal binding, whereas external binding was governed by changes in enthalpy.

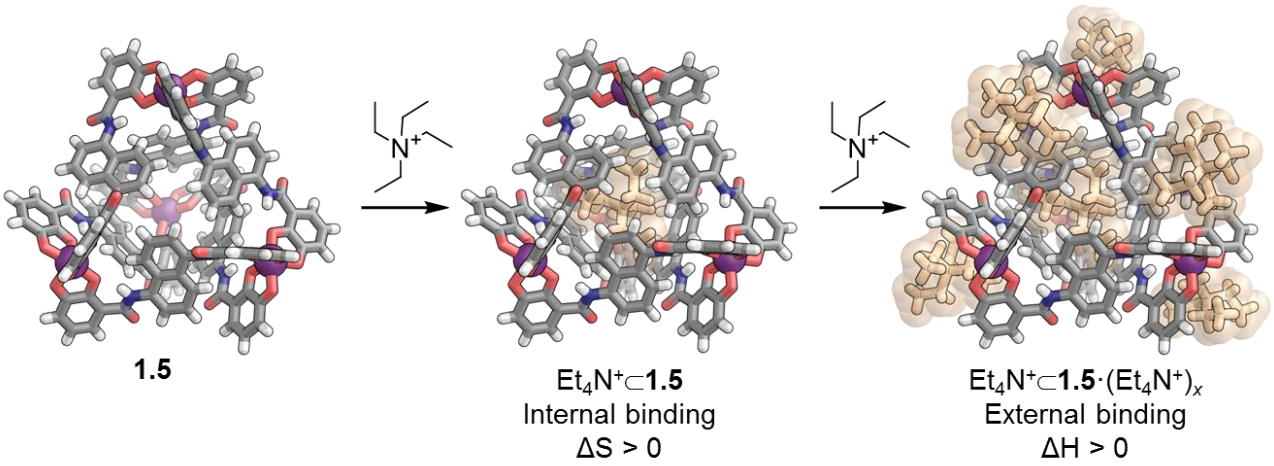

Figure 1.27 | The binding of Et_3N^+ guests (orange) inside **1.5** is entropically favourable; the binding of guests to the external faces of **1.5** is enthalpically favourable. External binding events (K_a = 10^2 M^{-1}) occur with a lower affinity than internal ones (K_a = 10^4 M^{-1}).[23]

1.4.6 Metal coordination

Direct coordination to unsaturated metal sites can be used to promote through-bond electronic communication between the host and guest, regulating the behaviour of subsequent binding events. Aida, Tashira *et al.* reported the preparation of cyclic architecture **1.46**, constructed from a set of cofacial diporphyrin units enclosing a central cavity (Figure 1.28).[81] The arrangement of these metal sites promoted positive heterotropic cooperativity: the co-encapsulation of one diamine molecule with one molecule of C_{60} was favoured over the binding of homotropic guest configurations, which displayed anticooperative binding.

The coordination sphere of metal ions in supramolecular constructs is sometimes completed with coordinating anions or solvent molecules. These can be displaced: Shionoya *et al.* reported an octahedron wherein anions coordinated to the internally-facing sites could be exchanged for *p*-toluenesulfonimide anions; the exterior-facing anions remained triflate.[82] More recently, Nitschke *et al.* used coordinatively unsaturated Cd^{II} sites in $Cd^{II}_4L_2$ receptor **1.47** to cooperatively load and release croconate guests (Figure 1.29).[83] The binding of one guest molecule between two unsaturated Cd^{II} sites led to a configuration better adapted to bind a second guest, leading to positive cooperativity.

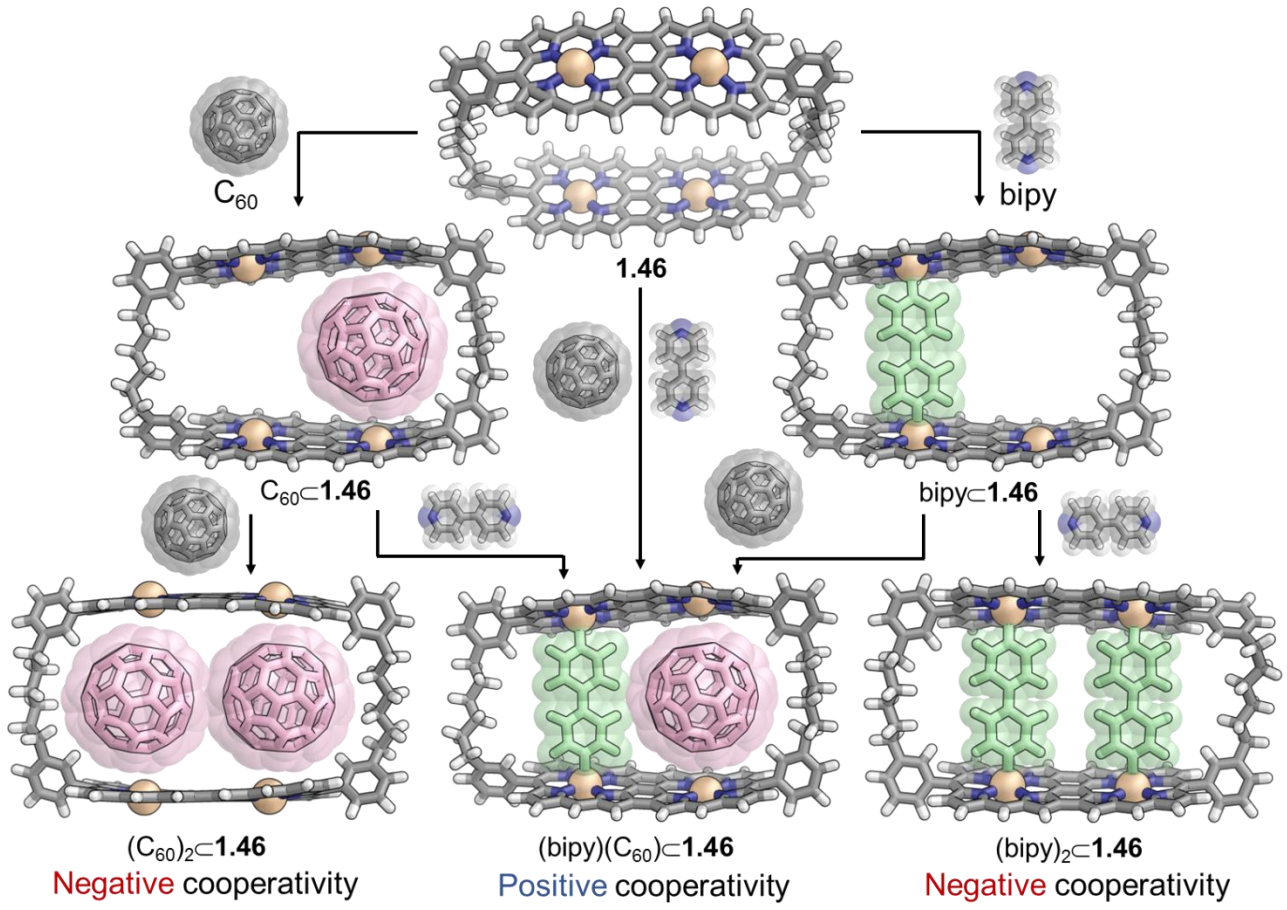

Figure 1.28 | The binding of C_{60} (pink) and 4,4'-bipyridne (bipy, green) guests was observed to proceed by different modes of cooperativity with macrocycle **1.46**, depending on whether a homotropic or heterotropic guest pair was bound. Negative cooperativity was observed for homotropic guest pairing; positive cooperativity was observed for heterotropic guest pairing (Zn^{II} – light yellow).[81]

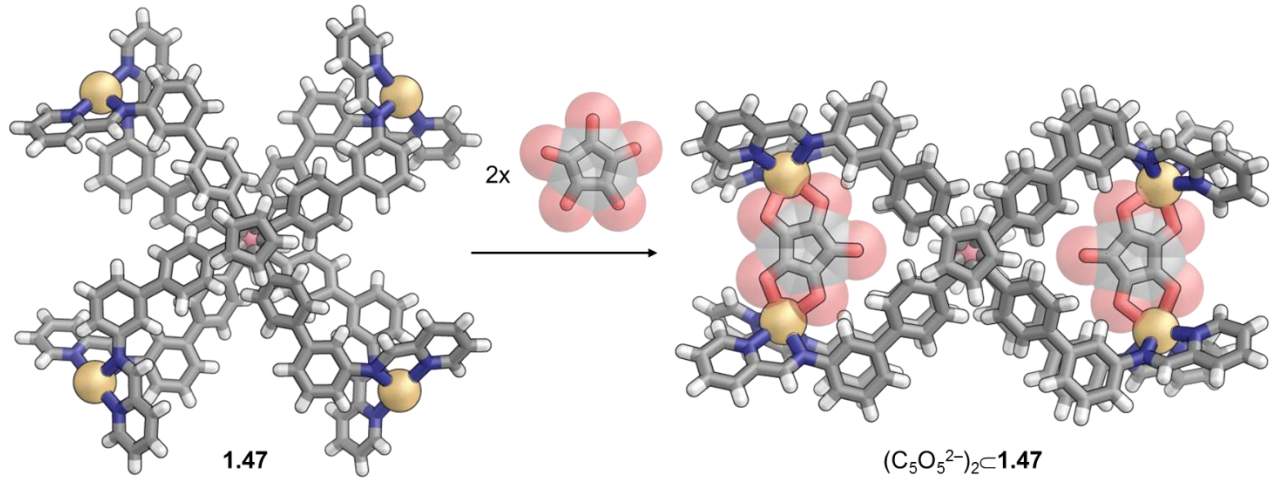

Figure 1.29 | The addition of croconate anions ($C_5O_5^{2-}$) to **1.47** induced a cooperative structural rearrangement to bind guests at previously-unsaturated Cd^{II} sites (the coordination sphere of Cd^{II} is completed with MeCN and H_2O in the crystal structure of **1.47**) (Cd^{II} – light yellow).[83]

1.5 Applications of multiple guest bindings: beyond allostery

Beyond the use of allosteric sites for the modulation of binding affinity, binding sites away from the central cavity of coordination cages can engender unique forms of synthetic, structural, and dynamic chemistry.

1.5.1 Architectural templation

Prime among the advantages of non-central binding configurations is their ability to promote the generation of novel architectural arrays. Nitschke *et al.* have demonstrated the power of this technique in the generation of a series of *mer*-cornered D_x-symmetric architectures based on C_2 symmetric ligands (Figure 1.30).[84,85] In all cases, specific anions located in the peripheral pockets of architectures **1.48–1.50** are necessary for their generation; the anions collectively template the formation of these structures, and the displacement of these anions leads to structural rearrangement. In the largest case, seven anions are required to template **1.50**: six are located in aperture pockets, while one is observed in the central cavity. The size of peripheral cavities in **1.50** scales with the ionic radius of the metal ions, allowing pocket size to scale with different assembling components.[84]

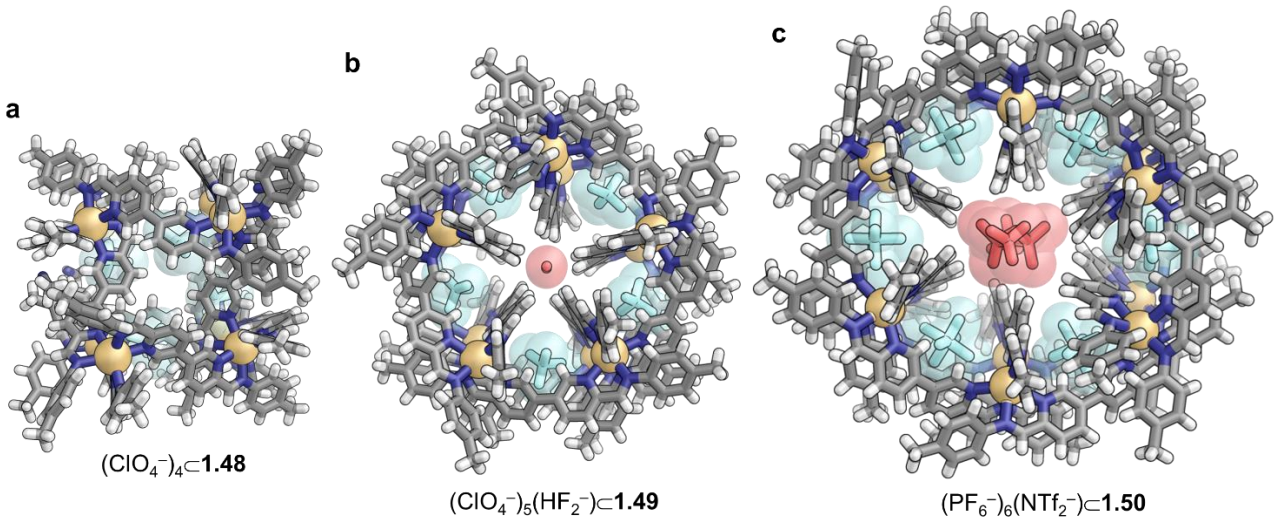

Figure 1.30 | Barrel-like architectures are template by internal (red) and peripheral (blue) anions. **a**, D_4-symmetric $Cd^{II}_8L_{12}$ structure **1.48** is template by four ClO_4^- anions. **b**, D_5-symmetric $Cd^{II}_{10}L_{15}$ structure **1.49** is template by five peripherally-bound ClO_4^- anions and one centrally-bound HF_2^- anion. **c**, D_6-symmetric $Cd^{II}_{12}L_{18}$ structure **1.50** is templated by six peripherally-bound PF_6^- anions and one centrally-bound NTf_2^- anion.

These architectures can also bind two sulfonated guests at their pentagonal faces. Inserting structural congeners of **1.49** into ion channels enables the free-flow of chloride though the central channel; adding dodecylsulfate (which binds non-cooperatively to the pentagonal faces) leads to a current gating effect, where the guest blocks the movement of chloride though the channel.[86]

A simpler version of this templation concept was shown by Lützen *et al*. in the generation of twisted architecture **1.51**, based on 1,1'-bi-2-naphthol (BINOL) cores (Figure 1.31a).[87] Two molecules of BF_4^- template this unique structure, sitting in opposite corners. Fujita *et al.* also demonstrated this concept in the generation of **1.52**, where two aromatic, anionic guests (biphenylcarboxylate) template a tubular structure (Figure 1.31b).[88] The guests in this cage cap the ends of the tube, rather than bind centrally. Uniquely, a void is formed in the centre of both these structures. No guests occupy these cavities in solution, suggesting that this technique may enable subsequent guest encapsulation phenomena.

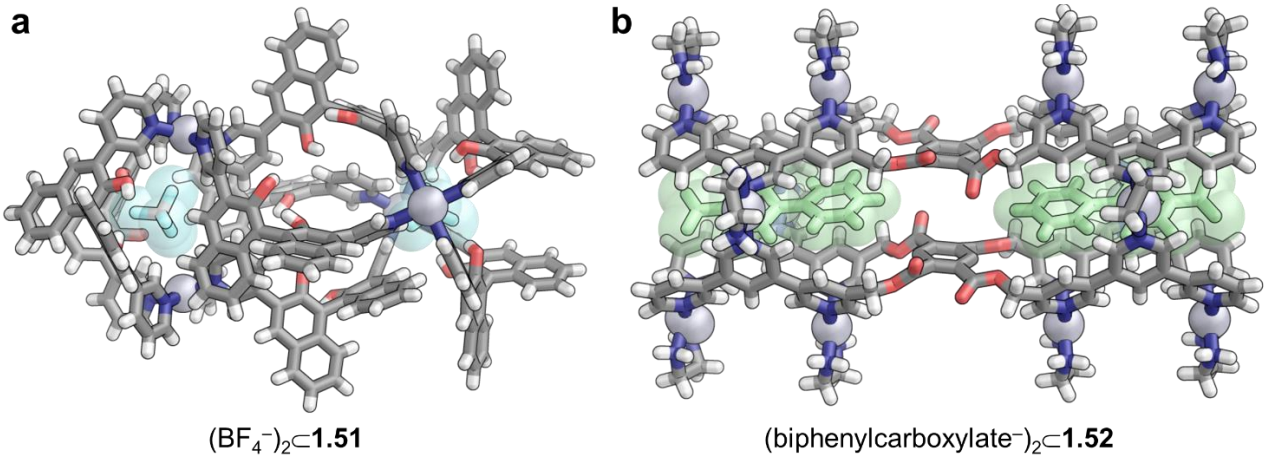

Figure 1.31 | **a**, Enantiomerically-pure $Pd^{II}_4L_8$ cage **1.51** binds two BF_4^- anions (blue), proximal to the Pd^{II} ions.[87] **b**, $Pd^{II}_{12}L_2$ tube **1.52** is templated by two molecules of biphenylcarboxylate (green), which sit at either end of the structure.[88]

1.5.2 New modes of synthetic chemistry

The ability to confine two molecules in proximity enables chemistry within synthetic cavities, in the fashion of enzymes.[89,90] Diels-Alder cyclisation reactions inside self-assembled architectures are particularly prevalent. The first example of this strategy was reported in an organic host by Rebek *et al.*;[57] a similar procedure was subsequently used by Fujita *et al.* to synthesise cyclised products using either thermal or photochemical stimuli (Figure 1.32).[89] Many reactions such as these proceed due to a decrease in the free energy associated with transition states, often *via* the geometric stabilisation of a reactive intermediary. The confinement (and oftentimes the enforced orientation) of these molecules during reaction makes coordination cages particularly ideal for size- and regio-selective bi- or tri-molecular reactions.

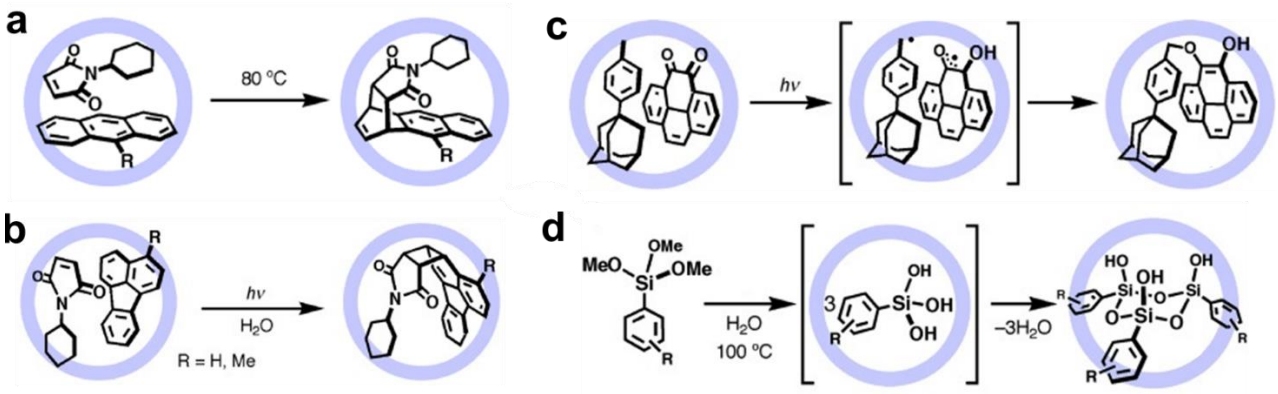

Figure 1.32 | Different reactions promoted within the cavity of **1.4** (purple circle): **a**, thermally-activated Diels-Alder reaction; **b**, light-activated asymmetric [2+2] dimerisation; **c**, regio- and stereo-selective bimolecular radical addition; and **d**, the polycondensation of trialkyoxysilanes. Figure adapted from reference 89.

Cage **1.53**, reported by Mukherjee *et al.*, is capable of binding two aldehyde-substituted aromatic guests, followed by their condensation with Meldrum's acid *in situ* (Figure 1.33).[91] The Knoevenagel condensation that occurs within **1.53** is in essence a dehydration reaction; due to the hydrophobic nature of the cavity, water is easily eliminated from the central pocket, driving the reaction forwards. Diels-Alder reactions also occurred with bound heterotropic guest pairs.

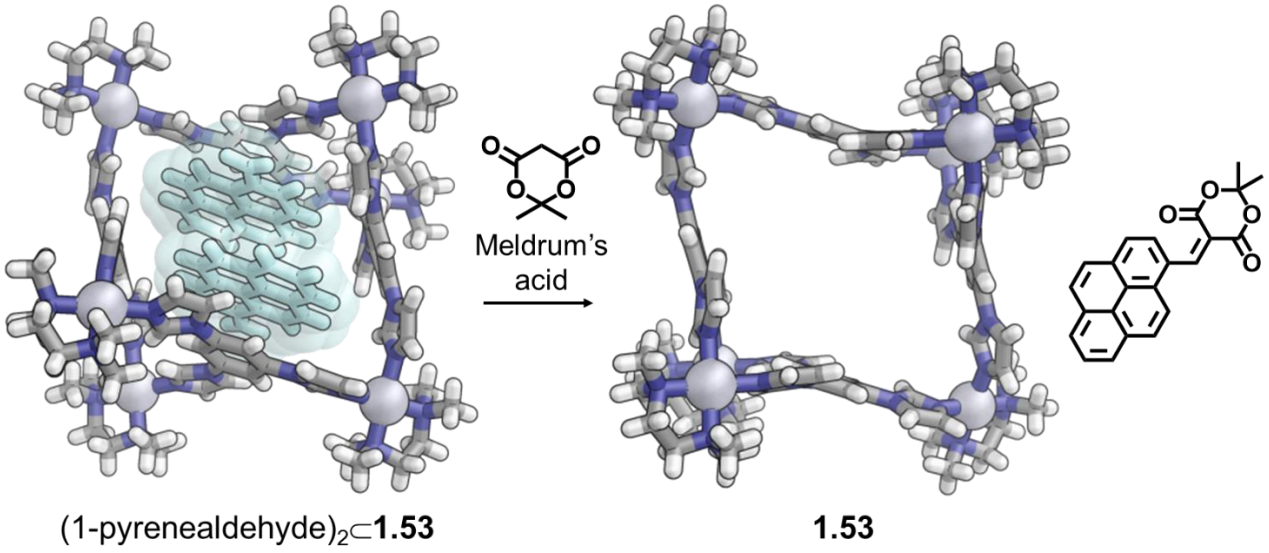

Figure 1.33 | The Knoevenagel condensation of 1-pyrenealdehyde (teal) with Meldrum's acid occurs catalytically within **1.53** due to the hydrophobic expulsion of H_2O generated in the cavity during the reaction.

Recent catalytic pathways have approached chemical transformations from an electrostatic perspective, employing the peripheral windows of architectures, and the positive charge of the coordination complex, to enforce the proximity of hydroxide ions at allosteric binding sites, promoting catalytic interactions with bound guests. Cage **1.1** catalyses the Kemp elimination with

high efficiency by employing the increased local concentration of OH^- around its open apertures (Figure 1.34a).[92] Turnover within the system is driven by the change in charge of the guest from neutral to anionic; while the starting material is hydrophobic and binds with high affinity to **1.1**, the product of the reaction is hydrophilic, and is thus ejected from the cage upon completion of the catalysis (Figure 1.34b).

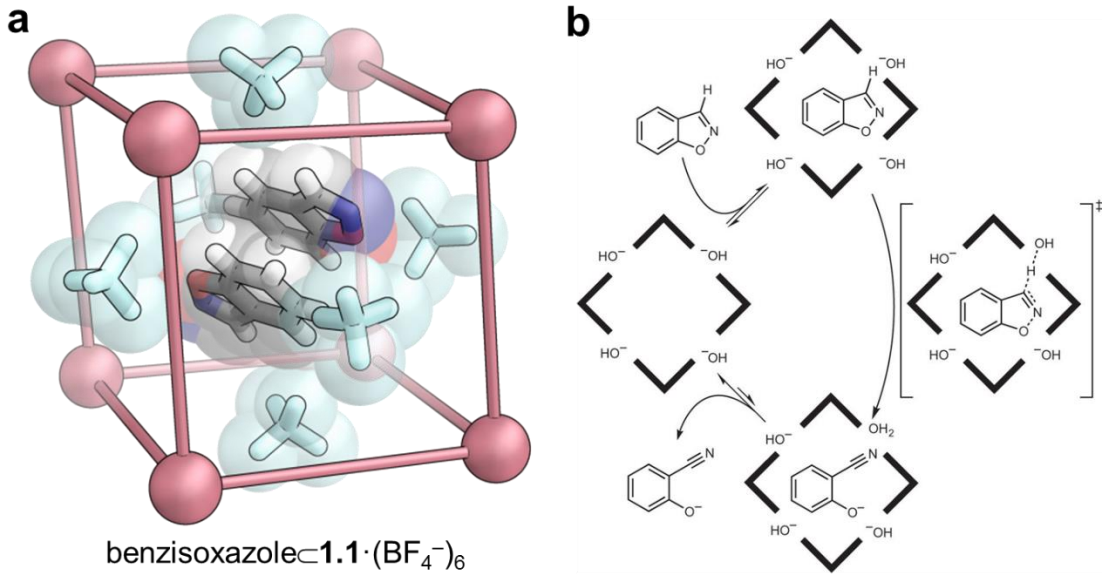

Figure 1.34 | The Kemp elimination within the cavity of **1.1**. **a**, The crystal structure of benzisoxazole⊂**1.1**, where every open aperture of **1.1** is occupied by a BF_4^- anion (teal), suggesting strong electrostatic attraction between the host and small negatively-charged species (like OH^-) in solution (the cubic framework generated by the Co^{II} ions is highlighted with pink lines; two guest orientations, each with 50% occupancy, are displayed). **b**, Cartoon representation of the catalytic reaction cycle, where bound benzisoxazole is polarised by the cage, transformed to anionic 2-cyanophenolate upon reaction with OH^- at the apertures of **1.1**, and is subsequently ejected from the cage. Figure **b** is adapted from reference 92.

1.5.3 Structural rearrangements

The interconversion of one structure to another is often driven by the association of guests;[93,94] however, it remains rare that this process is concerted, involving more than one templating unit. Kuroda *et al.* reported the ability of two naphthalenesulfonate anions to induce the transformation of interdigitated cage **1.54** to its monomeric form **1.55**, a process that could be reversed by adding NO_3^-, which occupied three separate pockets of the catenane (Figure 1.35a).[95,96] More recently, interconversion between macrocycle sizes was reported by Sun *et al.*: different anions were observed to template structures ranging from 4 to 9 repeat units in size.[97] Importantly, two or more anions were often necessary to accomplish these conversions, with the models used suggesting an induced fit of the guests, akin to substrate recognition by enzymes.

Conversion between an interlocked and single architecture was also demonstrated by Chi *et al.* using two electron-rich moieties (Figure 1.35b).[98] Alone, two cages interpenetrate to generate **1.56**,

but the addition of pyrene molecules leads to formation of cage **1.57**, housing two bound guest molecules, with both edge-to-face and face-to-face aromatic interactions between the host and guest being identified.

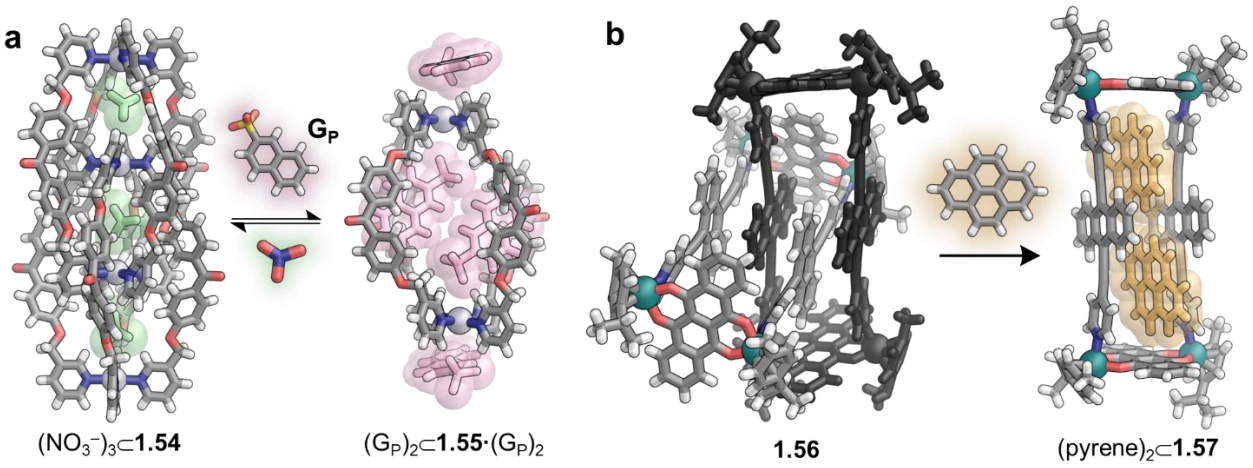

Figure 1.35 | **a**, Transformation between interdigitated $Pd^{II}_4L_8$ structure **1.54** and non-catenated $Pd^{II}_2L_4$ cage **1.55** was induced by the addition of naphthalenesulfonate (G_P, pink); the reverse reaction could be induced by adding NO_3^- (green). **b**, Interdigitated $Ru^{II}_8L_4L'_4$ assembly **1.56** can be converted irreversibly to $Ru^{II}_4L_2L'_2$ cage **1.57** by the templation of two pyrene guests (orange).

1.6 Aims and objectives

The binding of multiple guests within a single entity can lead to new modes of host-guest interactions and new applications for supramolecular chemistry. With the aim of developing modular systems that can promote and adapt to allosteric binding events, this thesis presents a series of investigations into the structural and functional consequences of binding more than one guest in more than one location within coordination cages. In particular, emphasis will be placed on engendering cooperativity between guest species, with a view towards generating new molecular architectures and novel modes of guest binding. New structural motifs, and methods of engendering function from these configurations, will form much of the focus of this thesis.

As the formal definition of allostery relates exclusively to the *regulation* of guest binding events, this thesis introduces the concept of 'allosteric interactions' between networked components of complex systems, wherein different modes of non-central guest binding, and the applications to which these novel interactions can be put, are included. This thesis will show that promoting allosteric interactions in coordination cages can lead to new templation methods, tuneable modes of intermolecular cooperativity, adaptive structural reorganisations, metal-complex stabilisation and the emergence of unique electrochemical properties.

1.7 References

[1] Papin, J.A., Hunter, T., Palsson, B.O., and Subramaniam, S., *Nat. Rev. Mol. Cell Biol.*, **2005**, 6, 99-111.

[2] Krauss, G., *Biochemistry of Signal Transduction and Regulation*. 2014: Wiley.

[3] Monod, J., Wyman, J., and Changeux, J.-P., *J. Mol. Biol.*, **1965**, 12, 88-118.

[4] Motlagh, H.N., Wrabl, J.O., Li, J., and Hilser, V.J., *Nature*, **2014**, 508, 331-339.

[5] Wootten, D., Christopoulos, A., and Sexton, P.M., *Nat. Rev. Drug Discov.*, **2013**, 12, 630-644.

[6] Whitesides, G.M. and Boncheva, M., *Proc. Natl. Acad. Sci. USA*, **2002**, 99, 4769-4774.

[7] Lehn, J.-M., *Chem. Soc. Rev.*, **2017**, 46, 2378-2379.

[8] Lehn, J.-M., *Proc. Natl. Acad. Sci. USA*, **2002**, 99, 4763-4768.

[9] Saalfrank, R.W., Maid, H., and Scheurer, A., *Angew. Chem. Int. Ed.*, **2008**, 47, 8794-8824.

[10] Voloshin, Y., Belaya, I., and Krämer, R., *The Encapsulation Phenomenon: Synthesis, Reactivity and Applications of Caged Ions and Molecules*. 2016: Springer International Publishing.

[11] Gale, Philip A., Howe, Ethan N.W., and Wu, X., *Chem*, **2016**, 1, 351-422.

[12] Chakrabarty, R., Mukherjee, P.S., and Stang, P.J., *Chem. Rev.*, **2011**, 111, 6810-6918.

[13] Northrop, B.H., Chercka, D., and Stang, P.J., *Tetrahedron*, **2008**, 64, 11495-11503.

[14] Yoshizawa, M. and Klosterman, J.K., *Chem. Soc. Rev.*, **2014**, 43, 1885-1898.

[15] Mecozzi, S. and Rebek, J.J., *Chem. – Eur. J.*, **1998**, 4, 1016-1022.

[16] Turega, S., Cullen, W., Whitehead, M., Hunter, C.A., and Ward, M.D., *J. Am. Chem. Soc.*, **2014**, 136, 8475-8483.

[17] Paul, R.L., Argent, S.P., Jeffery, J.C., Harding, L.P., Lynam, J.M., and Ward, M.D., *Dalton Trans.*, **2004**, 3453-3458.

[18] Han, M., Michel, R., He, B., Chen, Y.-S., Stalke, D., John, M., and Clever, G.H., *Angew. Chem. Int. Ed.*, **2013**, 52, 1319-1323.

[19] Roberts, D.A., Pilgrim, B.S., and Nitschke, J.R., *Chem. Soc. Rev.*, **2018**, 47, 626-644.

[20] Suzuki, K., Takao, K., Sato, S., and Fujita, M., *J. Am. Chem. Soc.*, **2010**, 132, 2544-2545.

[21] Grunwald, E. and Steel, C., *J. Am. Chem. Soc.*, **1995**, 117, 5687-5692.

[22] Yoshizawa, M., Kusukawa, T., Kawano, M., Ohhara, T., Tanaka, I., Kurihara, K., Niimura, N., and Fujita, M., *J. Am. Chem. Soc.*, **2005**, 127, 2798-2799.

[23] Leung, D.H., Bergman, R.G., and Raymond, K.N., *J. Am. Chem. Soc.*, **2008**, 130, 2798-2805.

[24] Sgarlata, C., Mugridge, J.S., Pluth, M.D., Tiedemann, B.E.F., Zito, V., Arena, G., and Raymond, K.N., *J. Am. Chem. Soc.*, **2010**, 132, 1005-1009.

[25] Metherell, A.J., Cullen, W., Williams, N.H., and Ward, M.D., *Chem. – Eur. J.*, **2018**, 24, 1554-1560.

[26] Biedermann, F., Uzunova, V.D., Scherman, O.A., Nau, W.M., and De Simone, A., *J. Am. Chem. Soc.*, **2012**, 134, 15318-15323.

[27] Bolliger, J.L., Ronson, T.K., Ogawa, M., and Nitschke, J.R., *J. Am. Chem. Soc.*, **2014**, 136, 14545-14553.

[28] Bilbeisi, R.A., Ronson, T.K., and Nitschke, J.R., *Angew. Chem. Int. Ed.*, **2013**, 52, 9027-9030.

[29] Wise, M.D., Holstein, J.J., Pattison, P., Besnard, C., Solari, E., Scopelliti, R., Bricogne, G., and Severin, K., *Chem. Sci.*, **2015**, 6, 1004-1010.

[30] Liu, Y., Sengupta, A., Raghavachari, K., and Flood, A.H., *Chem*, **2018**, 3, 411-427.

[31] August, D.P., Nichol, G.S., and Lusby, P.J., *Angew. Chem. Int. Ed.*, **2016**, 55, 15022-15026.

[32] Szaloki, G., Croue, V., Allain, M., Goeb, S., and Salle, M., *Chem. Commun.*, **2016**, 52, 10012-10015.

[33] Szalóki, G., Croué, V., Carré, V., Aubriet, F., Alévêque, O., Levillain, E., Allain, M., Aragó, J., Ortí, E., Goeb, S., and Sallé, M., *Angew. Chem. Int. Ed.*, **2017**, 129, 16490-16494.

[34] Colomban, C., Szalóki, G., Allain, M., Gómez, L., Goeb, S., Sallé, M., Costas, M., and Ribas, X., *Chem. – Eur. J.*, **2017**, 23, 3016-3022.

[35] Kishi, N., Li, Z., Yoza, K., Akita, M., and Yoshizawa, M., *J. Am. Chem. Soc.*, **2011**, 133, 11438-11441.

[36] Ramsay, W.J., Szczypiński, F.T., Weissman, H., Ronson, T.K., Smulders, M.M.J., Rybtchinski, B., and Nitschke, J.R., *Angew. Chem. Int. Ed.*, **2015**, 54, 5636-5640.

[37] Ronson, T.K., Meng, W., and Nitschke, J.R., *J. Am. Chem. Soc.*, **2017**, 139, 9698-9707.

[38] O'Sullivan, M.C., Sprafke, J.K., Kondratuk, D.V., Rinfray, C., Claridge, T.D.W., Saywell, A., Blunt, M.O., O'Shea, J.N., Beton, P.H., Malfois, M., and Anderson, H.L., *Nature*, **2011**, 469, 72-75.

[39] Liu, P., Hisamune, Y., Peeks, M.D., Odell, B., Gong, J.Q., Herz, L.M., and Anderson, H.L., *Angew. Chem. Int. Ed.*, **2016**, 55, 8358-8362.

[40] Rickhaus, M., Vargas Jentzsch, A., Tejerina, L., Grübner, I., Jirasek, M., Claridge, T.D.W., and Anderson, H.L., *J. Am. Chem. Soc.*, **2017**, 139, 16502-16505.

[41] Anderson, S., Anderson, H.L., Bashall, A., McPartlin, M., and Sanders, J.K.M., *Angew. Chem. Int. Ed.*, **1995**, 34, 1096-1099.

[42] Liu, S., Kondratuk, D.V., Rousseaux, S.A.L., Gil-Ramírez, G., O'Sullivan, M.C., Cremers, J., Claridge, T.D.W., and Anderson, H.L., *Angew. Chem. Int. Ed.*, **2015**, 54, 5355-5359.

[43] Otte, M., Kuijpers, P.F., Troeppner, O., Ivanović-Burmazović, I., Reek, J.N.H., and de Bruin, B., *Chem. – Eur. J.*, **2014**, 20, 4880-4884.

[44] Otte, M., Kuijpers, P.F., Troeppner, O., Ivanović-Burmazović, I., Reek, J.N.H., and de Bruin, B., *Chem. – Eur. J.*, **2013**, 19, 10170-10178.

[45] Resendiz, M.J.E., Noveron, J.C., Disteldorf, H., Fischer, S., and Stang, P.J., *Org. Lett.*, **2004**, 6, 651-653.

[46] Amouri, H., Mimassi, L., Rager, M.N., Mann, B.E., Guyard-Duhayon, C., and Raehm, L., *Angew. Chem. Int. Ed.*, **2005**, 44, 4543-4546.

[47] Amouri, H., Desmarets, C., Bettoschi, A., Rager, M.N., Boubekeur, K., Rabu, P., and Drillon, M., *Chem. – Eur. J.*, **2007**, 13, 5401-5407.

[48] Desmarets, C., Policar, C., Chamoreau, L.-M., and Amouri, H., *Eur. J. Inorg. Chem.*, **2009**, 2009, 4396-4400.

[49] Liao, P., Langloss, B.W., Johnson, A.M., Knudsen, E.R., Tham, F.S., Julian, R.R., and Hooley, R.J., *Chem. Commun.*, **2010**, 46, 4932-4934.

[50] Kusukawa, T. and Fujita, M., *J. Am. Chem. Soc.*, **2002**, 124, 13576-13582.

[51] Mahata, K., Frischmann, P.D., and Würthner, F., *J. Am. Chem. Soc.*, **2013**, 135, 15656-15661.

[52] He, Q., Tu, P., and Sessler, J.L., *Chem*, **2018**, 4, 46-93.

[53] Croué, V., Goeb, S., Szalóki, G., Allain, M., and Sallé, M., *Angew. Chem. Int. Ed.*, **2016**, 55, 1746-1750.

[54] Chifotides, H.T., Giles, I.D., and Dunbar, K.R., *J. Am. Chem. Soc.*, **2013**, 135, 3039-3055.

[55] Chepelin, O., Ujma, J., Wu, X., Slawin, A.M.Z., Pitak, M.B., Coles, S.J., Michel, J., Jones, A.C., Barran, P.E., and Lusby, P.J., *J. Am. Chem. Soc.*, **2012**, 134, 19334-19337.

[56] Cookson, N.J., Henkelis, J.J., Ansell, R.J., Fishwick, C.W.G., Hardie, M.J., and Fisher, J., *Dalton Trans.*, **2014**, 43, 5657-5661.

[57] Kang, J. and Rebek Jr, J., *Nature*, **1997**, 385, 50-52.

[58] Kang, J., Hilmersson, G., Santamaría, J., and Rebek, J., *J. Am. Chem. Soc.*, **1998**, 120, 3650-3656.

[59] Yoshizawa, M., Tamura, M., and Fujita, M., *Science*, **2006**, 312, 251-254.

[60] Sawada, T., Yoshizawa, M., Sato, S., and Fujita, M., *Nat. Chem.*, **2009**, 1, 53-56.

[61] Sawada, T. and Fujita, M., *J. Am. Chem. Soc.*, **2010**, 132, 7194-7201.

[62] Yamashina, M., Sartin, M.M., Sei, Y., Akita, M., Takeuchi, S., Tahara, T., and Yoshizawa, M., *J. Am. Chem. Soc.*, **2015**, 137, 9266-9269.

[63] Leenders, S.H.A.M., Becker, R., Kumpulainen, T., de Bruin, B., Sawada, T., Kato, T., Fujita, M., and Reek, J.N.H., *Chem. – Eur. J.*, **2016**, 22, 15468-15474.

[64] Vasdev, R.A.S., Preston, D., and Crowley, J.D., *Chem. – Asian J.*, **2017**, 12, 2513-2523.

[65] Baxter, P.N.W., Lehn, J.-M., Kneisel, B.O., Baum, G., and Fenske, D., *Chem. – Eur. J.*, **1999**, 5, 113-120.

[66] Crowley, J.D., Goshe, A.J., and Bosnich, B., *Chem. Commun.*, **2003**, 2824-2825.

[67] Crowley, J.D., Steele, I.M., and Bosnich, B., *Eur. J. Inorg. Chem.*, **2005**, 2005, 3907-3917.

[68] Preston, D., Lewis, J.E.M., and Crowley, J.D., *J. Am. Chem. Soc.*, **2017**, 139, 2379-2386.

[69] Yazaki, K., Akita, M., Prusty, S., Chand, D.K., Kikuchi, T., Sato, H., and Yoshizawa, M., *Nat. Commun.*, **2017**, 8, 15914.

[70] Fujita, M., Fujita, N., Ogura, K., and Yamaguchi, K., *Nature*, **1999**, 400, 52-55.

[71] Han, M., Engelhard, D.M., and Clever, G.H., *Chem. Soc. Rev.*, **2014**, 43, 1848-1860.

[72] Yamauchi, Y., Yoshizawa, M., and Fujita, M., *J. Am. Chem. Soc.*, **2008**, 130, 5832-5833.

[73] Freye, S., Michel, R., Stalke, D., Pawliczek, M., Frauendorf, H., and Clever, G.H., *J. Am. Chem. Soc.*, **2013**, 135, 8476-8479.

[74] Chang, S.-Y., Jang, H.-Y., and Jeong, K.-S., *Chem. – Eur. J.*, **2004**, 10, 4358-4366.

[75] Lu, Y., Deng, Y.-X., Lin, Y.-J., Han, Y.-F., Weng, L.-H., Li, Z.-H., and Jin, G.-X., *Chem*, **2017**, 3, 110-121.

[76] Löffler, S., Lübben, J., Krause, L., Stalke, D., Dittrich, B., and Clever, G.H., *J. Am. Chem. Soc.*, **2015**, 137, 1060-1063.

[77] Mirtschin, S., Slabon-Turski, A., Scopelliti, R., Velders, A.H., and Severin, K., *J. Am. Chem. Soc.*, **2010**, 132, 14004-14005.

[78] Ramsay, W.J., Ronson, T.K., Clegg, J.K., and Nitschke, J.R., *Angew. Chem. Int. Ed.*, **2013**, 52, 13439-13443.

[79] Ramsay, W.J. and Nitschke, J.R., *J. Am. Chem. Soc.*, **2014**, 136, 7038-7043.

[80] Sgarlata, C. and Raymond, K.N., *Anal. Chem.*, **2016**, 88, 6923-6929.

[81] Sato, H., Tashiro, K., Shinmori, H., Osuka, A., Murata, Y., Komatsu, K., and Aida, T., *J. Am. Chem. Soc.*, **2005**, 127, 13086-13087.

[82] Hiraoka, S., Harano, K., Shiro, M., Ozawa, Y., Yasuda, N., Toriumi, K., and Shionoya, M., *Angew. Chem. Int. Ed.*, **2006**, 45, 6488-6491.

[83] Gan, Q., Ronson, T.K., Vosburg, D.A., Thoburn, J.D., and Nitschke, J.R., *J. Am. Chem. Soc.*, **2015**, 137, 1770-1773.

[84] Riddell, I.A., Ronson, T.K., Clegg, J.K., Wood, C.S., Bilbeisi, R.A., and Nitschke, J.R., *J. Am. Chem. Soc.*, **2014**, 136, 9491-9498.

[85] Riddell, I.A., Smulders, M.M.J., Clegg, J.K., Hristova, Y.R., Breiner, B., Thoburn, J.D., and Nitschke, J.R., *Nat. Chem.*, **2012**, 4, 751-756.

[86] Haynes, C.J.E., Zhu, J., Chimerel, C., Hernández-Ainsa, S., Riddell, I.A., Ronson, T.K., Keyser, U.F., and Nitschke, J.R., *Angew. Chem. Int. Ed.*, **2017**, 56, 15388-15392.

[87] Klein, C., Gütz, C., Bogner, M., Topić, F., Rissanen, K., and Lützen, A., *Angew. Chem. Int. Ed.*, **2014**, 53, 3739-3742.

[88] Tashiro, S., Tominaga, M., Kusukawa, T., Kawano, M., Sakamoto, S., Yamaguchi, K., and Fujita, M., *Angew. Chem. Int. Ed.*, **2003**, 42, 3267-3270.

[89] Yoshizawa, M., Klosterman, J.K., and Fujita, M., *Angew. Chem. Int. Ed.*, **2009**, 48, 3418-3438.

[90] Zarra, S., Wood, D.M., Roberts, D.A., and Nitschke, J.R., *Chem. Soc. Rev.*, **2015**, 44, 419-432.

[91] Samanta, D., Mukherjee, S., Patil, Y.P., and Mukherjee, P.S., *Chem. – Eur. J.*, **2012**, 18, 12322-12329.

[92] Cullen, W., Misuraca, M.C., Hunter, C.A., Williams, N.H., and Ward, M.D., *Nat. Chem.*, **2016**, 8, 231-236.

[93] Wood, D.M., Meng, W., Ronson, T.K., Stefankiewicz, A.R., Sanders, J.K.M., and Nitschke, J.R., *Angew. Chem. Int. Ed.*, **2015**, 54, 3988-3992.

[94] Wang, S., Sawada, T., Ohara, K., Yamaguchi, K., and Fujita, M., *Angew. Chem. Int. Ed.*, **2016**, 55, 2063-2066.

[95] Sekiya, R., Fukuda, M., and Kuroda, R., *J. Am. Chem. Soc.*, **2012**, 134, 10987-10997.

[96] Sekiya, R. and Kuroda, R., *Chem. Commun.*, **2011**, 47, 12346-12348.

[97] Zhang, T., Zhou, L.-P., Guo, X.-Q., Cai, L.-X., and Sun, Q.-F., *Nat. Commun.*, **2017**, 8, 15898.

[98] Lee, H., Elumalai, P., Singh, N., Kim, H., Lee, S.U., and Chi, K.-W., *J. Am. Chem. Soc.*, **2015**, 137, 4674-4677.

Chapter 2

Materials and methods

2.1 General

Unless otherwise specified, all reagents were purchased from commercial sources and used as received. For electrochemical experiments, dry solvents were purchased from Sigma-Aldrich and purged with argon before use, and *n*Bu_4NPF_6 was recrystallised three times from absolute EtOH. 2-Formylphenanthroline,[1] $Cd(OTf)_2$,[2] $Co(OTf)_2$,[3] $Co(NTf_2)_2 \cdot 6H_2O$,[3] Zn- and Ni-centered tetra(*p*-aminophenyl)porphyrins (**5A** and **6D**, respectively),[4] triamine **6C**,[5] di(4-pyridyl)-naphthalenediimide **G6**,[6] macrocycle **G7**,[7] macrocycle **G8**,[8] metalated tetra(4-pyridyl)porphyrin adducts **G2-G4**,[9] **6.3**[10] and **7.1**[11] were synthesised following literature procedures. **G7** and **G8** were synthesised by Dr Sam Black, and **6C** was synthesised by Dr Angela Grommet.

2.2 Nuclear Magnetic Resonance (NMR) spectroscopy

NMR spectra were recorded using a 400 MHz Avance III HD Smart Probe (routine and wide-sweep ^{1}H NMR), DCH 500 MHz dual cryoprobe (high-resolution ^{13}C and 2D experiments), DPX S5 500 MHz BB ATM (variable temperature NMR) and 500 MHz TCI-ATM cryo (1D selective NOESY and ROESY experiments, performed by Derrick Roberts at the University of Cambridge) NMR spectrometers. Chemical shifts for ^{1}H, ^{13}C and ^{19}F are reported in ppm on the δ scale; ^{1}H and ^{13}C were referenced to the residual solvent peak and ^{19}F was referenced to an internal standard of C_6F_6 in CD_3CN at −164.9 ppm. Coupling constants (*J*) are reported in hertz (Hz). The following abbreviations are used to describe signal multiplicity for ^{1}H NMR spectra: s: singlet, d: doublet, t: triplet, dd: doublet of doublets; dt: doublet of triplets; m: multiplet, br: broad. All proton signals of diamagnetic compound were assigned with the aid of 2D NMR spectra.

Wide sweep paramagnetic NMR spectra were recorded in the analogue digitisation mode with a spectral width (SW) of 372.98 ppm, a transmitter frequency offset (O1P) of 100.00 ppm and the line width set to 10.0 Hz. Due to the experimental difficulties associated with collecting NMR data for ^{1}H nuclei with vastly different relaxation times, differences between measured and theoretical integration values were in some cases observed. While the paramagnetic nature of the complexes precluded complete assignment of the proton environments, it is proposed that through-bond proximity of the proton environment to each Co^{II} centres dictates the extent of downfield shifting of each signal, as observed in previous reports.[3,12]

DOSY NMR experiments were performed on a Bruker 500 MHz TCI-ATM cryo NMR spectrometer (DOSY experiments in Chapter 3 were performed by Anna McConnell at the University of Cambridge) or 500 MHz DPX S5 500 MHz BB ATM spectrometer. Maximum gradient strength was 6.57 G/cm A. The standard Bruker pulse program, ledbpgp2s, employing a stimulated echo and

longitudinal eddy-current delay (LED) using bipolar gradient pulses for diffusion using 2 spoil gradients was utilised. Rectangular gradients were used with a total duration of 1.5 ms. Gradient recovery delays were 875 –1400 μs. Individual rows of the S4 quasi-2D diffusion databases were phased and baseline corrected.

2.3 Mass spectrometry (MS)

Low resolution electrospray ionisation mass spectrometry (LR-ESI-MS) was undertaken on a Micromass Quattro LC mass spectrometer (cone voltage 10-30 eV; desolvation temperature 313 K; ionisation temperature 313 K) infused from a Harvard syringe pump at a rate of 10 μL min^{-1}. High resolution electrospray ionisation mass spectrometry (HRMS-ESI) was performed on a Waters LCT Premier Mass Spectrometer featuring a Z spray source with electrospray ionisation and modular LockSpray interface. Travelling Wave Ion Mobility (TWIM) Quadrupole Time-of-Flight (TOF) ion mobility mass spectra (IM-MS) were collected on a Waters Vion IMS QTof Mass Spectrometer equipped with XS Ion Optics and the QuanTof2 detection system.

2.4 X-ray crystallography

Data were collected using either a Bruker D8 VENTURE diffractometer equipped with high-brilliance IμS Cu-Kα radiation (1.54178 Å), with ω and ψ scans at 180(2) K, or at Beamline I19 of Diamond Light Source employing silicon double crystal monochromated synchrotron radiation (0.6889 Å) with ω scans at 100(2) K. Data integration and reduction were undertaken with SAINT[13] in the APEX3 software suite for data collected on the Bruker diffractometer; data integration and reduction on synchrotron collections were undertaken with either CrysalisPRO[14] or xia2.[15] Multi-scan empirical absorption corrections were applied to the data using SADABS[16] or xia2.[15] Subsequent computations were carried out using the WinGX-32 graphical user interface.[17] Structures were solved by direct methods using SHELXT-2013[18] then refined and extended with SHELXL-2013.[18] In general, non-hydrogen atoms with occupancies greater than 0.5 were refined anisotropically. Carbon-bound hydrogen atoms were included in idealised positions and refined using a riding model. Disorder was modelled using standard crystallographic methods including constraints, restraints and rigid bodies where necessary. In cases involving the use of SQUEEZE[19], molecular formulas were determined firstly from the required number of charge-balancing anions, and then confirmed from the number of electrons identified in the disordered portion of the crystal by SQUEEZE.[19] The amount of solvent quoted in each formula is only that which could be assigned directly from the electron density map.

2.5 Molecular modelling

Molecular model simulations (MM2 and MM3 force fields) of supramolecular complexes were performed using CAChe Worksystems Pro (Fujitsu Ltd., Beaverton, Oregon, 2000–2006) and SCIGRESS version FJ 2.6 (EU 3.1.9) Build 5996.8255.20141202.

2.6 VOIDOO calculations

In order to determine the available void space within the cages presented in this thesis, VOIDOO calculations[20] were performed using MM3 minimized CACHE or SCIGRESS models, or the crystal structures of available compounds. A virtual probe with the minimum radius such that it would not exit the cavity of the structures was employed for all cages. The following parameters were changed from their default values, following a previously published procedure.[21]

Probe radius: 3.3 Å for octahedra, 3.5 Å for cuboctahedra, 1.4 Å for triangular prisms
Primary grid spacing: 0.1
Maximum number of volume-refinement cycles: 30
Minimum size of secondary grid: 1
Grid for plot files: 0.2

2.7 UV-Vis spectroscopy

UV-Visible absorption spectroscopy was performed using a Perkin Elmer Lambda 750 or Agilent Cary 5000 UV-Vis-NIR spectrophotometer. Spectra were obtained in double beam mode using only the (front) analyte beam to record spectra, with air in the (rear) reference path. A background spectrum of the neat solvent was recorded using the analyte beam prior to each experiment and baseline correction applied using the Perkin Elmer WinLab software suite. Samples were analysed using quartz cuvettes with optical path lengths of 10 mm.

2.8 Cyclic voltammetry

Solution state cyclic voltammetry (CV) was performed using a BioLogic SP-150 potentiostat with ferrocene (Fc) as an internal reference. Measurements were conducted under an Ar atmosphere using a conventional three-electrode cell: a glassy carbon working electrode, a Pt wire auxiliary electrode, and a Ag/Ag^+ quasi-reference electrode. A 0.1 M nBu$_4$NPF$_6$/CH$_3$CN electrolyte was used (unless specified otherwise), with scan rates in the range 25–1000 mV s^{-1}.

2.9 References

[1] Zhang, M., Gao, R., Hao, X., and Sun, W.-H., *J. Organomet. Chem.*, **2008**, 693, 3867-3877.

[2] Meng, W., Ronson, T.K., Clegg, J.K., and Nitschke, J.R., *Angew. Chem. Int. Ed.*, **2013**, 52, 1017-1021.

[3] Riddell, I.A., Smulders, M.M.J., Clegg, J.K., Hristova, Y.R., Breiner, B., Thoburn, J.D., and Nitschke, J.R., *Nat. Chem.*, **2012**, 4, 751-756.

[4] Meng, W., Breiner, B., Rissanen, K., Thoburn, J.D., Clegg, J.K., and Nitschke, J.R., *Angew. Chem. Int. Ed.*, **2011**, 50, 3479-3483.

[5] Bolliger, J.L., Ronson, T.K., Ogawa, M., and Nitschke, J.R., *J. Am. Chem. Soc.*, **2014**, 136, 14545-14553.

[6] Koshkakaryan, G., Klivansky, L.M., Cao, D., Snauko, M., Teat, S.J., Struppe, J.O., and Liu, Y., *J. Am. Chem. Soc.*, **2009**, 131, 2078-2079.

[7] Black, S.P., Stefankiewicz, A.R., Smulders, M.M.J., Sattler, D., Schalley, C.A., Nitschke, J.R., and Sanders, J.K.M., *Angew. Chem. Int. Ed.*, **2013**, 52, 5749-5752.

[8] Mullen, K.M., Johnstone, K.D., Nath, D., Bampos, N., Sanders, J.K.M., and Gunter, M.J., *Org. Biomol. Chem.*, **2009**, 7, 293-303.

[9] Fleischer, E.B., *Inorg. Chem.*, **1962**, 1, 493-495.

[10] Rizzuto, F.J., Kieffer, M., and Nitschke, J.R., *Chem. Sci.*, **2018**, 9, 1925-1930.

[11] Wood, D.M., Meng, W., Ronson, T.K., Stefankiewicz, A.R., Sanders, J.K.M., and Nitschke, J.R., *Angew. Chem. Int. Ed.*, **2015**, 54, 3988-3992.

[12] Wood, C.S., Ronson, T.K., Belenguer, A.M., Holstein, J.J., and Nitschke, J.R., *Nat. Chem.*, **2015**, 7, 354-358.

[13] Bruker, *SAINT*. 2012, Madison, Wisconsin, USA: Bruker ASX Inc.

[14] Agilent, *Crysalis PRO*. 2014, Yarnton, Oxfordshire, England: Agilent Technologies, Ltd.

[15] Winter, G., *J. Appl. Crystallogr.*, **2010**, 43, 186-190.

[16] Bruker, *SADABS*. 2001, Madison, Wisconsin, USA: Bruker AXS, Inc.

[17] Farrugia, L., *J. Appl. Crystallogr.*, **2012**, 45, 849-854.

[18] Sheldrick, G.M., *Acta Crystallogr. Sect. A*, **2015**, 71, 3-8.

[19] Spek, A.L., *Acta Crystallogr. Sect C*, **2015**, 71, 9-18.

[20] Kleywegt, G.J. and Jones, T.A., *Acta Crystallogr. Sect. D*, **1994**, 50, 178-185.

[21] Hristova, Y.R., Smulders, M.M.J., Clegg, J.K., Breiner, B., and Nitschke, J.R., *Chem. Sci.*, **2011**, 2, 638-641.

Chapter 3

Peripheral templation generates an $M^{II}_6L_4$ guest-binding capsule

3.1 Introduction

The ability for supramolecular cages to centrally encapsulate guests makes them ideal candidates for molecular recognition; however, biological receptors rarely employ central binding pockets. Guest recongition tyically occurs around the periphery of these strucutres, enabling a greater ease of guest association and eventual release upon information transmission (Figure 3.1).[1] Despite this, few cages have the ability to bind molecules in more than one mode or location.[2-4] The strategies outlined in the Introduction of this thesis have thus far proven useful in the stabilisation of multiple guest adducts within the cavities of cages; however, design principles to generate architectures that can bind guests peripherally remain largely elusive. The solvophobicity of guests, the size complementarity between a guest and the cavity of a host, and the cooperative enthalpic interactions that result from having multiple ligands enclosing a central species tend to favour internal encapsulation, making it the predominant mode of binding observed in supramolecular systems.[5]

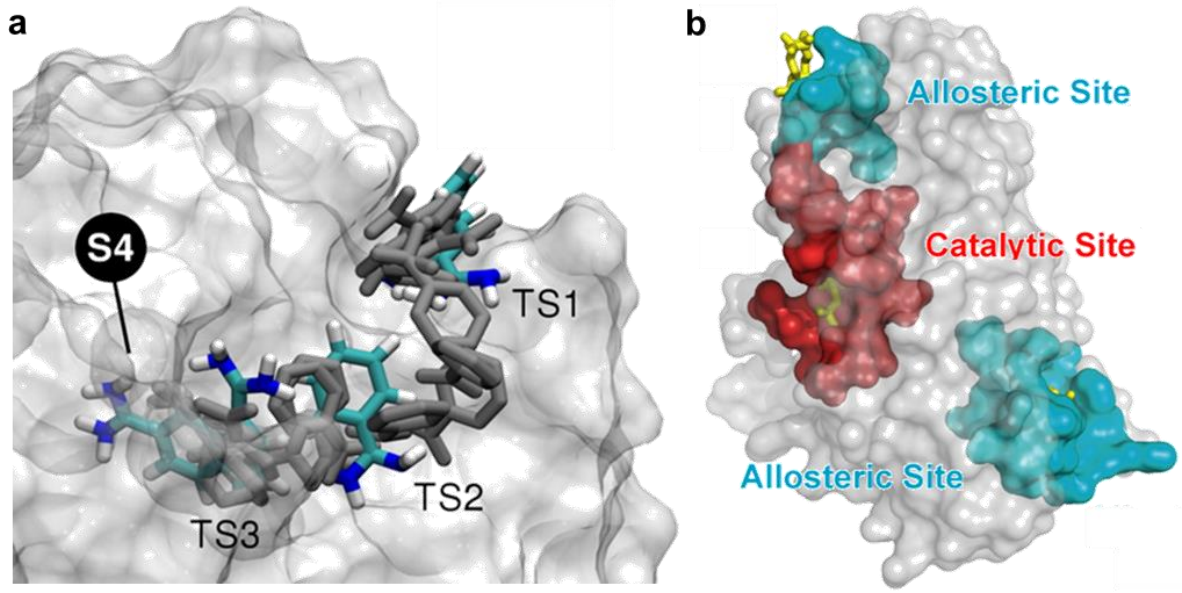

Figure 3.1 | **a**, By binding at a series of locations around the periphery of the enzyme, the transition states (TS1-3) of the substrate are stabilised, leading to a final product (S4) that binds in a different peripheral location. **b**, A bioreceptor with one catalytic site and two peripheral allosteric sites, the latter of which regulate the catalytic activity of the receptor. Figures adapted from reference 6.

Templation, likewise, typically involves a series of subunits assembling around a central structure-defining feature.[7-11] When this feature remains bound within the product structure, no cavity is available for storing other molecules; only when the template is displaced can the structure bind a different guest.[12]

In this Chapter,[13] the syntheses and host-guest chemistry of a new class of supramolecular *pseudo*-octahedra are presented. These structures are capable of binding neutral and anionic guests in both internal and peripheral pockets. This new $M^{II}_6L_4$ architecture was generated by employing

2-formylphenanthroline (a tridentate component) in place of 2-formylpyridine (a bidentate component) during the subcomponent self-assembly process.[14] Binding investigations of this host with a range of tetrahedral, octahedral and icosahedral guests revealed that one cage could simultaneously bind two guests in two different locations, and that peripheral guests bound more strongly than internal ones.

In one case peripheral guests were observed to template $M^{II}_6L_4$ structure formation, despite the failure of this structure to form either directly by subcomponent self-assembly or through the use of guest templation with centrally encapsulated guests. Once formed *via* peripheral templation, this capsule was capable of encapsulating guests centrally.

3.2 Synthesis of pseudo-octahedra from a tridentate building block

Preliminary investigations into the syntheses of *pseudo*-octahedral architectures were carried out by Dr Wen-Yuan Wu. The reaction of 2-formylphenanthroline (12 equiv), zinc(II) trifluoromethanesulfonate (triflate, OTf^-) (6 equiv) and either triamine **3A** or **3B** in CH_3CN led to the formation of $Zn^{II}_6L_4$ assembly **3.1** or **3.2**, respectively, after heating for 16 hours at 70 °C (Figure 3.2), as confirmed by ESI mass spectrometry. ^{1}H NMR spectra indicated the formation of highly symmetrical products in solution (Figure 3.3).

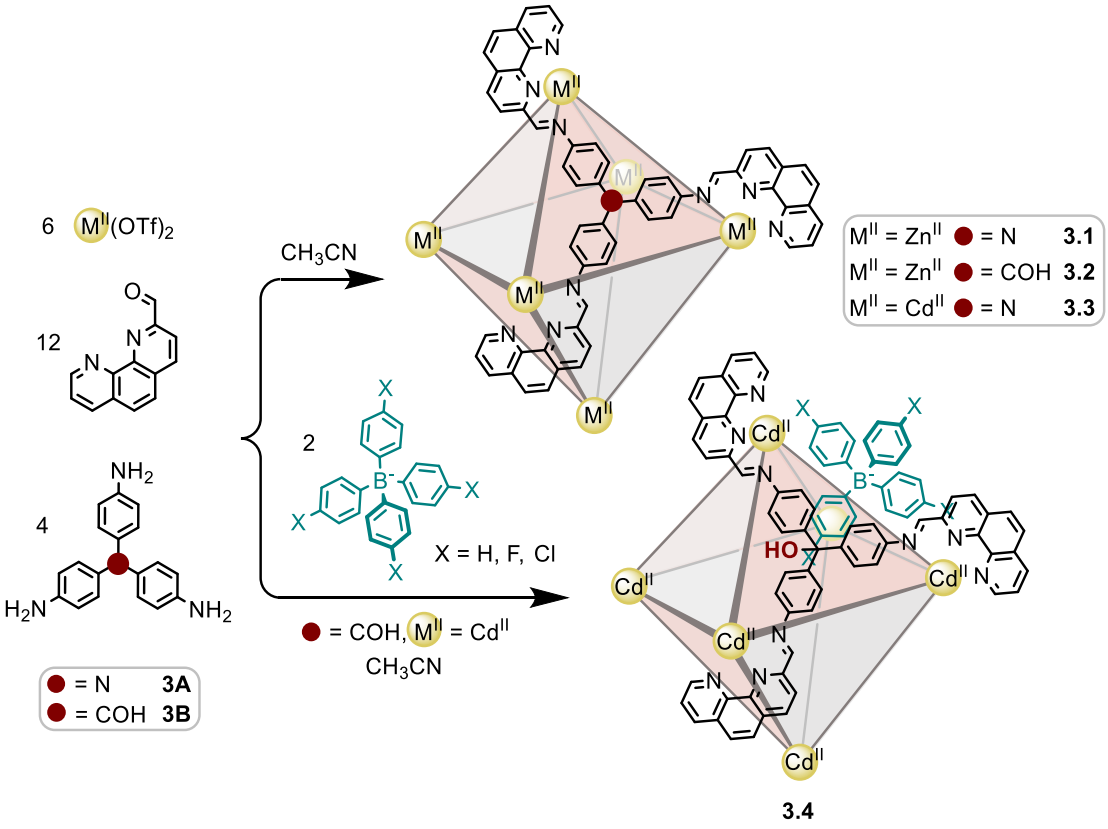

Figure 3.2 | Syntheses of $M^{II}_6L_4$ capsules **3.1**–**3.3** (top) compared to the synthesis of **3.4** (bottom), which only formed in the presence of tetraphenylborates. Red faces are occupied by ligands, grey faces are open.

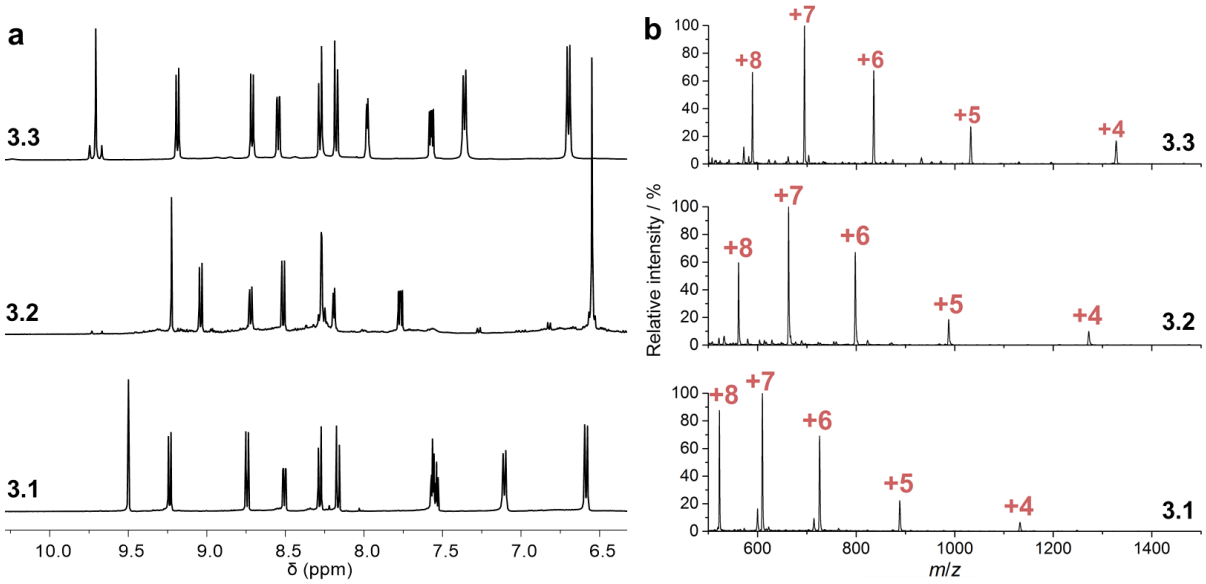

Figure 3.3 | **a**, ^{1}H NMR spectra (400 MHz, 298 K, CD_3CN) and **b**, ESI mass spectra of **3.1**–**3.3** (sequentially from bottom to top).

Under all conditions tried, **3.4** was never observed to assemble from Cd^{II}, **3B** and 2-formylphenanthroline; only in the presence of a peripherally bound tetraphenylborate template was **3.4** observed (Figure 3.2). Subcomponent **3A**, however, was observed to assemble with Cd^{II} and 2-formylphenanthroline to yield **3.3**. ESI-MS confirmed the 4:6 metal:ligand ratio of the structure, while NMR spectroscopy revealed a highly symmetric species, as with **3.1** and **3.2 (**Figure 3.3). High resolution ESI-MS unambiguously established the stoichiometry in all cases.

Single crystals of **3.1** and **3.2** were grown by slow diffusion of Et_2O or $^{i}Pr_2O$, respectively, into CH_3CN solutions. X-ray diffraction analyses confirmed that both $Zn^{II}_6L_4$ complexes comprise an octahedral framework of metal ions, in which the octahedron faces are alternately occupied by a ligand or an open aperture (Figure 3.4). The connectivity of **3.1** and **3.2** is thus akin to the those of the hexanuclear architectures reported by Fujita[15] and Yan.[16] Both asymmetric units contain two whole octahedra, and both unit cells contain a racemic mixture of the all-Δ and all-Λ stereochemistry exclusively. This observation is consistent with their solution NMR spectra, which indicate that both **3.1** and **3.2** contain metal centers of a single handedness, with approximate *T* (chiral tetrahedral) point symmetry.

The crystal structure of **3.2** presents a more distorted octahedral Zn^{II} coordination environment than in **3.1**; the angles between the chelate planes of the imino-phenanthrolines were observed to be 82–90° in **3.1**, against 71–90° in **3.2**. Similarly, whereas **3.1** displayed uniform diagonal Zn^{II}–Zn^{II} distances of *ca.* 17 Å, the corresponding diagonals in **3.2** measured *ca.* 15 × 16 × 19 Å (an average of the two whole octahedra in the asymmetric unit), reflecting a significant axial elongation and

equatorial compression in **3.2**. While of similar areas (20–30 Å^2), the open triangular apertures of **3.2** resultantly present a less equilateral surface than **3.1**. Void volumes, calculated using VOIDOO[17], revealed cavities of 282 Å^3 for **3.1** and 423 Å^3 for **3.2**. These volumes are approximately ten times larger than those of the $M^{II}_4L_4$ tetrahedra formed from the same triamines using 2-formylpyridine.[18,19]

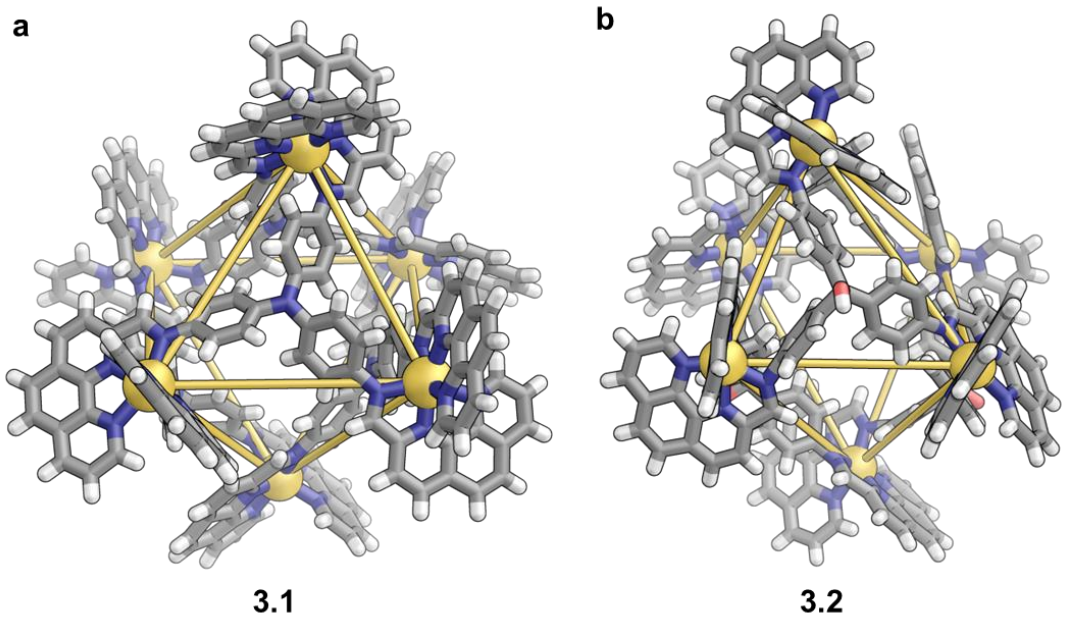

Figure 3.4 | Crystal structures of **a**, **3.1** and **b**, **3.2**, viewed down the C_3 axis, with metal ion connectivity highlighted with yellow lines (Zn – yellow, N – blue, O – red, C – gray, H – white; anions and solvent are omitted for clarity).

3.3 Internal and peripheral host-guest chemistry

The tetrahedrally arranged apertures of the hosts suggested that the voids of **3.1**–**3.3** may bind tetrahedral guests. Three classes of tetrahedral prospective guests were investigated: neutral molecules, small anions, and larger anions incorporating aromatic units. While the anions BF_4^-, ClO_4^-, SO_4^{2-} and PO_4^{3-} were not observed by ^{1}H or ^{19}F NMR spectroscopy to bind within **3.1**–**3.3** at 25 °C, the addition of polyhalogenated CI_4, CBr_4 or CI_3H led to shifts in the ^{1}H NMR spectrum of **3.2**, consistent with binding in fast exchange on the NMR timescale (Figure 3.5). The most pronounced shifts were observed for the phenylene protons of **3.2**, suggesting that binding occurs centrally. No binding was observed for the smaller $CHBr_3$, CCl_4 or less symmetric CH_2BrI, $CHCl_3$ or CH_2Cl_2 molecules.

Tetraphenylborate (BPh_4^-) was observed to bind in intermediate exchange on the NMR timescale (significant broadening of cage resonances, followed by the appearance of sharp signals) with **3.1** and **3.3**, whereas this anion was observed by ^{1}H NMR to bind in fast exchange with **3.2** (Figure 3.6). Significant shielding of the phenylene protons of the ligand was observed in all cases, indicative of guest interaction at the face of the structure; however, substantial shifts for signals attributed to the

imine and its nearest phenanthroline protons were also observed. In both **3.1** and **3.3**, shifts upfield exceeding 2 ppm were observed, consistent with strong electronic perturbation at the windows of the architecture.

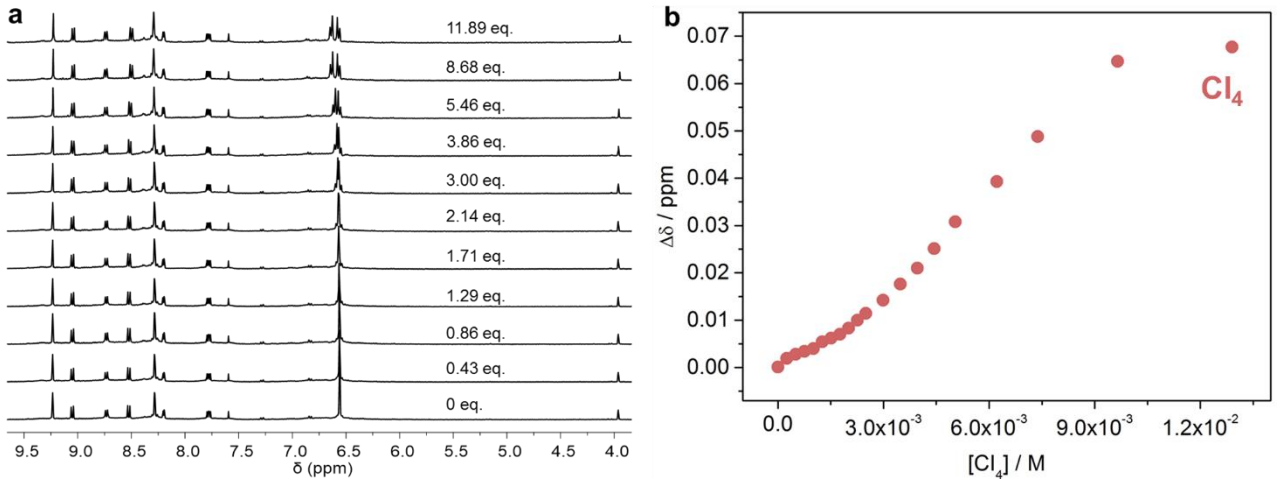

Figure 3.5 | **a**, ^{1}H NMR titration (400 MHz, 298 K, CD_3CN) of CI_4 into a solution of **3.2** in CD_3CN. **b**, Plot of the shift in the phenylene protons of **3.2** *vs.* the concentration of CI_4 added. This isotherm could not be fitted to either 1:1 or 1:2 models, suggesting that higher binding stoichiometries may be present.

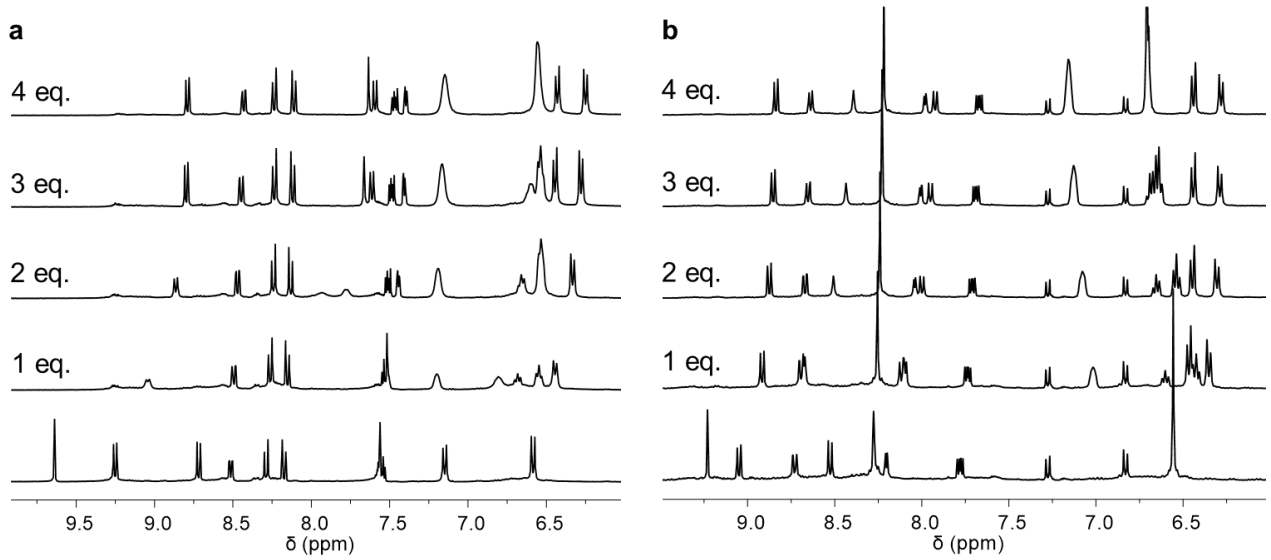

Figure 3.6 | ^{1}H NMR titrations (400 MHz, 298 K, CD_3CN) of nBu$_4$NBPh$_4$ into solutions of **a**, **3.1** or **b**, **3.2** in CD_3CN. Binding occurred in intermediate exchange (**a**) or fast exchange (**b**) on the NMR timescale, depending on the ligand employed during self-assembly.

MM3 molecular modelling revealed two potential binding modes of BPh_4^- within **3.1**–**3.3**: internal encapsulation, where the phenyl rings branch outwards through the apertures of the structure, or peripheral binding, where only one phenyl ring enters the cavity and the remaining three sit in pockets formed by the bis-phenanthroline corners (Figure 3.7a).

Tandem 1D selective ^{1}H NOESY and ROESY experiments performed on the BPh_4^- adducts of **3.1**–**3.3** (see Figure 3.7b for a representative example) indicated strong NOE peaks between the *ortho* protons of BPh_4^- and the phenylene, imine and adjacent phenanthroline protons of **3.1**–**3.3**. Irradiation

of the *meta* BPh_4^- protons revealed considerably weaker NOEs to the phenylene protons of **3.1**–**3.3** and the two phenanthroline protons closest to the imine; no NOEs were observed between the *para* BPh_4^- protons and **3.1**–**3.3**. Consideration of the molecular models of BPh_4^-•**3.3** revealed that only in the peripherally-bound structure were the *ortho* protons of BPh_4^- sufficiently close to the phenanthroline corners to produce the observed NOE peaks (Figure 3.7a). Although adjacent to the phenylene rings of the ligand, the *ortho* protons of an internally bound BPh_4^- would be too far away for NOEs to be observed with the imine or phenanthroline protons. Consequently, a peripheral binding model, in which a phenyl ring of the guest protrudes through a window of the architecture, best describes the binding of BPh_4^- anions by **3.1**–**3.3**. This mode is distinct from the external binding described by Raymond *et al.*, wherein guests undergo non-specific interactions with the exterior of the cage and are not directly bound in a cavity.[20]

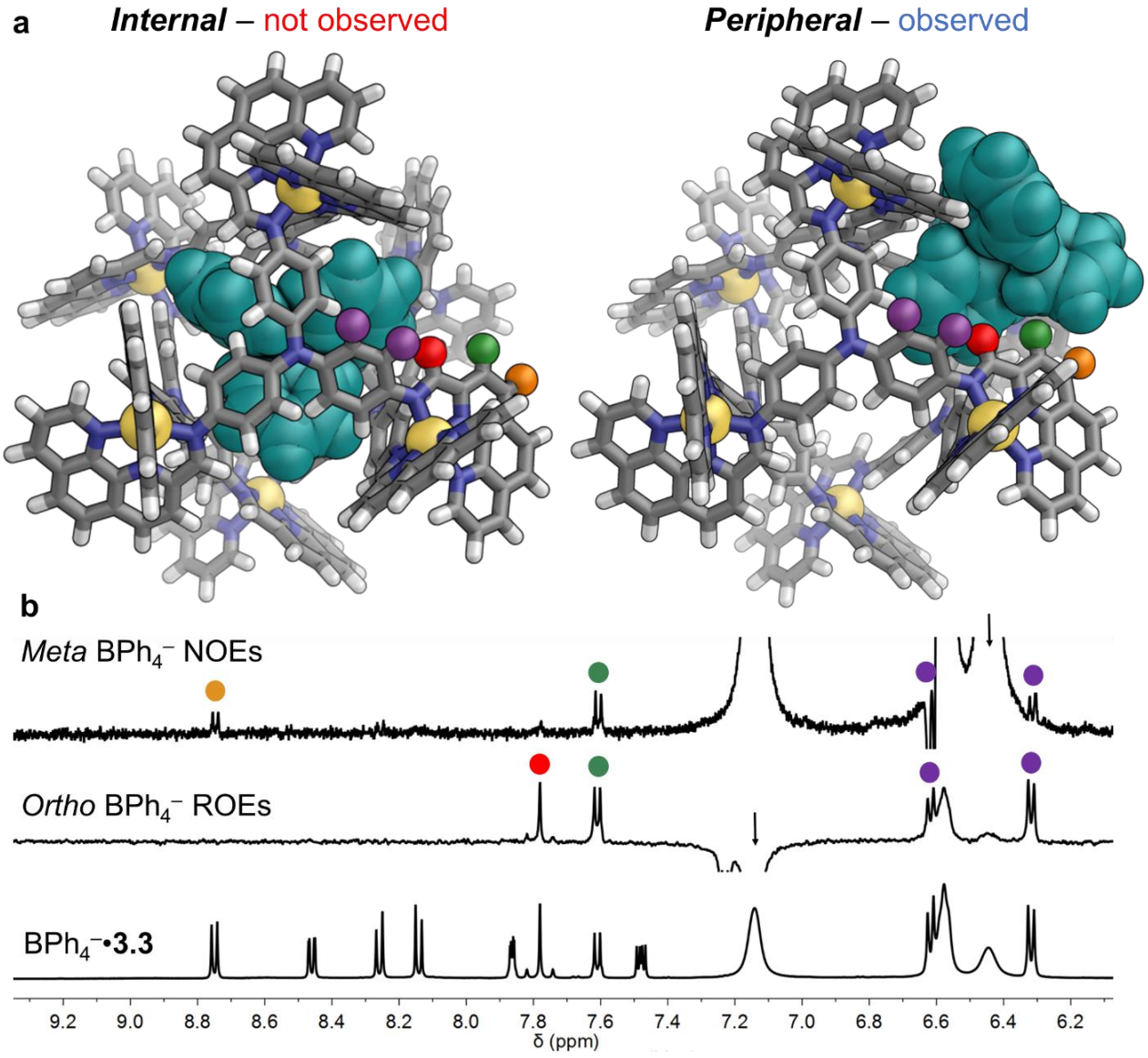

Figure 3.7 | a, MM3 molecular models optimised for the internal and peripheral binding of BPh_4^- to **3.3**. **b**, Tandem 1D selective ^{1}H NOESY and ROESY NMR spectra revealed that BPh_4^- bound to the periphery of the cages. NOE correlations corresponding to interior encapsulation were not observed. Coloured dots mark NOE correlations to coloured protons in the above structures.

To further probe the binding abilities of **3.1**–**3.3**, these hosts were treated with tetra-*p*-F and tetra-*p*-Cl substituted tetraphenylborate anions ($B(C_6H_4F)_4^-$ and $B(C_6H_4Cl)_4^-$, respectively), both of which were observed to bind in fast exchange on the NMR timescale to **3.1**–**3.3** (see Figure 3.8 for a representative example with **3.2**). No binding was observed for penta-fluoro- or bis-*m*-CF_3-substituted tetraphenylborates, or for the structurally analogous tetraphenylmethane. The increased steric bulk of the poly-substituted tetraphenylborates may prevent the outward-pointing phenyl rings from resting on the corners of the structure.

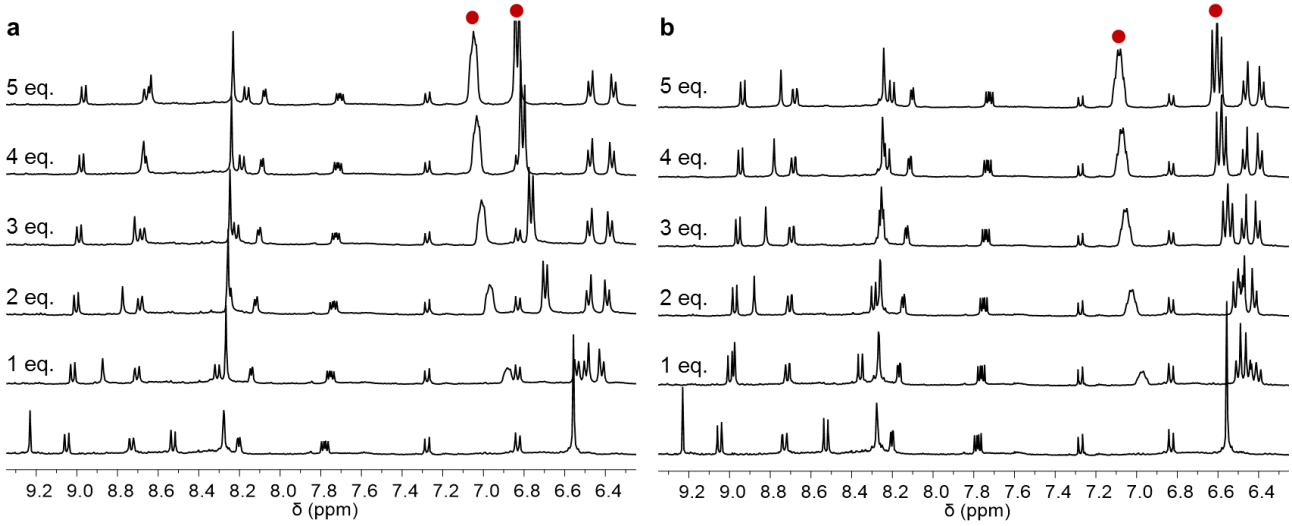

Figure 3.8 | ^{1}H NMR titration (400 MHz, 298 K, CD_3CN) of **a**, $NaB(C_6H_4Cl)_4$ and **b**, $KB(C_6H_4F)_4$ into solutions of **3.2** in CD_3CN. Equivalents added are marked on each spectrum; red dots mark guest signals.

A ^{1}H–^{19}F HOESY NMR spectrum of $B(C_6H_4F)_4^-$•**3.3** (Figure 3.9) furthermore revealed NOEs between the *para*-fluorine substituent of the guest and the 5 and 6 protons of the phenanthroline moiety. These NOEs are consistent with the phenyl rings of $B(C_6H_4F)_4^-$ resting on the triangular corners of **3.3**. No such NOE interactions are possible should the guest be internally bound.

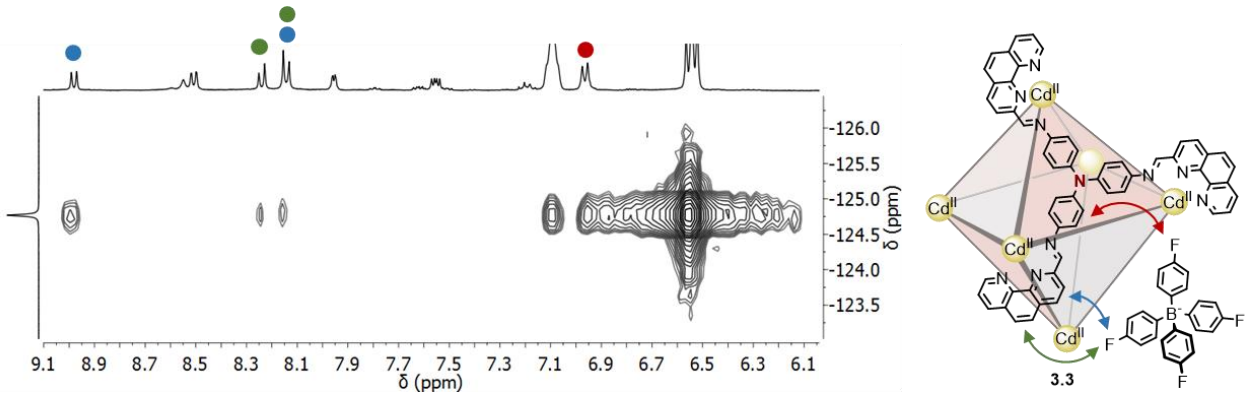

Figure 3.9 | ^{1}H-^{19}F HOESY NMR spectrum (400 MHz, 298 K, CD_3CN) of $B(C_6H_4F)_4^-$•**3.3**. Coloured dots correspond to correlations observed between the ^{19}F signals of $B(C_6H_4F)_4^-$ and the proton signals of **3.3**, represented by coloured arrows.

Binding constants for the tetraphenylborates (measured using UV-Vis spectroscopy for **3.1** and **3.3**, and ^{1}H NMR spectroscopy for **3.2**) were fitted using 1:1 binding isotherms (Figure 3.10 and Table 3.1). In most cases, it was inferred that rapid exchange of the tetraphenylborates between sites serves to block the binding of more than one equivalent simultaneously; the high residuals of some fitting profiles may be due to the interaction of more than one anion with the cages at higher guest concentrations (notes, Table 3.1).

Notably, **3.1** and **3.3** bound all peripheral guests more strongly than **3.2**. The more regular shapes of the apertures of **3.1** and **3.3**, as compared to those of **3.2** (Figure 3.4), may account for this difference in binding strength. No relationship was observed between the Hammett parameters of the *para* substituents of the tetraphenylborates and their strength of binding, possibly due to the countervailing electronic and steric effects of the different substituents. Unsubstituted BPh_4^- universally bound more strongly than its *para* halogenated analogs.

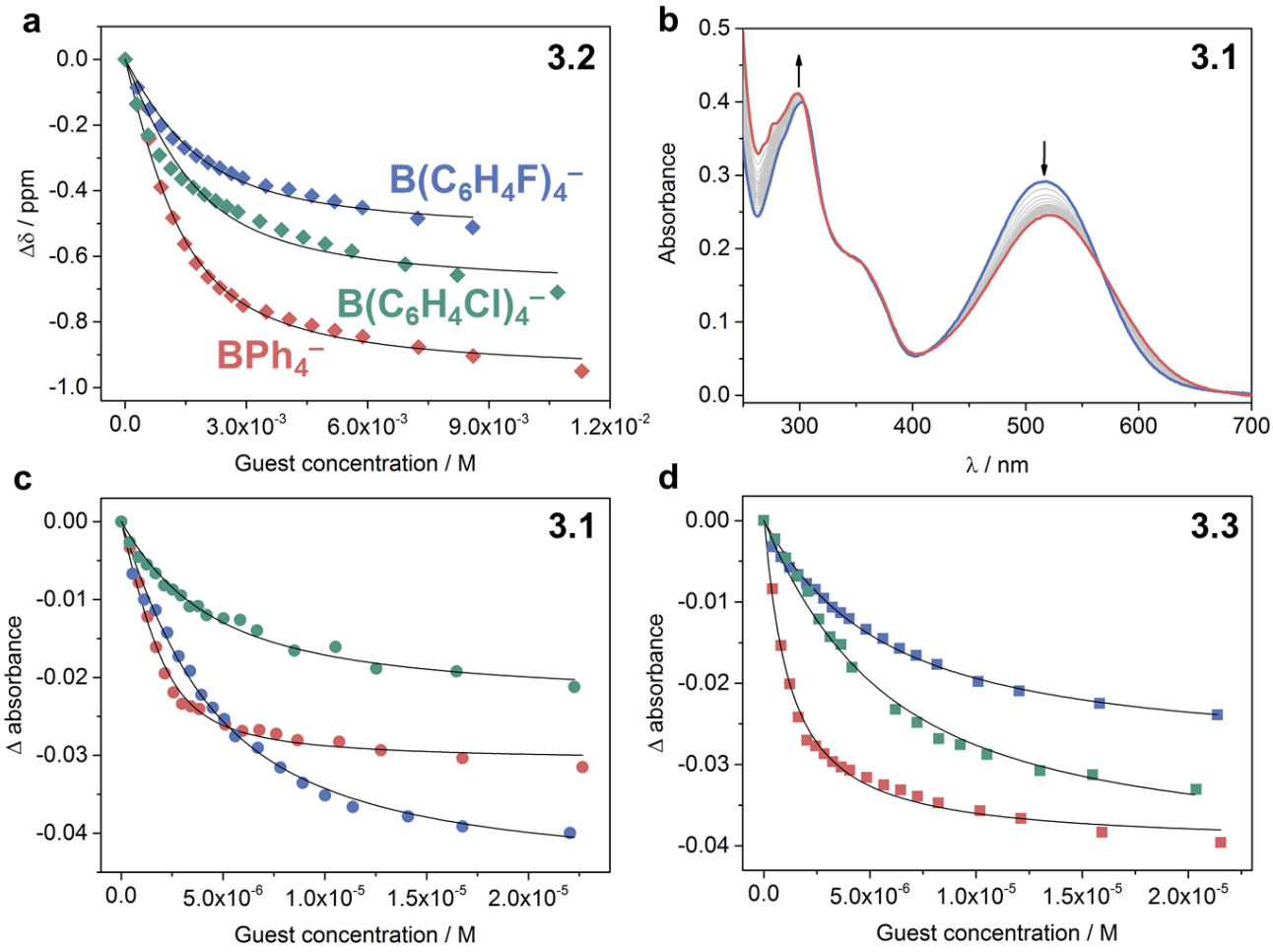

Figure 3.10 | Titration experiments between either **3.2** (**a**, diamonds), **3.1** (**c**, circles) or **3.3** (**d**, squares) and either BPh_4^- (red), $B(C_6H_4Cl)_4^-$ (green) or $B(C_6H_4F)_4^-$ (blue), fitted to 1:1 binding isotherms (black lines). **b**, The UV-Vis titration of BPh_4^- into a solution of **3.1** in MeCN, where arrows indicate the direction of spectral progression from the initial to final spectrum (blue to red spectra).

Table 3.1 Summary of the binding constants (K_a, M^{-1}) of monoanionic guests with capsules **3.1**–**3.3**.

Guest	**3.1**[a]	**3.2**[b]	**3.3**[a]
BPh_4^-	$(1.8 \pm 0.2) \times 10^6$	$(1.7 \pm 0.1) \times 10^3$	$(9 \pm 2) \times 10^5$
$B(C_6H_4F)_4^-$	$(3.6 \pm 0.2) \times 10^5$	$(1.2 \pm 0.2) \times 10^3$[d]	$(2.3 \pm 0.2) \times 10^5$
$B(C_6H_4Cl)_4^-$	$(3.3 \pm 0.4) \times 10^5$	$(1.4 \pm 0.3) \times 10^3$[d]	$(2.4 \pm 0.2) \times 10^5$
$CB_{11}H_{12}^-$	[c]	$(1.18 \pm 0.02) \times 10^2$	[c]
PF_6^-	[c]	$(2.99 \pm 0.06) \times 10^1$	[c]
AsF_6^-	[c]	$(2.41 \pm 0.03) \times 10^1$	[c]
SbF_6^-	[c]	$(1.53 \pm 0.09) \times 10^1$	[c]

[a] Measured by UV-Vis spectroscopy. [b] Measured by ^{1}H NMR spectroscopy. [c] No binding observed. [d] Higher residuals indicate that a second, weak binding event may be occurring at high concentrations of guest.

While **3.2** did not display any significant optical change during titration with any of the tetraphenylborates, UV-Vis titrations of these anions into acetonitrile solutions of **3.1** and **3.3** consistently gave a redshift of the $\pi \rightarrow \pi^*$ transition of the triphenylamine chromophore as the titration progressed (Figure 3.10b). This shift is consistent with a donation of electron density from guest to host, and a narrowing of the band gap upon anion binding.

Cyclic voltammetry was also employed to monitor the electronic changes occurring in **3.3** upon titration with BPh_4^- (Figure 3.11). With increasing guest concentration, the first and second reduction waves became positively-shifted, indicating a decrease in the energy of the LUMO, consistent with the observed contraction of the optical band gap. Attributed to the reduction of the imino-phenanthroline motif, shifts in these waves further imply peripheral binding of BPh_4^- to **3.3**.

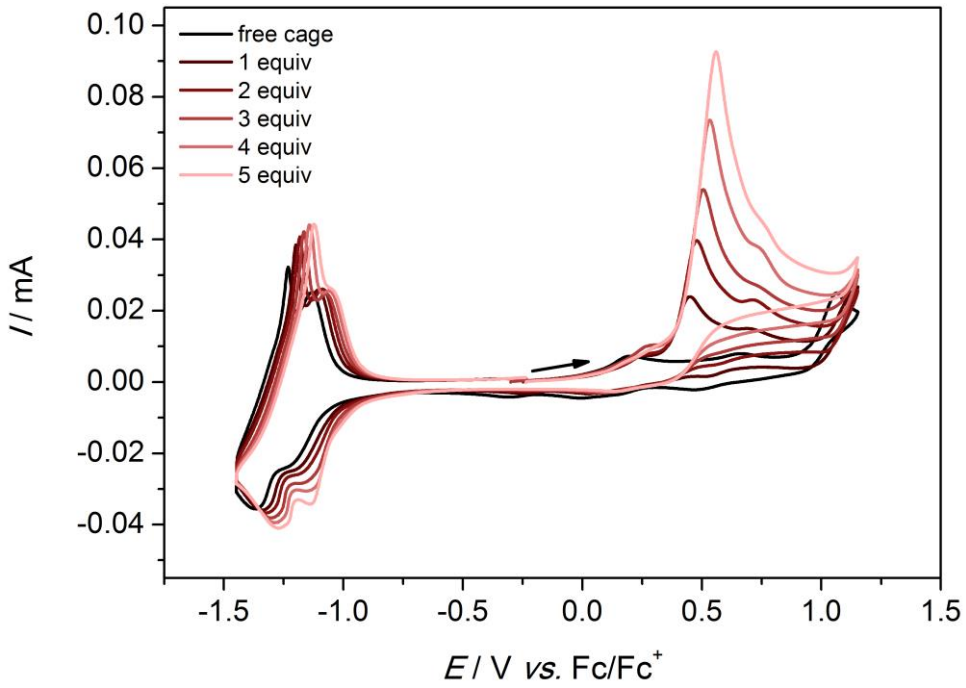

Figure 3.11 | Cyclic voltammograms of **3.3** in 0.1 M nBu$_4$NPF$_6$/CH$_3$CN electrolyte (scan rate = 100 mV s^{-1}), with increasing equivalents of nBu$_4$NBPh$_4$. The arrow indicates the direction of the forward scan.

Having established that neutral tetrahedral molecules bind internally and that tetraphenylborates bind peripherally, the binding abilities of guests of different shapes and sizes were investigated. Octahedral hexafluorinated monoanions were observed to bind in fast exchange on the NMR timescale with **3.2**; downfield shifting of its phenylene protons, along with movement of the imine and adjacent phenanthroline protons, indicated proximity of the anions to the central cavity of the cage. Broadening of the ^{19}F signals for AsF_6^- and SbF_6^- was likewise observed, consistent with binding in fast exchange on the NMR timescale (Figure 3.12b). These anions exhibited only weak association, however, with binding affinities <40 M^{-1}, as determined through ^1H NMR titrations (Figure 3.12a and Table 3.1).

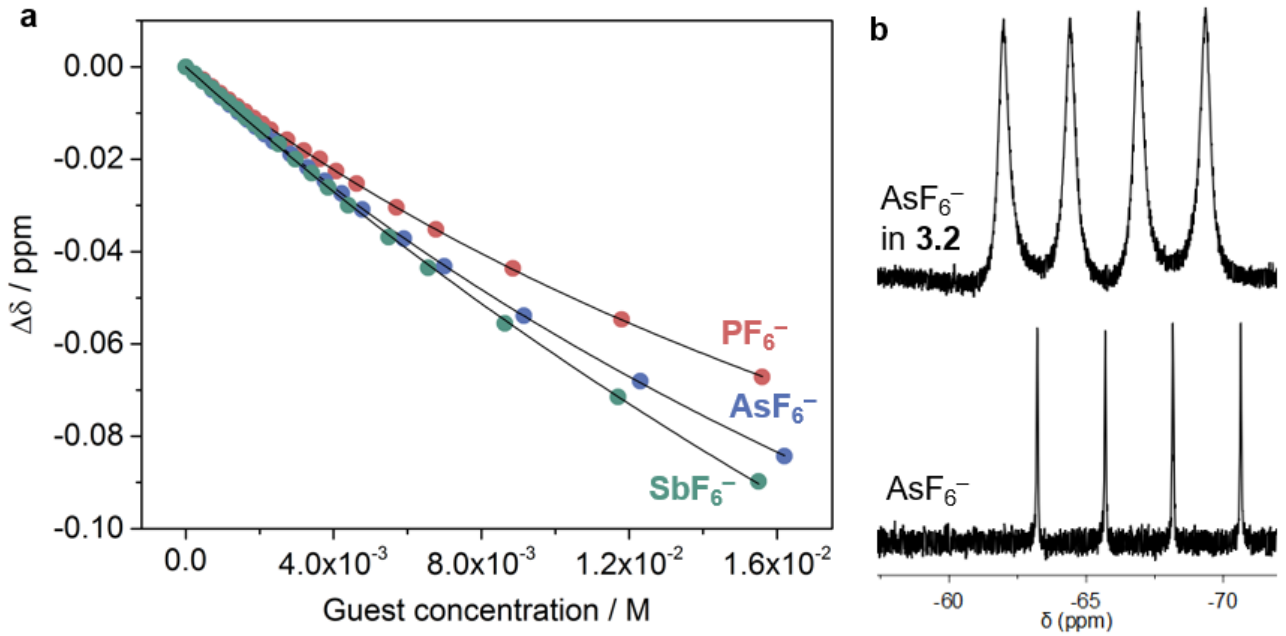

Figure 3.12 | a, Binding isotherms (1:1 system) fit to the chemical shift of the imine proton of **3.2** *vs.* the concentration of either *n*BuNPF$_6$ (red), KAsF$_6$ (blue) or NaSbF$_6$ (green) added to determine binding affinity (K_a). Chemical shifts were measured by ^1H NMR titrations (400 MHz, 298 K, CD_3CN). **b**, ^{19}F NMR spectra (376 MHz, 298 K, CD_3CN) of AsF_6^- before (bottom) and after (top spectrum) the addition of **3.2**.

A higher affinity for **3.2** was exhibited by the larger carborate anion $CB_{11}H_{12}^-$, which bound in fast exchange with **3.2** on the NMR timescale (Figure 3.13a). The $B_{12}H_{12}^{2-}$ and $B_{12}F_{12}^{2-}$ dianions were also observed to bind within **3.2** by ^1H NMR in fast exchange (Figure 3.13c&d), although their limited solubilities precluded the quantification of their binding affinities. Nevertheless, splitting and downfield shifting of the overlapping peaks corresponding to the phenylene protons of **3.2** upon titration with $B_{12}F_{12}^{2-}$ and $CB_{11}H_{12}^-$ anions indicated their uptake within the cage cavity. Treatment of **3.1** or **3.3** with the same octahedral and icosahedral anions led either to no significant spectral change, or to broadening of the ^1H NMR spectrum, which could not be resolved even at –40 °C.

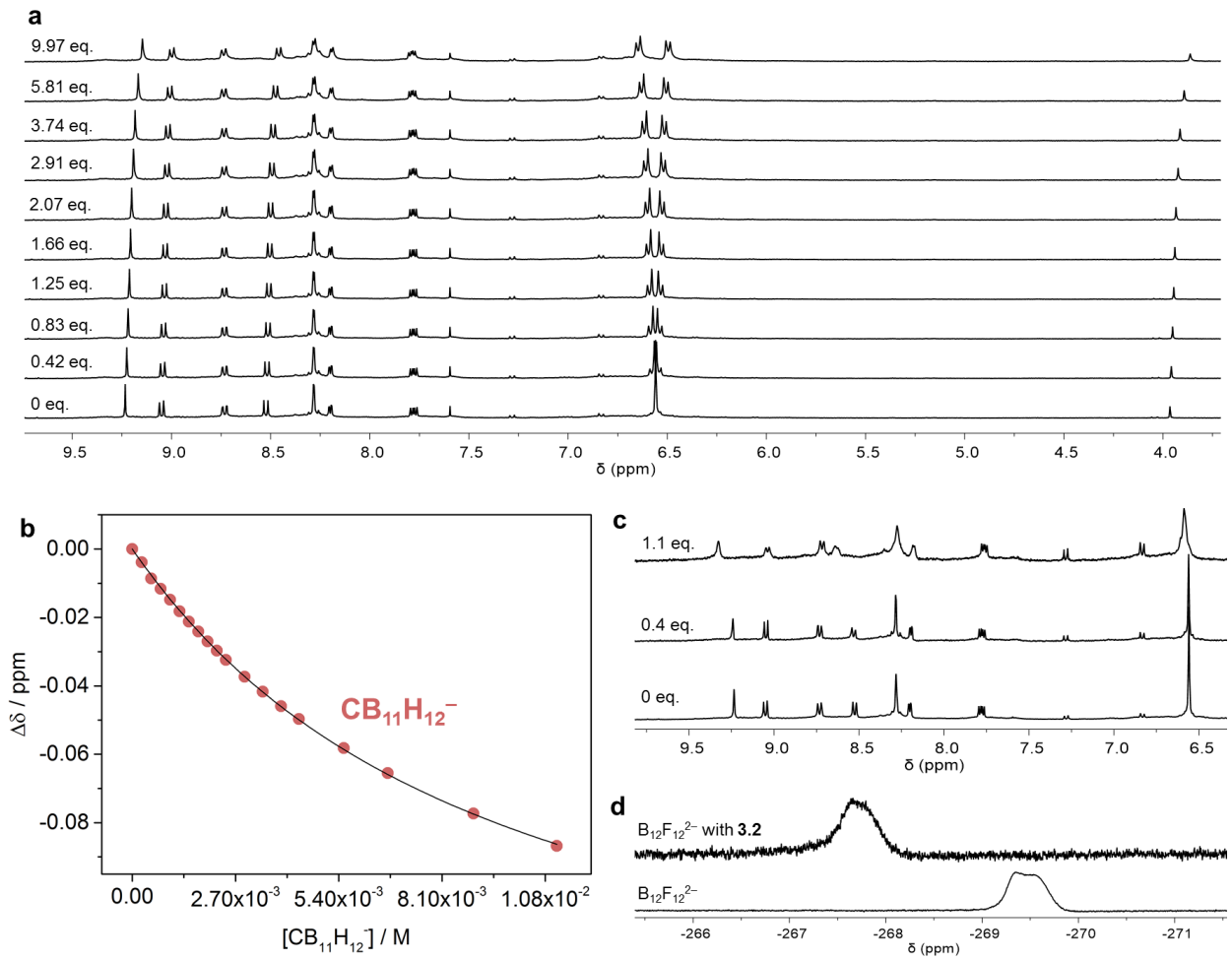

Figure 3.13 | Investigations into the binding of icosahedral guests within **3.2**. **a**, ^{1}H NMR titration (400 MHz, 298 K, CD_3CN) of $CsCB_{11}H_{12}$ into a solution of **3.2** in CD_3CN. **b**, Binding isotherm (1:1 system) fit to the chemical shift of the imine proton of **3.2** *vs.* the concentration of $CsCB_{11}H_{12}$ added to determine the binding affinity (K_a). **c**, ^{1}H NMR titration (400 MHz, 298 K, CD_3CN) of $Cs_2B_{12}H_{12}$ into **3.2**. **d**, Comparison of the ^{19}F NMR spectrum (376 MHz, 298 K, CD_3CN) of free $B_{12}F_{12}^{-}$ (bottom) compared to **3.2** with 1 equivalent of $B_{12}F_{12}^{-}$ (top).

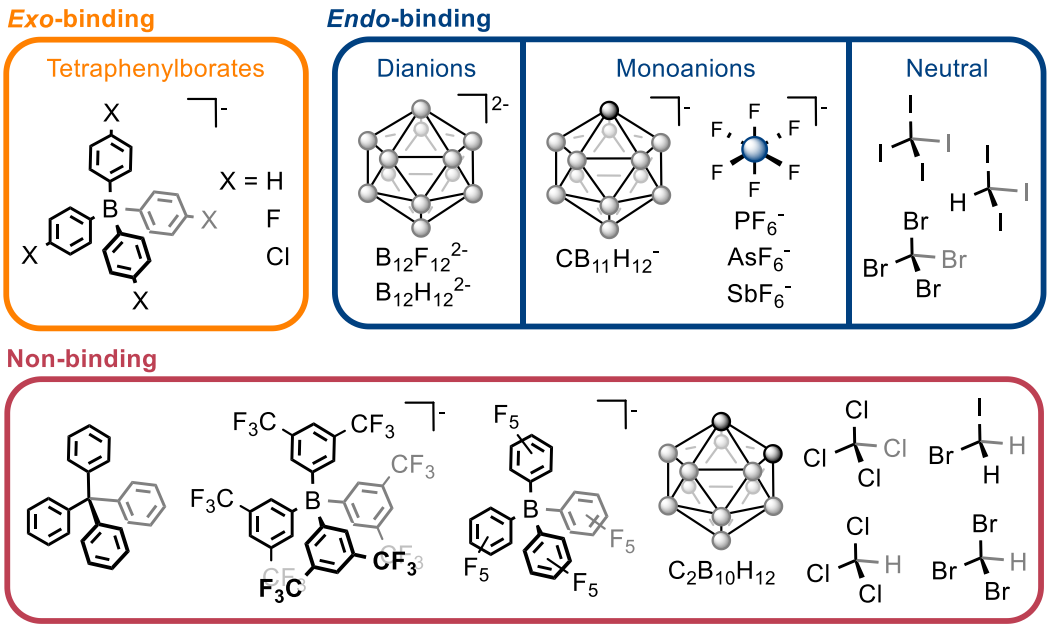

Figure 3.14 | Summary of the host-guest chemistry of capsule **3.2** (all boxes) and capsule **3.1** and **3.3** (*exo*-bound guests only).

3.4 Allostery investigations

Having thus established that host **3.2** possesses multiple binding sites that each bind specific anionic guests, the allosteric effects engendered by treating **3.2** simultaneously with a guest specific to each site were explored (Figure 3.15). The titration of $CsCB_{11}H_{12}$ into a solution of BPh_4^-•**3.2** in CD_3CN led to shifts in the ^1H NMR signals corresponding to **3.2**, but did not lead to a significant shift in the signals of the bound BPh_4^- ($\Delta\delta_{ortho}$ = –0.02 ppm), suggesting that concurrent binding of *exo*-BPh_4^- and *endo*-$CB_{11}H_{12}^-$ had occurred (Figure 3.15c). Furthermore, the presence of peripherally-bound BPh_4^- had no significant effect on the binding affinity of $CB_{11}H_{12}^-$ to the inside of **3.2** (K_a = (1.59 ± 0.08) × 10^2 M^{-1}), nor did the presence of *endo*-bound $CB_{11}H_{12}^-$ considerably alter the binding strength of BPh_4^- to the periphery of the cage (K_a = (2.8 ± 0.4) × 10^3 M^{-1}) (Figure 3.15e&f). Increasing the concentration of the other guest in both cases did not significantly change the binding constant of either the *endo*- or *exo*-bound guest (Table 3.2).

Table 3.2 | Summary of the binding constants (K_a, M^{-1}) determined from the titration of either $CB_{11}H_{12}^-$ or BPh_4^- into BPh_4^-•**3.2** or $CB_{11}H_{12}^-$⊂**3.2**, respectively, using different concentrations of bound guests.

Analyte	Titrant	K_a, M^{-1}
3.2	$CB_{11}H_{12}^-$	(1.18 ± 0.02) × 10^2
3.2 with 1 eq. BPh_4^-	$CB_{11}H_{12}^-$	(1.59 ± 0.08) × 10^2
3.2 with 4 eq. BPh_4^-	$CB_{11}H_{12}^-$	(1.7 ± 0.2) × 10^2
3.2	BPh_4^-	(1.7 ± 0.1) × 10^3
3.2 with 1 eq. $CB_{11}H_{12}^-$	BPh_4^-	(2.8 ± 0.4) × 10^3
3.2 with 4 eq. $CB_{11}H_{12}^-$	BPh_4^-	(2.6 ± 0.3) × 10^3

$B_{12}F_{12}^{2-}$ and BPh_4^- were likewise observed to bind to **3.2** simultaneously. The addition of $K_2B_{12}F_{12}$ to a solution of BPh_4^-•**3.2** led to ^1H and ^{19}F NMR shifts consistent with the encapsulation of $B_{12}F_{12}^{2-}$ (Figure 3.16a&b). Reversing the order of titration by adding *n*Bu_4NBPh_4 to $B_{12}F_{12}^{2-}$⊂**3.2** did not significantly alter the ^{19}F NMR chemical shift of encapsulated $B_{12}F_{12}^{2-}$, indicating that $B_{12}F_{12}^{2-}$ was not ejected from the capsule upon the peripheral binding of BPh_4^- (Figure 3.16d). The system thus appears to bind internal and peripheral guests concurrently, with neither allosteric inhibition nor enhancement of binding affinity.

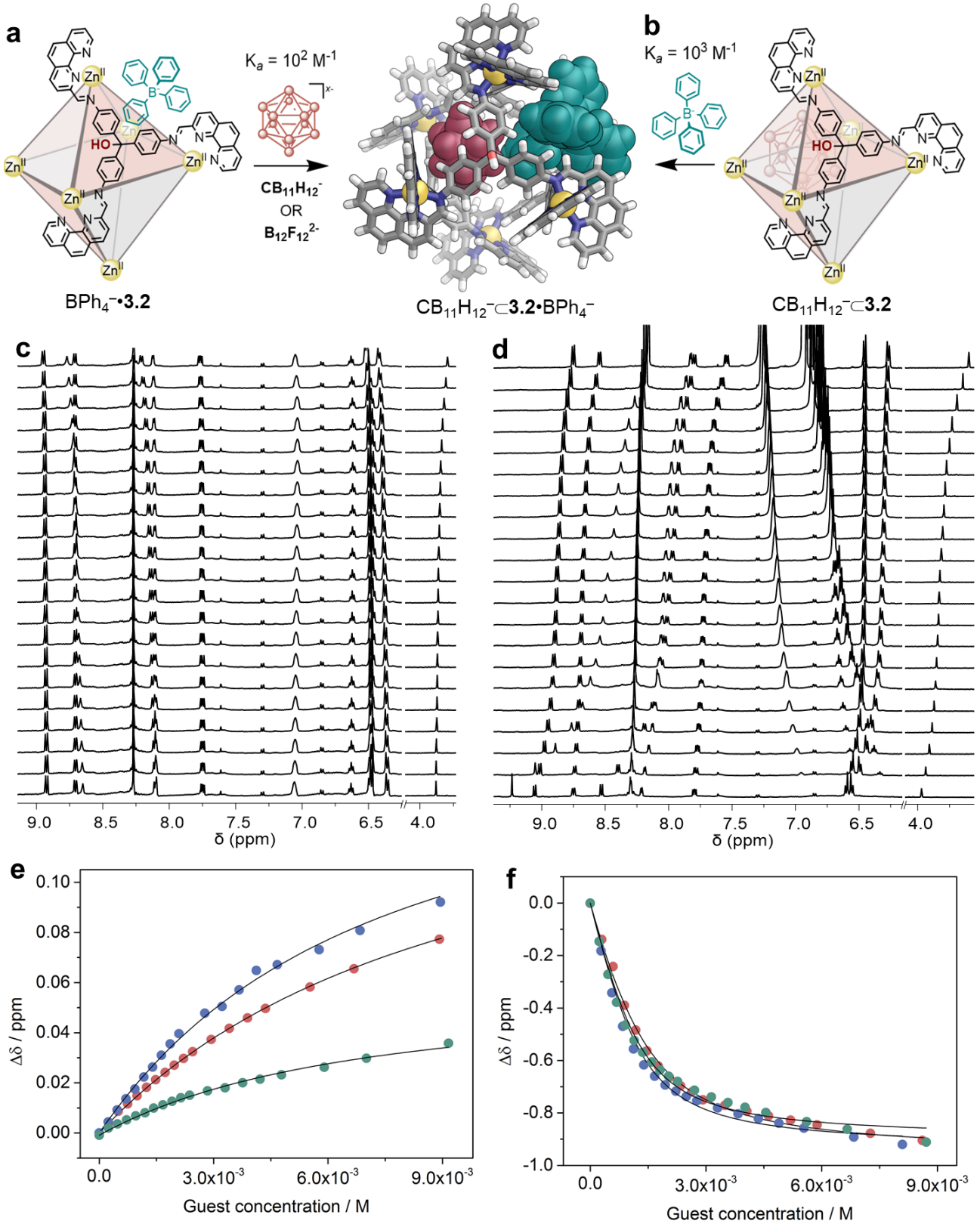

Figure 3.15 | Binding allostery investigations with **3.2**. **a**, The addition of icosahedral anions to BPh_4^-•**3.2** or **b**, tetraphenylborates to $CB_{11}H_{12}^-$⊂**3.2** or $B_{12}F_{12}^{2-}$⊂**3.2** led to concurrent binding of two guests at two different locations. **c&d**, ^{1}H NMR titrations (400 MHz, 298 K, CD_3CN) for the binding processes depicted in **a** and **b**, respectively, employing one equivalent of the 'other guest' already occupying **3.2**. **e&f**, Binding isotherms (1:1 system) fit to the chemical shift of **3.2** *vs.* the concentration of either BPh_4^- or $CB_{11}H_{12}^-$ added to determine the binding affinity (red dots = no 'other' guest, blue dots = 1 equivalent of 'other' guest, green dots = 4 equivalents of 'other' guest).

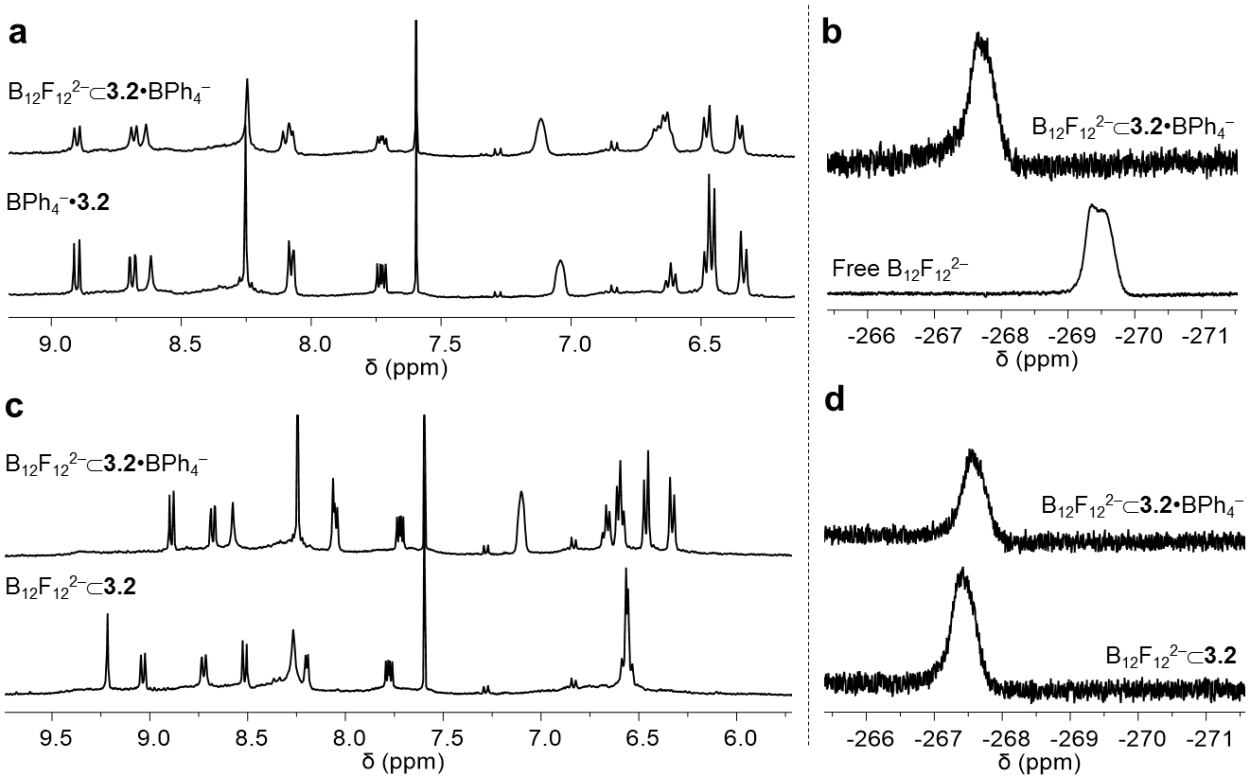

Figure 3.16 | ^{1}H NMR (400 MHz, 298 K, CD_3CN, left spectra) and ^{19}F NMR spectra (376 MHz, 298 K, CD_3CN, right spectra) investigating the concurrent binding of BPh_4^- and $B_{12}F_{12}^{2-}$ to **3.2**. **a**, The addition of $B_{12}F_{12}^{2-}$ to BPh_4^-•**3.2** led to host shifts (top spectrum) and **b**, a signal for encapsulated $B_{12}F_{12}^{2-}$ (top) distinct from that of free $B_{12}F_{12}^{2-}$ (bottom). **c**, The addition of BPh_4^- to $B_{12}F_{12}^{2-}$⊂**3.2** led to host shifts (top spectrum) and **d**, no significant change in the signal corresponding to encapsulated $B_{12}F_{12}^{2-}$ was observed.

3.5 Peripheral templation

Similar conditions to those used for the syntheses of **3.1**–**3.3** proved ineffective for the synthesis of the marginally larger structure **3.4**. Heating 2-formylphenanthroline (12 equiv), $Cd(OTf)_2$ (6 equiv) and **3B** (4 equiv) in CH_3CN to 60 °C overnight resulted in a broad, ill-defined aromatic region in the ^{1}H NMR spectrum; only free **3B** could be positively identified. Having elucidated the unique binding abilities of **3.2**, the generation of **3.4** was attempted *via* guest templation (Figure 3.17). Although the addition of internally-binding guests resulted in no significant change in the broad ^{1}H NMR spectrum of the precursors of **3.4**, the addition of *n*Bu_4NBPh_4 (2 equiv) led to the development of signals corresponding to the host-guest species BPh_4^-•**3.4** during 12 hours of heating at 50 °C. The diffusion coefficient of capsule **3.4** was measured to be 9.2×10^{-8} m^2 s^{-1} by DOSY NMR spectroscopy (Figure 3.18), similar to the values found for **3.1** and **3.2**; BPh_4^- bound to **3.4** was observed to diffuse more slowly than free BPh_4^-. Low and high resolution ESI-MS confirmed the expected $Cd^{II}_6L_4$ stoichiometry of the resulting species (Figure 3.19). Notably, MS signals corresponding to the free cage (without BPh_4^-) could not be identified, reflecting the strong binding of this anion to **3.4**.

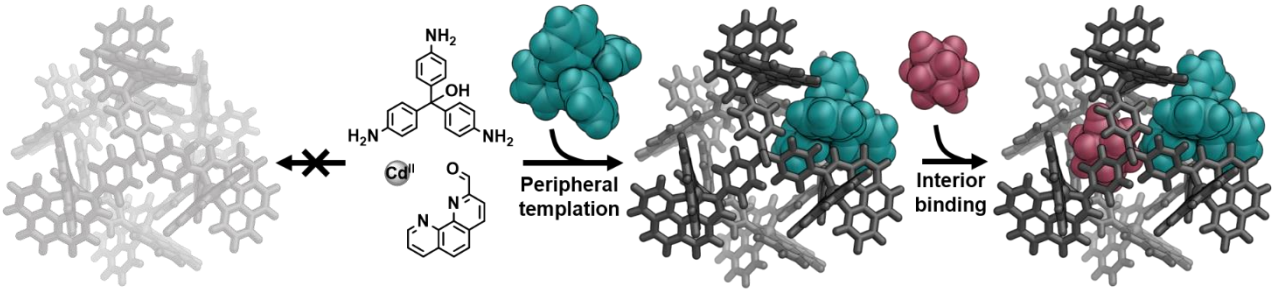

Figure 3.17 | Representation of the peripheral templation of **3.4** with BPh_4^- and its ability to subsequently bind guests internally. The formation of **3.4** did not proceed in the absence of template, or in the presence of internally-binding guests.

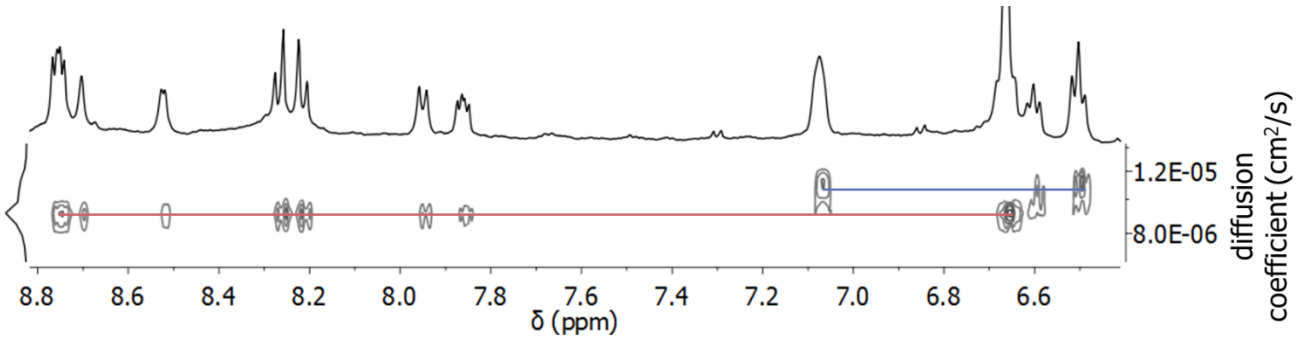

Figure 3.18 | ^{1}H DOSY NMR spectrum (400 MHz, 298 K, CD_3CN) of BPh_4^-•**3.4**. Cage peaks are marked with a red line; peaks corresponding to rapidly-exchanging BPh_4^- are marked with a blue line.

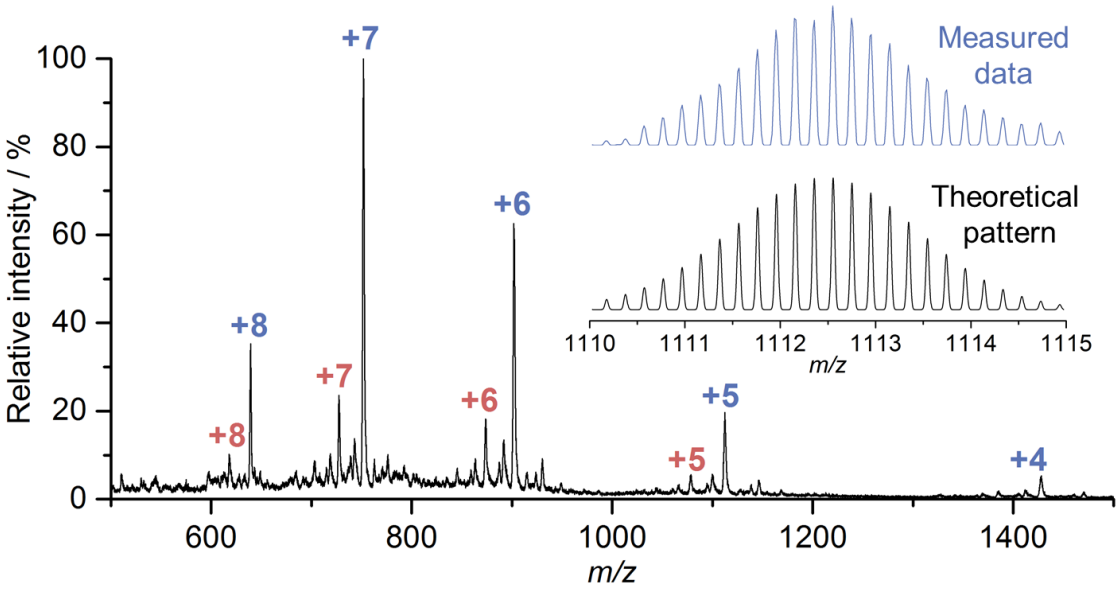

Figure 3.19 | ESI mass spectrum of BPh_4^-•**3.4**, where blue charges represent two associated BPh_4^- anions and red charges correspond to one associated BPh_4^- anion. Inset shows the high resolution ESI mass spectrum of the z = +5 charge fragment corresponding to **3.4**$(OTf)_5(BPh_4)_2^{5+}$ (top), compared to the theoretical isotope pattern (bottom).

The one-pot reaction of 2-formylphenanthroline (12 equiv), $Cd(OTf)_2$ (6 equiv), **3B** (4 equiv) and $n$$Bu_4NBPh_4$ (2 equiv) likewise led to the formation of BPh_4^-•**3.4** after heating to 50 °C over 6 h (Figure 3.2). Precipitation of the product with Et_2O and washing with CH_2Cl_2 led to the removal of $n$$Bu_4N(OTf)$, while bound BPh_4^- was still observed by ^{1}H NMR spectroscopy. The assembly also formed when *para*-substituted tetraphenylborate templates were employed, although two or more

equivalents of template were consistently necessary for the formation of the host in all cases (Figure 3.20). Templation did not, however, occur in the presence of any centrally binding guest; the addition of $CB_{11}H_{12}^-$ or $B_{12}F_{12}^{2-}$ to its precursors did not produce **3.4**.

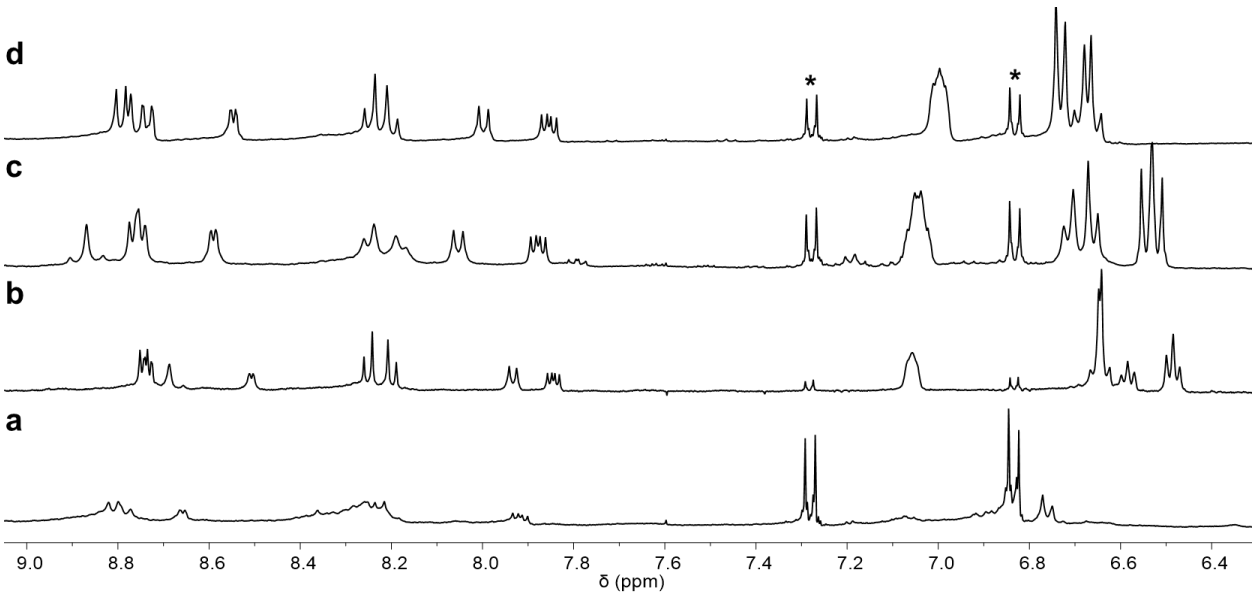

Figure 3.20 | a, ^{1}H NMR spectrum (400 MHz, 298 K, CD_3CN) of a mixture of **3B**, $Cd(OTf)_2$ and 2-formylphenanthroline heated to 50 °C for 16 hours, showing no clean formation of **3.4**. The addition of 2 equivalents of a tetraphenylborate salt to this solution (or during initial synthesis) led to the templation of **b**, BPh_4^-•**3.4** **c**, $B(C_6H_4F)_4^-$•**3.4** and **d**, $B(C_6H_4Cl)_4^-$•**3.4**. Resonances corresponding to the free subcomponent **3B** are marked with an asterisk.

NOE measurements on BPh_4^-•**3.4** revealed the same mode of peripheral binding as was observed in the cases of **3.1**–**3.3** (Figure 3.21). The ability of BPh_4^- to template the formation of **3.4** is thus highly unusual – a template typically sits at the center of the chemical structure that it brings into being, forming a symmetrical host-guest adduct. Furthermore, the high symmetry reflected in the ^{1}H NMR spectra of the adducts of **3.4** with tetraphenylborate and its halogenated congeners indicates that the guest remains in fast exchange between different sites on the host on the NMR timescale at 25 °C. Subsequent examples of a rapidly exchanging, *exo*-bound agent templating the formation of a metal-organic capsule have since been described, echoing these findings.[21]

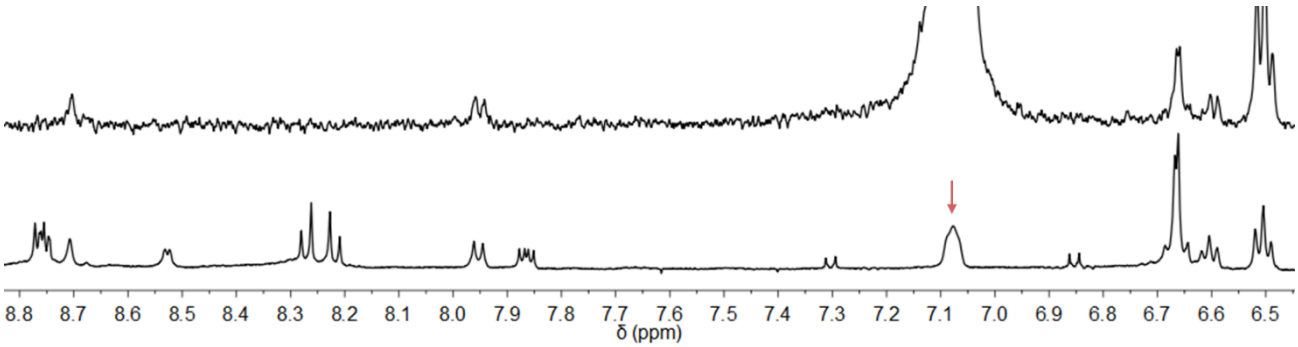

Figure 3.21 | ^{1}H NMR spectrum (500 MHz, 298 K, CD_3CN) of BPh_4^-•**3.4** (bottom) compared to the 1D selective ^{1}H NOESY spectrum (500 MHz, 298 K, CD_3CN) of BPh_4^-•**3.4**, irradiating the *ortho* proton of the BPh_4^- guest (top spectrum, irradiation point marked with a red arrow). From left to right, NOE peaks to the imine, proximal phenanthroline and phenylene protons were observed.

Although carborate did not serve as a competent template for the formation of **3.4**, once formed **3.4** was observed to bind $CB_{11}H_{12}^-$. The titration of $CsCB_{11}H_{12}$ into a CD_3CN solution of BPh_4^-•**3.4** resulted in ^1H NMR shifts consistent with the encapsulation of the carborane anion, with a simultaneous shift in the protons of BPh_4^- ($\Delta\delta_{ortho}$ = +0.15 ppm) (Figure 3.22). The $CB_{11}H_{12}^-$ binding affinity of BPh_4^-•**3.4** was calculated to be (1.37 ± 0.03) × 10^2 M^{-1}, similar to its Zn^{II} analog **3.2**.

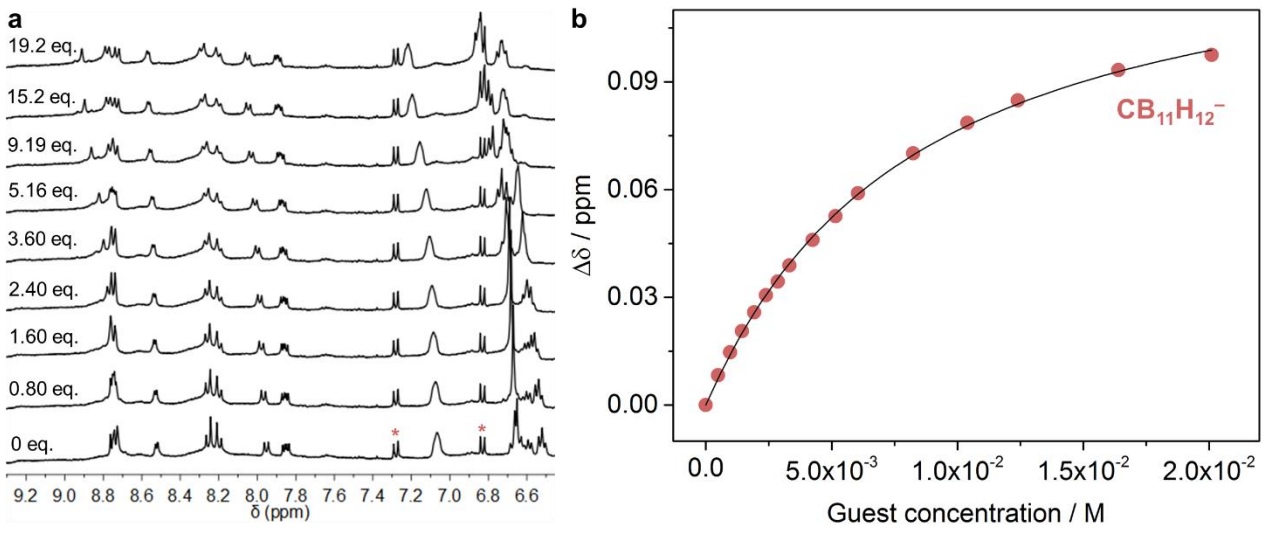

Figure 3.22 | a, ^1H NMR titration (500 MHz, 298 K, CD_3CN) of $CsCB_{11}H_{12}$ into a solution of BPh_4^-•**3.4** in CD_3CN (equivalents of anion are labeled on individual spectra, red asterisks mark a small portion of **3B**). **b,** Binding isotherm (1:1 system) fit to the chemical shift of the imine proton *vs.* the concentration of nBu$_4$NBPh$_4$ added to determine the binding affinity (K_a).

3.6 Conclusions and future work

Employing 2-formylphenanthroline in place of 2-formylpyridine during subcomponent self-assembly thus led to the formation of larger structures with significantly expanded cavities. Understanding the host-guest chemistry of these structures enabled the development of a new mode of templation. The addition of a rapidly-exchanging, peripherally bound guest engendered the formation of **3.4**, which could not be achieved in the template's absence. Moreover, the inclusion complex BPh_4^-•**3.4** could still participate in host-guest chemistry. This new mode of templation, which is allosteric in nature, enables the exploration of more complex chemical systems that are capable of responses to multiple stimuli.

More broadly, these cages underpin an important conclusion with respect to engineering favourable host-guest interactions – that designing the space around supramolecular capsules can be as important as designing the cavity inside them. In the cases of *pseudo*-octahedra presented herein, the use of tridentate ligand coordination enabled the generation of well-defined aperture environments that formed ideal spaces for recognising guests.

Further studies on these architectures, not presented in this thesis,[22] have looked at generating larger octahedra from larger threefold-symmetric subcomponents. The host-guest chemistry of these larger species has yet to be investigated. Future work may thus focus on allosteric recognition between the peripheral and internal environments within larger octahedral capsules. Tuning the solubility of the capsules by altering the face-capping units or counterions would also provide a means of promoting guest recognition at different spaces within these significantly larger capsules.

3.7 Experimental section

3.7.1 Synthesis and characterisation of 3.1

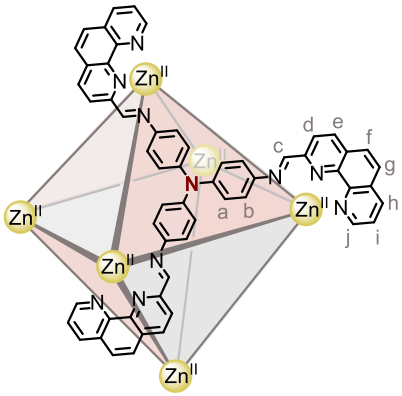

Tris(4-aminophenyl)amine **3A** (13.9 mg, 4.80 × 10^{-5} mol, 4 equiv), 2-formylphenanthroline (30.0 mg, 1.44 × 10^{-5} mol, 12 equiv) and either $Zn(BF_4)_2{\cdot}xH_2O$ (17.2 mg, 7.20 × 10^{-5} mol, 6 equiv based on anhydrous base) or $Zn(OTf)_2$ (26.2 mg, 7.20 × 10^{-5} mol, 6 equiv) were combined in CH_3CN and stirred at 70 °C overnight. The solvent was evaporated and the solid triturated with Et_2O to yield **3.1** as a dark purple crystalline solid (**3.1**$(BF_4)_{12}$: 53.2 mg, 1.08 × 10^{-5} mol, 90%; **3.1**$(OTf)_{12}$: 62.5 mg, 1.11 × 10^{-5} mol, 93%). **^{1}H NMR** (500 MHz, 298 K, CD_3CN): δ 9.50 (s, 12H, H_c), 9.24 (d, J = 8.3 Hz, 12H, H_e), 8.74 (d, J = 8.3 Hz, 12H, H_d), 8.51 (dd, J = 8.1, 1.7 Hz, 12H, H_h), 8.28 (d, J = 9.2 Hz, 12H, H_f), 8.17 (d, J = 9.2 Hz, 12H, H_g), 7.61 – 7.49 (m, 24H, H_i & H_j), 7.11 (d, J = 8.9 Hz, 24H, H_b), 6.59 (d, J = 8.9 Hz, 24H, H_a) ppm. **^{13}C NMR** (126 MHz, 298 K, CD_3CN): δ 155.3, 149.1, 147.8, 145.9, 143.5, 140.2, 140.0, 139.9, 139.7, 131.5, 129.9, 129.6, 127.0, 126.6, 126.5, 125.2, 124.1 ppm. Note: The ^{1}H and ^{13}C spectral data for **3.1**$(BF_4)_{12}$ and **3.1**$(OTf)_{12}$ were identical. **LR-ESI-MS** [charge fragment, calculated for **3.1**$(BF_4)_{12}$]: *m/z* = 1539.0 [**3.1**$(BF_4)_9^{3+}$, 1539.2], 1132.6 [**3.1**$(BF_4)_8^{4+}$, 1132.7], 888.6 [**3.1**$(BF_4)_7^{5+}$, 888.8], 725.8 [**3.1**$(BF_4)_6^{6+}$, 726.2], 609.8 [**3.1**$(BF_4)_5^{7+}$, 610.0], 522.6 [**3.1**$(BF_4)_4^{8+}$, 522.9]. **HR-ESI-MS**: *m/z* calculated for **3.1**$(BF_4)_7^{5+}$ = 888.7694, observed = 888.7686.

3.7.2 Synthesis and characterisation of 3.2

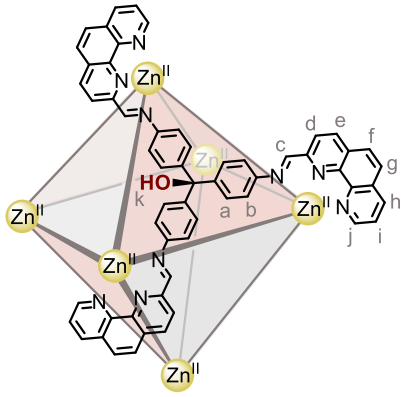

Pararosaniline base **3B** (14.7 mg, 4.80 × 10^{-5} mol, 4 equiv), 2-formylphenanthroline (30.0 mg, 1.44 × 10^{-5} mol, 12 equiv) and $Zn(OTf)_2$ (26.2 mg, 7.20 × 10^{-5} mol, 6 equiv) were combined in CH_3CN and stirred at 70 °C overnight. The complex was precipitated by adding the crude solution to excess Et_2O dropwise. The suspension was centrifuged and filtered to retrieve a purple solid. This was washed with CH_2Cl_2 (2 × 10 mL), EtOH (1 × 10 mL) and $CHCl_3$ (2 × 10 mL) and filtered. The remaining solid was dried *in vacuo* to yield a dark pink solid (55.3 mg, 9.73 × 10^{-6} mol, 82%). **^{1}H NMR** (500 MHz, 298 K, CD_3CN): δ 9.22 (s, 12H, H_c), 9.04 (d, J = 8.3 Hz, 12H, H_e), 8.72 (dd, J = 8.3, 1.5 Hz, 12H, H_h), 8.51 (d, J = 8.3 Hz, 12H, H_d), 8.27 (m, 24H, H_f &H_g), 8.19 (dd, J = 4.8, 1.5 Hz, 12H, H_j), 7.77 (dd, J = 8.3, 4.8 Hz, 12H, H_i), 6.55 (m, 48H, H_a & H_b), 3.96 (s, 4H, H_k) ppm. **^{13}C NMR** (126 MHz, 298 K,

CD_3CN): δ 160.7, 151.0, 147.5, 146.7, 146.0, 143.9, 141.3, 141.0. 132.0, 130.9, 130.5, 129.4, 128.0, 127.7, 127.5, 123.2, 121.0, 120.6 ppm. **LR-ESI-MS** [charge fragment, calculated for **3.2**$(OTf)_{12}$]: *m/z* = 1272.2 [**3.2**$(OTf)_8^{4+}$, 1272.2], 987.8 [**3.2**$(OTf)_7^{5+}$, 988.0], 798.3 [**3.2**$(OTf)_6^{6+}$, 798.4], 663.0 [**3.2**$(OTf)_5^{7+}$, 663.1], 561.4 [**3.2**$(OTf)_4^{8+}$, 561.6], 482.5 [**3.2**$(OTf)_3^{9+}$, 482.6]. **HR-ESI-MS**: *m/z* calculated for **3.2**$(OTf)_7^{5+}$ = 987.8994, observed = 987.8970.

3.7.3 Synthesis and characterisation of 3.3

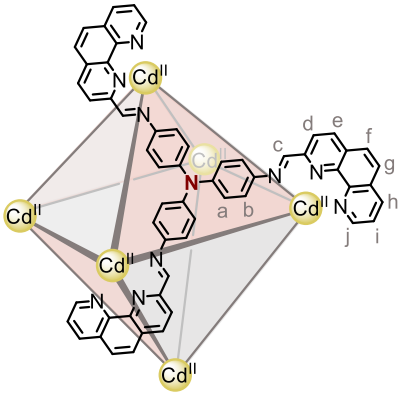

Tris(4-aminophenyl)amine **3A** (13.9 mg, 4.80×10^{-5} mol, 4 equiv), 2-formylphenanthroline (30.0 mg, 1.44×10^{-5} mol, 12 equiv) and $Cd(OTf)_2$ (29.6 mg, 7.20×10^{-5} mol, 6 equiv) were combined in CH_3CN and stirred at room temperature for 16 h. The solvent was evaporated and the solid triturated with THF (2 × 20 mL, or until the supernatant was colourless). The mixture was filtered and the residue dried *in vacuo* to yield a dark pink microcrystalline solid (58.5 mg, 9.91×10^{-6} mol, 83%). **^{1}H NMR** (500 MHz, 298 K, CD_3CN): δ 9.71 (s, 12H, H_c), 9.18 (d, *J* = 8.3 Hz, 12H, H_e), 8.71 (d, *J* = 8.3 Hz, 12H, H_d), 8.54 (dd, *J* = 8.3, 1.6 Hz, 12H, H_h), 8.27 (d, *J* = 9.2 Hz, 12H, H_f), 8.17 (d, *J* = 9.2 Hz, 12H, H_g), 7.97 (dd, *J* = 4.8, 1.6 Hz, 12H, H_j), 7.57 (dd, *J* = 8.3, 4.8 Hz, 12H, H_i), 7.35 (d, *J* = 8.5 Hz, 24H, H_b), 6.69 (d, *J* = 8.5 Hz, 24H, H_a) ppm. **^{13}C NMR** (126 MHz, 298 K, CD_3CN): δ 157.1, 151.3, 148.3, 147.3, 143.8, 141.5, 141.4, 141.1, 140.9, 132.8, 131.1, 130.4, 128.7, 127.7, 127.1, 125.7, 125.4, 123.3, 120.8 ppm. **LR-ESI-MS** [charge fragment, calculated for **3.3**$(OTf)_{12}$]: *m/z* = 1327.3 [**3.3**$(OTf)_8^{4+}$, 1327.7], 1032.3 [**3.3**$(OTf)_7^{5+}$, 1032.4], 835.4 [**3.3**$(OTf)_6^{6+}$, 835.5], 694.7 [**3.3**$(OTf)_5^{7+}$, 694.8], 589.2 [**3.3**$(OTf)_4^{8+}$, 589.3]. **HR-ESI-MS**: *m/z* calculated for **3.3**$(OTf)_7^{5+}$ = 1032.4681, observed = 1032.2681.

3.7.4 Synthesis and characterisation of BPh_4^-•3.4

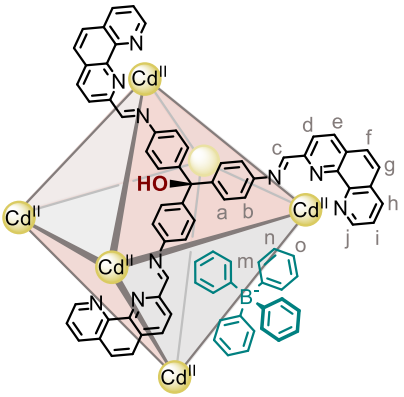

Pararosaniline base **3B** (4.90 mg, 1.60×10^{-5} mol, 4 equiv), $Cd(OTf)_2$ (9.86 mg, 2.40×10^{-5} mol, 6 equiv), 2-formylphenanthroline (10.0 mg, 4.80×10^{-5} mol, 12 equiv) and tetrabutylammonium tetraphenylborate (4.50 mg, 8.00×10^{-6} mol, 2 equiv) were combined in CH_3CN and stirred at 50 °C for 16 hours. The solvent was evaporated and the remaining solid washed alternatively with CH_2Cl_2 (3 × 15 mL) and EtOAc (3 × 15 mL). The residue was dried *in vacuo* to yield a purple crystalline solid (19.6

mg, 3.11 × 10^{-6} mol, 77%). **^{1}H NMR** (500 MHz, 298 K, CD_3CN): δ 8.74 (d, J = 8.3 Hz, 12H, H_e), 8.73 – 8.70 (m, 12H, H_h), 8.58 (s, 12H, H_c), 8.46 (d, J = 4.7 Hz, 12H, H_j), 8.24 (d, J = 9.1 Hz, 12H, H_g), 8.20 (d, J = 9.1 Hz, 12H, H_f), 7.88 (d, J = 8.3 Hz, 12H, H_d), 7.82 (dd, J = 8.3, 4.7 Hz, 12H, H_i), 7.09 (b, 16H, H_m), 6.62 (m, 48H, H_a & H_b), 6.60 (br, 8H, H_o), 6.59 – 6.47 (m, 16H, H_n), 3.85 (s, 4H, H_k) ppm. **^{13}C NMR** (126 MHz, 298 K, CD_3CN): δ 159.6, 151.1, 146.5, 145.5, 141.8, 140.8, 140.5, 140.4, 140.0, 135.8, 131.2, 130.2, 129.4, 128.7, 128.0, 126.7, 126.3, 125.7, 122.2, 122.1, 120.8, 114.3 ppm. **LR-ESI-MS** [charge fragment, calculated for **3.4**$(OTf)_x(BPh_4)_{12-x}$]: *m/z* = 1427.9 [**3.4**$(OTf)_6(BPh_4)_2^{4+}$, 1427.8], 1112.2 [**3.4**$(OTf)_5(BPh_4)_2^{5+}$, 1112.4], 1078.8 [**3.4**$(OTf)_6(BPh_4)^{5+}$, 1078.4], 901.8 [**3.4**$(OTf)_4(BPh_4)_2^{6+}$, 902.2], 873.8 [**3.4**$(OTf)_5(BPh_4)^{6+}$, 873.8], 751.9 [**3.4**$(OTf)_3(BPh_4)_2^{7+}$, 752.0], 727.5 [**3.4**$(OTf)_4(BPh_4)^{7+}$, 727.7], 639.3 [**3.4**$(OTf)_2(BPh_4)_2^{8+}$, 639.4], 617.8 [**3.4**$(OTf)_3(BPh_4)$,$^{8+}$ 618.1]. **HR-ESI-MS**: *m/z* calculated for **3.4**$(OTf)_5(BPh_4)_2^{5+}$ = 1112.5540, observed = 1112.5508.

Note: (a) While dilute samples of BPh_4^-•**3.4** were pure by ^{1}H NMR spectroscopy, some portion of subcomponent **3B** was always found to persist in solution in more concentrated samples, despite numerous purification cycles. These signals are attributed to dissociation of the cage in solution; however, the cage was stable in its solid form. Thus, 2D NMR and ^{13}C NMR spectra all contain a portion of free **3B**. (b) *n*$Bu_4N(OTf)$ was observed to be washed out of the reaction mixture during work-up.

3.7.5 Titrations

Procedure for UV-Vis titrations: A solution of host (2.0–3.2 × 10^{-6} M in CH_3CN) in a UV-Vis cuvette was titrated with a solution of the same concentration of host and excess guest such that the concentration of the host remained constant with each addition of guest. Upon each addition, the solution was manually stirred for 1 min before acquiring the UV-Vis spectrum.

Procedure for NMR titrations: A 0.6 mL solution of host (1.2–1.4 × 10^{-3} M) in CD_3CN was titrated with a concentrated solution of guest. The total change in concentration of the host was 5.3–9.6% over the course of the titration, and the error involved was assumed to be negligible. Upon each addition, the solution was manually stirred for 1 min before acquiring the spectrum, which allowed equilibrium to be reached between the host and guest.

3.7.6 Allosteric binding studies on 3.2

General procedure for $CB_{11}H_{12}^-$ as the internally-binding guest: To a 0.6 mL solution of **3.2** (1.18×10^{-3} M) in CD_3CN was added either 5 or 20 µL (corresponding to 1 or 4 equivalents per cage) of a concentrated solution of either nBu$_4$NBPh$_4$ (1.42×10^{-1} M) or $CsCB_{11}H_{12}$ (1.46×10^{-1} M). The resulting solution was then titrated against the other guest, as per the usual procedure.

General procedure for $B_{12}F_{12}^{2-}$ as the internally-binding guest: To a solution of **3.2** (4.0 mg) in CD_3CN (0.6 mL) was added approximately one equivalent of either nBu$_4$NBPh$_4$ (0.41 mg) or $K_2B_{12}F_{12}$ (0.32 mg) and the NMR spectra (^{1}H and ^{19}F) recorded. The other guest was then added to the solution, and the NMR spectra recorded again. No titration could be conducted due to the insolubility of the host with more than 2 equivalents of $B_{12}F_{12}^{2-}$.

3.7.7 Crystallography

The crystals employed in this Chapter rapidly lost solvent after removal from the mother liquor and rapid handling prior to flash cooling in the cryostream was required to collect data. Due to the less than ideal resolution, bond lengths and angles within pairs of organic ligands were restrained to be similar to each other (SAME) and thermal parameter restraints (SIMU, DELU) were applied to all non-metal atoms to facilitate anisotropic refinement. Ligand-based atoms that still displayed thermal parameters greater than 0.4 were further refined to approximate isotropic behaviour (ISOR). In both cases, the remaining anions present in the asymmetric unit could not be successfully assigned despite numerous attempts at modelling, including the use of rigid bodies. Consequently, the SQUEEZE[23] function of PLATON[24] was employed to remove the contribution of the electron density associated with the anions and the remaining highly disordered solvent molecules.

*3.7.7.1 Crystal structure of **3.1**·12BF$_4$·5.25MeCN·0.5Et$_2$O*

Formula $C_{240.50}H_{164.75}B_{12}F_{48}N_{45.25}O_{0.50}Zn_6$, M 5130.36, Triclinic, space group $P\bar{1}$ (#2), a 21.2908(17), b 34.428(3), c 40.373(3) Å, α 96.128(4), β 94.327(4), γ 101.218(5)°, V 28721(4) Å^3, D_c 1.186 g cm^{-3}, Z 4, crystal size 0.550 by 0.150 by 0.050 mm, colour purple, habit block, temperature 180(2) Kelvin, λ(CuKa) 1.54178 Å, μ(CuKa) 1.279 mm^{-1}, T(SADABS)$_{min,max}$ 0.5715, 0.7475, $2\theta_{max}$ 69.64, *hkl* range –15 15, –25 25, –29 29, N 134350, N_{ind} 24167(R_{merge} 0.0821), N_{obs} 16347(I > 2σ(I)), N_{var} 5805, residuals* $R1(F)$ 0.1598, $wR2(F^2)$ 0.4286, GoF(all) 1.141, $\Delta\rho_{min,max}$ –0.532, 0.966 e$^-$ Å^{-3}, CCDC 1456932. *$R1 = \Sigma||F_o| - |F_c||/\Sigma|F_o|$ for $F_o > 2\sigma(F_o)$; $wR2 = (\Sigma w(F_o^2 - F_c^2)^2/\Sigma(wF_c^2)^2)^{1/2}$ all reflections $w=1/[\sigma^2(F_o^2)+(0.2000P)^2+750.0000P]$ where $P=(F_o^2+2F_c^2)/3$

Specific refinement details

Crystals of **3.1**·12BF_4·5.25MeCN·0.5Et_2O were grown by slow diffusion of diethyl ether into an acetonitrile solution of **3.1**$(BF_4)_{12}$. Despite the use of high intensity laboratory source radiation, few reflections at greater than 1.35 Å resolution were observed; nevertheless, the quality of the data is more than sufficient to establish the connectivity of the structure.

The asymmetric unit contains two whole octahedra. Most tetrafluoroborate anions showed a significant amount of thermal motion; bond length and thermal parameter restraints were required for the realistic modelling of these anions. Some anions displayed positional disorder and were modelled over two (sometimes three) locations. All anions and solvent molecules were refined with isotropic thermal parameters. Three of the twenty-four anions present in the asymmetric unit could not be successfully resolved despite numerous attempts at modelling, including the use of rigid bodies.

The SQUEEZEd portion of the cell totals 1,618 electrons per unit cell, with a solvent accessible void volume of 7,741 $Å^3$ per unit cell. This equates to 405 electrons per structure, where $Z = 4$. This density accounts for the 1.5 unresolved BF_4^- molecules per structure (1.5 × 42 e^- = 63 e^-) and further unresolved solvent molecules (342 e^-).

*3.7.7.2 Crystal structure of **3.2**·12OTf·0.5MeCN*

Formula $C_{245}H_{149.50}F_{36}N_{36.50}O_{40}S_{12}Zn_6$, M 5705.44, Monoclinic, space group $P2_1/c$ (#14), a 39.1746(9), b 37.7597(8), c 44.3076(9) Å, β 103.755(2), V 63661(2) $Å^3$, D_c 1.191 g cm^{-3}, Z 8, crystal size 0.600 × 0.100 × 0.020 mm, colour purple, habit needle, temperature 100(2) Kelvin, λ(synchrotron) 0.6889 Å, μ(synchrotron) 0.556 mm^{-1}, $T(\text{SADABS})_{min,max}$ 0.2787, 0.7440, $2\theta_{max}$ 31.99, *hkl* range –31 31, –30 30, –30 31, N 370024, N_{ind} 31456(R_{merge} 0.1150), N_{obs} 23888($I > 2\sigma(I)$), N_{var} 5123, residuals* $R1(F)$ 0.1986, $wR2(F^2)$ 0.4765, GoF(all) 1.066, $\Delta\rho_{min,max}$ –0.476, 0.862 e^- $Å^{-3}$, CCDC 1456933. *$R1 = \Sigma||F_o| - |F_c||/\Sigma|F_o|$ for $F_o > 2\sigma(F_o)$; $wR2 = (\Sigma w(F_o^2 - F_c^2)^2/\Sigma(wF_c^2)^2)^{1/2}$ all reflections $w=1/[\sigma^2(F_o^2)+(0.2000P)^2+750.0000P]$ where $P=(F_o^2+2F_c^2)/3$

Specific refinement details

Crystals of **3.2**·12OTf·0.5MeCN were grown by slow diffusion of diisopropylether into an acetonitrile solution of **3.2**$(OTf)_{12}$. Despite the use of synchrotron radiation, few reflections at greater than 1.2 Å resolution were observed. In addition, the crystals appeared to decay during data collection, resulting in lower than ideal completeness and high residuals. Nevertheless, the quality of the data is more than sufficient to establish the connectivity of the structure.

The asymmetric unit contains two whole octahedra. Bond length and thermal parameter restraints were required for the realistic modelling of all triflate anions and solvent molecules; these were refined with isotropic thermal parameters. Only 5 anions could be successfully resolved in the asymmetric unit, despite numerous attempts at modelling, including the use of rigid bodies.

The SQUEEZEd portion of the cell totals 30,518 electrons per unit cell, with a solvent accessible void volume of 8,167 $Å^3$ per unit cell. This equates to 3,815 electrons per structure, where $Z = 8$. This density accounts for the 9.5 unresolved OTf^- molecules per structure ($9.5 \times 74\ e^- = 703\ e^-$) and further unresolved solvent molecules (3,112 e^-).

3.8 References

[1] Motlagh, H.N., Wrabl, J.O., Li, J., and Hilser, V.J., *Nature*, **2014**, 508, 331-339.

[2] Ramsay, W.J. and Nitschke, J.R., *J. Am. Chem. Soc.*, **2014**, 136, 7038-7043.

[3] Sato, H., Tashiro, K., Shinmori, H., Osuka, A., Murata, Y., Komatsu, K., and Aida, T., *J. Am. Chem. Soc.*, **2005**, 127, 13086-13087.

[4] Zarra, S., Smulders, M.M.J., Lefebvre, Q., Clegg, J.K., and Nitschke, J.R., *Angew. Chem. Int. Ed.*, **2012**, 51, 6882-6885.

[5] Schneider, H.-J., *Angew. Chem. Int. Ed.*, **2009**, 48, 3924-3977.

[6] Yang, J.-S., Seo, S.W., Jang, S., Jung, G.Y., and Kim, S., *PLoS Comput. Bio.*, **2012**, 8, e1002612.

[7] Ayme, J.-F., Beves, J.E., Leigh, D.A., McBurney, R.T., Rissanen, K., and Schultz, D., *Nature Chem.*, **2012**, 4, 15-20.

[8] Chifotides, H.T., Giles, I.D., and Dunbar, K.R., *J. Am. Chem. Soc.*, **2013**, 135, 3039-3055.

[9] Albrecht, M., *Supramolecular Templating in the Formation of Helicates*, in *Templates in Chemistry I*, C.A. Schalley, F. Vögtle, and K.H. Dötz, Editors. 2004, Springer Berlin Heidelberg. p. 105-139.

[10] Li, S., Wei, M., Huang, X., Yang, X.-J., and Wu, B., *Chemm. Commun.*, **2012**, 48, 3097-3099.

[11] Kaufhold, O., Stasch, A., Pape, T., Hepp, A., Edwards, P.G., Newman, P.D., and Hahn, F.E., *J. Am. Chem. Soc.*, **2009**, 131, 306-317.

[12] Kumazawa, K., Biradha, K., Kusukawa, T., Okano, T., and Fujita, M., *Angew. Chem. Int. Ed.*, **2003**, 42, 3909-3913.

[13] Rizzuto, F.J., Wu, W.Y., Ronson, T.K., and Nitschke, J.R., *Angew. Chem. Int. Ed.*, **2016**, 128, 8090-8094.

[14] Ronson, T.K., Zarra, S., Black, S.P., and Nitschke, J.R., *Chem. Commun.*, **2013**, 49, 2476-2490.

[15] Fujita, M., Oguro, D., Miyazawa, M., Oka, H., Yamaguchi, K., and Ogura, K., *Nature*, **1995**, 378, 469-471.

[16] He, C., Lin, Z., He, Z., Duan, C., Xu, C., Wang, Z., and Yan, C., *Angew. Chem. Int. Ed.*, **2008**, 47, 877-881.

[17] Kleywegt, G.J. and Jones, T.A., *Acta Crystallogr. Sect. D*, **1994**, 50, 178-185.

[18] Bilbeisi, R.A., Clegg, J.K., Elgrishi, N., Hatten, X.d., Devillard, M., Breiner, B., Mal, P., and Nitschke, J.R., *J. Am. Chem. Soc.*, **2012**, 134, 5110-5119.

[19] Jiménez, A., Bilbeisi, R.A., Ronson, T.K., Zarra, S., Woodhead, C., and Nitschke, J.R., *Angew. Chem. Int. Ed.*, **2014**, 53, 4556-4560.

[20] Sgarlata, C., Mugridge, J.S., Pluth, M.D., Tiedemann, B.E.F., Zito, V., Arena, G., and Raymond, K.N., *J. Am. Chem. Soc.*, **2010**, 132, 1005-1009.

[21] Bai, X., Jia, C., Zhao, Y., Yang, D., Wang, S.-C., Li, A., Chan, Y.-T., Wang, Y.-Y., Yang, X.-J., and Wu, B., *Angew. Chem. Int. Ed.*, **2018**, 57, 1851-1855.

[22] Rizzuto, F.J., Kieffer, M., and Nitschke, J.R., *Chem. Sci.*, **2018**, 9, 1925-1930.

[23] Spek, A.L., *Acta Crystallogr. Sect C*, **2015**, 71, 9-18.

[24] Spek, A.L., *Acta Crystallogr. Sect. D*, **2009**, 65, 148-155.

Chapter 4

Stereochemical plasticity modulates cooperative binding in a $Co^{II}_{12}L_6$ cuboctahedron

4.1 Guest cooperativity in large architectures

Supramolecular complexes can manifest different stereochemistries[1] with distinct morphology and cavity differences. M_6L_4 tetrahedra, for example, can manifest three distinct isomers as a result of statistical distributions of Δ/Λ metal isomers at their vertices: complexes with *T*, S_4 or C_3 symmetry are typically all generated, unless a suitable stimulus or geometric restriction is present.[2] These complexes can adapt to guest stimuli to express specific isomeric forms, realising conformational changes to the host upon guest binding.[3]

Promoting guest recognition in larger architectures, however, relies on engineering complementary of size and electrostatics between host and guest in large volumes of space.[4] As a result, large architectures capable of binding small substrates are rare, and the methods thus far reported to engineer guest binding in large hosts (see Chapter 1) often rely on pre-programmed features within the assembly. A more flexible approach would entail the preparation of a capsule capable of adapting its geometry,[5] altering the size of its cavity, the dimensions of its faces, the lengths of its edges or the areas of its apertures in response to guest binding events. Realising these structural reconfigurations would change the landscape for subsequent guests, bringing about cooperativity.

The conformational changes exhibited by biological receptors upon substrate binding mirror this idea.[6] Both positive and negative cooperative binding, wherein the first binding event either improves or worsens the second,[7] respectively, are commonplace in these molecules. The ability of haemoglobin to cooperatively bind oxygen enhances its carrying capacity (Figure 4.1), whereas the negative cooperative binding of glyceraldehyde-3-phosphate to the dehydrogenase GAPDH normalises the rate of sugar digestion.[8] The efficacy of these systems relies on small electronic or structural changes propagating through a system following the first binding event, regulating the affinity of the second binding. Translating cooperativity into complex supramolecular systems is a current challenge in chemistry; it relies on balancing dynamic rearrangement with structural integrity, and maintaining guest recognition upon geometric alteration.

A supramolecular system capable of both adapting to and regulating cooperative interactions could lead to a new means of control over the amplification of binding events.[9-12] This Chapter[13] thus focuses on developing a method for modulating the cooperativity of binding of a new $Co^{II}_{12}L_6$ assembly through the guest-mediated transformation of its stereochemistry. Upon binding C_{60} or C_{70}, the stereochemistry of the metal centres of this capsule was observed to reconfigure to optimise host-guest interactions, consequently influencing successive binding events at the triangular apertures of the cage (Figure 4.2). When no guests were centrally bound, *O*-symmetric architecture **4.1** displayed a negative cooperative interaction with icosahedral anionic guests. Following the binding of two fullerenes, host **4.1** was observed to transform into its S_6-symmetric isomer **4.2**, which

displayed positive cooperativity during the binding of two $B_{12}F_{12}^{2-}$ guests, in contrast to **4.1**. Stereochemical transformations within this system thus led to the regulation of long range interactions between guests, modulating the specific modes and degrees of cooperativity (either positive or negative) expressed around the periphery of the cages.

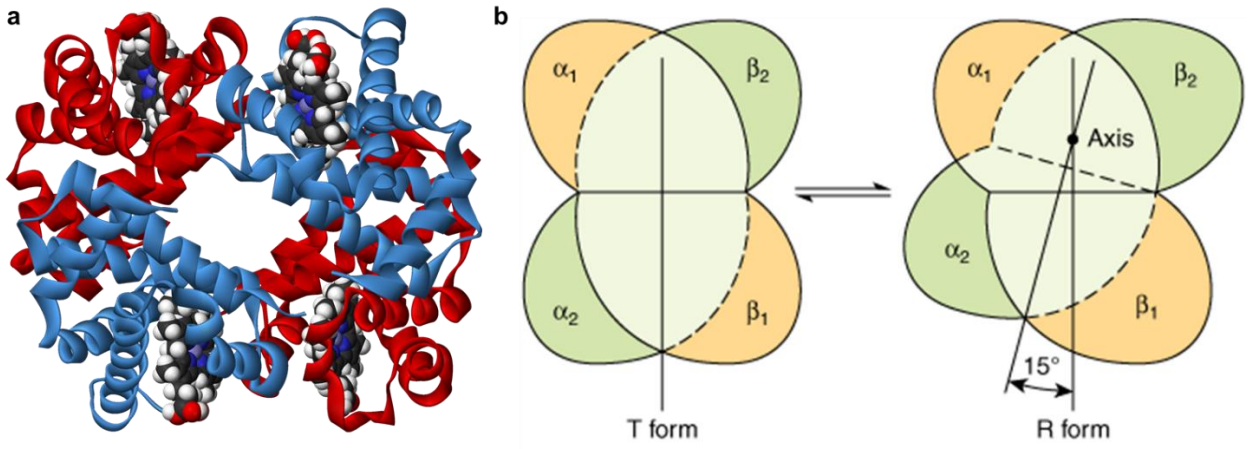

Figure 4.1 | Conformational changes in haemoglobin upon binding oxygen. **a**, X-ray crystal structure of haemoglobin, with O_2-binding porphyrin sites displayed in space filling representation. **b**, Conformational changes in the receptor upon binding O_2 at each site, wherein the symmetry of the receptor is broken. Figures adapted from reference 14.

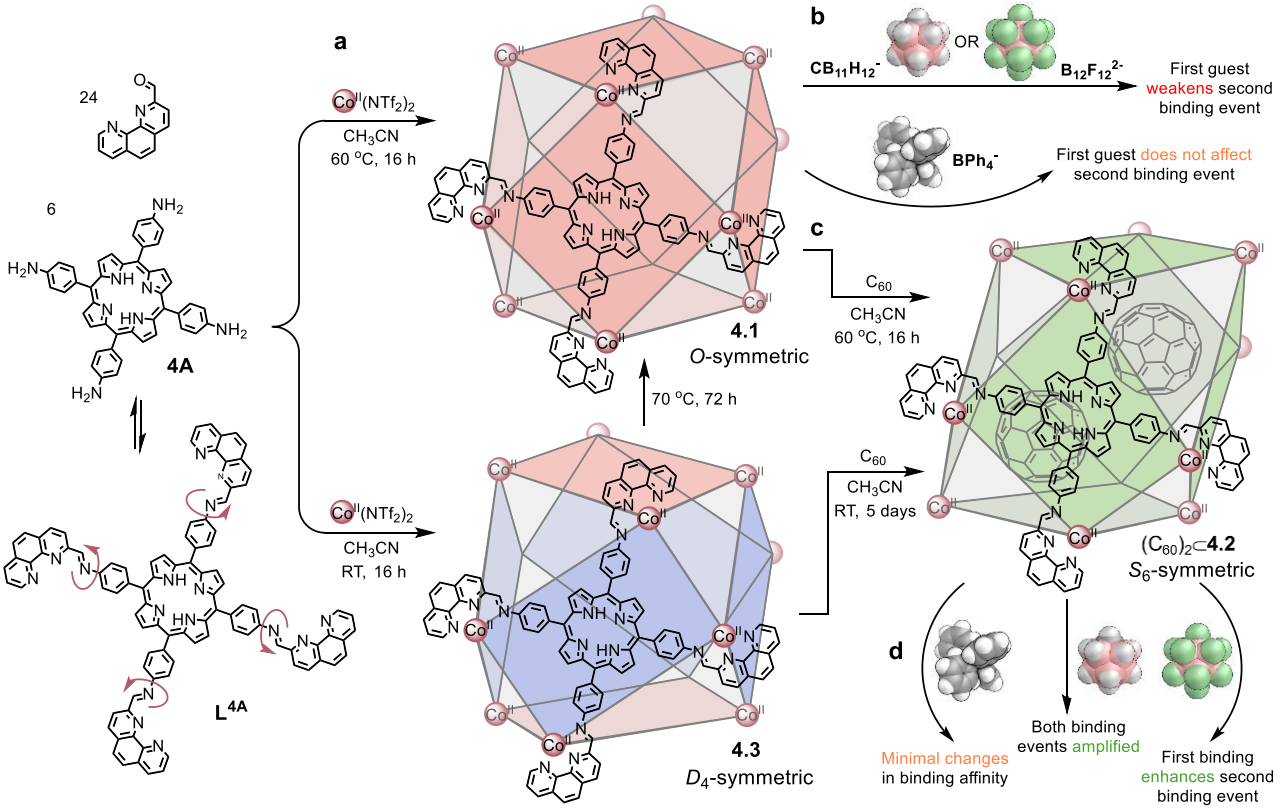

Figure 4.2 | Syntheses of the $Co^{II}_{12}L_6$ isomers **4.1**–**4.3** and their responses to the binding of large anionic guests. **a**, *O*-symmetric **4.1** (pink faces represent ligands on C_4 symmetry axes) and D_4-symmetric **4.3** (blue faces depict ligands on C_2 symmetry axes). **b**, In **4.1**, icosahedral anionic guests repel each other, leading to negative cooperativity. **c**, The addition of C_{60} to either **4.1** or **4.3** leads to the generation of the S_6-symmetric framework of **4.2** (green faces depict the ligands, which do not lie on symmetry axes). **d**, $(C_{60})_2$⊂**4.2** binds the same anions as **4.1**, but with dramatically altered cooperativities and affinities.

4.2 Synthesis and characterisation of 4.1

The self-assembly of free base tetrakis(*p*-aminophenyl)porphyrin **4A** (6 equiv) and 2-formylphenanthroline (24 equiv) subcomponents with cobalt(II) trifluoromethanesulfonimide (triflimide, NTf_2^-, 12 equiv) was observed by ESI-MS to produce $Co^{II}_{12}L_6$ cage **4.1**, following heating at 60 °C overnight in CH_3CN (Figure 4.2a). The wide-sweep ^1H NMR spectrum indicated that the product was highly symmetric; dispersion of the thirteen proton signals of the ligand over the range 240 to –20 ppm confirmed their coordination to paramagnetic Co^{II} centres with maintenance of fourfold ligand symmetry. Even when 30% excess of Co^{II} was used, no metalation of the free base porphyrin was observed during the assembly process.

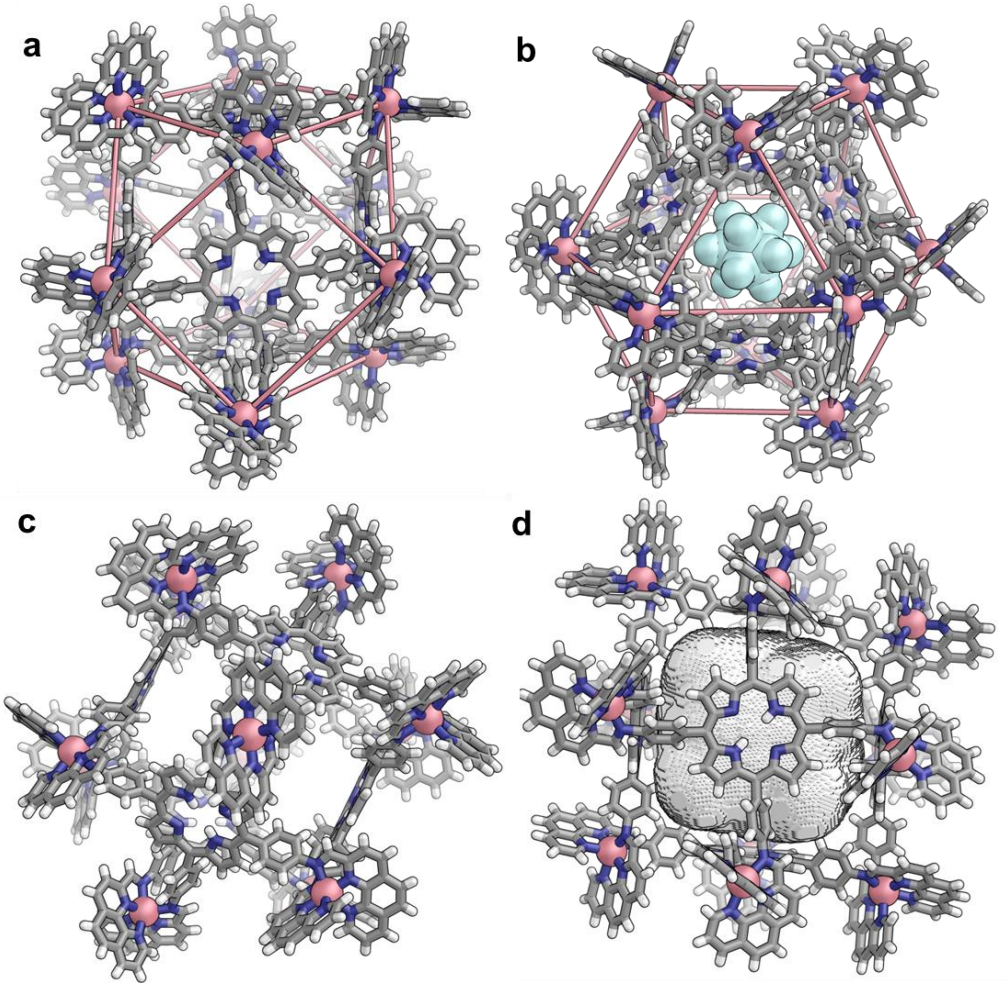

Figure 4.3 | X-ray crystal structure of **4.1**. **a & b**, Two views showing the cuboctahedral framework of Co^{II} ions of **4.1** (highlighted with solid pink lines), with **b** additionally depicting one of three $CB_{11}H_{12}^-$ anions localised in a triangular pocket of **4.1**. c, Side-on view depicting the bis-tridentate coordination environment around the Co^{II} ions. **d**, Viewed down a fourfold symmetry axis perpendicular to a square face. The central void is highlighted as a light grey solid. Solvent and anions are removed for clarity (Co^{II} – pink, C – grey, N – blue, H – white, $CB_{11}H_{12}^-$ – cyan).

Slow diffusion of $^iPr_2O$ into a solution of **4.1** containing $CsCB_{11}H_{12}$ (12 equiv) in CH_3CN provided X-ray quality crystals suitable for diffraction analysis (Figure 4.3). The cationic portion of the crystal structure revealed a cuboctahedral arrangement of Co^{II} ions, presenting six square faces

occupied by ligands and eight triangular apertures between ligands. All metal centres within a structure have the same Δ or Λ handedness. Both enantiomers of **4.1** are observed in the crystal. The architecture has approximate *O* (chiral octahedral) point symmetry, consistent with its ^{1}H NMR spectrum, and encloses an interior cavity of 2888 Å^3, calculated using VOIDOO[15] (Figure 4.3d). The chelation planes[16] of the two imino-phenanthroline moieties bound to each Co^{II} centre intersect at an angle of 79–84°. Adjacent Co^{II}–Co^{II} distances average 14.7 Å and antipodal metal centres are separated by *ca.* 30.0 Å. This work builds upon reports of *edge-linked* Archimedean solids by the groups of Ward,[17] Stang[18] and Fujita[19] to construct the first *face-capped* cuboctahedral structure, enabling an unprecedented enclosure of the central cavity of **4.1**.

4.3 Cooperative templation of 4.2

Host-guest investigations revealed that **4.1** bound fullerenes with high affinity. The addition of the acetonitrile-insoluble fullerenes C_{60}, C_{70} or [6,6]-phenyl C_{61} butyric acid methyl ester (PCBM) (*ca.* 5 equiv each, excess) to a solution of **4.1** led to significant changes in the wide-sweep ^{1}H NMR spectra after heating at 60 °C for 16 h. In all cases approximately four times the original number of signals were observed (Figure 4.4a). ESI-MS revealed the presence of an adduct of two fullerenes in all cases (Figure 4.4b).

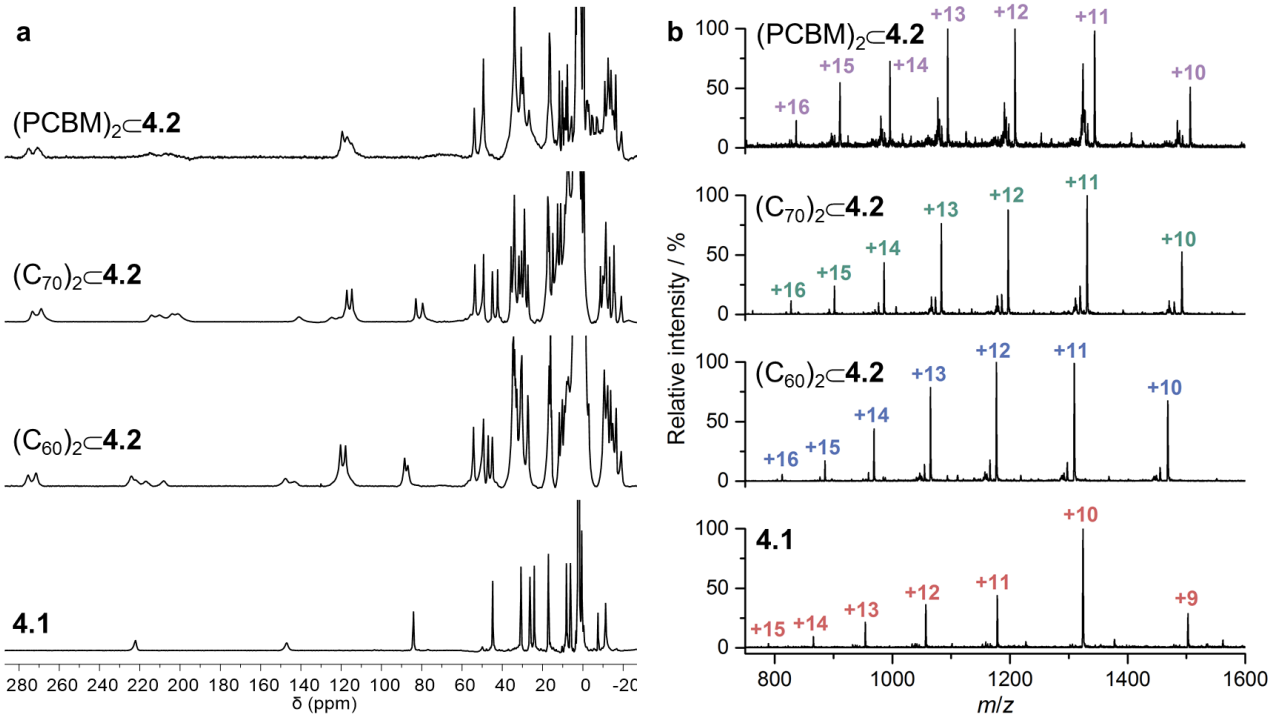

Figure 4.4 | Characterisation data for **4.1**, $(C_{60})_2$⊂**4.2**, $(C_{70})_2$⊂**4.2** and **(**$PCBM)_2$⊂**4.2**. **a**, Wide sweep ^{1}H NMR spectra (400 MHz, 298 K, CD_3CN) and **b**, ESI mass spectra.

Single crystal X-ray diffraction analysis unambiguously revealed that C_{60} induced a significant stereochemical alteration to **4.1**, generating isomer **4.2** (Figure 4.5). Unexpectedly, the vertices of $(C_{60})_2$⊂**4.2** were not all of the same handedness – both Δ- and Λ-handed metal centres were present in a 1:1 ratio. On each ligand, one set of transverse branches was *syn*, while the other was *anti*, resulting in overall C_1 symmetry of the ligands. This is consistent with the ^{1}H NMR data (Figure 4.4a), which suggests complete desymmetrisation of the ligand environments in $(C_{60})_2$⊂**4.2**.

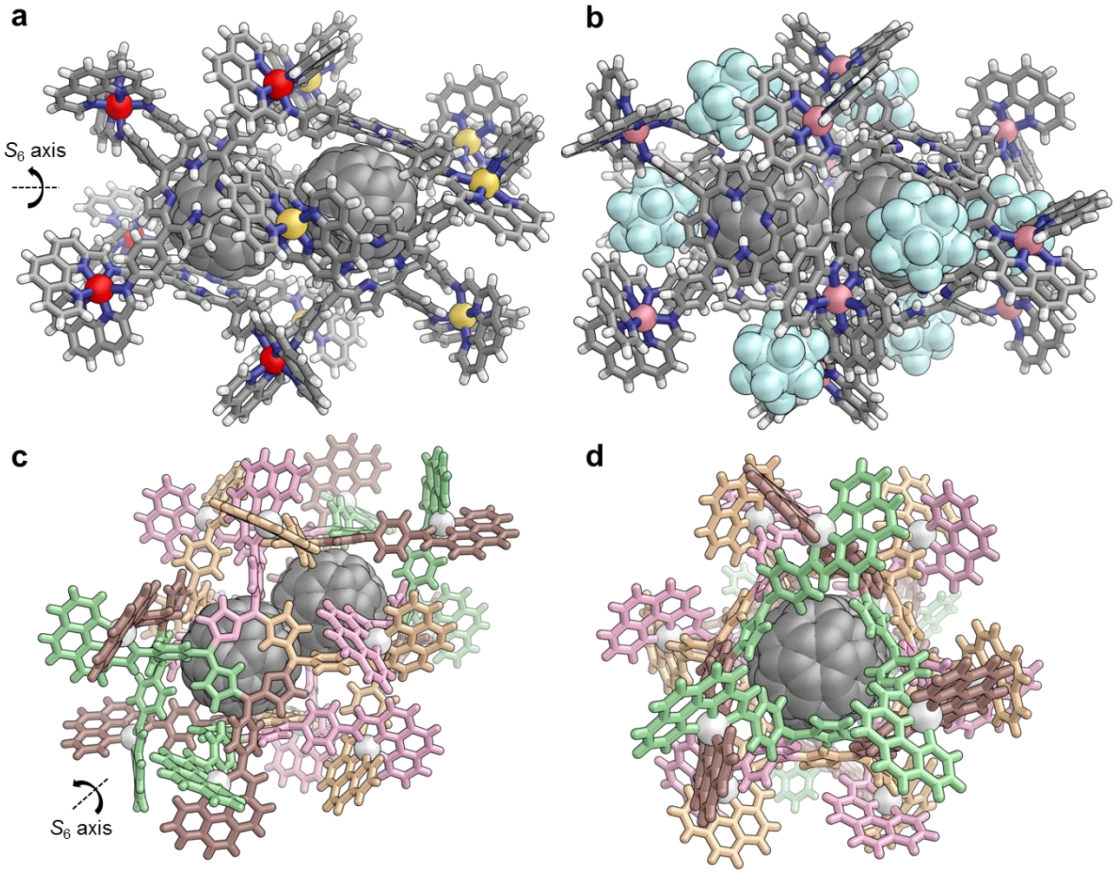

Figure 4.5 | Four views of the X-ray crystal structure of $(C_{60})_2$⊂**4.2**. **a**, Λ metal centres are coloured red and Δ centres are coloured yellow. **b**, Shown with the $CB_{11}H_{12}^-$ anions that are localised at the triangular apertures of the architecture. **c**, View perpendicular to a ligand face, and **d**, view down the S_6 axis, where each colour represents a different ligand environment and Co^{II} is coloured white.

Structurally, this reconfiguration results in a compression of the metal-metal distances along the equatorial belt, accompanied by a lengthening of the shortest distances between axial and equatorial metal centres. Adjacent Co^{II}–Co^{II} vectors thus generate six irregular quadrilateral faces, occupied by ligands. The apertures of the structure comprise two equilateral triangles at the axial ends, orthogonal to the S_6 axis of the cage, and six approximately right-angled triangles around the equator, maintaining the cuboctahedral connectivity of the assembly. The degree of strain around the Co^{II} ions was inferred to be larger than in **4.1**, with the angles between chelation planes in the range 74–89°. The S_6 point symmetry of **4.2** renders it achiral, with each metal centre of Δ handedness related by inversion to a metal centre of Λ handedness (Figure 4.5a).

The axial elongation and stereochemical reconfiguration of **4.1** to generate **4.2** thus maximises contacts both between fullerenes and between the host and guests. The rearrangement required in order to bind the first fullerene leads to the formation of a configuration better able to bind the second, leading to cooperativity.

Adding equimolar amounts of C_{60} and C_{70} concurrently to **4.1** led to a statistical mixture of fullerene adducts of **4.2**. Each of $(C_{60})_2$⊂**4.2**, $C_{60}C_{70}$⊂**4.2** and $(C_{70})_2$⊂**4.2** were observed by ESI-MS and ^{1}H NMR spectroscopy (Figure 4.6). Integration of the ^{1}H NMR spectrum (Figure 4.6b) indicated that $(C_{70})_2$⊂**4.2** was slightly more abundant than $C_{60}C_{70}$⊂**4.2**, and that both of these were more abundant than $(C_{60})_2$⊂**4.2** (the ratio of $(C_{60})_2$⊂**4.2**:$C_{60}C_{70}$⊂**4.2**:$(C_{70})_2$⊂**4.2** was *ca.* 2:9:10). The similarity of the proton spectra between each fullerene-occupied species (Figure 4.4a) suggests that all three fullerenes induce the same stereochemical change from **4.1** to **4.2**. The rate of conversion from **4.1** to **4.2** could not be measured, due to the lack of stability of **4.1** in any solvent capable of dissolving fullerenes.

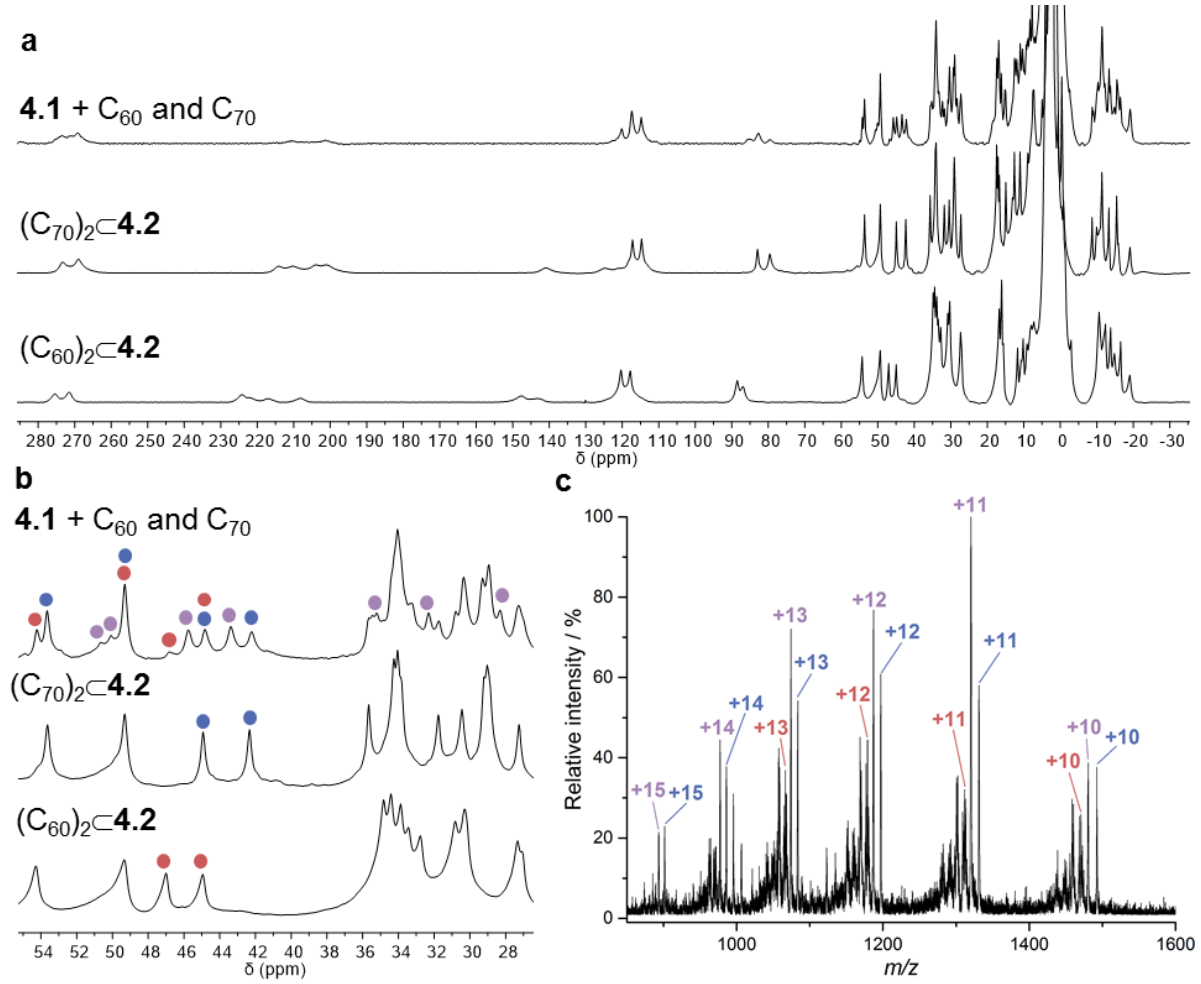

Figure 4.6 | **a**, When equal amounts of C_{60} and C_{70} (excess of both) were added to a solution of **4.1** and heated at 60 °C overnight, the topmost spectrum was observed, showing a combination of $(C_{60})_2$⊂**4.2** (bottom spectrum), $(C_{70})_2$⊂**4.2** (middle spectrum) and heterotropic host-guest species $C_{60}C_{70}$⊂**4.2**. **b**, A zoomed view of the region 23–58 ppm, showing $(C_{60})_2$⊂**4.2** (red circles), $(C_{70})_2$⊂**4.2** (blue circles) and signals attributed to $C_{60}C_{70}$⊂**4.2** (purple circles). **c**, ESI-MS of the product distribution, showing all three species.

In order to probe the stability of the singly occupied host-guest complex, 1.5 equivalents of C_{60} were added to a CD_3CN solution of **4.1** and heated to 60 °C for 16 h. Both ^1H NMR and ESI-MS showed only peaks corresponding to the free cage and the doubly-occupied host-guest species; no singly occupied species could be identified (Figure 4.7). This experiment reflects all-or-nothing cooperative binding of fullerenes within the cavity of the assembly.

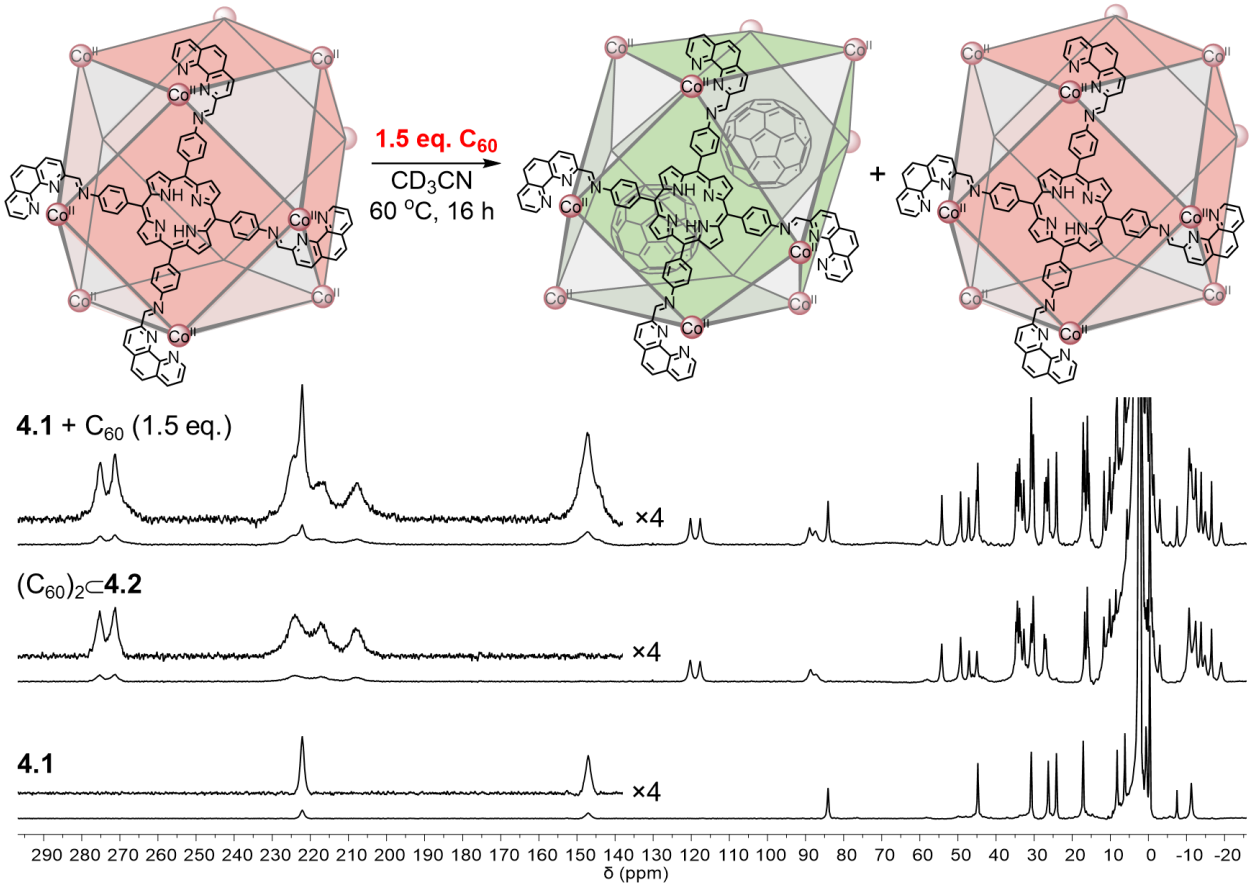

Figure 4.7 | When 1.5 equivalents of C_{60} were added to **4.1** and heated at 60 °C for 16 h, the topmost spectrum was observed, showing a mixture of **4.1** (bottom spectrum) and $(C_{60})_2\subset$**4.2** (middle spectrum). No other species were observed by wide sweep ^1H NMR spectroscopy.

4.4 Regulation of cooperative binding events

Further host-guest investigations revealed the propensity of **4.1** to bind large anionic guests (Figure 4.2). While both carborate ($CB_{11}H_{12}^-$) and tetraphenylborate (BPh_4^-) anions were observed to bind in fast exchange with **4.1** by ^1H NMR ((Figure 4.8), the rate of exchange of $B_{12}F_{12}^{2-}$ with **4.1** was slower, approximating intermediate exchange on the NMR timescale. A sample of **4.1** containing $B_{12}F_{12}^{2-}$ (5 equiv) gave a single ^{19}F signal distinct from the chemical shift of free $B_{12}F_{12}^{2-}$, verifying binding to **4.1** (Figure 4.9a). For both $CB_{11}H_{12}^-$ and BPh_4^-, the proton signals of the guest were observed to shift downfield by 1–4 ppm, relative to their unbound states, after binding to **4.1**.

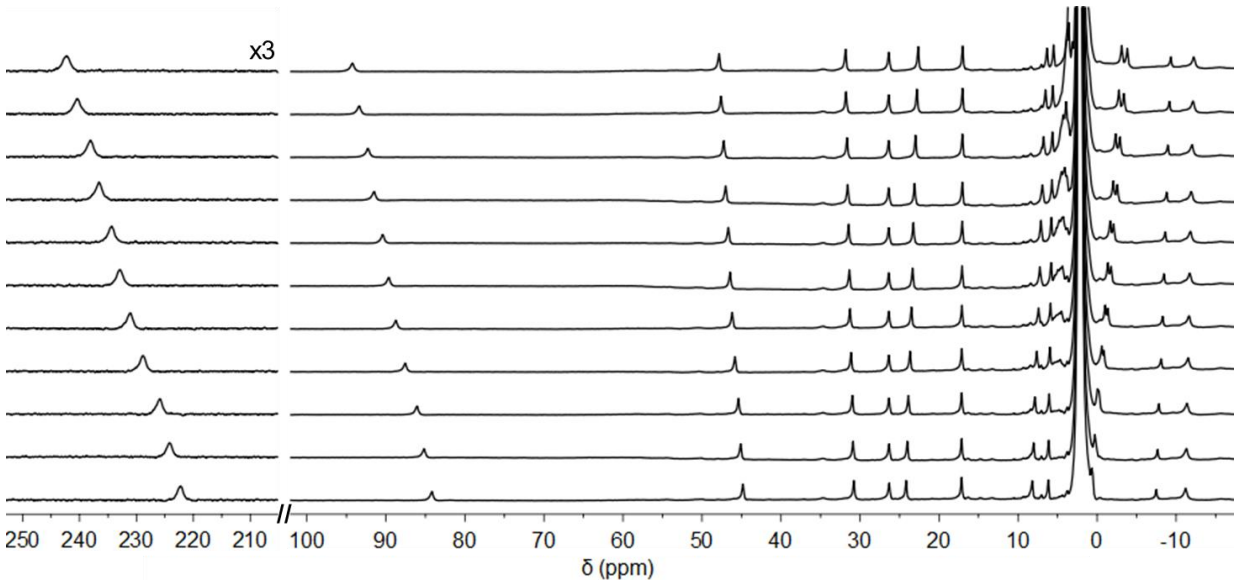

Figure 4.8 | ^{1}H NMR titration (400 MHz, 298 K, CD_3CN) of $CB_{11}H_{12}^-$ into a solution of **4.1** in CD_3CN, with anion equivalents increasing from the bottom spectrum to the top. Similar signal shifting directions were observed for the cage signals during the titration of BPh_4^- and $B_{12}F_{12}^{2-}$.

Affinity constants for $CB_{11}H_{12}^-$ and BPh_4^- were determined by ^{1}H NMR titrations, while the affinity of $B_{12}F_{12}^{2-}$ was determined by UV-Vis titration. All anions produced sigmoidal residuals when fitted to a 1:1 binding isotherm. When instead fitted to 1:2 binding isotherms, only random residuals were observed, indicating two distinct binding events to **4.1** (Figure 4.9c and Figure 4.10). In all cases, the affinity constants for the first and second bindings (K_1 and K_2, respectively) were determined from a global shift analysis of the titration data using Bindfit[20,21]; the results were averaged over two runs. The cooperativity was quantified using the allosteric cooperativity factor α (where $\alpha = 4K_2/K_1$: $\alpha > 1$ indicates positive cooperativity, $\alpha < 1$ indicates negative cooperativity, and $\alpha = 1$ indicates non-cooperative binding). Both $CB_{11}H_{12}^-$ and $B_{12}F_{12}^{2-}$ displayed negative cooperative binding to **4.1**, while BPh_4^- was observed to approximate non-cooperative behaviour. These data are displayed in Table 4.1 and depicted graphically in Figure 4.13 (*vida infra*).

Guest localisations were inferred by considering the crystallographic and titration data together. In **4.1**, guests appear localised around the eight triangular apertures of the architecture, given that three of the twelve resolved carborate anions are nestled within the triangular apertures of the architecture (Figure 4.3b), and that the most significant proton shifts were observed for the most downfield-shifted protons (that is, those closest to the Co^{II} centres) for all guest titrations (Figure 4.8). However, solid-state guest localisations do not necessarily reflect binding stoichiometries in solution.[22] As a 1:2 host:guest isotherm represents the simplest model to adequately fit the titration data, rapid exchange of the guests between the triangular sites is inferred, preventing the observation of higher binding stoichiometries in solution.

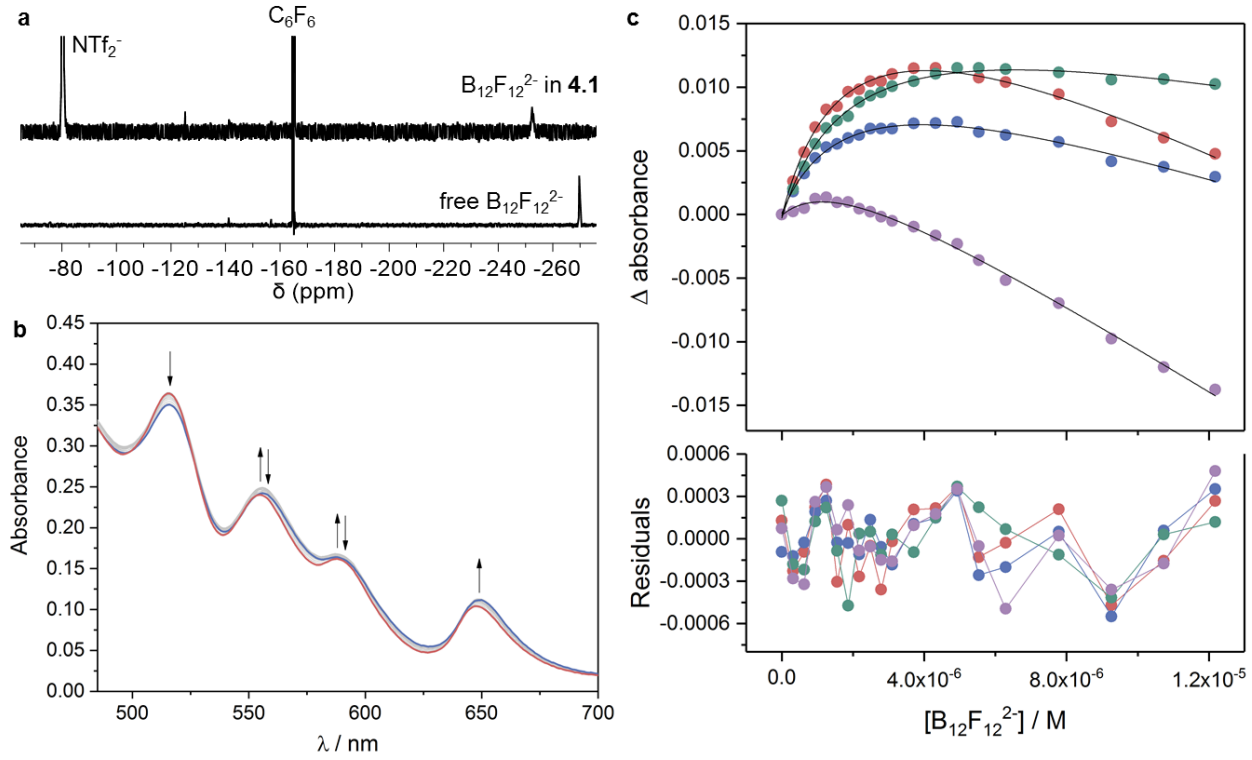

Figure 4.9 | Binding of $B_{12}F_{12}^{2-}$ to **4.1**. **a**, ^{19}F NMR spectra (376 MHz, 298 K, CD_3CN) comparing free $B_{12}F_{12}^{2-}$ (bottom spectrum) to $B_{12}F_{12}^{2-}$ bound by **4.1** (top spectrum). **b**, UV-Vis titration of $K_2B_{12}F_{12}$ into **4.1** in CH_3CN (initial spectrum is shown in red, final spectrum is shown in blue; arrows show direction of spectral progression). **c**, Binding isotherms (1:2 model) fit to the absorbance shift of the four Q bands of **4.1** *vs.* the concentration of $B_{12}F_{12}^{2-}$ added to determine the binding affinity (top); and the residual plot from the fit (bottom).

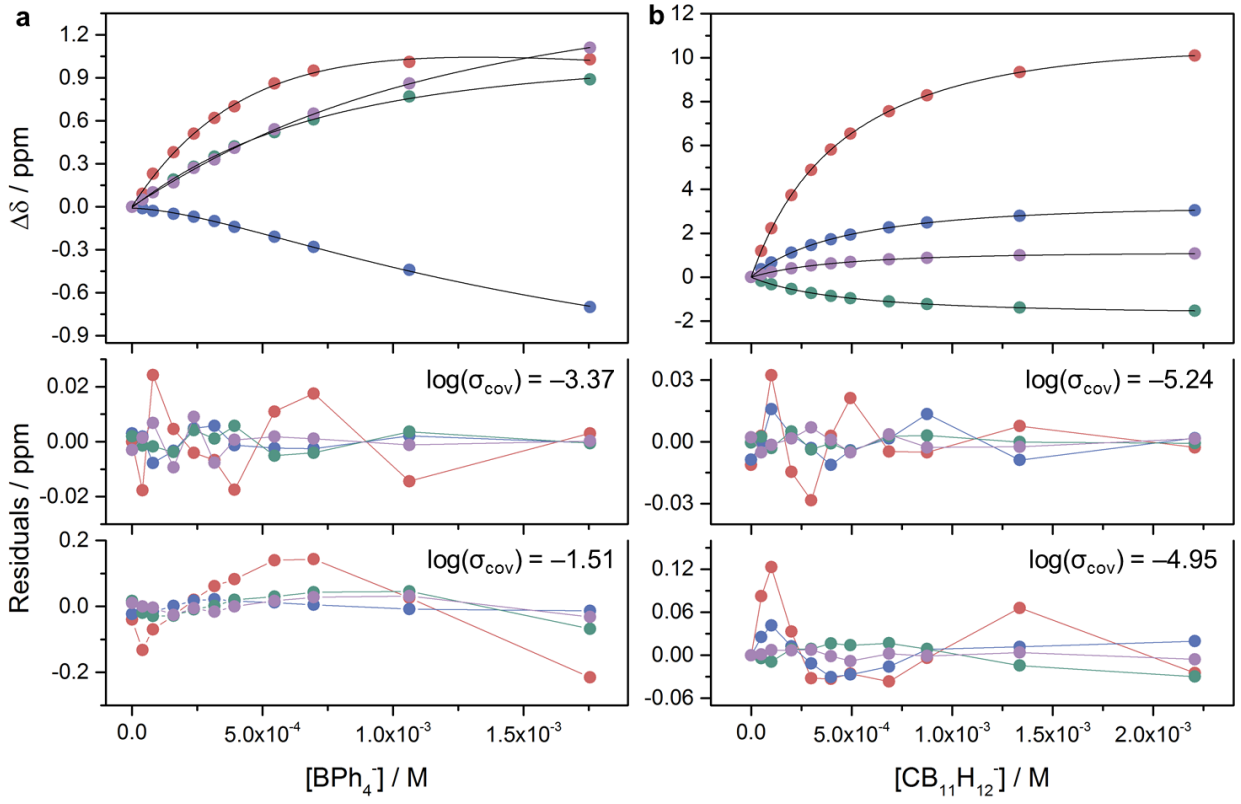

Figure 4.10 | Binding isotherms (1:2 system) fit to the chemical shift of four proton signals (each different colours) *vs.* the concentration of either **a**, BPh_4^- or **b**, $CB_{11}H_{12}^-$ added to determine the binding affinities (top); and the residual plots from the fit (middle). The bottom graphs show the residuals from fitting the data to a 1:1 system. High covariances (σ_{cov}) and sigmoidal residuals were observed upon fitting to the 1:1 model.

The dispersion of the fifty-two unique proton signals of $(C_{60})_2$⊂**4.2** and $(C_{70})_2$⊂**4.2** over their wide-sweep ^{1}H NMR spectra enabled the binding affinities of $CB_{11}H_{12}^-$, BPh_4^- and $B_{12}F_{12}^{2-}$ to be quantified by global proton shift analysis.[20] All anionic guests induced distinct proton shifts throughout their titration, consistent with fast exchange binding on the NMR timescale (see Figure 4.11 for representative titrations). As with **4.1**, a 1:2 binding model best fit the titration data (Figure 4.12). The affinity of BPh_4^- showed little difference between assemblies; however, $CB_{11}H_{12}^-$ binding was enhanced, and $B_{12}F_{12}^{2-}$ decreased, when fullerenes were present in the cage (Table 4.1). In the case of $CB_{11}H_{12}^-$, K_1 increased fourfold in $(C_{60})_2$⊂**4.2** and $(C_{70})_2$⊂**4.2**, as compared to **4.1**; K_2 was nine times larger in $(C_{60})_2$⊂**4.2** than in $(C_{70})_2$⊂**4.2** or **4.1**. When binding $B_{12}F_{12}^{2-}$, K_1 decreased by three orders of magnitude in $(C_{60})_2$⊂**4.2** and two orders of magnitude in $(C_{70})_2$⊂**4.2**, from the baseline of **4.1**. Furthermore, whereas most anions exhibited negative cooperative binding to $(C_{60})_2$⊂**4.2** and $(C_{70})_2$⊂**4.2**, $B_{12}F_{12}^{2-}$ was observed to bind to $(C_{60})_2$⊂**4.2** with positive cooperativity (Figure 4.13). A decrease in the kinetic uptake ratio k_{in}/k_{out} of the binding of $B_{12}F_{12}^{2-}$ was also observed when going from **4.1** to $(C_{60})_2$⊂**4.2**, as reflected in the transition from intermediate to fast exchange binding of $B_{12}F_{12}^{2-}$ on the NMR timescale (Figure 4.11).

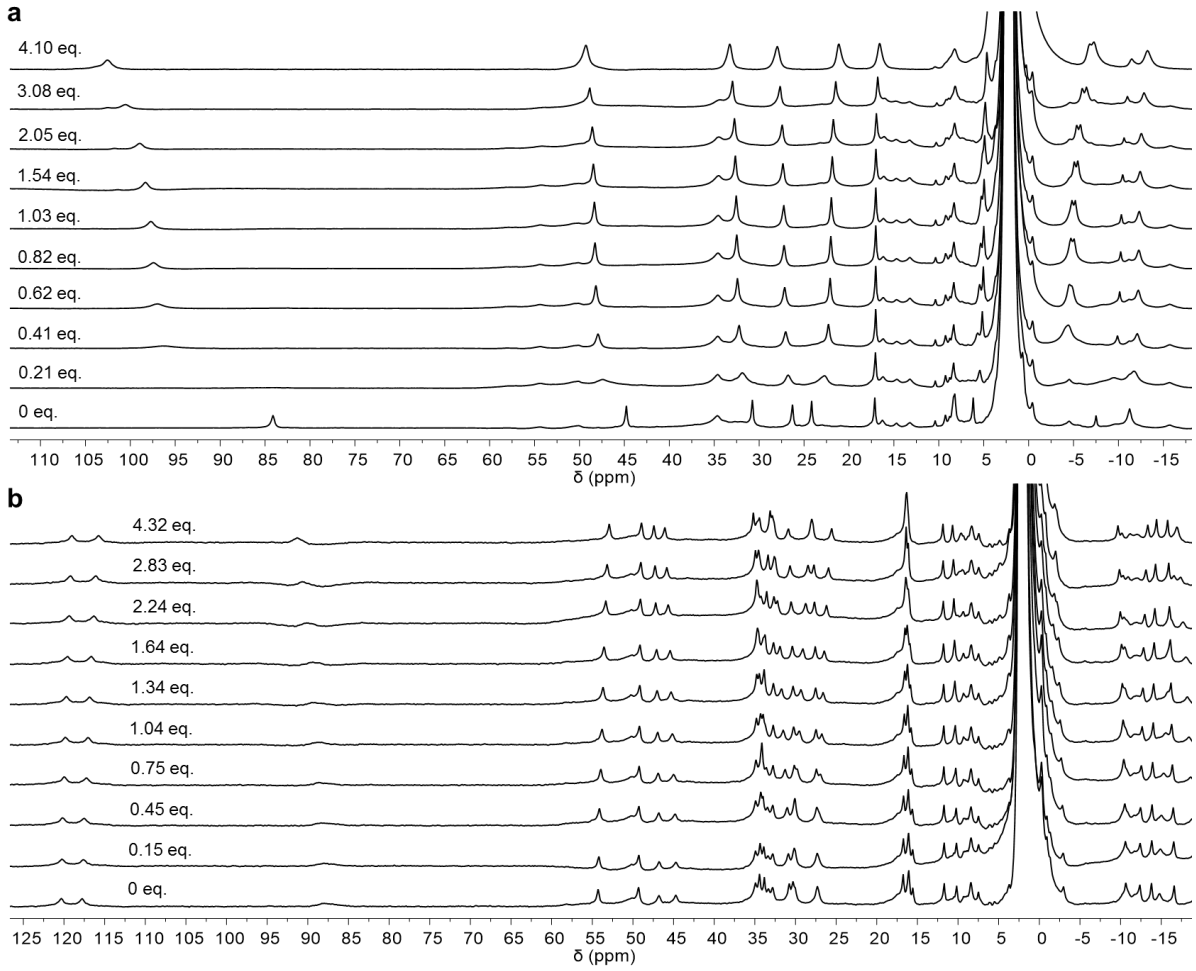

Figure 4.11 | ^{1}H NMR titrations (400 MHz, 298 K, CD_3CN) of $B_{12}F_{12}^{2-}$ into **a**, **4.1** and **b**, $(C_{60})_2$⊂**4.2**. The former displays intermediate exchange binding (broadening followed by sharpening of signals) while the latter displayed fast exchange binding on the NMR timescale.

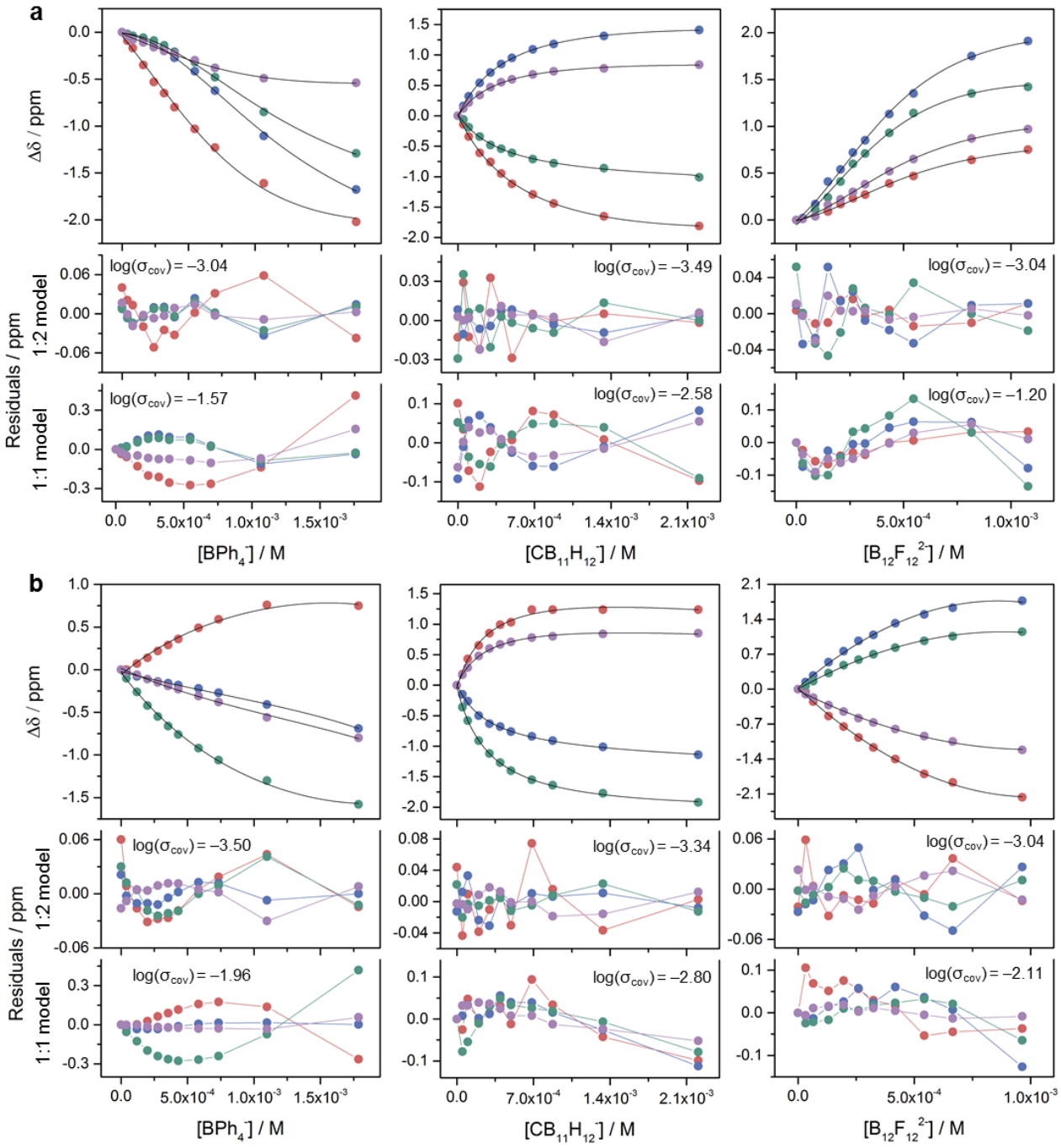

Figure 4.12 | Binding isotherms (1:2 system) fit to the chemical shift of four proton signals of either **a**, $(C_{60})_2$⊂**4.2** or **b**, $(C_{70})_2$⊂**4.2** *vs.* the concentration of BPh_4^- (left), $CB_{11}H_{12}^-$ (middle) or $B_{12}F_{12}^{2-}$ (right) added to determine the binding affinities (top graph). The residuals from both the 1:2 (middle graph) and 1:1 (bottom graph) fits are shown in all cases. Each showed sigmoidal residuals and high errors when fitted to a 1:1 model.

The regulation of binding events observed for $(C_{60})_2$⊂**4.2** and $(C_{70})_2$⊂**4.2**, compared to **4.1**, is surprising given that the central voids of $(C_{60})_2$⊂**4.2** and $(C_{70})_2$⊂**4.2** are too small to accommodate guests of this size. Two explanations appear plausible: firstly, the cage framework may be flexible enough to expand and accommodate guests, or secondly, binding may occur on the exterior of the structure. All twenty-four carborate anions were resolved in the crystal structure of $(C_{60})_2$⊂**4.2**, none

of which are located in the cavity of the assembly. However, a carborate anion was observed around every aperture: two cap the axial apertures along the S_6 axis, at opposite ends of the cage, and six sit in the triangular pockets ringing its equator (Figure 4.5b). Guests thus appear to associate with the exterior pockets, rather than interior cavity, of the cage.

Table 4.1 | Summary of the binding constants (K_1 and K_2, M^{-1}) of anionic guests with capsule **4.1**, $(C_{60})_2\subset$**4.2** and $(C_{70})_2\subset$**4.2**. Values are reported as the weighted average of two titrations.

Guest		**4.1**	$(C_{60})_2\subset$**4.2**	$(C_{70})_2\subset$**4.2**
BPh_4^-	K_1	$(1.86 \pm 0.02) \times 10^3$	$(2.63 \pm 0.03) \times 10^3$	$(2.43 \pm 0.03) \times 10^3$
	K_2	$(5.9 \pm 0.1) \times 10^2$	$(6.56 \pm 0.02) \times 10^2$	$(3.5 \pm 0.1) \times 10^2$
	α	1.3 ± 0.1	1.00 ± 0.01*	0.58 ± 0.02
$CB_{11}H_{12}^-$	K_1	$(2.61 \pm 0.02) \times 10^3$	$(1.1 \pm 0.1) \times 10^4$	$(1.0 \pm 0.1) \times 10^4$
	K_2	$(1.7 \pm 0.2) \times 10^2$	$(1.56 \pm 0.05) \times 10^3$	$(1.3 \pm 0.1) \times 10^2$
	α	0.26 ± 0.03	0.57 ± 0.05	0.052 ± 0.007
$B_{12}F_{12}^{2-}$	K_1	$(1.5 \pm 0.1) \times 10^6$	$(1.5 \pm 0.1) \times 10^3$	$(2.2 \pm 0.1) \times 10^4$
	K_2	$(1.89 \pm 0.02) \times 10^4$	$(1.4 \pm 0.1) \times 10^4$	$(3.2 \pm 0.1) \times 10^3$
	α	0.050 ± 0.003	37 ± 4	0.58 ± 0.03

* Regression was restrained to approximate non-cooperative behaviour ($K_1 = 4K_2$).

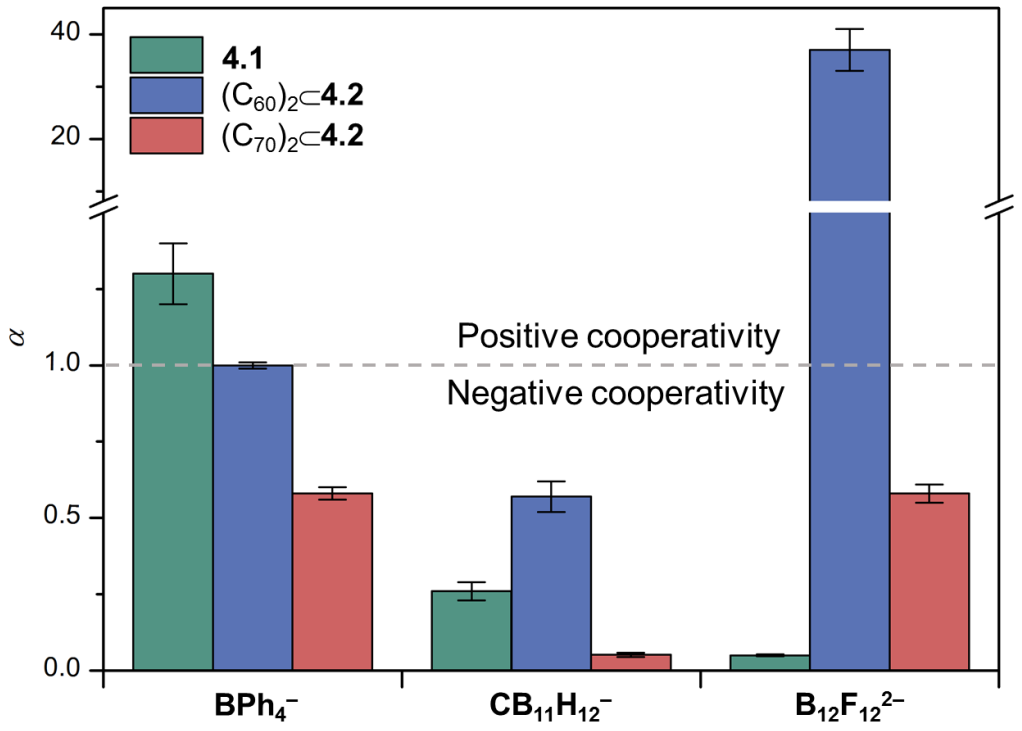

Figure 4.13 | The changes observed in the cooperativity parameter ($\alpha = 4K_2/K_1$) when fullerenes were present in the cage. The dashed line represents the border between positive and negative cooperative binding. Asymptotic errors are calculated at the 95% Confidence Interval level.

Among all anionic guests, the presence of C_{60} produced higher K_2 and α values than the presence of C_{70} (Table 4.1 and Figure 4.13). This indicates that the inclusion of C_{70} enforces a stronger negative cooperative interaction than C_{60} in **4.2**. The variances in cooperativity were initially ascribed to the different electronic properties of the fullerene guests (acceptors) interacting with porphyrin units (donors).[23] Although the UV-Vis spectra of all fullerene-bound complexes revealed red shifts in the Soret (+7 nm) and Q bands (*ca.* +5 nm) of the porphyrin units compared to **4.1**, the contraction of the HOMO/LUMO gap appeared uniform across all host-guest complexes (Figure 4.14).

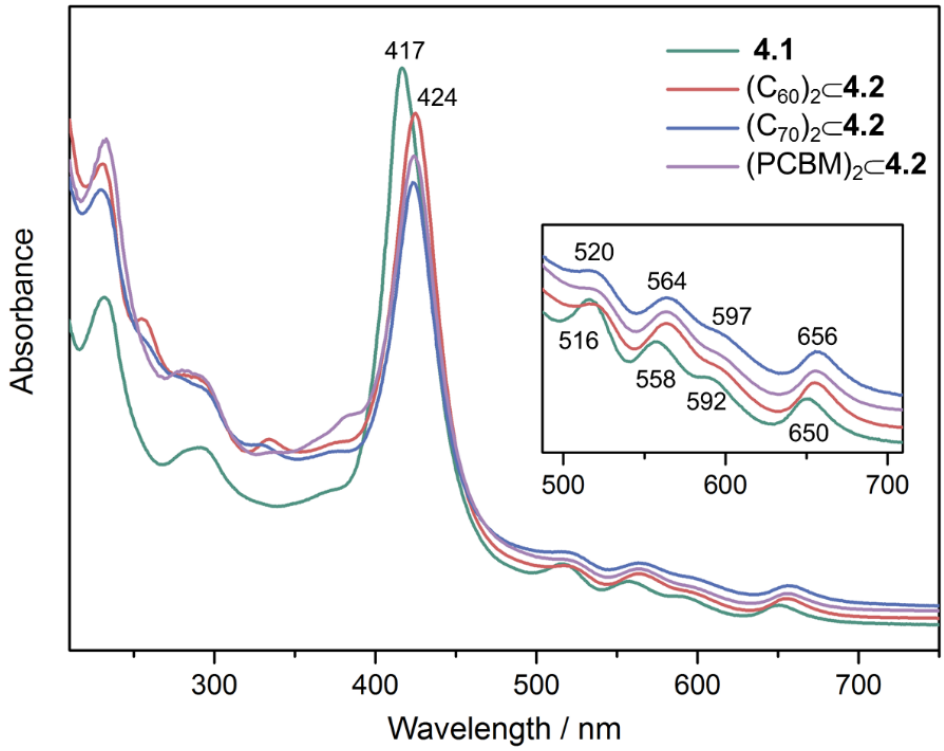

Figure 4.14 | UV-Vis spectra of **4.1**, $(C_{60})_2$⊂**4.2**, $(C_{70})_2$⊂**4.2** and $(PCBM)_2$⊂**4.2** in CH_3CN. Red-shifts were observed for all bands of cages with bound fullerenes. Labels mark the wavelengths of host and host-guest bands.

It is thus hypothesised that the observed differences in cooperativity instead result from the dissimilarities in sphericity and aperture-blocking character engendered by the two fullerenes. Upon binding, both fullerenes are expected to exhibit a δ^- polarisation close to the Co^{II} cations, resulting in a balancing δ^+ polarisation pointing inwards to the cavity. As elliptical C_{70} is larger than spherical C_{60}, the fullerene surface area adjacent to the apertures will be larger in $(C_{70})_2$⊂**4.2** than in $(C_{60})_2$⊂**4.2**. A greater surface area of δ^- polarisation will therefore occur near the apertures of $(C_{70})_2$⊂**4.2** compared to $(C_{60})_2$⊂**4.2**, potentially increasing the degree of charge repulsion experienced by anionic guests around the apertures of the cage. Slight structural differences between the cages in accommodating fullerenes of different sizes may also be a contributing factor to the observed differences in guest binding strengths.

4.5 Further stereochemical diversity

The stereochemical plasticity of $\mathbf{L^{4A}}$, exhibited in the distinct geometries of both **4.1** and **4.2**, prompted an investigation into whether the same set of subcomponents and Co^{II} might form other diastereomers without templation. The same building blocks that formed **4.1** (after 16 h at 60 °C in CD_3CN) were observed to form another species when stirred in CD_3CN at room temperature overnight. The wide sweep ^1H NMR spectrum of this new species exhibited a series of broader, shifted peaks (Figure 4.15). Intriguingly, the ESI mass spectrum of this mixture corresponded to a $Co^{II}_{12}L_6$ species, despite the absence of signals attributable to **4.1** by ^1H NMR spectroscopy.

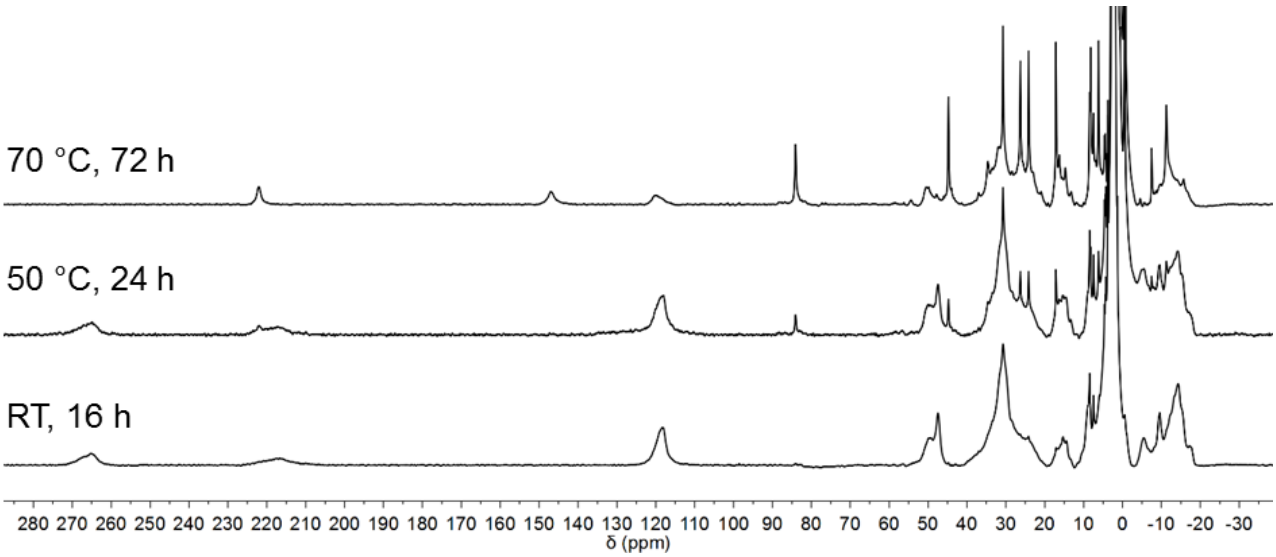

Figure 4.15 | ^1H NMR spectra (400 MHz, 298 K, CD_3CN) following the conversion of **4.3** (bottom spectrum) to **4.1** (top spectrum) after heating at 70 °C for three days.

The subsequent diffusion of Et_2O into this solution (containing approximately 20 equivalents of nBu$_4$NBF$_4$) yielded single crystals of **4.3** (Figure 4.16). X-ray diffraction revealed a similar cuboctahedral metal connectivity as **4.1** and **4.2**, however, the assembly displayed D_4 symmetry: four ligands on twofold symmetry axes span the equatorial plane of the structure, and two ligands, each with fourfold rotational symmetry, cap the axial positions (Figure 4.16b). The structure thus presents a mixture of square and rectangular ligand-occupied faces with scalene triangular apertures, as opposed to the square faces and equilateral triangular apertures of **4.1** (Figure 4.2).

The chiral structure contains a 1:2 ratio of Δ and Λ metal nodes. Both enantiomers are present in the crystal. The angles between the chelation planes of the imino-phenanthroline moieties are in a similar range (79–85°) to those of **4.1**, indicating that there is little coordinative strain difference between the two structures.

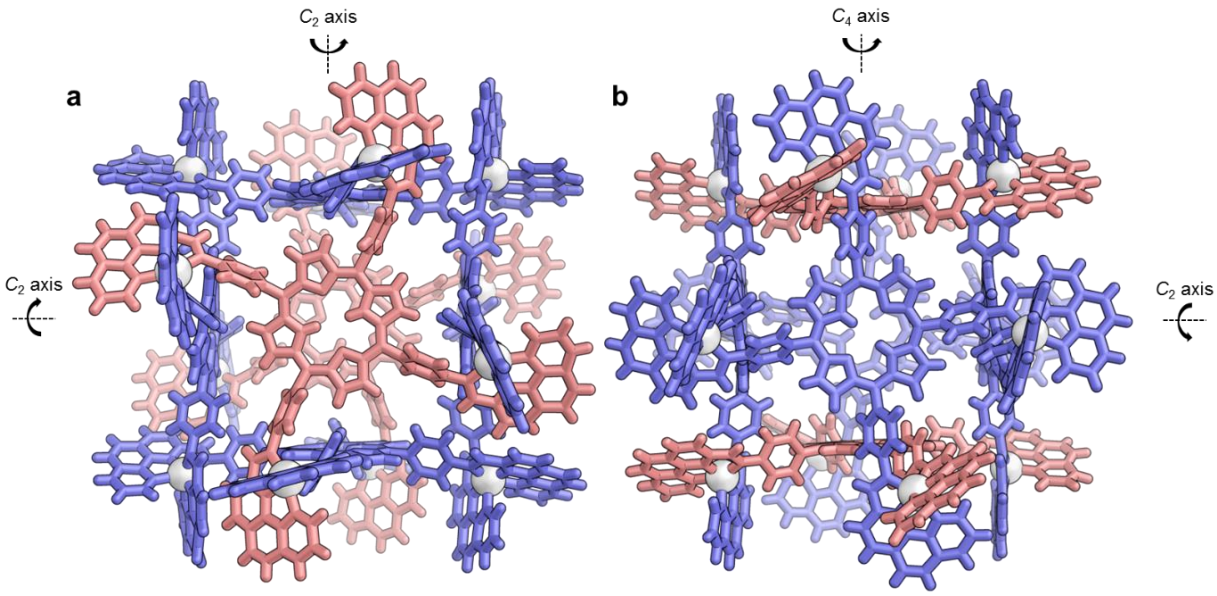

Figure 4.16 | Two views of the X-ray crystal structure of D_4-symmetric **4.3**. **a**, Perpendicular to a fourfold-symmetric ligand (pink). **b**, Perpendicular to a twofold-symmetric ligand (blue) (Co^{II}, white).

Despite its broad ^{1}H NMR spectrum, travelling wave ion mobility ESI mass spectra (IM-MS) of **4.3** revealed only a single drift time for each signal corresponding to an $Co^{II}_{12}L_6$ architecture (Figure 4.17), suggesting that **4.3** is the principal product in solution. When **4.3** was heated to 50 °C for a further 24 hours, the ^{1}H NMR signals of **4.1** were observed to grow into the spectrum (Figure 4.15). *O*-symmetric cage **4.1** was observed by ^{1}H NMR spectroscopy to predominate after heating the mixture to 70°C for 72 hours. Likewise, the addition of C_{60} or C_{70} to **4.3** generated $(C_{60})_2\subset$**4.2** and $(C_{70})_2\subset$**4.2** after stirring at room temperature for five days.

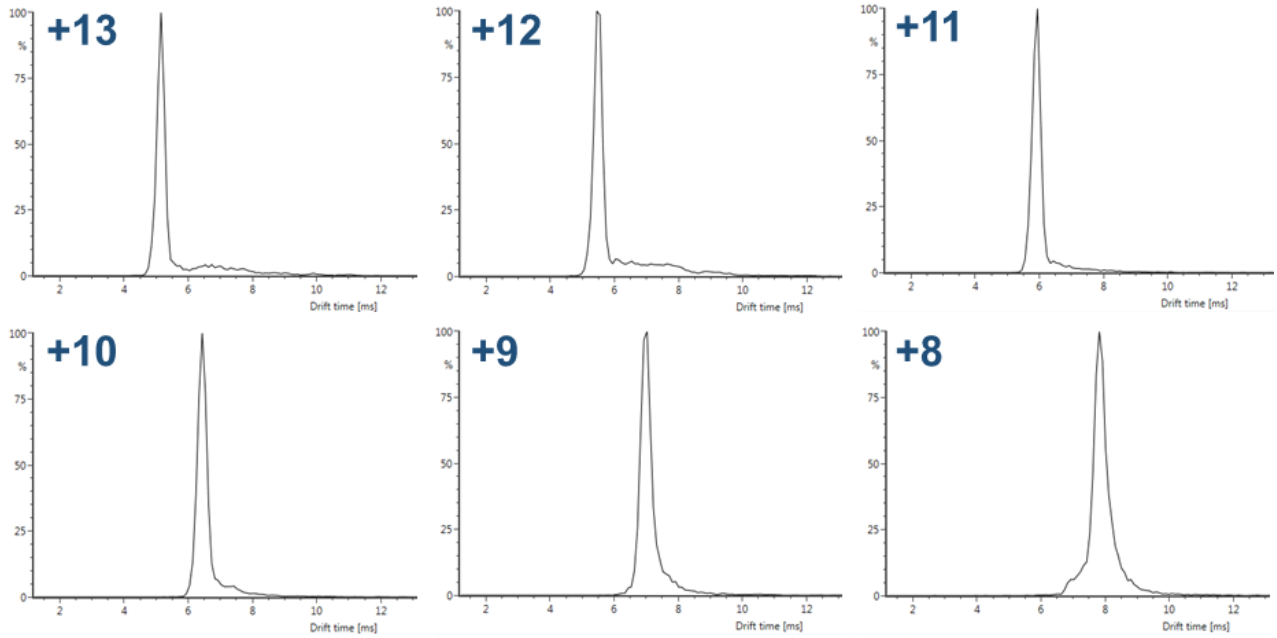

Figure 4.17 | Drift times observed for the z = +13 to +8 charges of **4.3**, measured by IM-MS. Each *m/z* signal produced a single predominant peak. A very small (ca. 5% relative intensity) portion of higher drift times were sometimes observed.

4.6 Conclusions and future work

A molecular scaffold was developed that can alter its geometry without altering its stoichiometry, providing a new platform for understanding flexible and adaptable chemical systems. The ability of **4.1** to exhibit three distinct isomeric forms, converting from a D_4- to *O*- to S_6-symmetric architecture, is unprecedented for a supramolecular entity of its size. Using cooperative templation by fullerene guests, the stereochemistry of the capsule can be altered. This leads to a change in cage morphology without altering the connectivity of the framework, resulting in the regulation of cooperative intermolecular interactions. This study provides a novel method for both tuning the strength of guest binding and optimising the system to exhibit specific modes of cooperativity.

Further investigations into the regulation of binding cooperativity upon structural adaptation is essential for generating systems that replicate the allosteric signals received by biological receptors. Employing components that can exist in multiple configurations is key to this process – metal ions that can adopt more than one geometry, or ligands with rotational degrees of freedom can be employed to generate adaptive systems. Future work in this area will therefore focus on developing methods by which the rearrangement of an architecture impacts upon the binding of guests, specifically with a view to either engendering changes in the cooperativity of binding, or switching between guest binding stoichiometries (for instance, binding a single guest in one state, and multiple guests in another).

A deficiency of the current system is that **4.2** cannot be converted back to **4.1**. One way to achieve this may be to use a chemically-fueled process (light, redox or pH stimuli) to switch between cage configurations. The following system is envisioned: **4.2** is treated with a chemical fuel that disassembles the structure, the fullerenes are sequestered by precipitation, and after the fuel is consumed the system reassembles in the absence of fullerenes to generate **4.1**. Developing a chemical network such as this would lead to a system that switches reversibly between positive and negative cooperative binding of guests.

4.7 Experimental section

4.7.1 Synthesis and characterisation of 4.1

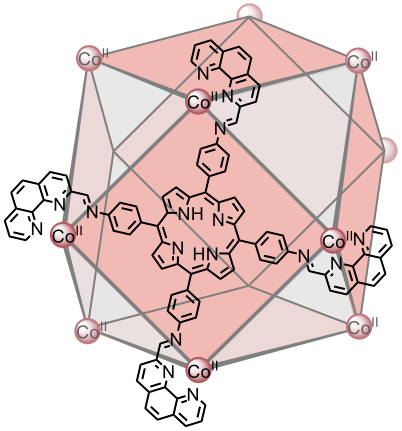

Free base tetrakis(*p*-aminophenyl)porphyrin **4A** (41.5 mg, 60.0 μmol, 6 equiv), $Co(NTf_2)_2 \cdot 6H_2O$ (87.4 mg, 120 μmol, 12 equiv) and 2-formylphenanthroline (50.0 mg, 240 μmol, 24 equiv) were stirred in CD_3CN (5.00 mL) at 60 °C for 16 h in a sealed vessel, yielding a dark orange stock solution upon cooling (2.00 mM). Standard solutions of 0.200 mM (0.050 mL of stock solution made up to 0.500 mL) were used for ^{1}H NMR titrations. **^{1}H NMR** (400 MHz, 298 K, CD_3CN): δ 222.2, 147.1, 84.1, 44.8, 30.8, 26.3, 24.1, 17.1, 8.2, 6.2, 0.6, –7.5, –11.3 ppm. **^{19}F NMR** (376 MHz, 298 K, CD_3CN): δ –79.1 ppm. **LR-ESI-MS** [charge fragment, calculated for **4.1**$(NTf_2)_{24}$]: *m/z* = 1502.3 [**1**$(NTf_2)_{15}^{9+}$, 1502.6], 1324.0 [**1**$(NTf_2)_{14}^{10+}$, 1324.3] 1178.2 [**1**$(NTf_2)_{13}^{11+}$, 1178.4], 1056.8 [**1**$(NTf_2)_{12}^{12+}$, 1056.9], 953.9 [**1**$(NTf_2)_{11}^{13+}$, 954.0], 865.7 [**1**$(NTf_2)_{10}^{14+}$, 865.9], 789.2 [**1**$(NTf_2)_9^{15+}$, 789.5]. **HR-ESI-MS**: *m/z* calculated for **4.1**$(NTf_2)_{13}^{11+}$ = 1178.3778, observed = 1178.3754. X-ray quality crystals were grown from the slow diffusion of *i*Pr_2O into a solution of **4.1** containing $CsCB_{11}H_{12}$ (*ca.* 12 equivalents) in CD_3CN.

4.7.2 Syntheses and characterisation of host-guest complexes of 4.2

To a solution of **4.1** (2.00 mM in CD_3CN, 1 mL) was added C_{60} (13 mg, 5 equiv) or C_{70} (15 mg, 5 equiv) directly. PCBM (7 mg, 5 equiv) was added to a sample of **4.1** (0.5 mL, 1.00 mM in CD_3CN). The mixtures were sonicated for 10 minutes, then stirred at 60 °C for 16 h in a sealed vessel. Upon cooling, the mixture was centrifuged. The supernatant was collected and used without further purification (concentration = 2.00 mM). For subsequent NMR titrations, 0.05 mL of these solutions was made up to 0.5 mL with CD_3CN, yielding 0.200 mM stock solutions. In all cases, the paramagnetic nature of the complexes hampered complete signal assignment.

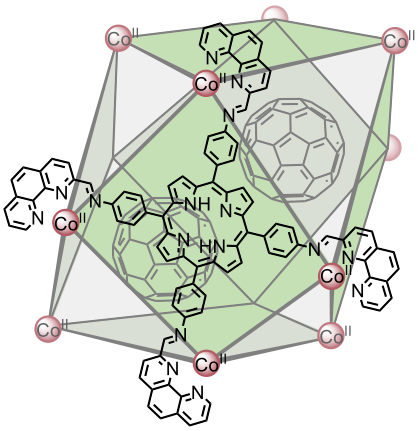

$(C_{60})_2\subset$**4.2**. **^{1}H NMR** (400 MHz, 298 K, CD_3CN): δ 275.4, 271.5, 224.3, 223.0, 217.1, 208.5, 147.7, 142.8, 120.4, 117.8, 88.5, 87.0, 54.3, 49.3, 47.0, 45.0, 34.8, 34.4, 33.9, 33.4, 32.8, 30.8, 30.3, 27.3, 27.1, 16.8, 16.1, 15.6, 11.7, 10.7, 10.2, 9.1, 8.0, 7.2, –0.9, –2.9, –10.6, –12.4, –13.8, –14.8, –16.5, –19.0 ppm. **LR-ESI-MS** [charge fragment, calculated for $(C_{60})_2\subset$**4.2**$(NTf_2)_{24}$]: *m/z* = 1468.2 [$(C_{60})_2\subset$**4.2**$(NTf_2)_{14}^{10+}$, 1468.4], 1309.3 [$(C_{60})_2\subset$**4.2**$(NTf_2)_{13}^{11+}$,

1309.5], 1176.8 [$(C_{60})_2$⊂**4.2**$(NTf_2)_{12}^{12+}$, 1177.0], 1064.9 [$(C_{60})_2$⊂**4.2**$(NTf_2)_{11}^{13+}$, 1064.9], 968.8 [$(C_{60})_2$⊂**4.2**$(NTf_2)_{10}^{14+}$, 968.8], 885.6 [$(C_{60})_2$⊂**4.2**$(NTf_2)_9^{15+}$, 885.6], 812.7 [$(C_{60})_2$⊂**4.2**$(NTf_2)_8^{16+}$, 812.7]. **HR-ESI-MS**: *m/z* calculated for $(C_{60})_2$⊂**4.2**$(NTf_2)_{13}^{11+}$ = 1309.3781, observed = 1309.3755. X-ray quality crystals were grown from the slow diffusion of Et_2O into a solution of $(C_{60})_2$⊂**4.2** containing $CsCB_{11}H_{12}$ (*ca.* 30 equivalents) in CD_3CN.

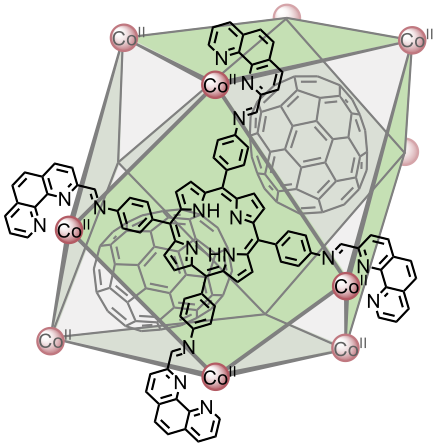

$(C_{70})_2$⊂**4.2**. **^{1}H NMR** (400 MHz, 298 K, CD_3CN): *δ* 273.3, 268.9, 214.2, 210.4, 204.1, 200.9, 141.0, 124.8, 117.2, 114.7, 83.0, 79.6, 53.6, 49.3, 44.9, 42.3, 35.7, 34.3, 34.1, 33.9, 31.8, 30.5, 29.2, 29.0, 27.3, 17.4, 17.1, 16.7, 15.0, 13.1, 12.6, 11.0, 8.9, 7.5, 7.2, 5.0, 0.6, –0.4, –8.7, –9.9, –10.9, –11.4, –13.3, –15.4, –15.9, –19.1 ppm. **LR-ESI-MS** [charge fragment, calculated for $(C_{70})_2$⊂**4.2**$(NTf_2)_{24}$]: *m/z* = 1492.3 [$(C_{70})_2$⊂**4.2**$(NTf_2)_{14}^{10+}$, 1492.4], 1331.1 [$(C_{70})_2$⊂**4.2**$(NTf_2)_{13}^{11+}$, 1331.3], 1196.8 [$(C_{70})_2$⊂**4.2**$(NTf_2)_{12}^{12+}$, 1197.0], 1083.3 [$(C_{70})_2$⊂**4.2**$(NTf_2)_{11}^{13+}$, 1083.4], 985.9 [$(C_{70})_2$⊂**4.2**$(NTf_2)_{10}^{14+}$, 986.0], 901.5 [$(C_{70})_2$⊂**4.2**$(NTf_2)_9^{15+}$, 901.6], 827.7 [$(C_{70})_2$⊂**4.2**$(NTf_2)_8^{16+}$, 827.7]. **HR-ESI-MS**: *m/z* calculated for $(C_{70})_2$⊂**4.2**$(NTf_2)_{13}^{11+}$ = 1331.1962, observed = 1331.1955.

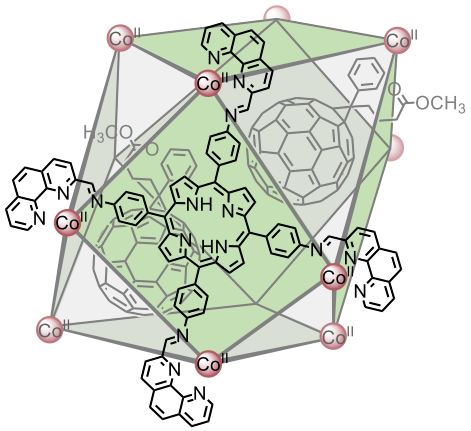

(PCBM)$_2$⊂**4.2**. **^{1}H NMR** (400 MHz, 298 K, CD_3CN): *δ* 275.3, 270.9, 227–195 (broad) 119.5, 117.7, 54.0, 50.1, 49.4, 34.5, 34.0, 30.7, 29.6, 26.7, 17.4, 16.7, 16.2, 11.7, 10.5, 10.2, 9.3, 9.0, 8.3, 7.8, 5.6, 3.5, 0.3, –1.7, –2.2, –2.9, –4.4, –4.9, –6.8, –7.0, –7.3, –10.9, –12.5, –13.9, –15.2, –16.3, –19.2 ppm. **LR-ESI-MS** [charge fragment, calculated for (PCBM)$_2$⊂**4.2**$(NTf_2)_{24}$]: *m/z* = 1506.3 [(PCBM)$_2$⊂**4.2**$(NTf_2)_{14}^{10+}$, 1506.5], 1343.8 [(PCBM)$_2$⊂**4.2**$(NTf_2)_{13}^{11+}$, 1344.0], 1208.6 [(PCBM)$_2$⊂**4.2**$(NTf_2)_{12}^{12+}$, 1208.7], 1094.1 [(PCBM)$_2$⊂**4.2**$(NTf_2)_{11}^{13+}$, 1094.2], 996.0 [(PCBM)$_2$⊂**4.2**$(NTf_2)_{10}^{14+}$, 996.0], 911.0 [(PCBM)$_2$⊂**4.2**$(NTf_2)_9^{15+}$, 910.9], 836.6 [(PCBM)$_2$⊂**4.2**$(NTf_2)_8^{16+}$, 836.5. **HR-ESI-MS**: *m/z* calculated for (PCBM)$_2$⊂**4.2**$(NTf_2)_{13}^{11+}$ = 1343.0304, observed = 1343.0336.

4.7.3 Synthesis and characterisation of 4.3

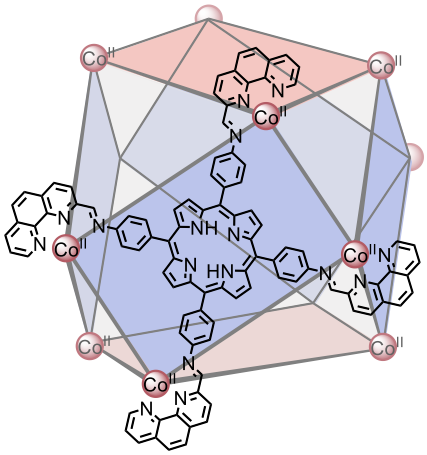

Free base tetrakis(*p*-aminophenyl)porphyrin **4A** (2.49 mg, 3.60 μmol, 6 equiv), $Co(NTf_2)_2 \cdot 6H_2O$ (5.24 mg, 7.20 μmol, 12 equiv) and 2-formylphenanthroline (3.00 mg, 14.4 μmol, 24 equiv) were stirred in CD_3CN (0.5 mL) at room temperature for 16 h in a sealed NMR tube, after which spectra were recorded. **^{1}H NMR** (400 MHz, 298 K, CD_3CN): δ 274–260 (broad), 228–210 (broad), 118.3, 49.8, 49.5, 47.4, 30.7, 24.6, 16.7, 15.3, 14.4, 8.5, 7.5, –0.6, –5.5, –9.6, –13.4, –14.2, –17.2 ppm. The broad paramagnetic signals hampered further peak identification. **ESI-MS:** as **4.1**. X-ray quality crystals were grown from the slow diffusion of Et_2O into a solution of **4.3** containing nBu$_4$NBF$_4$ (*ca.* 20 equivalents) in CD_3CN.

4.7.4 Titrations and binding constant determinations

Binding isotherms for all titrations were calculated using BINDFIT.[24] Generally, all signals showing 1 ppm shift or more by ^{1}H NMR spectroscopy over the course of the titration were used in a global proton shift analysis. All titrations were completed twice; a weighted average of the two runs was calculated and is displayed in Table 4.1. For the UV-Vis titration of $K_2B_{12}F_{12}$ into **4.1**, all four Q bands were used in the global data analysis.

The equations used for these analyses are available in the review by Thordarson.[20] For instances where residuals for 1:1 and 1:2 bindings were equally acceptable, the covariance of the fit (σ_{cov}, variance of the residuals divided by the variance in the data) was used: the model that showed the lowest covariance (at least 2-fold lower) was generally applied. Both sets of residuals for a 1:1 and 1:2 binding model have been shown for comparison and clarity in each case.

For all titrations (both UV-Vis and ^{1}H NMR) with $K_2B_{12}F_{12}$, the host was found to be insoluble past the addition of 6 equivalents of guest. This prevented the use of a host + excess guest solution for UV-Vis titrations; a dilution correction was applied using BINDFIT in this case. Global shift analysis was used to improve the error associated with K_1 in these instances.

The binding equations used in this study are idealised for this particular system. As it is hypothesised that anion binding occurs around the triangular apertures of the architectures, guests have eight pockets in which to bind in **4.1**; in $(C_{60})_2\subset$**4.2** and $(C_{70})_2\subset$**4.2**, one size of aperture has two possible binding positions, while the other has six. As all anion binding was observed to occur under

fast exchange on the NMR timescale, it is proposed that rapid exchange between sites serves to block higher binding stoichiometries, approximating a 1:2 binding system in each case. Solid state (*i.e.* crystallographic) occupancies do not necessarily represent occupancies in solution; the crystallographic evidence is thus only appropriate in representing guest localisation, and not binding stoichiometry.

4.7.4.1 Procedure for NMR titrations

A 0.5 mL solution of host (2.00×10^{-4} M) in CD_3CN was titrated with a concentrated solution of guest (*ca.* 2.5×10^{-4} M) in CD_3CN. The total change in concentration of the host was 5–8.9% over the course of the titration, and the error involved was assumed to be negligible. Upon each addition, the solution was manually stirred for 5-10 min before acquiring the spectrum, which allowed equilibrium to be reached between the host and guest.

4.7.4.2 Procedure for UV-Vis titrations

A solution of host (2.0×10^{-6} M) in CH_3CN in a UV-Vis cuvette was titrated with a solution of excess guest (2.9×10^{-4} M) in CH_3CN. Upon each addition, the solution was manually stirred for 2 min before acquiring the UV-Vis spectrum.

4.7.5 Crystallography

The crystals employed in this Chapter rapidly lost solvent after removal from the mother liquor and rapid handling prior to flash cooling in the cryostream was required to collect data. Due to the less than ideal resolution, bond lengths and angles within pairs of organic ligands were restrained to be similar to each other (SAME) and thermal parameter restraints (SIMU, DELU) were applied to all non-metal atoms to facilitate anisotropic refinement. Ligand-based atoms that still displayed thermal parameters greater than 0.4 were further refined to approximate isotropic behaviour (ISOR). In all cases, the remaining anions present in the asymmetric unit could not be successfully assigned despite numerous attempts at modelling, including the use of rigid bodies. Consequently, the SQUEEZE[25] function of PLATON[26] was employed to remove the contribution of the electron density associated with this anion and the remaining highly disordered solvent molecules.

*4.7.5.1 Crystal structure of **4.1**·10.5$CB_{11}H_{12}$·13.5NTf_2·7.5MeCN*

Formula $C_{628.50}H_{496.50}B_{115.50}Co_{12}F_{81}N_{117}O_{54}S_{27}$, *M* 14912.23, Trigonal, *R*3– (#148), *a* 48.517(5), *b* 48.517(5), *c* 64.134(7) Å, *γ* 120, *V* 130738(29) Å^3, D_c 1.136 g cm^{-3}, *Z* 6, crystal size 0.300 by 0.200 by 0.200 mm, colour purple, habit prism, temperature 100(2) Kelvin, *λ*(synchrotron) 0.6889 Å, *μ*(synchrotron) 0.340 mm^{-1}, $T(\text{xia2})_{\text{min,max}}$ 0.9931, 1.011, $2\theta_{\text{max}}$ 34.86, *hkl* range –42 42, –42 40, –55 55, *N* 98324, N_{ind} 19949(R_{merge} 0.0637), N_{obs} 10985(I > 2σ(I)), N_{var} 2532, residuals* *R*1(*F*) 0.1491, *wR*2(F^2) 0.3995, GoF(all) 1.208, $\Delta\rho_{\text{min,max}}$ –0.340, 0.729 e$^-$ Å^{-3}, CCDC 1510849. *$R1 = \Sigma||F_o| - |F_c||/\Sigma|F_o|$ for $F_o > 2\sigma(F_o)$; $wR2 = (\Sigma w(F_o^2 - F_c^2)^2/\Sigma(wF_c^2)^2)^{1/2}$ all reflections $w=1/[\sigma^2(F_o^2)+(0.2000P)^2+750.0000P]$ where $P=(F_o^2+2F_c^2)/3$

Specific refinement details

Crystals of **4.1**·10.5$CB_{11}H_{12}$·13.5NTf_2·7.5MeCN were grown by slow diffusion of diisopropyl ether into a CD_3CN solution of **4.1**$(NTf_2)_{24}$ containing 12 equivalents of $CsCB_{11}H_{12}$ (following the titration of this guest into **4.1**). Despite the use of synchrotron radiation, few reflections at greater than 1.25 Å resolution were observed; nevertheless, the quality of the data is more than sufficient to establish the connectivity of the structure and the handedness of each metal centre. The asymmetric unit contains one third of the overall structure.

Two carborate anions showed a significant amount of thermal motion; the SAME command was applied to all four unique anions to approximate icosahedral symmetry and realistically model these anions. Given the 12-fold-symmetric disorder of the carbon atom in $CB_{11}H_{12}^-$, all twelve atoms were assigned as boron; there was no indication that one of the atoms was carbon outright. One $CB_{11}H_{12}^-$ anion was modelled with half occupancy. Solvent molecules were refined with isotropic thermal parameters.

The SQUEEZEd portion of the structure totals 11,385 electrons per unit cell, corresponding to a solvent accessible void of 53,318 Å^3 per unit cell. This equates to 13.7 molecules of NTf_2^- (each with 138 electrons) for each molecule of **4.1**, where *Z* = 6. This diffuse electron density thus equates well to the 13.5 counterions necessary to satisfy the 24+ charge of **4.1**.

*4.7.5.2 Crystal structure of $(C_{60})_2$⊂**4.2**·24$CB_{11}H_{12}$·iPr_2O·19MeCN*

Formula $C_{764}H_{707}B_{264}Co_{12}N_{115}O$, *M* 15076.40, Triclinic, *P*1– (#2), *a* 26.438(13), *b* 30.374(16), *c* 31.047(10) Å, *α* 67.30(4), *β* 84.86(4), *γ* 78.93(7)º, *V* 22569(20) Å^3, D_c 1.109 g cm^{-3}, *Z* 1, crystal size 0.250 by 0.150 by 0.150 mm, colour purple, habit prism, temperature 100(2) Kelvin, *λ*(synchrotron)

0.6889 Å, μ(synchrotron) 0.249 mm^{-1}, T(xia2)$_{min,max}$ 0.9914, 1.008, 2θ_{max} 42.52, *hkl* range –27 27, –31 31, –32 32, N 216634, N_{ind} 55058 (R_{merge} 0.0957), N_{obs} 39439(I > 2σ(I)), N_{var} 5689, residuals* $R1(F)$ 0.1303, $wR2(F^2)$ 0.3628, GoF(all) 0.988, $\Delta\rho_{min,max}$ –0.751, 2.060 e$^-$ Å^{-3}, CCDC 1510850. *$R1 = \Sigma||F_o| - |F_c||/\Sigma|F_o|$ for $F_o > 2\sigma(F_o)$; $wR2 = (\Sigma w(F_o^2 - F_c^2)^2/\Sigma(wF_c^2)^2)^{1/2}$ all reflections $w=1/[\sigma^2(F_o^2)+(0.2000P)^2+750.0000P]$ where $P=(F_o^2+2F_c^2)/3$

Specific refinement details

Crystals of $(C_{60})_2\subset$**4.2**·24$CB_{11}H_{12}$·*i*Pr_2O·19MeCN were grown by slow diffusion of diisopropyl ether into a CD_3CN solution of $(C_{60})_2\subset$**4.2**$(NTf_2)_{24}$ containing approximately 30 equivalents of $CsCB_{11}H_{12}$. Despite the use of synchrotron radiation, few reflections at greater than 0.95 Å resolution were observed; nevertheless, the quality of the data is more than sufficient to establish the connectivity of the structure, the helicity of each metal centre and the occupancy of guests. The asymmetric unit contains one half of the overall structure.

Given the 12-fold-symmetric disorder of the carbon atom in $CB_{11}H_{12}^-$, all twelve atoms were assigned as boron; there was no indication that one of the atoms was carbon outright. Four carborate anions showed a significant amount of thermal motion; the SAME command was applied to approximate icosahedral symmetry and realistically model these anions. Three carborate anions and two acetonitrile molecules were modelled as disordered over two positions. One of these disordered MeCN molecules was disordered over a 180° rotation; the complexity of the disorder prevented the determination of appropriate HFIX coordinates, even with AFIX 137. One carborate anion and multiple solvent molecules were modelled with half occupancy. Two phenanthroline rings and several acetonitrile molecules that still displayed thermal parameters greater than 0.4 were further refined to approximate isotropic behaviour (ISOR).

The SQUEEZEd portion of the structure totals 815 electrons per unit cell, corresponding to a solvent accessible void of 3,551 Å^3 per unit cell. As all but ½ of one $CB_{11}H_{12}^-$ anion was resolved in **4.2**, it is proposed that this extra density corresponds to highly disordered solvent molecules (MeCN, iPr_2O or H_2O).

*4.7.5.3 Crystal structure of **4.3**·5.5BF_4·18.5NTf_2·2.5MeCN*

Formula $C_{618}H_{355.50}B_{5.50}Co_{12}F_{133}N_{117}O_{74}S_{37}$, M 15083.51, Monoclinic, $P2_1/n$ (#14), a 40.2042(9), b 54.2465(18), c 40.2935(9) Å, b 90.408(2), V 87875(4) Å^3, D_c 1.140 g cm^{-3}, Z 4, crystal size 0.250 by 0.200 by 0.150 mm, colour purple, habit prism, temperature 100(2) Kelvin, λ(synchrotron) 0.6889 Å,

μ(synchrotron) 0.370 mm^{-1}, T(SADABS)$_{min,max}$ 0.5371, 0.7361, 2θ_{max} 30.73, *hkl* range –30 30, –41 41, –30 30, N 422285, N_{ind} 41581(R_{merge} 0.1087), N_{obs} 30511(I > 2σ(I)), N_{var} 6488, residuals* R1(F) 0.1492, $wR2(F^2)$ 0.4133, GoF(all) 1.289, $\Delta\rho_{min,max}$ –0.306, 0.569 e$^-$ Å^{-3}, CCDC 1510851. *$R1 = \Sigma||F_o| - |F_c||/\Sigma|F_o|$ for $F_o > 2\sigma(F_o)$; $wR2 = (\Sigma w(F_o^2 - F_c^2)^2/\Sigma(wF_c^2)^2)^{1/2}$ all reflections $w=1/[\sigma^2(F_o^2)+(0.2000P)^2+750.0000P]$ where $P=(F_o^2+2F_c^2)/3$

Specific refinement details

Crystals of **4.3**·5.5BF_4·18.5NTf_2·2.5MeCN were grown by slow diffusion of diethyl ether into a CD_3CN solution of **4.3**$(NTf_2)_{24}$ containing approximately 10 equivalents of *n*Bu_4NBF_4. Despite the use of synchrotron radiation, few reflections at greater than 1.3 Å resolution were observed; nevertheless, the quality of the data is more than sufficient to establish the connectivity of the structure and the handedness of each metal centre. The asymmetric unit contains one whole structure.

All anions were modelled with either half or quarter occupancy and refined with isotropic thermal parameters; many exhibited disorder beyond that which could be satisfactorily modelled given the quality of the data. Solvent molecules were likewise refined with isotropic thermal parameters.

The SQUEEZEd portion of the structure totals 9,975 electrons per unit cell, corresponding to a solvent accessible void of 46,883 Å^3 per unit cell. This equates to 18.1 molecules of NTf_2^- (each with 138 electrons) for each individual molecule of **4.3**, where Z = 4. This diffuse electron density thus corresponds well to the 18.5 counterions necessary to satisfy the 24+ charge of **4.3**.

4.8 References

[1] Beissel, T., Powers, R.E., Parac, T.N., and Raymond, K.N., *J. Am. Chem. Soc.*, **1999**, 121, 4200-4206.

[2] Meng, W., Ronson, T.K., and Nitschke, J.R., *Proc. Natl. Acad. Sci. U.S.A*, **2013**, 110, 10531-10535.

[3] Ronson, T.K., League, A.B., Gagliardi, L., Cramer, C.J., and Nitschke, J.R., *J. Am. Chem. Soc.*, **2014**, 136, 15615-15624.

[4] Mecozzi, S. and Rebek, J.J., *Chem. – Eur. J.*, **1998**, 4, 1016-1022.

[5] Wang, W., Wang, Y.-X., and Yang, H.-B., *Chem. Soc. Rev.*, **2016**, 45, 2656-2693.

[6] Pauling, L., *Nature*, **1948**, 161, 707-709.

[7] Hunter, C.A. and Anderson, H.L., *Angew. Chem. Int. Ed.*, **2009**, 48, 7488-7499.

[8] Conway, A. and Koshland, D.E., *Biochemistry*, **1968**, 7, 4011-4023.

[9] Mahadevi, A.S. and Sastry, G.N., *Chem. Rev.*, **2016**, 116, 2775-2825.

[10] Huang, Z., Qin, K., Deng, G., Wu, G., Bai, Y., Xu, J.-F., Wang, Z., Yu, Z., Scherman, O.A., and Zhang, X., *Langmuir*, **2016**, 32, 12352-12360.

[11] Badjić, J.D., Nelson, A., Cantrill, S.J., Turnbull, W.B., and Stoddart, J.F., *Acc. Chem. Res.*, **2005**, 38, 723-732.

[12] Rebek, J., Costello, T., Marshall, L., Wattley, R., Gadwood, R.C., and Onan, K., *J. Am. Chem. Soc.*, **1985**, 107, 7481-7487.

[13] Rizzuto, F.J. and Nitschke, J.R., *Nat. Chem.*, **2017**, 9, 903-908.

[14] Eaton, W.A., Henry, E.R., Hofrichter, J., and Mozzarelli, A., *Nat. Struct. Mol. Biol.*, **1999**, 6, 351.

[15] Kleywegt, G.J. and Jones, T.A., *Acta Crystallogr. Sect. D*, **1994**, 50, 178-185.

[16] Caulder, D.L. and Raymond, K.N., *Acc. Chem. Res.*, **1999**, 32, 975-982.

[17] Bell, Z.R., Jeffery, J.C., McCleverty, J.A., and Ward, M.D., *Angew. Chem. Int. Ed.*, **2002**, 41, 2515-2518.

[18] Ghosh, K., Hu, J., White, H.S., and Stang, P.J., *J. Am. Chem. Soc.*, **2009**, 131, 6695-6697.

[19] Sun, Q.-F., Sato, S., and Fujita, M., *Nat. Chem.*, **2012**, 4, 330-333.

[20] Thordarson, P., *Chem. Soc. Rev.*, **2011**, 40, 1305-1323.

[21] Garcia-Simon, C., Garcia-Borras, M., Gomez, L., Parella, T., Osuna, S., Juanhuix, J., Imaz, I., Maspoch, D., Costas, M., and Ribas, X., *Nat. Commun.*, **2014**, 5, 5557.

[22] Snyder, D.A., Chen, Y., Denissova, N.G., Acton, T., Aramini, J.M., Ciano, M., Karlin, R., Liu, J., Manor, P., Rajan, P.A., Rossi, P., Swapna, G.V.T., Xiao, R., Rost, B., Hunt, J., and Montelione, G.T., *J. Am. Chem. Soc.*, **2005**, 127, 16505-16511.

[23] Guldi, D.M., *Pure Appl. Chem.*, **2003**, 75, 1069-1075.

[24] Samanta, D., Mukherjee, S., Patil, Y.P., and Mukherjee, P.S., *Chem. – Eur. J.*, **2012**, 18, 12322-12329.

[25] Spek, A.L., *Acta Crystallogr. Sect C*, **2015**, 71, 9-18.

[26] Spek, A.L., *Acta Crystallogr. Sect. D*, **2009**, 65, 148-155.

Chapter 5

Self-assembly in the cavities of cuboctahedral coordination cages

5.1 Coordination chemistry in cages

Biomolecules use coordinated metal ions to harvest light, convert energy and regulate respiration;[1] industrial technologies use metal coordination processes for fuel production,[2] drug synthesis[3] and catalysis.[4] A wealth of metal-organic materials have thus been generated synthetically to mimic and meet these applications:[5] currently, the Cambridge Crystallographic Data Centre (CCDC) holds more than 420,000 transition metal-containing crystal structures (*ca.* 47% of the database), formed by either solution- or solid-state techniques.[6] However, many discrete complexes cannot be accessed by routine synthesis: for instance, polydentate ligands often generate infinite networks,[7] and labile components can re-equilibrate to express dynamic product mixtures.[8] The finite number of available methods to synthesise discrete metal-organic complexes has limited the production of new coordination complexes, along with the range of applications to which they might be put.

The structural rigidity of metal-organic cages makes them ideal candidates for directing the internal assembly of coordination systems. In the case of the *O*-symmetric architectures described herein, each of three pairs of square faces are parallel, enclosing a cubic void space. It was hypothesised that including coordination sites in the centres of ligands within these structures would direct the assembly of polydentate components within their cavities. This Chapter thus presents a set of methods for assembling coordination complexes within coordination cages, and synthesising new molecular gyroscopes. The structures bound within these cages do not exist outside them, due to the lability of the coordination interactions that hold them together. The high degree of cooperativity imposed by the regular array of coordination sites embedded in the frameworks of these cages could thus stabilise species that are otherwise too labile to exist in appreciable concentration. The confinement of self-assembled products within coordination cage cavities led to unique guest behaviour: guest compression and preorganisation led to the favouring of ordinarily inaccessible spin- and oxidation-state changes of internally-bound metal ions.

5.2 Host-guest chemistry of 5.1

Dinuclear Rh^{II}_2 paddlewheel **5A** was synthesised from commercial starting materials in refluxing diglyme, following an adapted literature procedure.[9] The reaction of **5A** (6 equiv) with 2-formylphenanthroline (24 equiv) and $Cd^{II}(OTf)_2$ (12 equiv) generated cuboctahedron **5.1** as the uniquely observed product (Figure 5.1). The fourfold symmetry of subcomponent **5A** was retained in the spectrum of **5.1**, consistent with a product of *O* point symmetry. ESI-MS confirmed the $Cd^{II}_{12}\mathbf{L}^{\mathbf{5A}}_6$ composition of **5.1** (Figure 5.1c).

Cage **5.1** crystallised in the cubic space group *Pn*3–; both enantiomers are present in the unit cell. The crystal structure confirmed a cuboctahedral arrangement of Cd^{II} ions enclosing a cubic cavity of *ca.* 1750 $Å^3$ (Figure 5.1b).

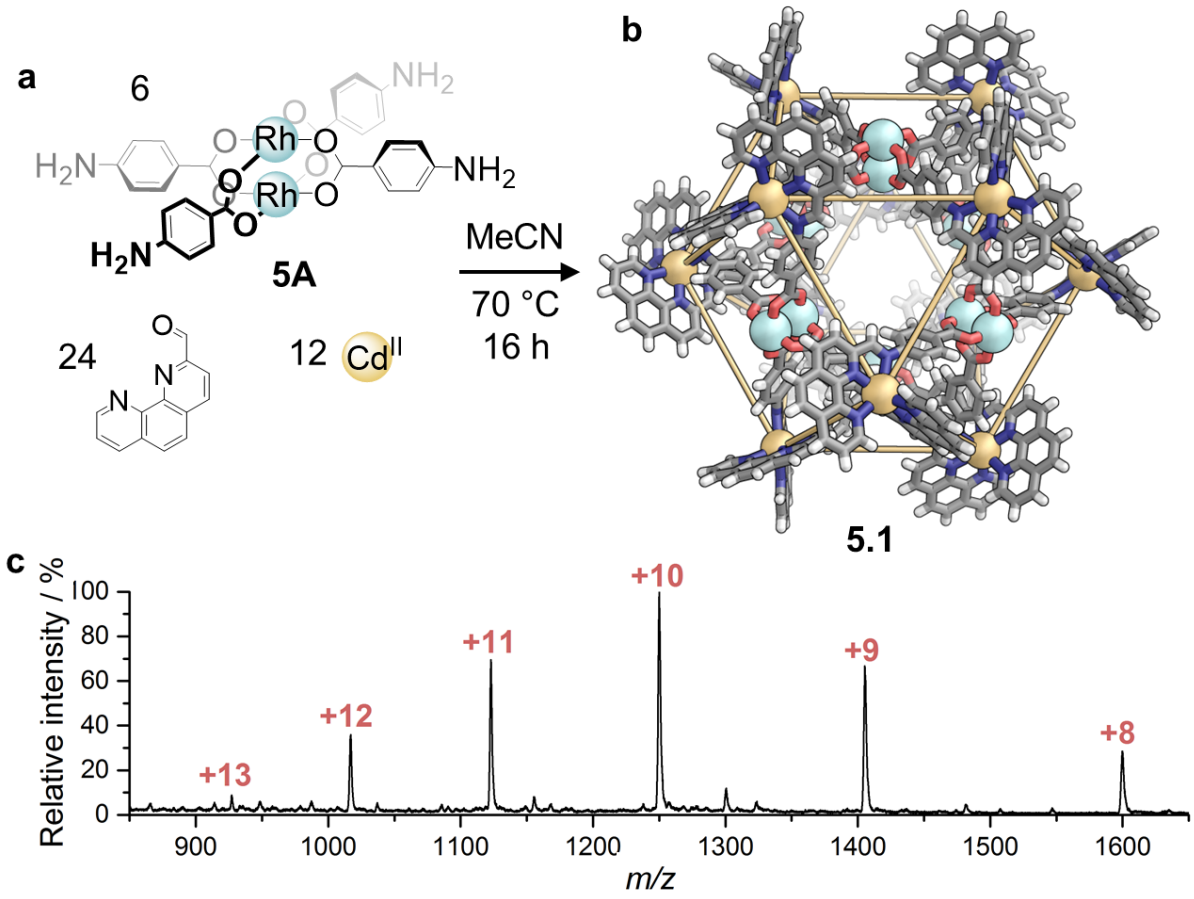

Figure 5.1 | **a,** Synthesis, **b**, crystal structure and **c**, ESI mass spectrum of **5.1** (solvent molecules and anions are omitted for clarity; metal ion connectivity highlighted with yellow lines (Cd – yellow, Rh – cyan, C – grey, N – blue, O – red, H – white).

Rh^{II}_2 paddlewheel units exhibit rich axial coordination chemistry.[10,11] Negatively-charged and neutral donors were thus observed to bind to the Rh^{II} coordination sites of **5.1** in fast exchange on the NMR timescale (Figure 5.2). Linear ditopic guests (tetrazine- and phenylene-centered dipyridyl guests) were observed to bind in slow exchange at the *endo*-Rh^{II} sites of **5.1**. Such internally-binding ligands bridged the cavity of **5.1**, as reflected in the three unique ligand environments identified in NMR spectra of the host (Figure 5.3). ESI mass spectra of these host-guest complexes indicated multiple species were bound to **5.1**. The symmetry breaking observed by NMR suggests that one guest binds internally, while subsequent guests bind around the periphery of **5.1**, coordinated to *exo*-Rh^{II} sites in a monodentate fashion. Larger anions such as $B_{12}F_{12}^{2-}$, Δ-TRISPHAT[12] and tetraphenylborate also produced distinct ^{1}H NMR shifts upon addition to **5.1**, consistent with fast-exchange binding with the host on the NMR timescale (Figure 5.2).

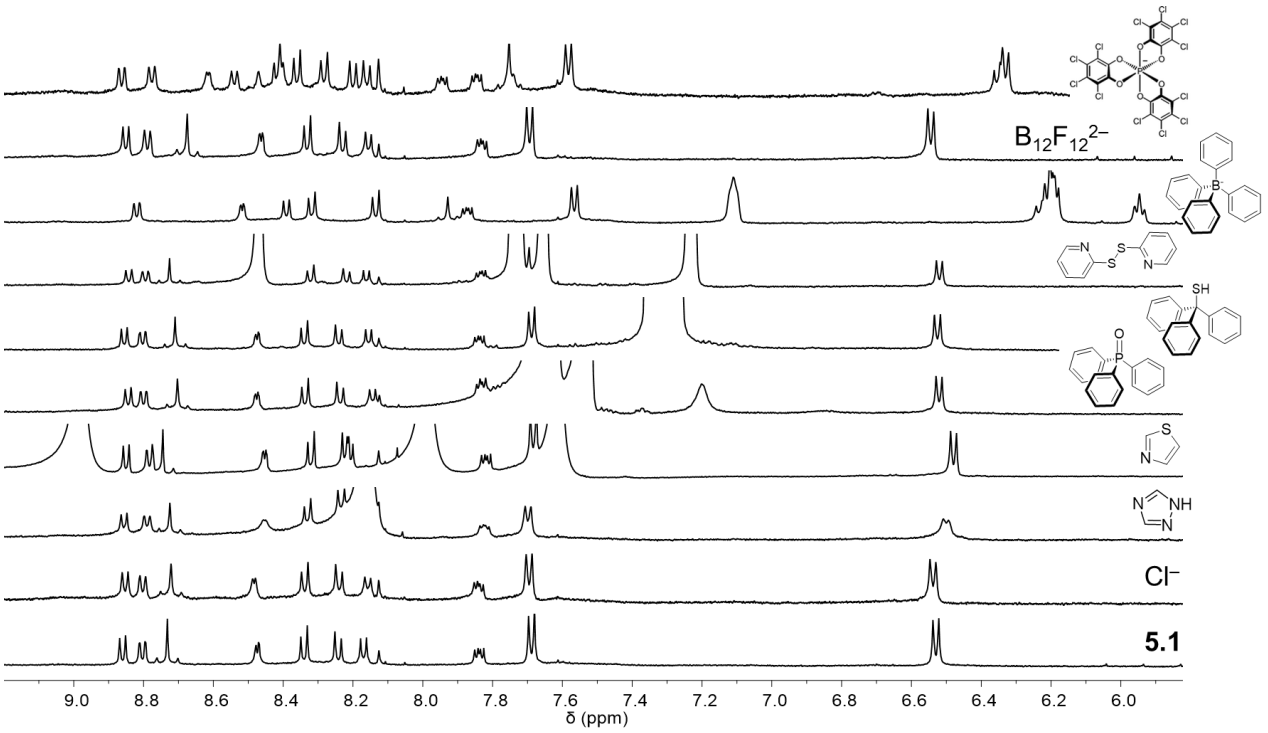

Figure 5.2 | Host-guest chemistry of **5.1**, monitored by ^{1}H NMR spectroscopy (500 MHz, 298 K, CD_3CN).

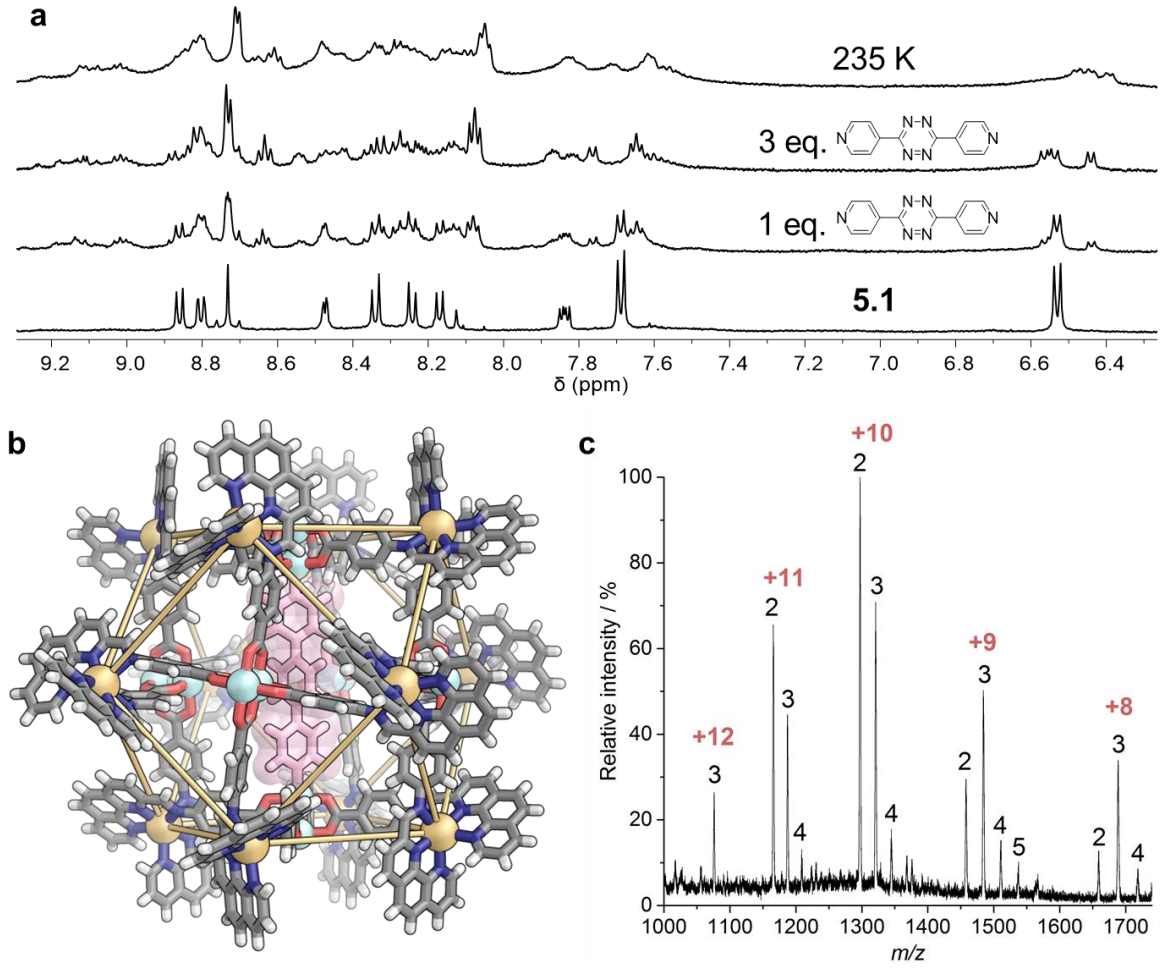

Figure 5.3 | Host-guest chemistry of **5.1** with bidentate bridging unit 4,4'-bipyridyltetrazine. **a**, The titration of 4,4'-bipyridyltetrazine into a solution of **5.1** monitored by ^{1}H NMR spectroscopy (500 MHz, 298 & 235 K, CD_3CN). **b**, An MM3 molecular model of the host-guest complex. **c**, An ESI mass spectrum of the host-guest complex, showing multiple species binding, where black numbers indicate the number of guests bound.

As the internal Rh^{II} sites of **5.1** bound bidentate ligands, the affinity of **5.1** for other polydentate potential binders was investigated. Pyrazine bound to **5.1** in fast exchange on the NMR timescale (Figure 5.4a). Remarkably, the addition of $Cd(OTf)_2$ following the saturation of **5.1** with pyrazine (20 equiv) led to further shifts in the NMR signals of **5.1**, suggesting interaction of Cd^{II} with the cage and encapsulated pyrazine: broadening of the cage signals was observed, suggesting cage desymmetrisation. Different products were observed at different cone voltages by ESI-MS: at low cone voltages (5–10 eV) [Cd(pyrazine)$_4$]⊂**5.1** was observed; at high cone voltages (30 eV) a distribution of products corresponding to [Cd(pyrazine)$_x$]⊂**5.1** (where $1 \leq x \leq 4$) was observed (Figure 5.4b&c).

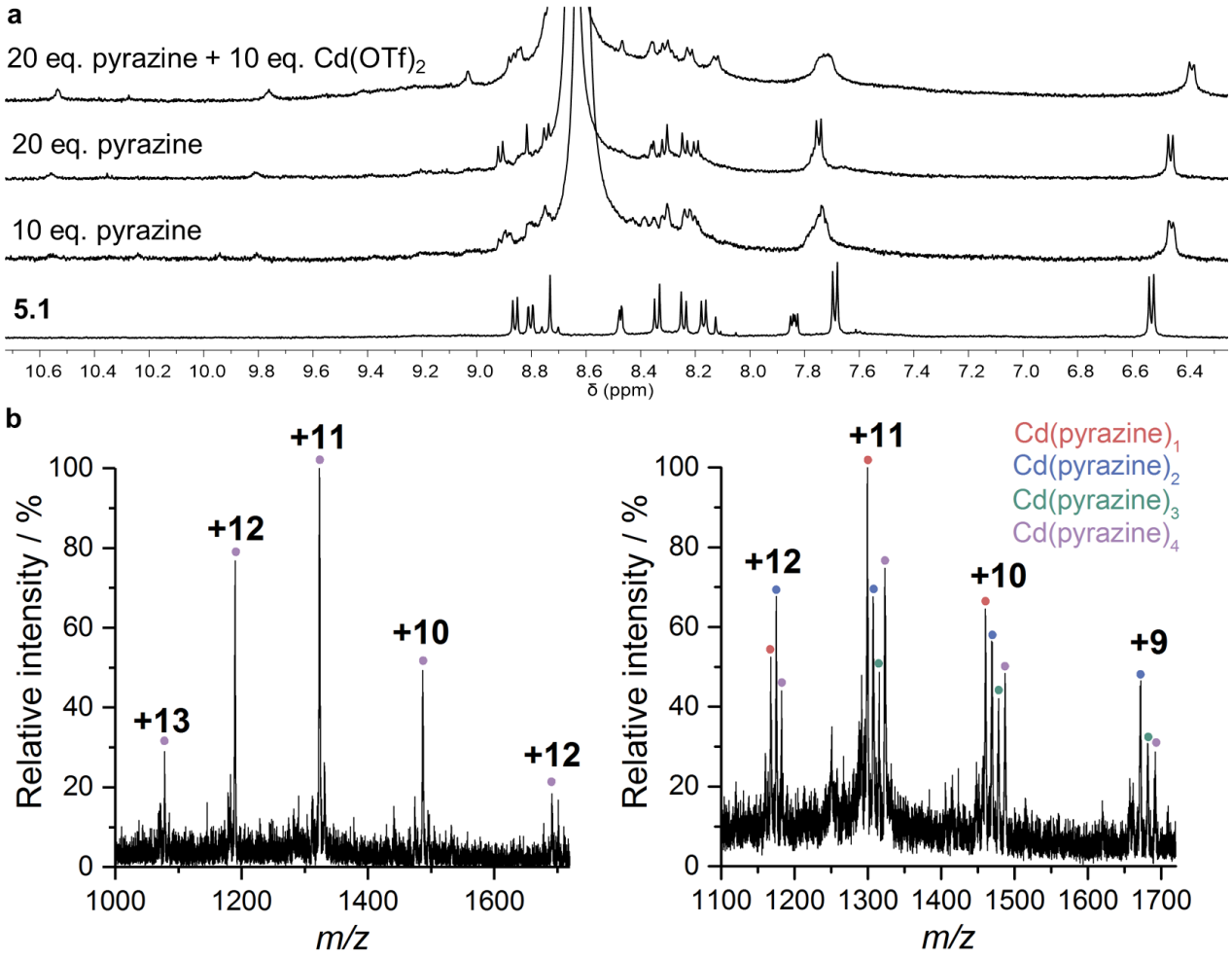

Figure 5.4 | Pyrazine binding within **5.1**. **a**, ^{1}H NMR spectra (500 MHz, 298 K, CD_3CN) monitoring the addition of pyrazine, followed by $Cd(OTf)_2$, into a solution of **5.1**. **b&c**, ESI mass spectra of the resulting host-guest complexes by ESI-MS: **b**, at low cone voltages only [Cd(pyrazine)$_4$]⊂**5.1** was observed; **c**, at high cone voltages (5-10 eV) a distribution of products corresponding to [Cd(pyrazine)$_x$]⊂**5.1** (where $1 \leq x \leq 4$) was observed.

Single-crystal X-ray measurement revealed that a unique metal complex was bound within **5.1** (Figure 5.5). The encapsulated metal complex consisted of a Cd^{II} ion coordinated to five molecules of pyrazine and one H_2O. To accommodate its heteroleptic guest, the cage distorts slightly: whereas

antipodal *endo*-Rh^{II}–Rh^{II} distances spanned 15.5 Å in the crystal structure of **5.1**, this distance was observed to contract to 14.8 Å around the equatorial belt of the cadmium pentapyrazine adduct, breaking the cubic symmetry of the void. The law of coordinative saturation[13] shaped the nature of the observed product: only a pair of water ligands are small enough to bind simultaneously to the *endo*-facing Rh^{II} atom and the encapsulated Cd^{II} ion, preventing formation of the hexakis(pyrazine) adduct. Unusually, hydrogen atoms on both H_2O molecules are in close contact (O-O distance 3.5 Å) while not being geometrically capable of engaging in hydrogen bonding with each other. This configuration thus stabilised an otherwise energetically unfavourable state through coordination. It is proposed that fragments of this encapsulated complex are observed in the gas phase due to the strong ionisation conditions required for ESI mass spectrometry.

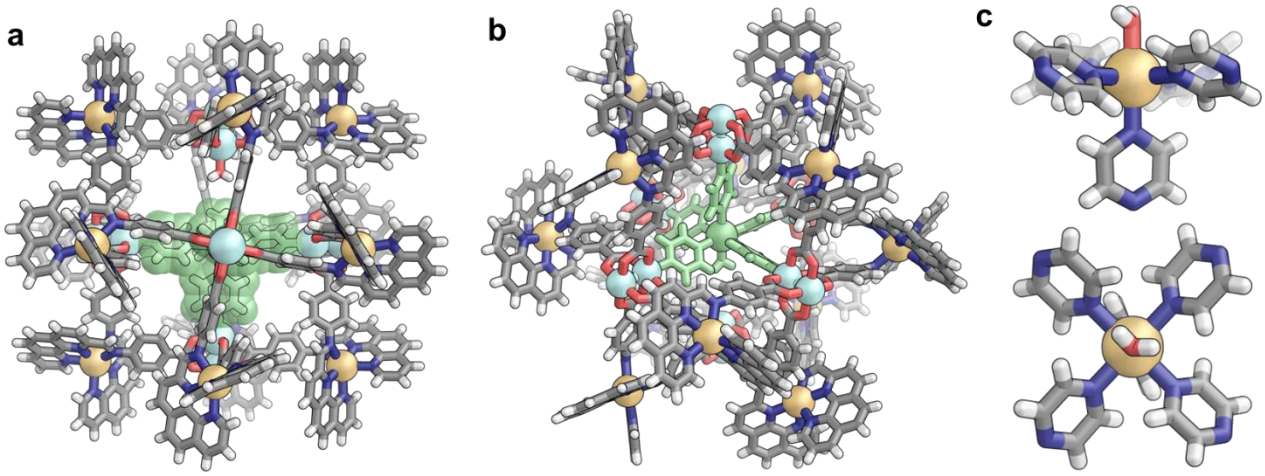

Figure 5.5 | **a&b**, X-ray crystal structure of [Cd(pyrazine)$_5$(H_2O)]⊂**5.1**, where the encapsulated complex is shown in green. **c**, Two views of the complex [Cd(pyrazine)$_5$(H_2O)]$^{2+}$ with the cage removed, rotated 90° with respect to each other. Externally-coordinated ligands, disorder, solvent molecules and anions are omitted for clarity (Cd – yellow, Rh – cyan, C – grey, N – blue, O – red, H – white).

Previous attempts to generate pentakis(pyrazine) complexes have relied on the preorganisation of pyrazine moieties into a pentadentate ligand.[14] The coordination motif presented here is instead organised by the host; [Cd(pyrazine)$_5$(H_2O)]$^{2+}$ is uniquely stabilised within cage **5.1** and does not exist outside of it. Pyrazine is usually a poor bridging ligand – coordination at one nitrogen atom tends to pull electron density away from the second, diminishing its coordination ability.[15] Cooperative effects within the cavity of **5.1** led to the stabilisation of a unique pentakis(pyrazine)Cd^{II} centre, in which all pyrazine ligands connect dications within a 26+ charged species. Pyrazine, previously employed for the generation of heteroleptic architectures[16,17] and coordination polymers,[18-20] thus adopts a new role in bridging labile Cd^{II} within a discrete, soluble structure.

5.3 *A more accommodating host for coordination chemistry*

Following the successful demonstration of discrete complex stabilisation within **5.1**, it was hypothesised that a larger cavity, carefully matched to the diameters of potential guests, might lead to the generation of a wider range of new endohedrally-bound metal complexes.

Cage **5.2** was thus synthesised, in which Zn^{II} porphyrins define the faces of a cuboctahedron. The reaction of subcomponents **5B** and 2-formylphenanthroline with $Zn^{II}(NTf_2)_2$ yielded *O*-symmetric $Zn^{II}_{12}\mathbf{L}^{5B}_6$ assembly **5.2** as the single product observed by ESI-MS and ^{1}H NMR spectroscopy (Figure 5.6). Slow rotation of the phenylene protons was observed on the NMR timescale, enabling differentiation between interior and exterior guest binding by ^{1}H NOESY spectroscopy (Figure 5.6b).

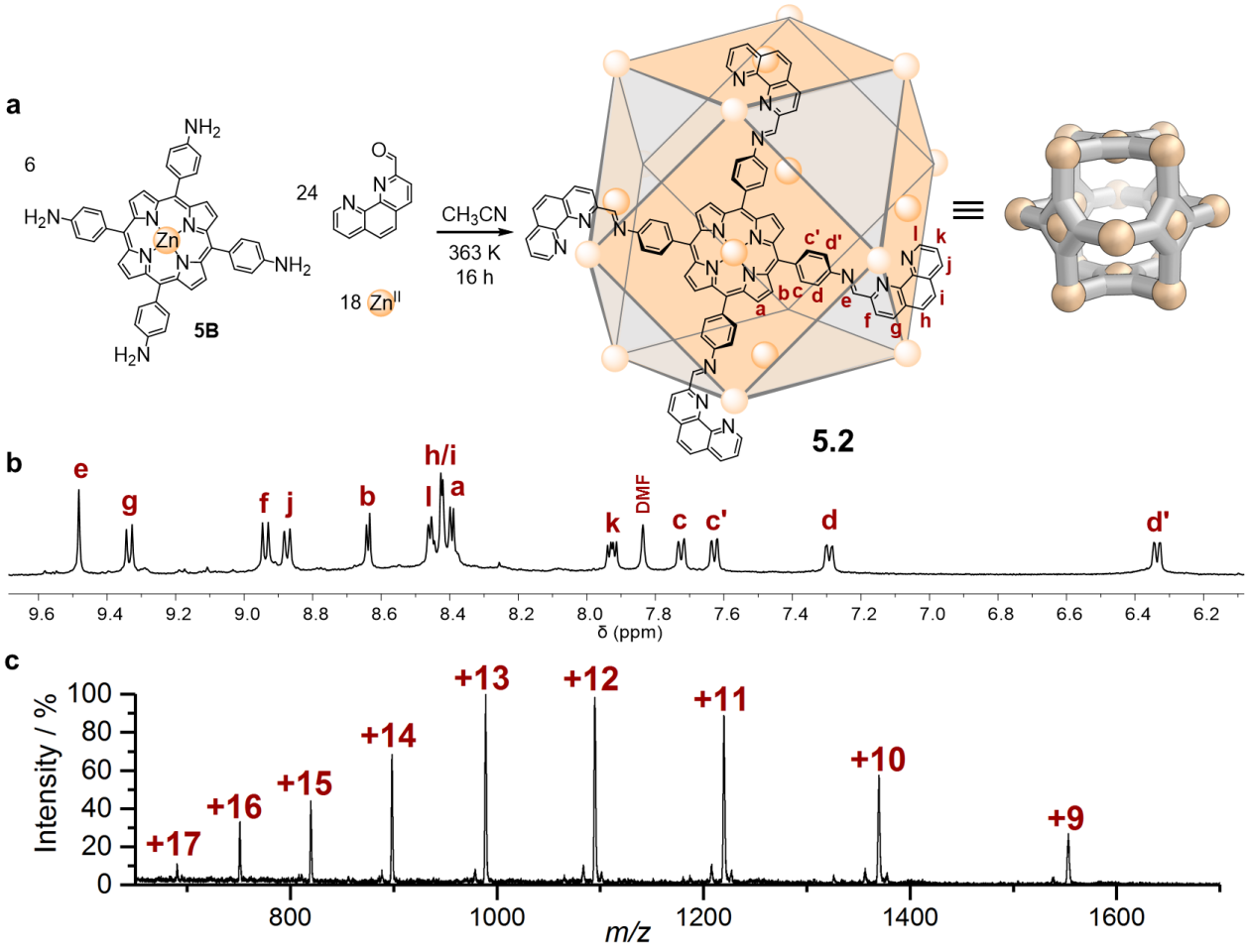

Figure 5.6 | Synthesis and characterisation of **5.2**. **a**, Synthetic scheme showing the assembly of **5.2** from subcomponents. **b**, The ^{1}H NMR spectrum (500 MHz, 298 K, CD_3CN) where c' and d' indicate exterior-facing proton environments. **c**, The ESI mass spectrum of **5.2**.

Cage **5.2** has a larger distance connecting porphyrin-bound Zn^{II} centres (*ca.* 19 Å, based on MM3 molecular models), as compared to the distance between Rh^{II} centres (15.5 Å) in **5.1** (Figure 5.7). The larger cavity of this structure (*ca.* 3000 Å^3) enabled a wider range of guests to be encapsulated, and thus greater diversity in the assembly of new species within the cage cavity.

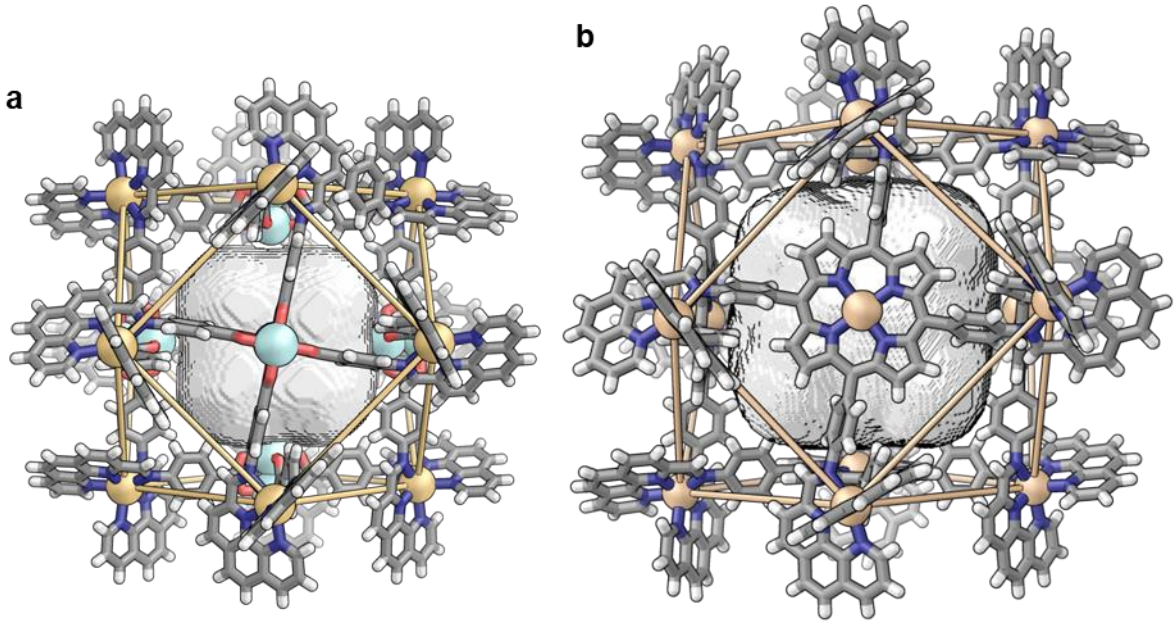

Figure 5.7 | VOIDOO calculations[21] on **a**, **5.1** and **b**, **5.2** with the cavity shown as a grey solid (*ca.* 1750 and 3000 Å^3, respectively).

The addition of 4,4'-bipyridine (**G1**) to a solution of **5.2** containing excess Zn^{II} (6 extra equiv) resulted in the internal binding of **G1** (Figure 5.8a); slow exchange binding of **G1** was observed on the NMR timescale (Figure 5.9a&b). No further binding of **G1** was observed once six equivalents had been added. ESI-MS revealed a charge increase of **5.2** from 24+ to 26+, with **5.2** encapsulating an ion of Zn^{II} and up to six molecules of **G1** simultaneously, consistent with the formation of an octahedral metal complex of formula $Zn(\mathbf{G1})_6^{2+}$ within **5.2** (Figure 5.9c). The slow exchange binding of this guest, with maintenance of *O* symmetry, suggested all-or-nothing cooperative binding of six molecules of **G1** around Zn^{II} (Figure 5.8a); all other guest binding stoichiometries would lead to a break in cage symmetry, which was not observed. When **G1** was titrated into purified **5.2**, it was observed to bind in fast exchange on the NMR timescale; excess Zn^{II} was necessary to bring about cooperative binding.

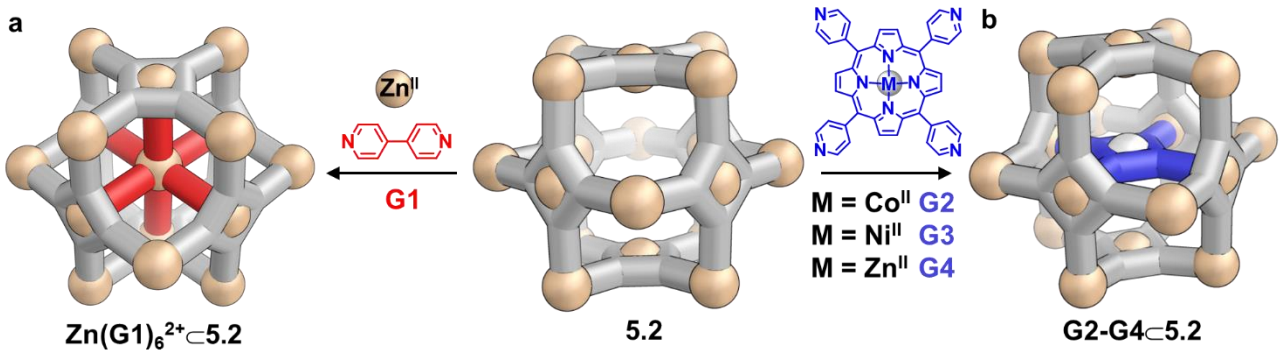

Figure 5.8 | **a**, Cage **5.2** was observed to bind both Zn^{II} and 4,4'-bipyridine (**G1**) simultaneously, generating $Zn(\mathbf{G1})_6^{2+}$⊂**5.2**. **b**, The addition of tetrapyridylporphyrins **G2-G4** led to the formation of **G2–G4**⊂**5.2**.

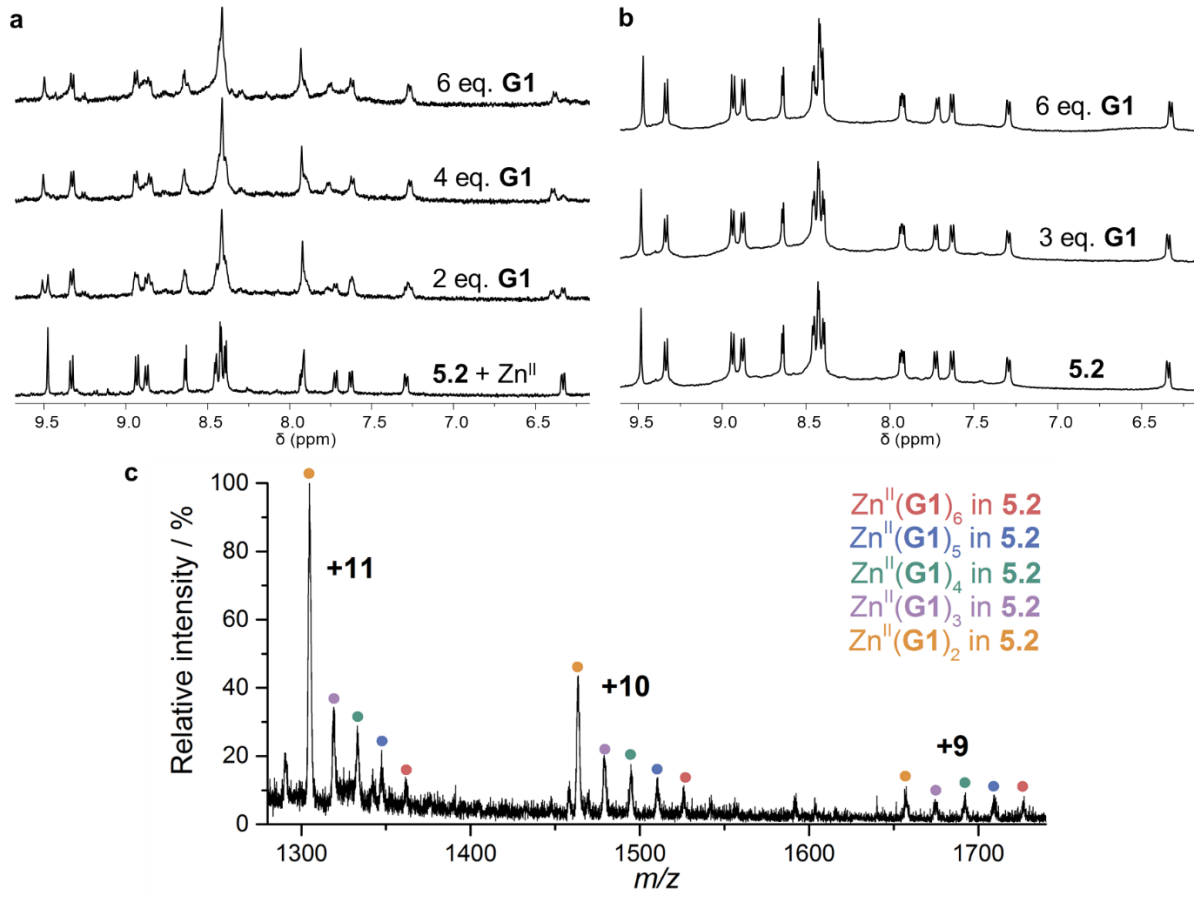

Figure 5.9 | **a**, The binding of **G1** to **5.2** was observed to proceed in slow exchange by ^{1}H NMR spectroscopy (500 MHz, 298 K, CD_3CN) in the presence of excess Zn^{II}. **b**, With no excess Zn^{II} present, the binding of **G1** proceeded by fast exchange. **c**, An ESI mass spectrum showed fragments corresponding to $Zn(\mathbf{G1})_x^{2+}\subset\mathbf{5.2}$ (where $2\leq x\leq 6$).

Fourfold-symmetric tetrapyridylporphyrins metalated with Co^{II}, Ni^{II} or Zn^{II} (**G2**, **G3** and **G4**, respectively) also bound within **5.2** (Figure 5.8b). The binding of **G2**–**G4** led to $O \rightarrow D_4$ desymmetrisation of the host framework on the NMR timescale: the top and bottom ligands of the host (as well as the guest) maintain fourfold symmetry, while the vertical and horizontal arms of the four ligands spanning the equator of the structure have distinct ^{1}H NMR environments (Figure 5.10). ^{1}H–^{1}H NOE correlations were observed between the interior-facing phenylene protons of $\mathbf{L^B}$ and the pyridyl protons of **G3** and **G4**, which were shielded by the ring current of the cage porphyrins, observed at *ca.* 2 and 5.4 ppm (Figure 5.11). Although no signals for paramagnetic guest **G2** could be identified, broadening of the interior-facing phenylene protons of the ligand and threefold splitting of signals were observed, consistent with the same mode of binding as observed for **G3** and **G4**.

The presence of these porphyrin guests partitions the cavity of **5.2** into two distinct, symmetry-equivalent regions, above and below the encapsulated metalloporphyrin. To further explore the potential of these species to form encapsulated metal complexes, the secondary encapsulation of 4,4'-bipyridine **G1**, which models suggested would provide an optimal fit between host and guest porphyrin sites, was investigated (Figure 5.12).

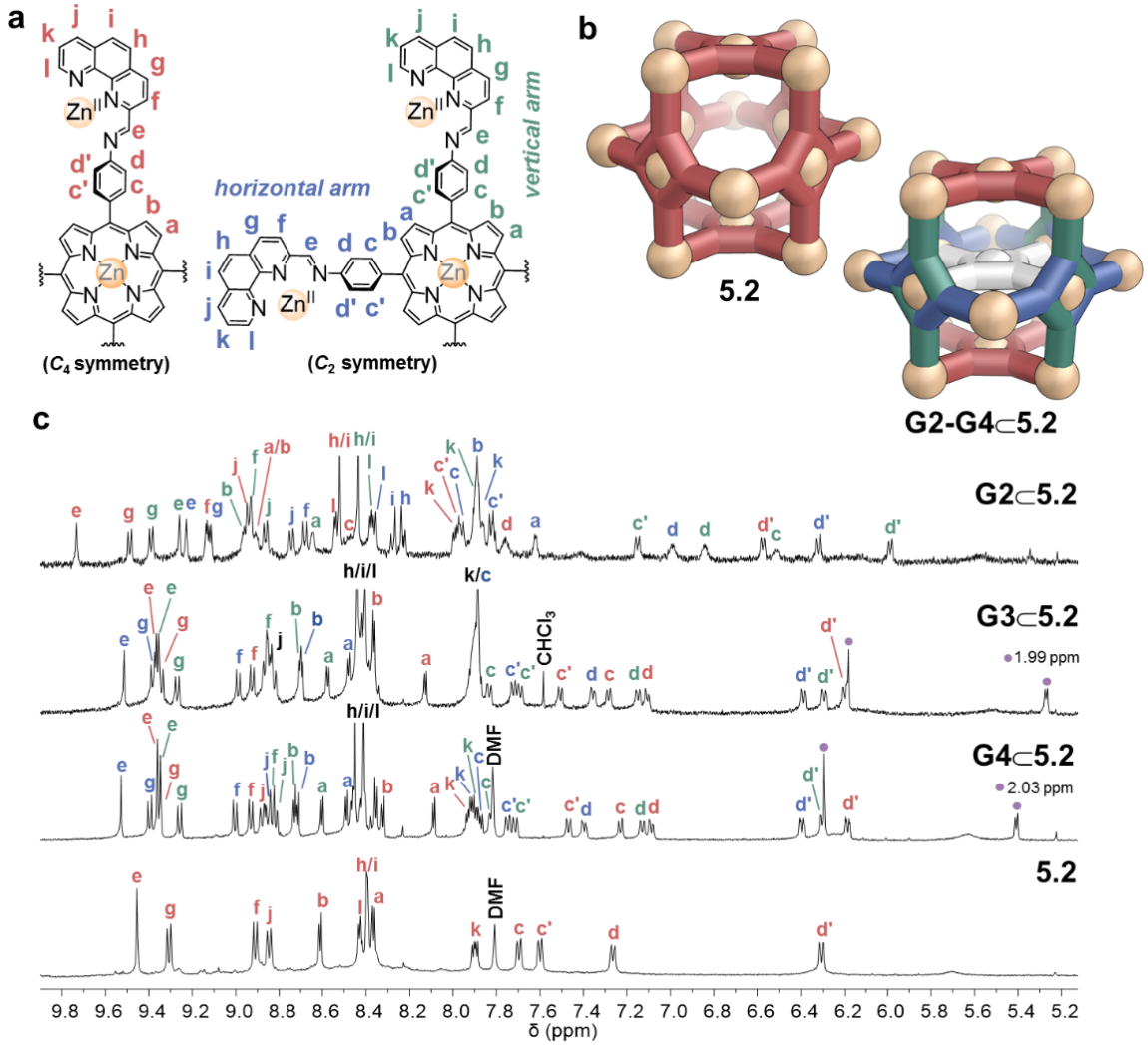

Figure 5.10 | Encapsulation of guests within **5.2** led to desymmetrisation of the cage framework. **a**, Ligand labels of **5.2** upon porphyrin encapsulation, where c' and d' are the exterior-facing protons of the phenylene rings. **b**, Equivalent environments within **5.2** upon binding **G2**–**G4**, colour-coded with the environments in **a**. In the absence of guests, all ligands in **5.2** have fourfold symmetry; in **G2**–**G4**⊂**5.2**, the ligands bound to the guest have twofold symmetry (blue and green arms), while the ligands parallel to the guest retain fourfold symmetry (red arms). **c**, ^{1}H NMR spectra (500 MHz, 298 K, CD_3CN) of host-guest complexes **G2**–**G4**⊂**5.2**, where letter colour corresponds to the ligand arm environment, black letters correspond to signals shared by each desymmetrised environment, and purple circles correspond to the encapsulated guest. No distinction between vertical and horizontal arms was observed by NMR experiments.

For all three metalloporphyrin guests, two molecules of bipyridine **G1** were observed to bind to the host-guest complexes by ESI-MS (Figure 5.13a). UV–Vis titrations of **G1** into host-guest complexes **G2**–**G4**⊂**5.2** were fitted to 1:2 binding isotherms; anticooperative binding was observed in each case (Figure 5.13b). The identity of the metal ion is understood to determine the axial coordination mode of metalloporphyrins:[22] Co^{II} porphyrins bind two ligands, whereas Zn^{II} porphyrins bind only one ligand, and low-spin Ni^{II} porphyrins only bind ligands in a very electron-deficient environment, which favours high-spin Ni^{II}. Within **5.2**, however, each bound porphyrin guest displayed distinct and atypical coordination chemistry. The confinement of metalloporphyrins within **5.2** facilitated both $Co^{II} \rightarrow Co^{III}$ oxidation and Ni^{II} low → high spin transitions, neither of which occurred outside the cavity of the cage (Figure 5.12).

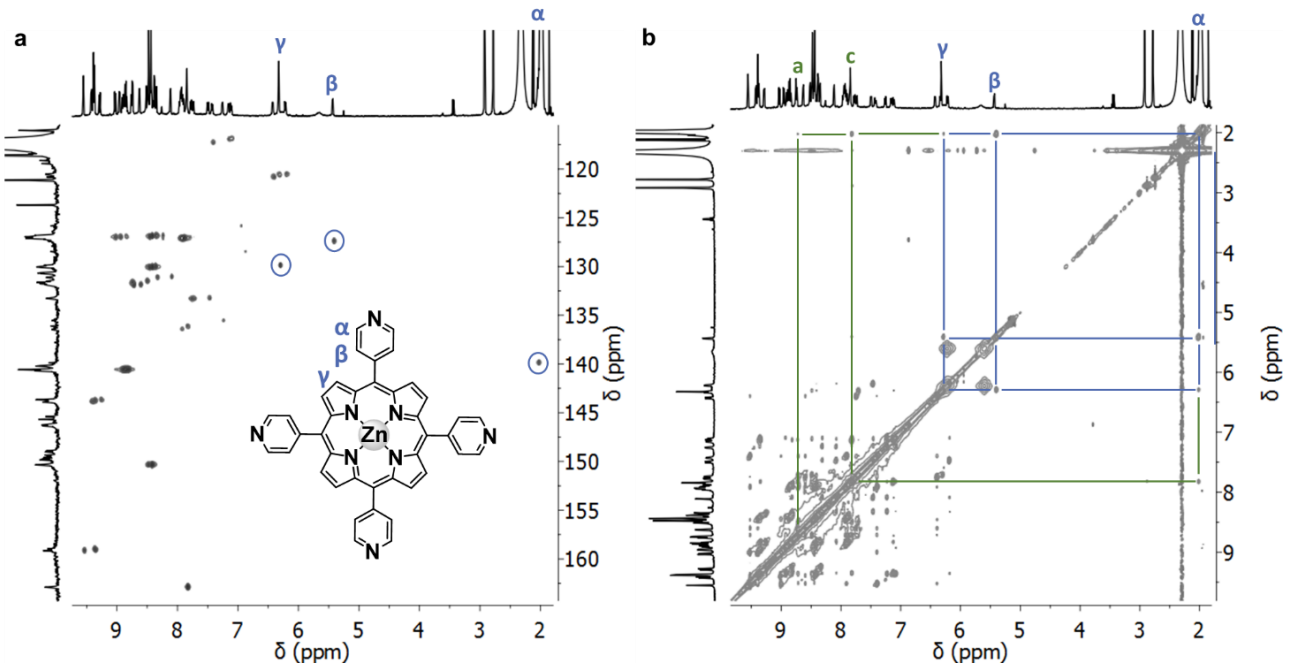

Figure 5.11 | **a,** $^{1}H–^{13}C$ HSQC NMR spectrum (500 MHz, 298 K, CD_3CN) of **G4⊂5.2**. Cross-peaks of guest signals are circled blue. **b**, $^{1}H–^{1}H$ NOESY NMR spectrum (500 MHz, 298 K, CD_3CN) of **G4⊂5.2**. Cross-peaks between guest protons are displayed as blue lines; cross-peaks between the host and guest (specifically the alpha pyridyl protons of **G4** to the pyrrolic and interiorly-facing phenyl rings of **5.2**) are displayed as green lines.

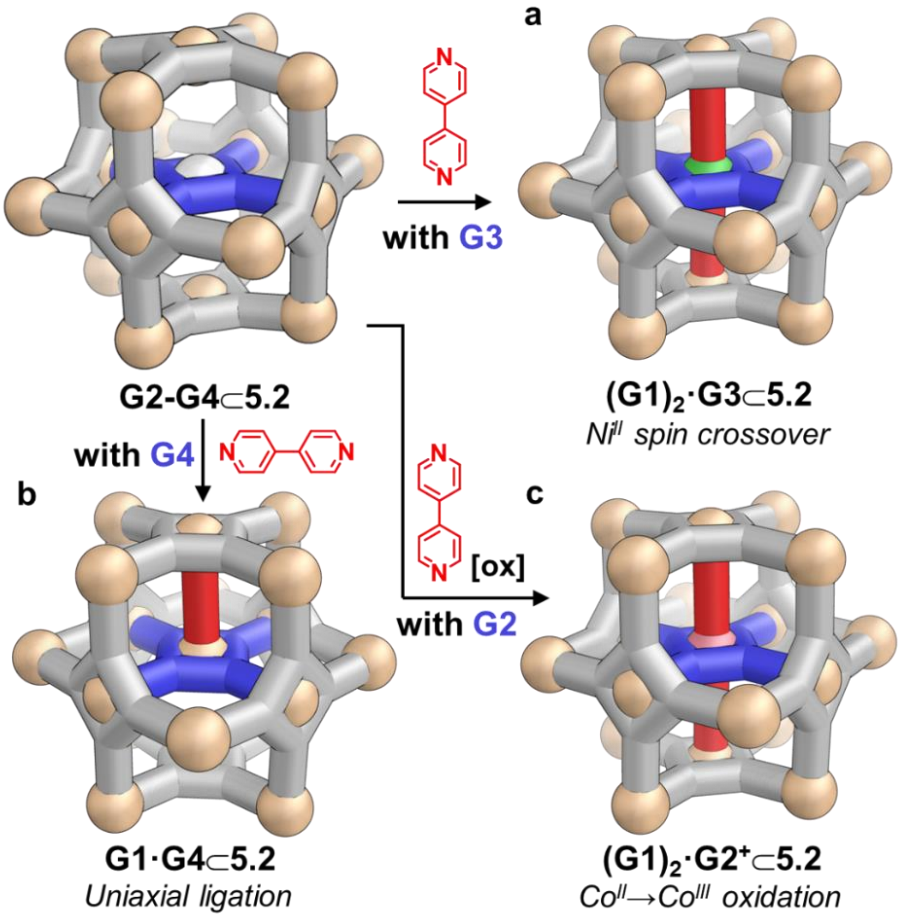

Figure 5.12 | Metalloporphyrin guests **G2**–**G4** divide the cavity of **5.2** upon binding, such that subsequent binding of **G1** brought about unique coordination chemistry within the cavity of **5.2**: **a**, Ni^{II} spin crossover occurred during the binding of two molecules of **G1** within **G3⊂5.2**; **b**, a single axial ligand bridged one of the two divisions in the case of **G4⊂5.2**; **c**, $Co^{II} \rightarrow Co^{III}$ oxidation spontaneously occurred under air following the addition of **G1** to **G2⊂5.2.**

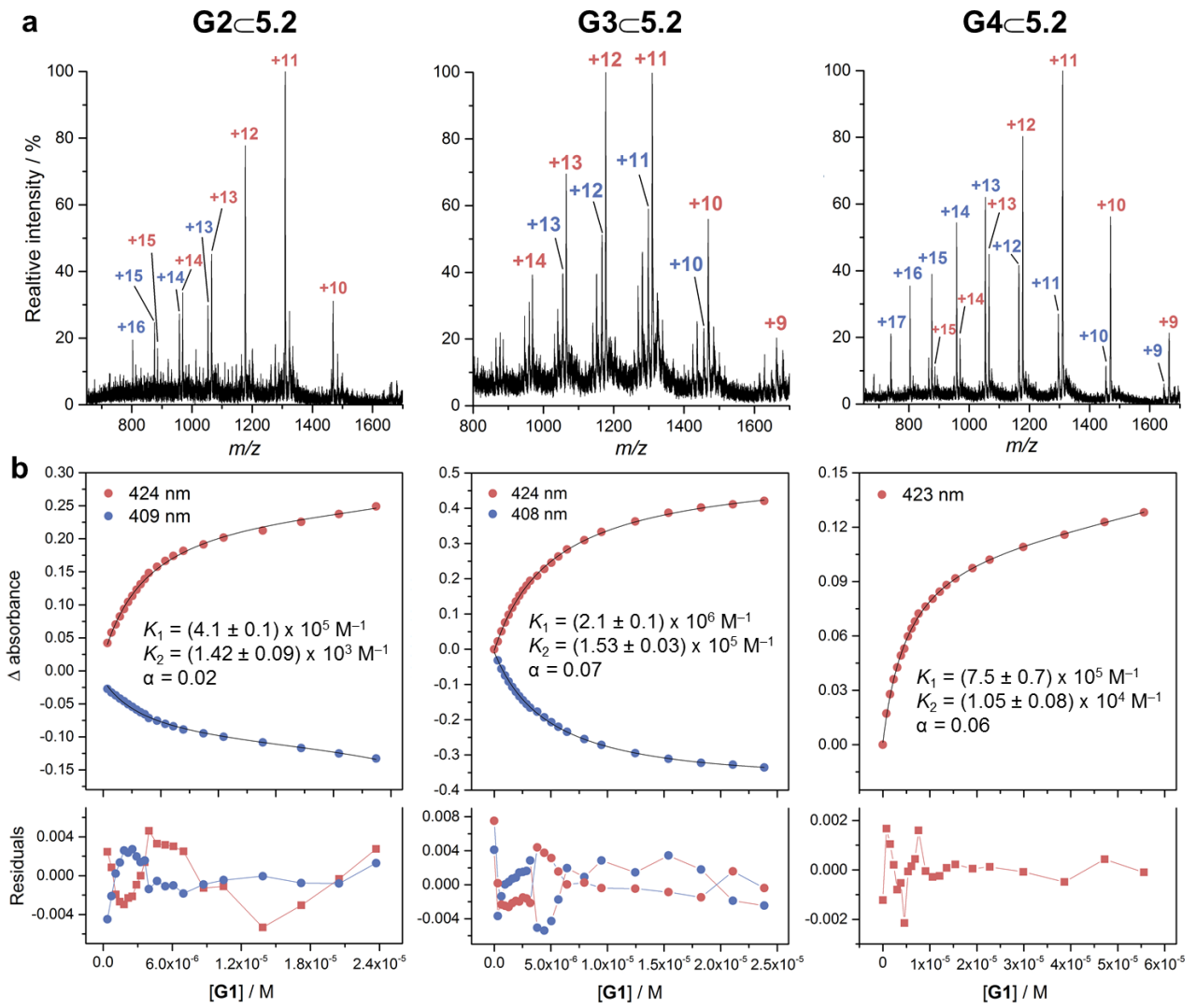

Figure 5.13 | Binding investigations of **G1** with **G2**–**G4⊂5.2**. **a**, ESI mass spectra of the host-guest complexes, with red signals corresponding to 2 bound molecules of **G1** and blue signals corresponding to 1 bound molecule of **G1** within **G2**–**G4⊂5.2**. **b**, Binding isotherms (1:2 model) fit to the absorbance shift of the Soret bands of **G2**–**G4⊂5.2** *vs.* the concentration of **G1** added to determine the binding affinity (top); and the residual plots from the fit (bottom).

The titration of **G1** into Co^{II} porphyrin-containing **G2⊂5.2** produced a distinct ^{1}H NMR spectrum consistent with fast exchange binding on the NMR timescale. However, owing to the paramagnetic Co^{II} centre of **G2**, no guest peaks could be observed from 233–298 K. After three days at 298 K, the NMR spectrum of (**G1**)$_2$·**G2⊂5.2** was observed to exhibit new, sharp peaks. An ESI mass spectrum indicated that the complex had increased in charge from +24 to +25, suggesting oxidation of the cobalt(II) centre to cobalt(III) (Figure 5.14a). ^{1}H NMR signal integration indicated two **G1** axial ligands, with D_4 symmetry overall (Figure 5.14b). It is proposed that the oxidation potential of the Co^{II} porphyrin decreases as a result of σ-donation from **G1**.[23] Steric compression, transmitted by the cage framework through **G1** to **G2**, may also stabilise the Co^{III} state, which has a smaller coordination sphere, upon axial ligation within **5.2**. Oxidation of **G2** under ambient conditions only occurred after binding **G1**; **G2⊂5.2** alone was stable in the Co^{II} state over the course of 3 months' monitoring.

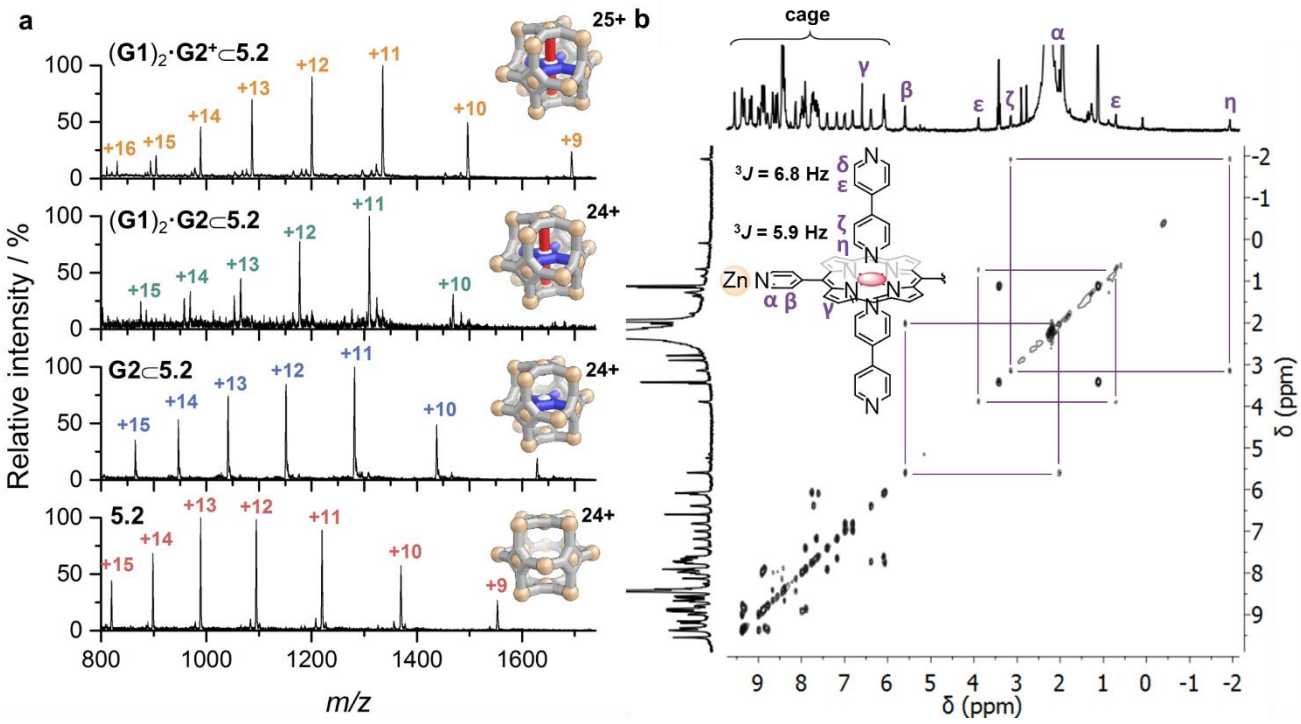

Figure 5.14 | Synthesis of diamagnetic (**G1**)$_2$·**G2**$^+$⊂**5.2**. **a**, ESI mass spectra charting the preparation of (**G1**)$_2$·**G2**$^+$⊂**5.2** from **5.2**, showing spectra of **5.2** (bottom spectrum, red), **G2**⊂**5.2** (2nd from the bottom, blue), (**G1**)$_2$·**G2**⊂**5.2** (2nd from the top, green) and (**G1**)$_2$·**G2**$^+$⊂**5.2** (top spectrum, orange). **b**, ^{1}H–^{1}H COSY NMR spectrum (400 MHz, 298 K, CD_3CN) of (**G1**)$_2$·**G2**$^+$⊂**5.2**, with guest signals and ^3J correlations in purple.

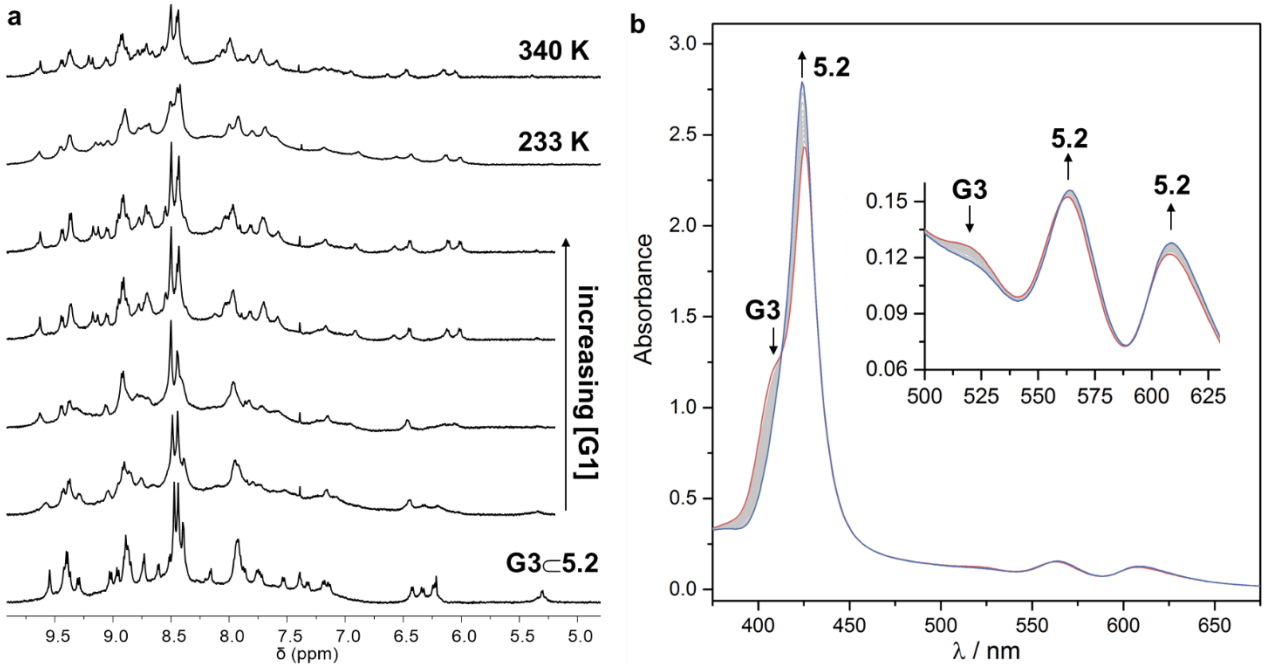

Figure 5.15 | **a**, ^{1}H NMR titration (500 MHz, CD_3CN) of **G1** into a solution of **G3**⊂**5.2** at 298 K, following by two variable temperature experiments at 233 and 340 K (top two spectra). **b**, UV-Vis titration of **G1** into a solution of **G3**⊂**5.2** in MeCN. Bands corresponding to **5.2** increase, while bands corresponding to **G3** decrease in intensity.

The addition of **G1** to Ni^{II} porphyrin-containing **G3**⊂**5.2** likewise led to broadening and shifting of the product ^{1}H NMR signals (Figure 5.15a). Neither the encapsulated porphyrin nor the binding

bipyridine signals could be identified, even at 233 K, although the binding of two molecules of **G1** was observed by ESI-MS (Figure 5.13). Similarities were observed between the proton spectra of paramagnetic **G2⊂5.2** and (**G1**)$_2$·**G3⊂5.2**, including the absence of guest signals and broadened interior-facing phenylene proton signals, and the Soret band of **G3** was observed to red-shift upon the titration of **G1** into **G3⊂5.2** (Figure 5.15b). These observations led to the hypothesis that **G1** had bound to the axial Ni^{II} sites of **G3** within **5.2**, causing the Ni^{II} centre to become high-spin.

The Evans method was used to determine whether Ni^{II} in **G3⊂2** had undergone a spin transition from low (S = 0) to high (S = 1) spin upon the addition of **G1**. To calculate the effective magnetic moment (μ_{eff}) of the assembly after the addition of 4,4'-bypridine **G1** the following equation published by Piguet[24] was employed

$$\mu_{eff} = 2.828\sqrt{\frac{T}{v_0 S_f}\left[\frac{\delta v^P M^P}{m^P} - \frac{\delta v^{dia} M^{dia}}{m^{dia}}\right]}$$

where T is the temperature (K), v_0 is the operating frequency of the NMR spectrometer (Hz), S_f is the shape factor of the magnet ($4\pi/3$ for a cylindrical sample in a superconducting magnet), m is the concentration of the solute (g/cm^3), M is the molecular mass of the dissolved compound (g mol^{-1}), δv is the shift in frequency (Hz) from the value found for the pure solvent, and superscripts ^{P} and ^{dia} refer to the paramagnetic and diamagnetic samples, respectively. This equation circumvents the need for solvent and diamagnetic corrections, which can prove difficult to quantify for supramolecular architectures of this size.

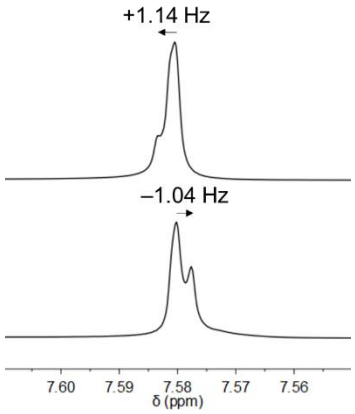

Term	Value
T (K)	298
v_0 (Hz)	4×10^8
m (g cm^{-3})	0.00836
M (g mol^{-1})	17138
δv^{dia} (Hz)	–1.04
δv^P (Hz)	1.14
μ_{eff} (Bohr mangetons)	2.52

Figure 5.16 | ^{1}H NMR spectra (400 MHz, 298 K, CD_3CN) showing the shift of $CHCl_3$ before (bottom) and after (top) the addition of **G1** to **G3⊂5.2** (left). The values used to determine the magnetic moment of (**G1**)$_2$·**G3⊂5.2** (right).

An effective magnetic moment (μ_{eff}) of 2.5 Bohr Magnetons was calculated for (**G1**)$_2$·**G3⊂5.2** using the Evans method, in good agreement with the spin-only moment of high-spin octahedral Ni^{II} (2.8 Bohr Magnetons) (Figure 5.16). Ni-porphyrins do not typically bind axial ligands in the absence

of strongly electron-withdrawing porphyrin substituents.[25] Preorganisation and host-guest size complementarity enabled the generation of this otherwise inaccessible high-spin Ni^{II} complex within **5.2**.

The ^{1}H NMR spectrum of Zn^{II} porphyrin-containing **G4⊂5.2** underwent desymmetrisation when a sub-stoichiometric amount of **G1** was added; following the addition of more than one equivalent of **G1**, the D_4 symmetry of the host-guest complex was re-established (Figure 5.17a–c). Upon cooling to 233 K, however, six distinct porphyrin cage environments were observed (Figure 5.17d). The pyridyl signals of **G4** split into two signals of equal intensity, and the four signals attributed to encapsulated **G1** shifted upfield. Integration of the proton signals attributed to **G1** against those of **G4** suggested a 1:1 ratio of these species within **5.2**. This is consistent with a square pyramidal geometry of the Zn^{II}-porphyrin centre, wherein **G4** defines the square plane and a single molecule of **G1** binds axially (Figure 5.17g). It was inferred that the addition of >1 equiv of **G1** led to rapid exchange between the two ligation sites, giving apparent D_4 symmetry at 298 K.

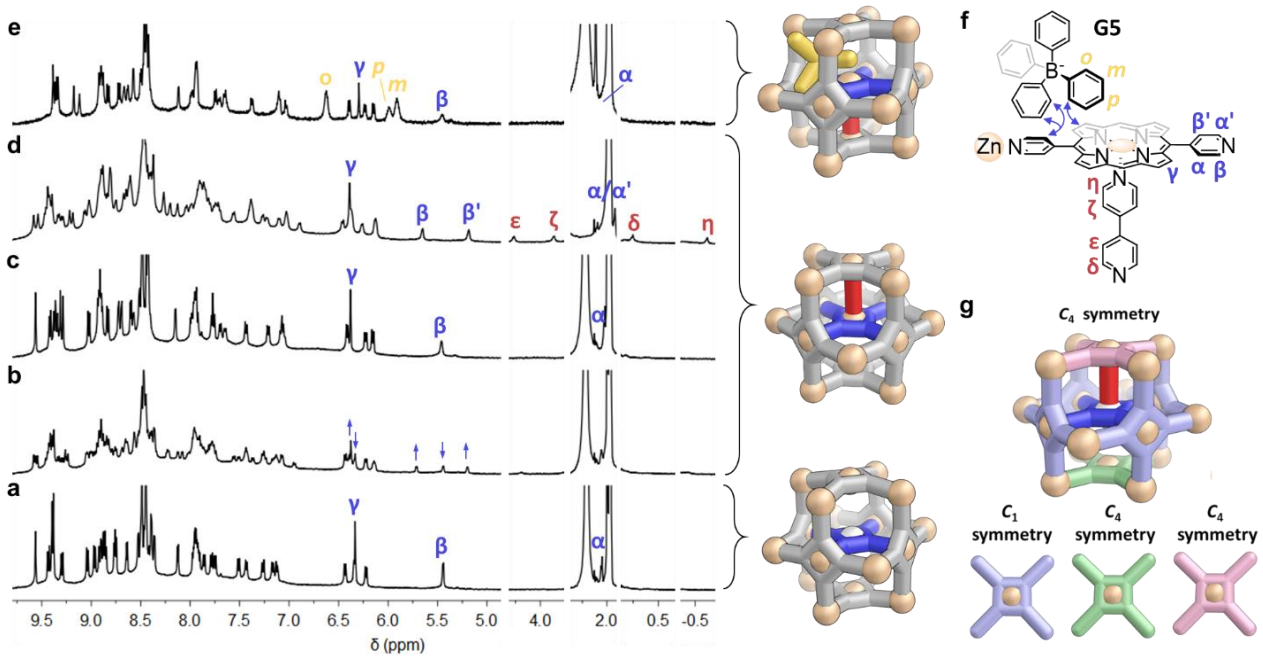

Figure 5.17 | Interactions of **G1** with **G4⊂5.2**. **a**, ^{1}H NMR spectrum (500 MHz, CD_3CN, 298 K) of **G4⊂5.2**. **b**, At 298 K, the titration of **G1** into a solution of **G4⊂5.2** in MeCN desymmetrised the host framework, and proceeded *via* slow exchange up to a threshold of one equivalent of **G1**. **c**, Rapid exchange of >1 equiv of **G1** between the two internal guest sites re-established the original D_4 symmetry of **G4⊂5.2**. **d**, Upon cooling this mixture to 233 K, peaks attributed to **G1·G4⊂5.2** resolved. **e**, The addition of nBu$_4$NBPh$_4$ **G5** to **G1·G4⊂5.2** led to shifts consistent with fast exchange BPh_4^- binding on the NMR timescale at 298 K. **f**, The three encapsulated guests, each binding within a specific region of **5.2**, with NOEs between **G4** and **G5** shown using blue arrows. **g**, Diagram showing the symmetry environment of each ligand within C_4-symmetric **G1·G4⊂5.2**.

A third level of host-guest chemistry was observed within the new void space created in **G1·G4⊂5.2**. The addition of nBu$_4$NBPh$_4$ led to distinct NMR shifts consistent with BPh_4^- (**G5**)

encapsulation in fast exchange on the NMR timescale (Figure 5.17e). ^{1}H–^{1}H NOESY NMR spectroscopy revealed correlations between the *ortho* and *meta* protons of **G5** and the pyrrolic and pyridyl protons of encapsulated **G4**, which suggested a binding configuration in which **G5** occupies the remaining cavity of **G1·G4⊂5.2**, localised around the apertures (Figure 5.18a). Although the ^{1}H NMR spectrum at 233 K was broad, ESI-MS confirmed that **G1** remained bound following the binding of **G5** (Figure 5.18b). Three distinct internal binding sites were thus concurrently occupied in this structure: one spanning the central cavity (**G4**), one occupying the top of this divided cavity (*endo*-bound **G1**), and another in the void created by this coordination (**G5**) (Figure 5.17f). This method of cavity segregation thus allows for three distinct components to be brought into proximity, in a manner that may prove useful for applications in catalysis or allosteric binding regulation.

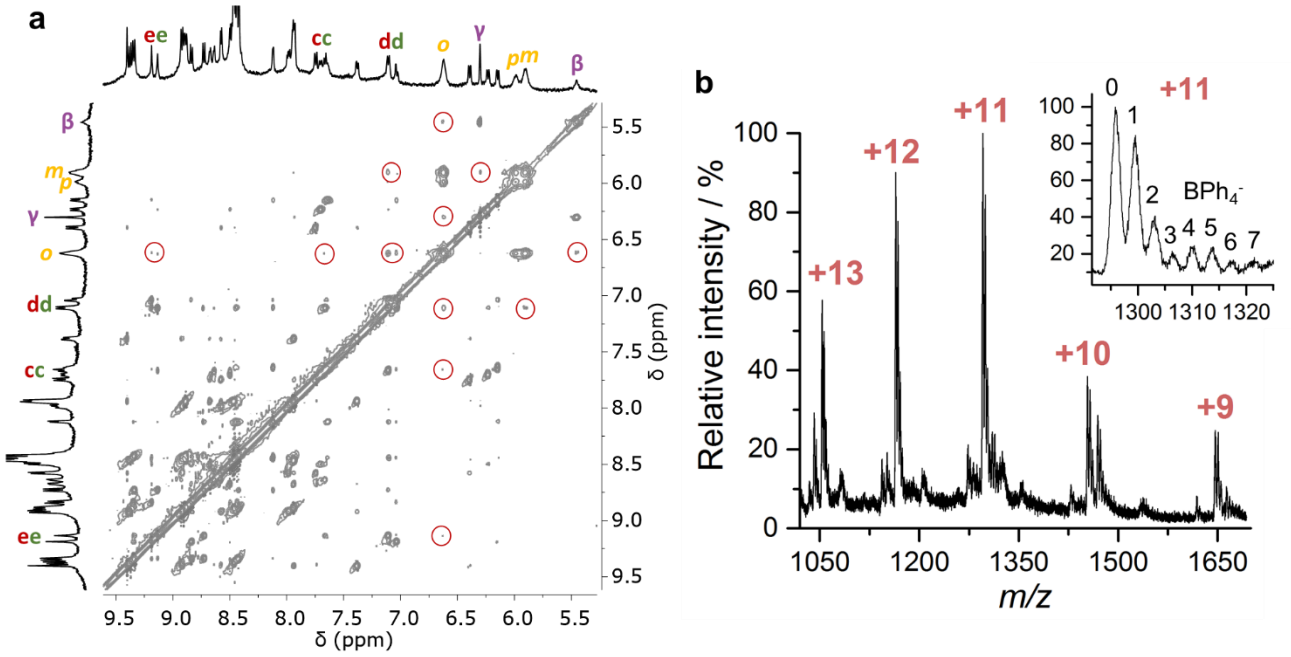

Figure 5.18 | **a**, ^{1}H–^{1}H NOESY NMR spectrum (500 MHz, 298 K, CD_3CN) of **G5·G1·G4⊂5.2**, with NOE correlations between BPh_4^- (yellow letters) and the cage framework (green and red letters) or encapsulated **G5** (purple letters) highlighted as red circles. **b**, ESI mass spectrum of **G5·G1·G4⊂5.2**, where red numbers correspond to charge fragments of **G1·G4⊂5.2**. Inset shows the *z* = +11 charge fragment, with the number of associated BPh_4^- anions coloured black.

5.4 Interlocked structures within 5.2

As with **5.1**, **5.2** was observed to bind suitably-sized linear 4,4'-dipyridyl guests (Figure 5.19a). The addition of 4,4'-dipyridyl naphthalenediimide (NDI) **G6** to **5.2** gave a product having an ESI mass spectrum consistent with multiple species binding (Figure 5.20b). The ^{1}H NMR spectrum was broad, suggesting rapid scrambling of the guest among the three possible interior binding axes (Figure 5.20a). Two-dimensional NMR spectra identified ^{1}H NMR peaks at 4.72 and 1.89 ppm that were assigned to the pyridyl protons of **G6** bound within **5.2** at 298 K; further peaks corresponding to the *exo*-bound guest were identified at 6.65 and 6.06 ppm at 233 K.

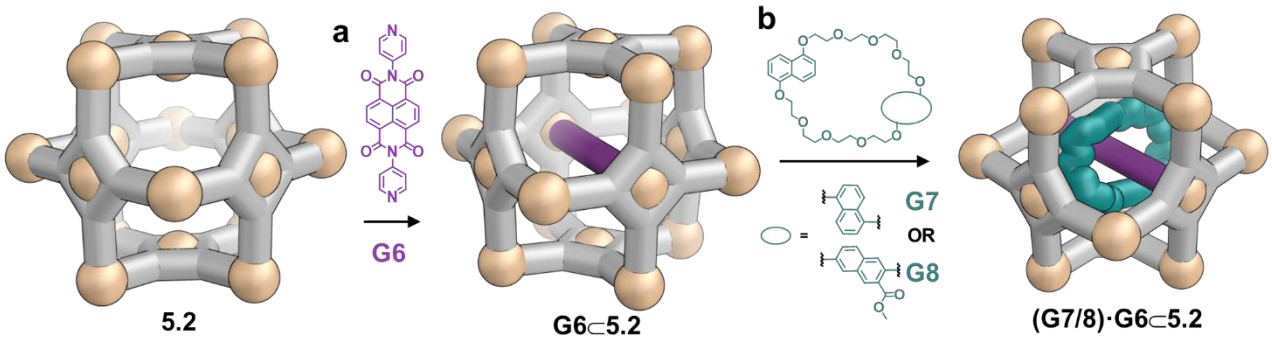

Figure 5.19 | The formation of endohedral rotaxanes within **5.2**. **a**, **G6** was coordinated to opposite ligand Zn^{II} units within **5.2**. **b**, The subsequent addition of either **G7** or **G8** led to the formation of an encapsulated rotaxane, **G7·G6⊂5.2** or **G8·G6⊂5.2**.

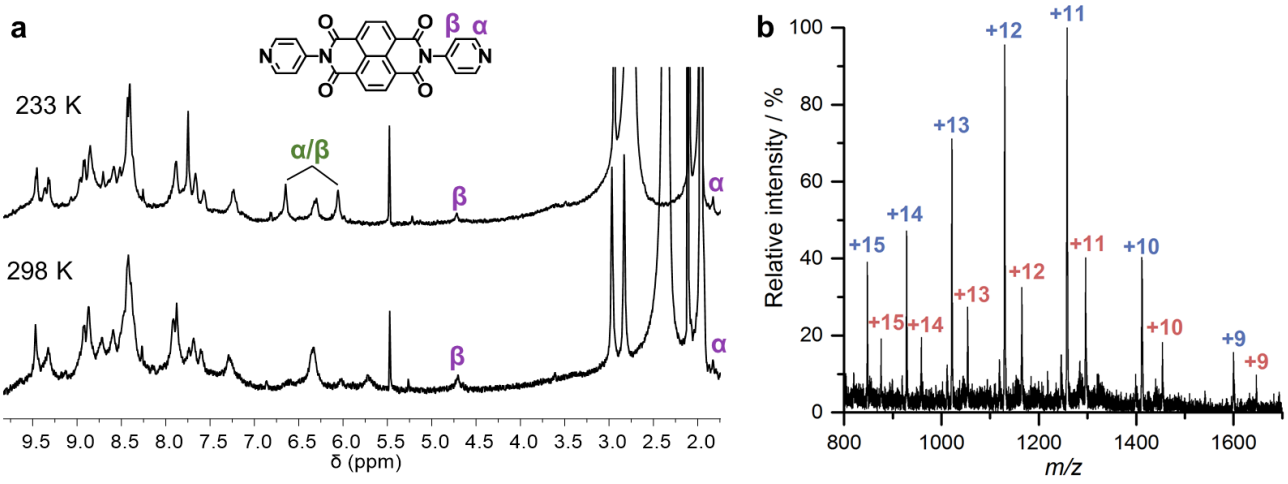

Figure 5.20 | **a**, Variable-temperature ^{1}H NMR spectra (500 MHz, CD_3CN) of **G6⊂5.2** at 298 K (bottom) and 233 K (top). Upon cooling, two peaks sharpen at 6.65 and 6.06 ppm (marked with green letters). These peaks are attributed to *exo*-bound **G6** guests. The internally bound **G6** guests appear at 4.72 and 1.89 ppm, as identified by 2D NMR spectroscopy. **b**, ESI mass spectrum of the host-guest complex, where blue charges correspond to one molecule of **G6** binding, and red charges correspond to two molecules of **G6** binding to **5.2**.

Electron deficient NDI units are known to bind to electron rich naphthalene units, with this interaction serving as a means for generating mechanically interlocked species.[26] It was hypothesised that **G6**, bound within **5.2**, might be threaded through a flexible macrocycle containing two cofacial naphthalene units (**G7**), thus inhibiting the motion of **G6** within **5.2** and generating an encapsulated rotaxane guest (Figure 5.19b).

The addition of **G7** to a MeCN solution of **G6⊂5.2** resulted in a sharpening of the ^{1}H NMR signals of the assembly, which displayed three distinct ligand environments (Figure 5.21a). This observation is consistent with restricted tumbling of **G7·G6** within **5.2** on the NMR timescale, effectively decreasing the rate of motion of the rotaxane within host **5.2**, wherein the apparent point symmetry was reduced from *O* to D_4. Signals attributed to **G7** were shifted upfield relative to their free values, as were signals attributed to **G6**. ^{1}H–^{1}H NOE correlations between **5.2** and **G6**, and **G6**

and **G7** could be identified, consistent with the encapsulation of a rotaxane guest (Figure 5.22a). ESI-MS confirmed **G7·G6⊂5.2** as the major product (Figure 5.23a). Combining **G6** and **G7** in MeCN in the absence of the cage led to an insoluble precipitate; rotaxane formation was observed only when axle **G6** was threaded with cycle **G7** after inclusion within the cage.

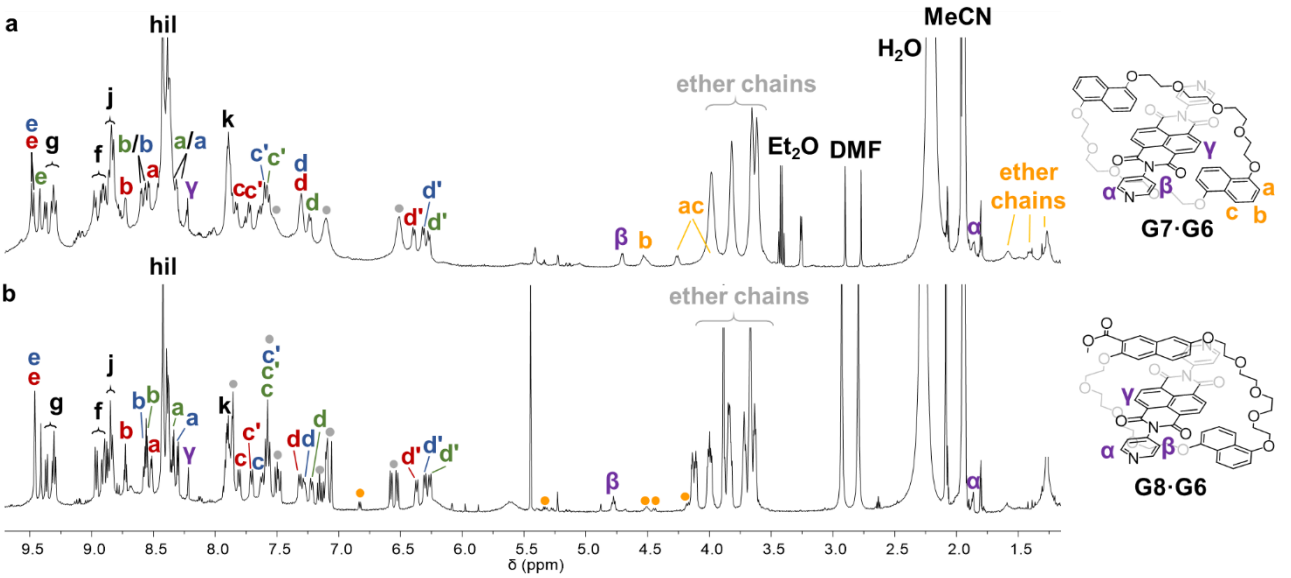

Figure 5.21 | ^{1}H NMR spectra (500 MHz, 298 K, CD_3CN) of **a**, **G7·G6⊂5.2** and **b**, **G8·G6⊂5.2** with signal assignment. Centrally-encapsulated macrocycles are shown in yellow; macrocycles binding in fast exchange with the exteriorly-bound **G6** guests are shown in grey. Coloured environments for **5.2** follow the representation in Figure 5.10.

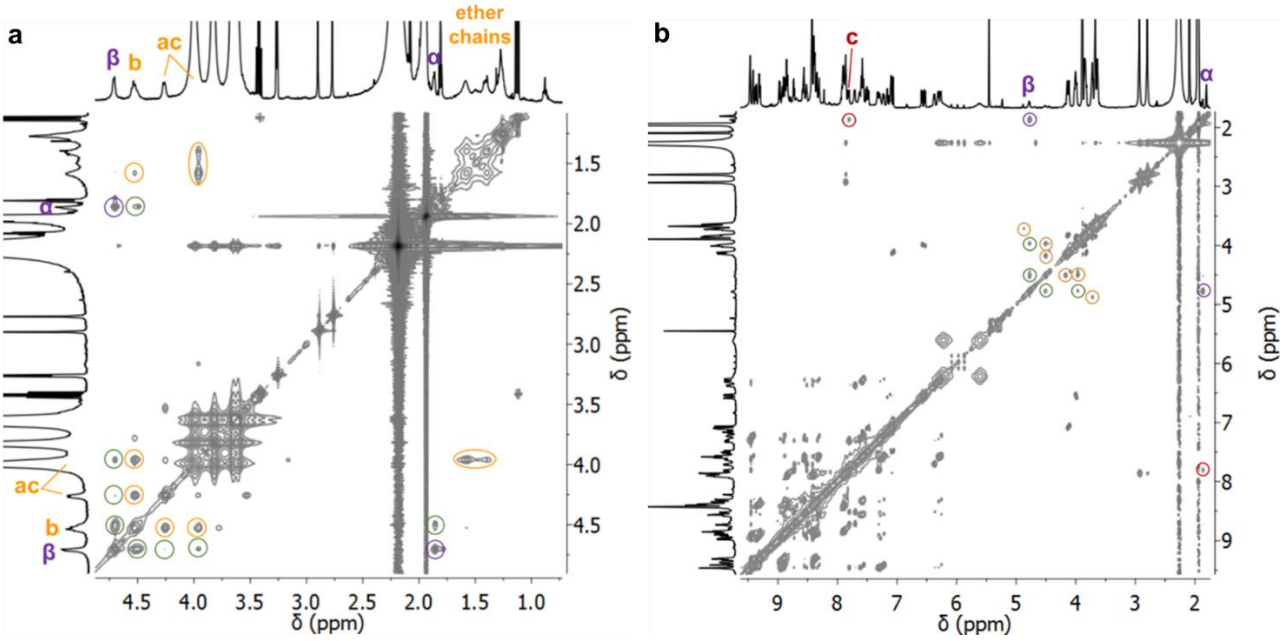

Figure 5.22 | ^{1}H–^{1}H NOESY NMR spectra (500 MHz, 298 K, CD_3CN) of **a**, **G7·G6⊂5.2** and **b**, **G8·G6⊂5.2**. Signals corresponding to **G6** are coloured purple, those attributed to the macrocycles are coloured yellow and protons corresponding to **5.2** are coloured red. Cross peaks between unique chemical species are shown in green (macrocycle to axle) or red (axle to cage).

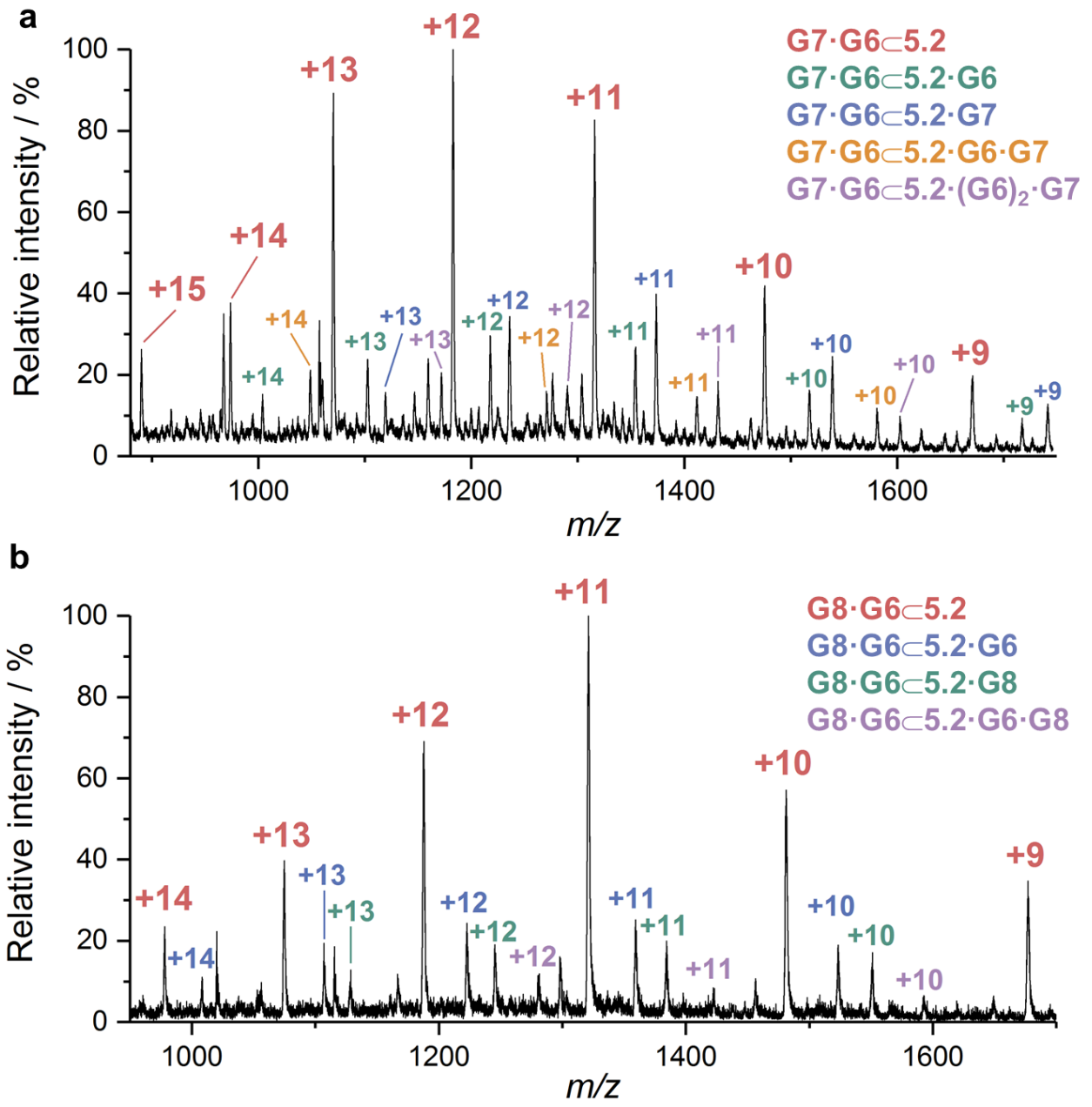

Figure 5.23 | ESI mass spectra of **a**, **G7·G6⊂5.2** and **b**, **G8·G6⊂5.2**. While the encapsulated rotaxane was observed as the major species in both cases (red signals), several signals attributed to *exo*-binding guests (other colours) were also observed.

Employing lower-symmetry macrocycle **G8** in place of **G7** produced a sharper ^{1}H NMR spectrum of the host-guest species (Figure 5.21b). In tandem with ESI-MS, 2D NMR confirmed the encapsulation of asymmetric rotaxane **G8·G6** (Figure 5.22b and Figure 5.23b). Splitting of the *β*-pyridyl protons of **G6** into two doublets, along with twofold desymmetrisation of the pyrrolic protons of the ligand to which **G6** was coordinated, suggests that the orientation of the macrocycle around the axle is fixed in place by coordination within **5.2**: the rotaxane is rotating rapidly about its axle, but it is not tumbling within the cavity. No NOE cross-peaks corresponding to chemical exchange were observed between different porphyrin ligand arms in either **G8·G6⊂5.2** or

G7·G6⊂5.2, consistent with the locked orientation of the rotaxanes within **5.2**. In going from **G6⊂5.2** to **G7·G6⊂5.2** or **G8·G6⊂5.2**, increased steric bulk within the cage decreases guest motion, as reflected in the transition from broad-to-sharp NMR signals in axle binding to rotaxane threading. The adducts **G6⊂5.2**, **G7·G6⊂5.2** and **G8·G6⊂5.2** may thus be considered new, soluble molecular gyroscopes.[27,28]

5.5 Conclusions and future work

Cages with a 24+ charge are able to overcome electrostatic repulsion to bind positively-charged complex ions, generating encapsulated coordination complexes. These capsules bound three different components simultaneously, enabling the sequential division and occupation of their inner phases. The ability to manipulate the electronics of metal ions within these systems upon secondary coordination events underpins the utility of confinement effects in generating novel synthetic products and unearthing new molecular dynamics. None of the complexes bound within **5.1** or **5.2** can be generated outside their cavities. These cages thus create unique chemical environments for self-assembly. New cage geometries with different cavity shapes will improve the range of assemblies that can be stabilised by this new approach to coordination-directed supramolecular synthesis.

While the investigations in this Chapter were largely concerned with generating new species within these cage environments, the Zn^{II} porphyrin binding sites may also be used to engineer specific binding stoichiometries of guests. For example, cage **5.2** has six potential binding sites for monodentate guests (such as pyridine), whereas **G6⊂5.2** has four sites, and **G2**–**G4⊂5.2** has two sites. By switching between these different internal guests, a system could be developed whereby the number of guests being bound, and potentially the cooperation between these guests, could be regulated. An interconverting set of host-guest species could thus act to regulate the binding stoichiometry of monodentate guests to the cage, leading to guest-induced modulation of binding cooperativity.

5.6 Experimental section

5.6.1 Synthesis and characterisation of 5A

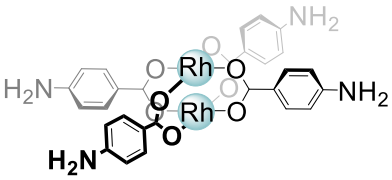

Rhodium acetate (100 mg, 230 μmol, 1 equiv) and *p*-aminobenzoic acid (250 mg, 1.8 mmol, 8 equiv) were refluxed in dried and degassed diglyme (20 mL) under N_2 for 16 hours. Upon cooling, the solution was centrifuged and the solvent decanted. The solid was washed three times with 1:1 Et_2O:MeOH (3 × 20 mL) and dried under vacuum, yielding **5A** as a light purple solid (128 mg, 171 μmol, 76%). **^{1}H NMR** (500 MHz, 298 K, d_6-DMSO): δ 7.44 (d, J = 8.7 Hz, 8H), 6.38 (d, J = 8.7 Hz, 8H), 5.75 (s, 8H) ppm. **^{13}C NMR** (126 MHz, 298 K, d_6-DMSO): δ 185.4, 153.1, 130.7, 118.9, 112.5 ppm. **HR-ESI-MS**: *m/z* calculated for $[C_{28}H_{28}N_4O_8Rh_2+H]^+$ = 755.0090; observed = 755.0084. **Elemental analysis**: calcd (%) for $C_{28}H_{24}N_4O_8Rh_2 \cdot C_6H_{14}O_3$: C 46.17, H 4.33, N 6.33; found: C 46.81, H 4.50, N 5.99.

5.6.2 Synthesis and characterisation of 5.1

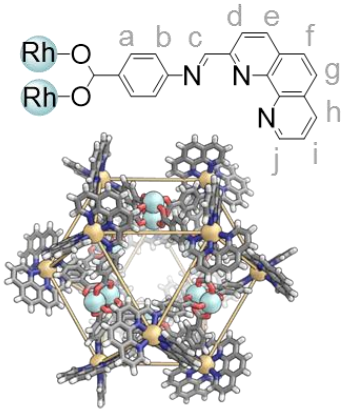

Subcomponent **5A** (13.5 mg, 36.0 μmol, 6 equiv), $Cd(OTf)_2$ (24.8 mg, 108 μmol, 18 equiv/xs) and 2-formylphenanthroline (15.0 mg, 144 μmol, 24 equiv) were combined in CD_3CN (4.0 mL) in a sealed vessel. The reaction mixture was heated at 343 K for 16 h, yielding a yellow-orange solution upon cooling to room temperature. The solution was used as synthesised, without further purification. Notes: (a) **5.1** can also be formed from 12 equiv $Cd(OTf)_2$. (b) A dry sample of **5.1** was obtained by evaporating the solvent with N_2; however, re-dissolving the cage in CD_3CN required heating the mixture at 343 K for a further 16 h. It is proposed that coordination of MeCN at the Rh^{II}_2 sites is necessary for solubility. For instance, **5.1** was not soluble in $MeNO_2$, which normally acts as a non-coordinating substitute solvent for MeCN. **^{1}H NMR** (500 MHz, 298 K, CD_3CN): δ 8.86 (d, J = 8.4 Hz, 24H, H_e), 8.80 (dd, J = 8.3, 1.5 Hz, 24H, H_h), 8.73 (s, $J_{Cd,H}$ = 14.7 Hz, 24H, H_c), 8.47 (dd, J = 4.9, 1.5 Hz, 24H, H_j), 8.34 (d, J = 9.2 Hz, 24H, H_g), 8.24 (d, J = 9.2 Hz, 24H, H_f), 8.17 (d, J = 8.4 Hz, 24H, H_d), 7.84 (dd, J = 8.3, 4.9 Hz, 24H, H_i), 7.69 (d, J = 8.5 Hz, 48H, H_a), 6.53 (d, J = 8.5 Hz, 48H, H_b) ppm. **^{13}C NMR** (126 MHz, 298 K, CD_3CN): δ 184.2, 160.8, 151.4, 150.0, 145.6, 142.2, 140.5, 131.9, 131.0, 130.5, 129.8, 127.9, 126.9, 126.6, 122.3, 121.2, 120.8, 119.7 ppm. **LR-ESI-MS** [charge, calculated for **5.1**$(OTf)_{24}$]: *m/z* = 1599.7 [**5.1**$(OTf)_{16}^{8+}$, 1600.1], 1405.3 [**5.1**$(OTf)_{15}^{9+}$, 1405.8], 1250.0 [**5.1**$(OTf)_{14}^{10+}$, 1250.3], 1122.9 [**5.1**$(OTf)_{13}^{11+}$, 1123.1], 1016.9 [**5.1**$(OTf)_{12}^{12+}$, 1017.0], 927.0 [**5.1**$(OTf)_{11}^{13+}$, 927.3].

5.6.3 Synthesis and characterisation of 5.2

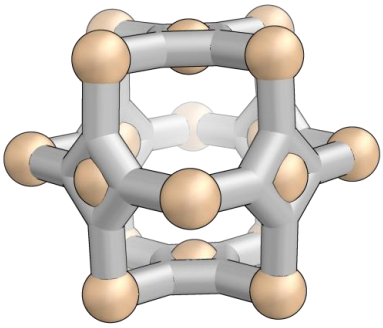

Zinc tetra(4-aminophenyl)porphyrin **5B** (17.2 mg, 23.3 μmol, 6 equiv), $Zn(NTf_2)_2$ (51.2 mg, 70.0 μmol, 18 equiv/xs) and 2-formylphenanthroline (19.4 mg, 93.4 μmol, 24 equiv) were combined in CD_3CN or CH_3CN (5.0 mL) in a sealed vessel. The reaction mixture was heated at 363 K for 16 h, yielding a dark yellow-green solution upon cooling to room temperature. A solid sample of the cage could be collected by precipitation with Et_2O, trituration with Et_2O and drying over N_2 (58.9 mg, 3.57 μmol, 92%), or else used as synthesised. **^{1}H NMR** (500 MHz, 298 K, CD_3CN): δ 9.48 (s, 24H), 9.34 (d, J = 8.3 Hz, 24H), 8.94 (d, J = 8.3 Hz, 24H), 8.87 (d, J = 8.2 Hz, 24H), 8.64 (d, J = 4.9 Hz, 24H), 8.46 (d, J = 4.8 Hz, 24H), 8.42 (m, 48H), 8.39 (d, J = 4.9 Hz, 24H), 7.93 (dd, J = 8.2, 4.8 Hz, 24H), 7.72 (dd, J = 8.2, 1.9 Hz, 24H), 7.63 (dd, J = 8.3, 1.9 Hz, 24H), 7.29 (dd, J = 8.2, 2.3 Hz, 24H), 6.34 (dd, J = 8.3, 2.3 Hz, 24H) ppm. See Figure 5.6b for signal assignment. **^{13}C NMR** (126 MHz, 298 K, CD_3CN): δ 158.9, 150.4, 149.3, 146.3, 145.4, 143.8, 140.7, 140.6, 140.2, 135.5, 133.4, 131.7, 131.4, 130.7, 130.2, 127.1, 127.0, 126.9, 123.7, 121.2, 120.6, 119.0, 117.3 ppm. **LR-ESI-MS** [charge, calculated for **5.2**$(NTf_2)_{24}$]: *m/z* = 1553.0 [**5.2**$(NTf_2)_{15}^{9+}$, 1553.4], 1369.8 [**5.2**$(NTf_2)_{14}^{10+}$, 1370.1], 1219.4 [**5.2**$(NTf_2)_{13}^{11+}$, 1220.0], 1094.8 [**5.2**$(NTf_2)_{12}^{12+}$, 1095.0], 989.0 [**5.2**$(NTf_2)_{11}^{13+}$, 989.2], 898.4 [**5.2**$(NTf_2)_{10}^{14+}$, 898.6], 819.8 [**5.2**$(NTf_2)_9^{15+}$, 820.0], 751.1 [**5.2**$(NTf_2)_8^{16+}$, 751.2], 690.3 [**5.2**$(NTf_2)_7^{17+}$, 690.6]. **HR-ESI-MS** *m/z* calculated for **5.2**$(NTf_2)_{12}^{12+}$ = 1094.9696, observed = 1094.9705.

5.6.4 Synthesis and characterisation of G2–G4⊂5.2

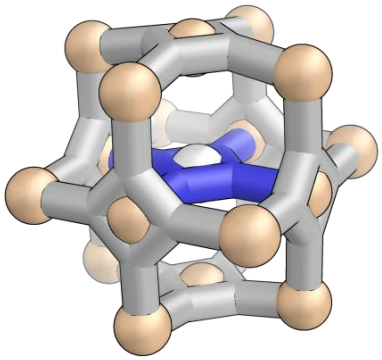

General procedure: A solid sample of **G2**–**G4** (*ca.* 5 mg, excess) was added to a solution of **2** (5.00 mg) in CD_3CN (0.6 mL) and heated at 343 K for 16 h. The solution was filtered and spectra recorded directly without further purification. See Figure 5.10 for proton assignments.

G2⊂5.2: **^{1}H NMR** (500 MHz, 298 K, CD_3CN): δ 9.76 (s, 8H), 9.52 (d, J = 7.9 Hz, 8H), 9.42 (d, J = 7.9 Hz, 8H), 9.29 (s, 8H), 9.26 (s, 8H), 9.17 – 9.12 (m, 16H), 9.02 – 8.91 (s, 40H), 8.89 (d, J = 7.9 Hz, 8H), 8.77 (d, J = 8.4 Hz, 8H), 8.71 (d, J = 9.0 Hz, 8H), 8.67 (br, 8H), 8.57 (d, J = 4.3 Hz, 8H), 8.55 (m, 16H), 8.50 (br, 8H), 8.46 (m, 16H), 8.42 – 8.37 (m, 16H), 8.30 (d, J = 9.0 Hz, 8H), 8.26 (d, J = 9.0 Hz, 8H), 8.04 – 7.96 (m, 24H), 7.94 – 7.88 (m, 24H), 7.85 (d, J = 8.5 Hz, 8H), 7.79 (br, 8H), 7.65 (br, 8H), 7.18 (d, J = 7.8 Hz, 8H), 7.02 (br, 8H), 6.87 (br, 8H), 6.60 (d, J = 7.3 Hz, 8H), 6.54 (br, 8H), 6.35 (d, J = 8.5 Hz, 8H),

6.02 (d, *J* = 7.8 Hz, 8H) ppm. **^{13}C NMR** (126 MHz, 298 K, CD_3CN): *δ* 159.3, 159.0, 158.9, 150.4, 150.3, 150.1, 149.1, 149.8, 149.8, 149.5, 149.4, 148.3, 148.2, 146.5, 146.2, 146.0, 145.9, 145.7, 145.2, 144.3, 142.0, 143.8, 143.5, 143.1, 142.7, 140.8, 140.7, 140.6, 140.5, 140.3, 140.2, 140.1, 137.8, 136.8, 136.2, 135.1, 133.6, 133.4, 132.8, 132.2, 131.9, 131.7, 131.5, 130.8, 130.7, 130.5, 130.2, 130.1, 129.9, 129.0, 128.5, 127.0, 126.8, 125.8, 123.7, 123.0, 122.6, 120.6, 120.3, 119.8, 119.4 ppm. **LR-ESI-MS** [charge, calculated for **G2⊂5.2**$(NTf_2)_{24}$]: *m/z* = 1628.5 [**G2⊂5.2**$(NTf_2)_{15}^{9+}$, 1628.5], 1437.7 [**G2⊂5.2**$(NTf_2)_{14}^{10+}$, 1437.6], 1281.5 [**G2⊂5.2**$(NTf_2)_{13}^{11+}$, 1281.5], 1151.2 [**G2⊂5.2**$(NTf_2)_{12}^{12+}$, 1151.3], 1041.4 [**G2⊂5.2**$(NTf_2)_{11}^{13+}$, 1041.2], 946.6 [**G2⊂5.2**$(NTf_2)_{10}^{14+}$, 946.8], 864.9 [**G2⊂5.2**$(NTf_2)_9^{15+}$, 865.0], 793.5 [**G2⊂5.2**$(NTf_2)_8^{16+}$, 793.5], 730.0 [**G2⊂5.2**$(NTf_2)_7^{17+}$, 730.3]. **HR-ESI-MS**: *m/z* calculated for **G2⊂5.2**$(NTf_2)_{13}^{11+}$ = 1281.4272, observed = 1281.4290.

G3⊂5.2: **^{1}H NMR** (500 MHz, 298 K, CD_3CN): *δ* 9.54 (s, 8H), 9.41 (d, *J* = 8.3 Hz, 8H), 9.39 (s, 8H), 9.38 (s, 8H), 9.37 (d, *J* = 8.3 Hz, 8H), 9.30 (d, *J* = 8.5 Hz, 8H), 9.02 (d, *J* = 8.1 Hz, 8H), 8.95 (d, *J* = 8.2 Hz, 8H), 8.91 – 8.83 (m, 32H), 8.73 (d, *J* = 4.0 Hz, 8H), 8.72 (d, *J* = 3.5 Hz, 8H), 8.60 (d, *J* = 4.9 Hz, 8H), 8.51 (d, *J* = 4.7 Hz, 8H), 8.48 – 8.42 (m, 72H), 8.39 (d, *J* = 4.5 Hz, 8H), 8.16 (d, *J* = 4.7 Hz, 8H), 8.00 – 7.88 (m, 32H), 7.86 (dd. *J* = 8.4, 1.9 Hz, 8H), 7.73 (dd, *J* = 8.1, 2.0 Hz, 8H), 7.70 (dd, *J* = 8.4, 1.9 Hz, 8H), 7.51 (dd, *J* = 8.0, 2.0 Hz, 8H), 7.36 (dd, *J* = 8.1, 2.4 Hz, 8H), 7.30 (dd, *J* = 8.2, 2.0 Hz, 8H), 7.15 (dd, *J* = 8.4, 2.3 Hz, 8H), 7.12 (dd, *J* = 8.1, 2.4 Hz, 8H), 6.40 (dd, *J* = 8.0, 2.4 Hz, 8H), 6.31 (dd, *J* = 8.4, 2.3 Hz, 8H), 6.21 (dd, *J* = 8.1, 2.4 Hz, 8H), 6.19 (s, 8H), 5.30 (d, *J* = 5.5 Hz, 8H), 1.99 (8H, under solvent MeCN, identified by ^{1}H–^{1}H COSY/NOESY spectra) ppm. **^{13}C NMR** (126 MHz, 298 K, CD_3CN): *δ* 159.1, 159.0, 150.4, 149.9, 149.8, 149.7, 149.7, 149.6, 149.3, 149.1, 149.0, 146.4, 146.2, 146.2, 145.7, 145.6, 145.4, 143.9, 143.8, 143.8, 143.7, 143.6, 140.7, 140.6, 140.4, 140.2, 133.4, 133.3, 131.8, 131.8, 131.7, 131.7, 131.6, 131.5, 131.2, 130.7, 130.6, 130.0, 127.1, 127.0, 126.9, 126.9, 123.7, 120.9, 120.8, 120.6, 119.4, 119.1, 118.8 ppm. **LR-ESI-MS** [charge, calculated for **G3⊂5.2**$(NTf_2)_{24}$]: *m/z* = 1628.4 [**G3⊂5.2**$(NTf_2)_{15}^{9+}$, 1628.5], 1437.6 [**G3⊂5.2**$(NTf_2)_{14}^{10+}$, 1437.6], 1281.2 [**G3⊂5.2**$(NTf_2)_{13}^{11+}$, 1281.4], 1151.3 [**G3⊂5.2**$(NTf_2)_{12}^{12+}$, 1151.3], 1041.1 [**G3⊂5.2**$(NTf_2)_{11}^{13+}$, 1041.2], 946.9 [**G3⊂5.2**$(NTf_2)_{10}^{14+}$, 946.8], 865.2 [**G3⊂5.2**$(NTf_2)_9^{15+}$, 865.0], 793.3 [**G3⊂5.2**$(NTf_2)_8^{16+}$, 793.4]. **HR-ESI-MS**: *m/z* calculated for **G3⊂5.2**$(NTf_2)_{12}^{12+}$ = 1151.3152, observed = 1151.3194.

G4⊂5.2: **^{1}H NMR** (500 MHz, 298 K, CD_3CN): *δ* 9.56 (s, 8H), 9.42 (d, *J* = 8.2 Hz, 8H), 9.41 – 9.36 (m, 24H), 9.29 (d, *J* = 8.5 Hz, 8H), 9.03 (d, *J* = 8.2 Hz, 8H), 8.96 (d, *J* = 8.2 Hz, 8H), 8.93 – 8.82 (m, 24H), 8.78 – 8.72 (m, 16H), 8.63 (d, *J* = 4.8 Hz, 8H), 8.52 (d, *J* = 4.8 Hz, 8H), 8.50 – 8.39 (m, 48H), 8.38 (d, *J* = 5.3 Hz, 8H), 8.35 (d, *J* = 4.6 Hz, 8H), 8.12 (d, *J* = 4.6 Hz, 8H), 7.99 – 7.89 (m, 32H), 7.87 – 7.83 (m, 8H, overlaid with solvent DMF), 7.78 (dd, *J* = 8.3, 1.6 Hz, 8H), 7.74 (dd, *J* = 8.4, 1.5

Hz, 8H), 7.50 (dd, *J* = 7.9, 1.8 Hz, 8H), 7.42 (dd, *J* = 7.9, 1.5 Hz, 8H), 7.26 (dd, *J* = 7.6, 1.6 Hz, 8H), 7.16 (dd, *J* = 8.4, 2.2 Hz, 8H), 7.12 (dd, *J* = 7.9, 2.1 Hz, 8H), 6.43 (dd, *J* = 8.0, 2.3 Hz, 8H), 6.35 – 6.31 (m, 16H), 6.22 (dd, *J* = 8.0, 2.3 Hz, 8H), 5.44 (d, *J* = 6.0 Hz, 8H), 2.03 (d, *J* = 6.0 Hz, 8H) ppm. **^{13}C NMR** (126 MHz, 298 K, CD_3CN): δ 162.9, 159.2, 159.0, 150.4, 149.8, 149.7, 149.6, 149.5, 149.4, 149.4, 149.0, 148.9, 146.4, 146.3, 146.2, 146.2, 145.7, 145.4, 143.9, 143.9, 143.8, 143.7, 140.7, 140.6, 140.5, 140.2, 140.2, 139.9, 133.3, 133.3, 133.2, 131.8, 131.7, 131.6, 131.5, 131.1, 130.7, 130.7, 130.6, 130.1, 130.0, 129.9, 127.1, 126.9, 126.8, 120.8, 120.6, 120.5, 119.4, 119.1 ppm. **LR-ESI-MS** [charge, calculated for **G4⊂5.2**$(NTf_2)_{24}$]: *m/z* = 1628.6 [**G4⊂5.2**$(NTf_2)_{15}^{9+}$, 1629.2], 1438.0 [**G4⊂5.2**$(NTf_2)_{14}^{10+}$, 1438.3], 1281.7 [**G4⊂5.2**$(NTf_2)_{13}^{11+}$, 1282.1], 1151.7 [**G4⊂5.2**$(NTf_2)_{12}^{12+}$, 1151.9], 1041.4 [**G4⊂5.2**$(NTf_2)_{11}^{13+}$, 1041.7], 947.1 [**G4⊂5.2**$(NTf_2)_{10}^{14+}$, 947.3], 865.0 [**G4⊂5.2**$(NTf_2)_9^{15+}$, 865.5], 793.5 [**G4⊂5.2**$(NTf_2)_8^{16+}$, 793.9], 730.4 [**G4⊂5.2**$(NTf_2)_7^{17+}$, 730.7]. **HR-ESI-MS**: *m/z* calculated for **G4⊂5.2**$(NTf_2)_{13}^{11+}$ = 1282.0630, observed = 1282.0686.

5.6.5 Synthesis and characterisation of (G1)$_2$·G2$^+$⊂5.2

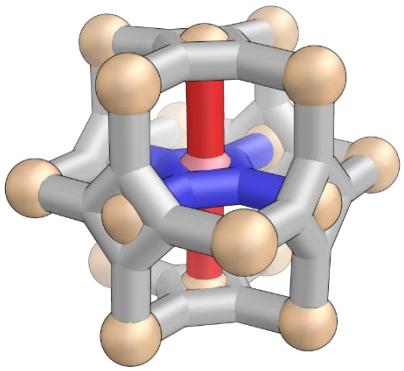

A sample of (**G1**)$_2$·**G2**⊂**5.2** (prepared from the addition of five equivalents of **G1** to a solution of **G2**⊂**5.2** in MeCN) was stirred in an open aired vessel at room temperature for 3 days. The host-guest complex was precipitated with Et_2O to remove excess 4,4'-bipyridine. T(he mixture was centrifuged, the supernatant decanted, and the solid dried under a stream of N_2 to furnish (**G1**)$_2$·**G2**$^+$⊂**5.2**. **^{1}H NMR** (400 MHz, 298 K, CD_3CN): δ 9.57 (s, 8H), 9.43 – 9.36 (m, 16H), 9.34 (d, *J* = 8.2 Hz, 8H), 9.22 (s, 8H), 9.18 (s, 8H), 9.01 (d, *J* = 8.1 Hz, 8H), 8.97 – 8.91 (m, 16H), 8.90 – 8.86 (m, 16H), 8.80 (d, *J* = 8.4 Hz, 8H), 8.70 (d, *J* = 4.8 Hz, 8H), 8.68 (d, 8H), 8.62 (d, *J* = 4.8 Hz, 8H), 8.60 – 8.54 (m, 16H), 8.50 – 8.38 (m, 64H), 8.16 (d, *J* = 4.5 Hz, 8H), 8.07 – 7.88 (m, 32H), 7.79 (d, *J* = 8.4 Hz, 8H), 7.75 (d, *J* = 8.4 Hz, 8H), 7.68 (d, *J* = 8.3 Hz, 8H), 7.63 (d, *J* = 8.7 Hz, 8H), 7.43 (d, *J* = 8.2 Hz, 8H), 7.20 (d, *J* = 8.4 Hz, 8H), 7.02 (d, *J* = 8.2 Hz, 8H), 6.83 (d, *J* = 8.1 Hz, 8H), 6.62 (s, 8H), 6.41 (d, *J* = 8.4 Hz, 8H), 6.17 – 6.02 (m, 16H), 5.62 (d, *J* = 5.3 Hz, 8H), 3.92 (d, *J* = 6.0 Hz, 4H), 3.17 (d, *J* = 6.4 Hz, 4H), 2.05 (d, *J* = 5.7 Hz, 8H), 0.74 (d, *J* = 6.4 Hz, 4H), –1.92 (d, *J* = 5.7 Hz, 8H) ppm. See Figure 5.24 for full proton assignment. **LR-ESI-MS** [charge, calculated for (**G1**)$_2$·**G2**⊂**5.2**$(NTf_2)_{25}$]: *m/z* = 1694.3 [(**G1**)$_2$·**G2**⊂**5.2**$(NTf_2)_{16}^{9+}$, 1694.3], 1496.6 [(**G1**)$_2$·**G2**⊂**5.2**$(NTf_2)_{15}^{10+}$, 1496.9], 1335.0 [(**G1**)$_2$·**G2**⊂**5.2**$(NTf_2)_{14}^{11+}$, 1335.3], 1200.4 [(**G1**)$_2$·**G2**⊂**5.2**$(NTf_2)_{13}^{12+}$, 1200.7], 1086.6 [(**G1**)$_2$·**G2**⊂**5.2**$(NTf_2)_{12}^{13+}$, 1086.8], 989.0 [(**G1**)$_2$·**G2**⊂**5.2**$(NTf_2)_{11}^{14+}$, 989.2], 904.2 [(**G1**)$_2$·**G2**⊂**5.2**$(NTf_2)_{10}^{15+}$, 904.5], 830.2

[(**G1**)$_2$·**G2**⊂**5.2**(NTf$_2$)$_9$$^{16+}$, 830.5]. **HR-ESI-MS**: *m/z* calculated for (**G1**)$_2$·**G2**⊂**5.2**(NTf$_2$)$_{12}$$^{13+}$ = 1086.7630, observed = 1086.7675.

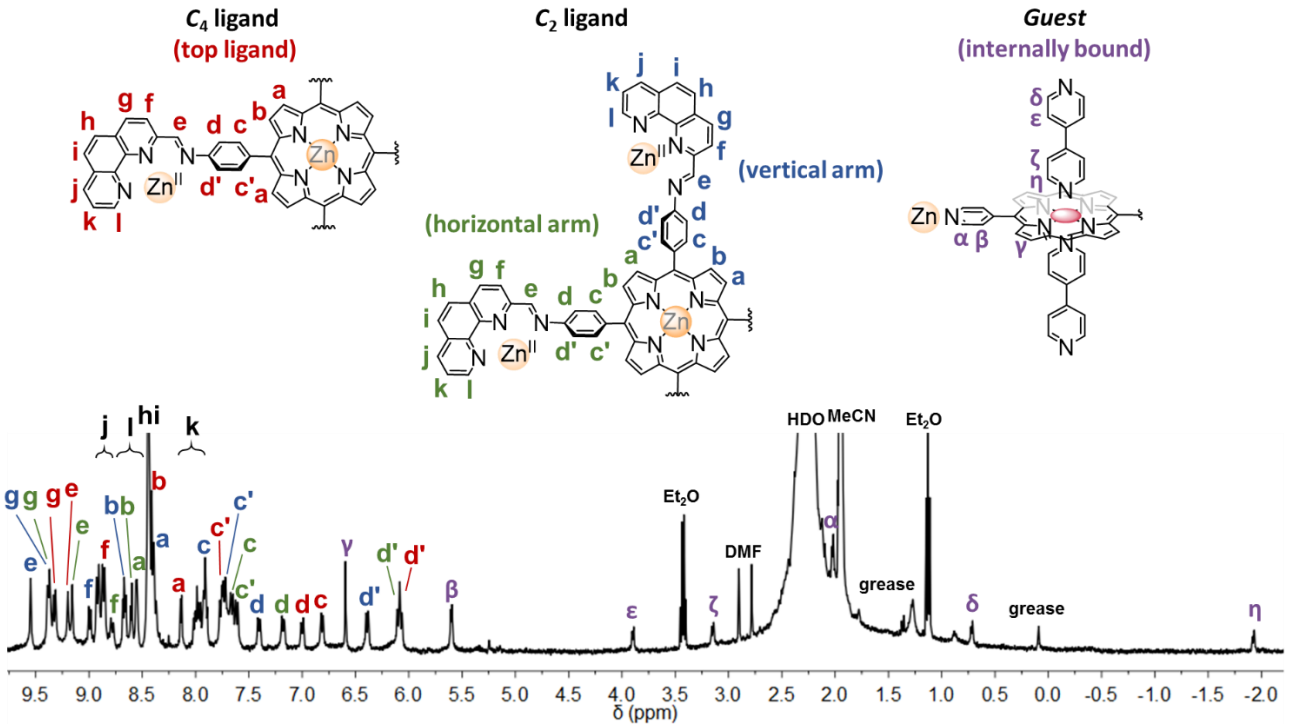

Figure 5.24 | ^{1}H NMR spectrum (400 MHz, 298 K, CD$_3$CN) of (**G1**)$_2$·**G2**$^+$⊂**5.2** with signal assignment.

5.6.6 Synthesis and characterisation G6⊂5.2

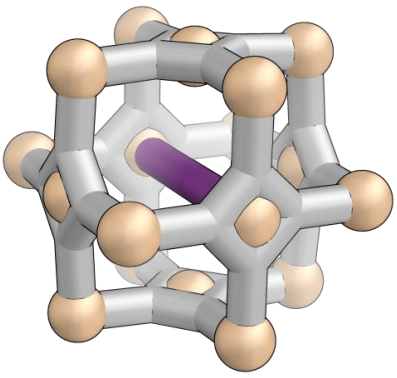

A solid sample of **G6** (*ca.* 3 mg, excess) was added to a solution of **5.2** (5.00 mg) in CD$_3$CN (0.6 mL) and heated at 343 K for 16 h. The solution was filtered and spectra recorded directly without further purification. **^{1}H NMR** (500 MHz, 298/233 K, CD$_3$CN): broad; *endo*-guest signals appear at 4.72 and 1.89 ppm at 298 K; *exo*-guest signals appear at 6.65 and 6.06 ppm upon cooling to 233 K. **LR-ESI-MS** [charge, calculated for **G6**⊂**5.2**(NTf$_2$)$_{24}$]: *m/z* = 1599.5 [**G6**⊂**5.2**(NTf$_2$)$_{15}$$^{9+}$, 1600.1], 1411.6 [**G6**⊂**5.2**(NTf$_2$)$_{14}$$^{10+}$, 1412.1], 1258.2 [**G6**⊂**5.2**(NTf$_2$)$_{13}$$^{11+}$, 1258.3], 1129.9 [**G6**⊂**5.2**(NTf$_2$)$_{12}$$^{12+}$, 1130.1], 1021.3 [**G6**⊂**5.2**(NTf$_2$)$_{11}$$^{13+}$, 1021.6], 928.4 [**G6**⊂**5.2**(NTf$_2$)$_{10}$$^{14+}$, 928.6], 847.7 [**G6**⊂**5.2**(NTf$_2$)$_9$$^{15+}$, 848.0] 777.5 [**G6**⊂**5.2**(NTf$_2$)$_8$$^{11+}$, 777.5]. **HR-ESI-MS**: *m/z* calculated for **G6**⊂**5.2**(NTf$_2$)$_{13}$$^{11+}$ = 1316.1757, observed = 1316.1814.

5.6.7 Synthesis and characterisation of encapsulated rotaxanes

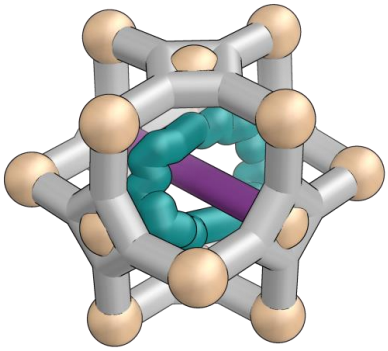

General procedure: To a solution of **G6⊂2** in CD_3CN (0.6 mL) was added a solid sample of either **G7** or **G8** (*ca.* 3 mg, excess). The mixture was heated at 343 K for 16 h. Upon cooling, the sample was centrifuged and the supernatant collected. A solid sample could be collected by precipitation with Et_2O. Note: the binding of more than one rotaxane guest was consistently observed by ESI-MS, suggesting that, while one rotaxane bound internally, several others were bound in a monodentate fashion at the *exo*-Zn^{II} sites of $\mathbf{L^{5B}}$. This is consistent with the NMR data, where 'free' macrocycle signals were shifted slightly from their free values, suggesting a weak interaction around the periphery of the cages.

G7·G6⊂5.2: **^{1}H NMR** (500 MHz, 298 K, CD_3CN): broad; see Figure 5.21a for signal assignment. **LR-ESI-MS** [charge, calculated for **G7·G6⊂5.2**$(NTf_2)_{24}$]: *m/z* = 1670.8 [**G7·G6⊂5.2**$(NTf_2)_{15}^{9+}$, 1670.9], 1475.6 [**G7·G6⊂5.2**$(NTf_2)_{14}^{10+}$, 1475.8], 1316.0 [**G7·G6⊂5.2**$(NTf_2)_{13}^{11+}$, 1316.2], 1183.0 [**G7·G6⊂5.2**$(NTf_2)_{12}^{12+}$, 1183.1], 1070.5 [**G7·G6⊂5.2**$(NTf_2)_{11}^{13+}$, 1070.6], 974.0 [**G7·G6⊂5.2**$(NTf_2)_{10}^{14+}$, 974.1], 890.2 [**G7·G6⊂5.2**$(NTf_2)_9^{15+}$, 890.5]. Note: these are only those signals attributed to **G7·G6⊂5.2**$(NTf_2)_{24}$; several signals corresponding to **(G7)$_x$·(G6)$_y$⊂5.2**$(NTf_2)_{24}$ were also observed. **HR-ESI-MS**: *m/z* calculated for **G7·G6⊂5.2**$(NTf_2)_{13}^{11+}$ = 1316.0849, observed = 1316.0907.

G8·G6⊂5.2: **^{1}H NMR** (500 MHz, 298 K, CD_3CN): δ 9.47 – 9.46 (m, 16H), 9.42 (s, 8H), 9.37 (d, J = 8.1 Hz, 8H), 9.34 – 9.29 (m, 16H), 8.97 (d, J = 8.2 Hz, 8H), 8.92 (dd, J = 8.7, 1.9 Hz, 8H), 8.89 (d, J = 8.4 Hz, 8H), 8.88 – 8.83 (m, 24H), 8.73 (dd, J = 4.7 Hz, 8H), 8.60 – 8.54 (m, 16H), 8.52 (dd, J = 4.9, 2.0 Hz, 8H), 8.43 – 8.37 (m, 24H), 8.35 (d, J = 4.8 Hz, 8H), 8.31 (d, J = 4.7 Hz, 8H), 8.22 (s, 4H), 7.95 – 7.84 (m, 24H), 7.81 (d, J = 8.2 Hz, 8H), 7.71 (d, J = 8.2 Hz, 8H), 7.63 (d, J = 8.6 Hz, 8H), 7.61 – 7.54 (m, 24H), 7.32 (d, J = 8.1 Hz, 8H), 7.29 (d, J = 7.6 Hz, 8H), 7.23 (d, J = 8.1 Hz, 8H), 6.37 (d, J = 8.1 Hz, 8H), 6.31 (d, J = 8.0 Hz, 8H), 6.27 (d, J = 8.4 Hz, 8H), 4.78 (dd, J = 6.4 Hz, 4H), 1.88 (d, J = 5.6 Hz, 4H). Hydrogen environments are only listed for the cage architecture and bound **G6** guest. Those attributed to **G8** were too weak or broad to be accurately assigned. Signals attributed to **G8** bound in fast exchange were observed at δ 7.51 (d, J = 8.7 Hz), 7.49 (d, J = 9.8 Hz), 7.17 (d, J = 8.1 Hz), 7.14 (d, J = 7.9 Hz), 7.12 – 7.05 (m), 6.58 (d, J = 7.7 Hz), 6.53 (d, J = 7.7 Hz), 4.13 (dt, J = 13.7, 4.4 Hz), 4.01 (dt, J = 9.8, 4.4 Hz), 3.89 (s), 3.84 (dt, J = 10.9, 4.1 Hz), 3.73 (ddt, J = 7.3, 4.4, 2.3 Hz), 3.68 (d, J = 5.3 Hz), 3.65 – 3.60 (m) ppm. See Figure 5.21b for signal assignment. **LR-ESI-MS** [charge, calculated for **G8·G6⊂5.2**$(NTf_2)_{24}$]: *m/z* = 1676.9 [**G8·G6⊂5.2**$(NTf_2)_{15}^{9+}$,

1677.3], 1481.2 [**G8·G6⊂5.2**$(NTf_2)_{14}^{10+}$, 1481.6], 1320.9 [**G8·G6⊂5.2**$(NTf_2)_{13}^{11+}$, 1321.4], 1187.9 [**G8·G6⊂5.2**$(NTf_2)_{12}^{12+}$, 1188.0], 1075.0 [**G8·G6⊂5.2**$(NTf_2)_{11}^{13+}$, 1075.0], 978.2 [**G8·G6⊂5.2**$(NTf_2)_{10}^{14+}$, 978.2]. **HR-ESI-MS**: *m/z* calculated for **G8·G6⊂5.2**$(NTf_2)_{13}^{11+}$ = 1321.4490, observed = 1321.4587.

5.6.8 Crystallography

The crystals employed in this Chapter rapidly lost solvent after removal from the mother liquor and rapid handling prior to flash cooling in the cryostream was required to collect data. Due to the less than ideal resolution, bond lengths and angles within pairs of organic ligands were restrained to be similar to each other (SAME) and thermal parameter restraints (SIMU, DELU) were applied to all non-metal atoms to facilitate anisotropic refinement. Ligand-based atoms that still displayed thermal parameters greater than 0.5 were further refined to approximate isotropic behaviour (ISOR). In all cases, the remaining anions present in the asymmetric unit could not be successfully assigned despite numerous attempts at modelling, including the use of rigid bodies. Consequently, the SQUEEZE[29] function of PLATON[30] was employed to remove the contribution of the electron density associated with these anions and the remaining highly disordered solvent molecules.

*5.6.8.1 Crystal structure of **5.1**·24OTf·12benzene*

Formula $C_{600}H_{396}Cd_{12}F_{72}N_{84}O_{120}Rh_{12}S_{24}$, *M* 15423.14, Cubic, *Pn*3–, *a* 37.6891(15) Å, *V* 53536(6) $Å^3$, D_c 0.957 g cm^{-3}, *Z* 2, crystal size 0.450 by 0.280 by 0.040 mm, colour yellow, habit plate, temperature 180(2) Kelvin, λ(CuKa) 1.54178 Å, μ(CuKa) 4.281 mm^{-1}, $T(SADABS)_{min,max}$ 0.4341, 0.7472, $2\theta_{max}$ 72.76, *hkl* range –28 9, –23 28, –29 27, *N* 37272, N_{ind} 4255(R_{merge} 0.0701), N_{obs} 3010(I > 2σ(I)), N_{var} 546, residuals* *R*1(*F*) 0.1231, *wR*2(F^2) 0.3559, GoF(all) 1.083, $\Delta\rho_{min,max}$ –0.815, 0.647 e^- $Å^{-3}$, CCDC 1830497. *$R1 = \Sigma||F_o| - |F_c||/\Sigma|F_o|$ for $F_o > 2\sigma(F_o)$; $wR2 = (\Sigma w(F_o^2 - F_c^2)^2/\Sigma(wF_c^2)^2)^{1/2}$ all reflections $w=1/[\sigma^2(F_o^2)+(0.1310P)^2+1894.0724P]$ where $P=(F_o^2 + 2F_c^2)/3$

Special refinement details

Crystals of **5.1**·24OTf·12benzene were grown by slow diffusion of benzene into a CD_3CN solution of **5.1**$(OTf)_{24}$. Despite the use of high intensity laboratory source radiation, few reflections at greater than 1.3 Å resolution were observed; nevertheless, the quality of the data is more than sufficient to establish the connectivity of the structure.

Due to the less than ideal resolution, extensive restraints were required to facilitate realistic modelling for the organic parts of the structure. The GRADE[31] program was employed using the GRADE Web Server[32] to generate a full set of bond distance and angle restraints (DFIX, DANG, FLAT) for the organic ligands.

The SQUEEZEd portion of the structure totals 7,261 electrons per unit cell, corresponding to a solvent accessible void of 33,081 Å^3 per unit cell. This accounts for all 24 molecules of OTf^- (each with 73 electrons = 1,752 electrons) for each molecule of **5.1**, where $Z = 2$. The extra 3,757 electrons per unit cell are attributed to unresolved solvent molecules (benzene and MeCN).

*5.6.8.2 Crystal structure of [Cd(pyrazine)$_5$(H$_2$O)]⊂**5.1**·3.3pyrazine·H$_2$O·24CB$_{11}$H$_{12}$·2OTf· 36.7MeCN· 38benzene*

Formula $C_{840.60}H_{951.30}B_{264}Cd_{13}F_6N_{125.30}O_{56}Rh_{12}S_2$, *M* 19433.99, Monoclinic, *C*2/*c* (#15), *a* 52.809(11), *b* 37.841(8), *c* 55.765(11) Å, *b* 107.03(3), *V* 106548(41) Å^3, D_c 1.212 g cm^{-3}, *Z* 4, crystal size 0.070 by 0.050 by 0.040 mm, colour dark orange, habit block, temperature 100(2) Kelvin, λ(synchrotron) 0.6889 Å, μ(synchrotron) 0.454 mm^{-1}, T(xia2)$_{min,max}$ 0.9123, 1.0, $2\theta_{max}$ 45.00, *hkl* range –58 58, –42 42, –61 61, *N* 432597, N_{ind} 76150(R_{merge} 0.0997), N_{obs} 55249(I > 2σ(I)), N_{var} 6913, residuals* *R*1(*F*) 0.1161, *wR*2(F^2) 0.3745, GoF(all) 1.122, $\Delta\rho_{min,max}$ –1.258, 3.508 e$^-$ Å^{-3}, CCDC 1830496. *$R1 = \Sigma||F_o| - |F_c||/\Sigma|F_o|$ for $F_o > 2\sigma(F_o)$; $wR2 = (\Sigma w(F_o^2 - F_c^2)^2/\Sigma(wF_c^2)^2)^{1/2}$ all reflections $w=1/[\sigma^2(F_o^2)+(0.2000P)^2+1200.0000P]$ where $P=(F_o^2 + 2F_c^2)/3$

Special refinement retails

Crystals of [Cd(pyrazine)$_5$(H$_2$O)]⊂**5.1**·3.3pyrazine·H$_2$O·24CB$_{11}$H$_{12}$·2OTf·36.7MeCN· 38benzene were grown by slow diffusion of benzene into a CD$_3$CN solution of **5.1**(OTf)$_{24}$ containing excess CsCB$_{11}$H$_{12}$, Cd(OTf)$_2$ and pyrazine. Despite the use of synchrotron radiation, few reflections at greater than 0.9 Å resolution were observed; nevertheless, the quality of the data is more than sufficient to establish the connectivity of the structure and the identity of the encapsulated compound.

The Cd(H$_2$O) portion of the encapsulated complex was modelled as disordered over two positions with the distance between Cd and H$_2$O molecules restrained to be similar over the disordered parts (SADI). On two *exo*-Rh sites, pyrazine and MeCN were modelled as disordered over the same position; the occupancies of these molecules were allowed to freely refine and were then fixed at the nearest 0.05. Angles and distances in all *exo*-bound pyrazines were restrained (DFIX, DANG). One coordinated pyrazine molecule sitting on a symmetry position was modelled as disordered over three sites; the hydrogens on the disordered part could not be accurately identified and were thus omitted

from the model. Hydrogens on all water molecules were identified firstly from the electron density map and then restrained to approximate the angles of H_2O (DANG, DFIX). A small portion of disorder was modelled for the phenanthroline moiety beginning C360.

Five carborate anions showed a significant amount of thermal motion; the SAME command was applied to all twelve unique anions to approximate icosahedral symmetry and realistically model these anions. Given the 12-fold-symmetric disorder of the carbon atom in $CB_{11}H_{12}^-$, all twelve atoms were assigned as boron; there was no indication that one of the atoms was carbon outright. Four $CB_{11}H_{12}^-$ anions were modelled as disordered over two positions; one $CB_{11}H_{12}^-$ anion was modelled with half occupancy. All benzene molecules were restrained as rigid hexagons with AFIX 66; eight benzenes were modelled as disordered over two positions; six were modelled with half occupancy.

The SQUEEZEd portion of the structure totals 2,764 electrons per unit cell, corresponding to a solvent accessible void of 10,471 $Å^3$ per unit cell. This accounts for the remaining molecule of $CB_{11}H_{12}^-$ (with 73 electrons) for each molecule of **1**, where $Z = 4$. The extra 2,472 electrons per unit cell are attributed to unresolved solvent molecules (benzene and MeCN). All significant residual peaks are located in unrealistic chemical positions near Cd or Rh atoms, presumably arising from absorption effects.

5.7 References

[1] Haas, K.L. and Franz, K.J., *Chem. Rev.*, **2009**, 109, 4921-4960.

[2] Liu, C., Colón, B.C., Ziesack, M., Silver, P.A., and Nocera, D.G., *Science*, **2016**, 352, 1210-1213.

[3] Ohata, J. and Ball, Z.T., *J. Am. Chem. Soc.*, **2017**, 139, 12617-12622.

[4] Ruiz-Castillo, P. and Buchwald, S.L., *Chem. Rev.*, **2016**, 116, 12564-12649.

[5] Rodríguez-Jiménez, S., Feltham, H.L.C., and Brooker, S., *Angew. Chem. Int. Ed.*, **2016**, 55, 15067-15071.

[6] Cambridge Crystallographic Database Centre (CCDC), <https://ccdc.cam.ac.uk/> accessed 26 February 2018.

[7] Tranchemontagne, D.J., Mendoza-Cortes, J.L., O'Keeffe, M., and Yaghi, O.M., *Chem. Soc. Rev.*, **2009**, 38, 1257-1283.

[8] Otto, S., Furlan, R.L.E., and Sanders, J.K.M., *Science*, **2002**, 297, 590-593.

[9] Ramsay, W.J., Ronson, T.K., Clegg, J.K., and Nitschke, J.R., *Angew. Chem. Int. Ed.*, **2013**, 52, 13439-13443.

[10] Sanada, K., Ube, H., and Shionoya, M., *J. Am. Chem. Soc.*, **2016**, 138, 2945-2948.

[11] Amo-Ochoa, P., Jiménez-Aparicio, R., Perles, J., Torres, M.R., Gennari, M., and Zamora, F., *Cryst. Growth & Design*, **2013**, 13, 4977-4985.

[12] Favarger, F., Goujon-Ginglinger, C., Monchaud, D., and Lacour, J., *J. Org. Chem.*, **2004**, 69, 8521-8524.

[13] Kramer, R., Lehn, J.M., and Marquis-Rigault, A., *Proc. Natl. Acad. Sci. USA*, **1993**, 90, 5394-5398.

[14] Chen, L., Khadivi, A., Singh, M., and Jurss, J.W., *Inorg. Chem. Frontiers*, **2017**, 4, 1649-1653.

[15] Miller, R.G. and Brooker, S., *Chem. Sci.*, **2016**, 7, 2501-2505.

[16] Stang, P.J., Cao, D.H., Saito, S., and Arif, A.M., *J. Am. Chem. Soc.*, **1995**, 117, 6273-6283.

[17] Kumazawa, K., Biradha, K., Kusukawa, T., Okano, T., and Fujita, M., *Angew. Chem. Int. Ed.*, **2003**, 42, 3909-3913.

[18] Kitazawa, T., Gomi, Y., Takahashi, M., Takeda, M., Enomoto, M., Miyazaki, A., and Enoki, T., *J. Mater. Chem.*, **1996**, 6, 119-121.

[19] Liu, D., Liu, Q., Li, Y., Wang, M., Yang, X., Wu, T., Moorefield, C., Wang, P., and Newkome, G.R., *Dalton Trans.*, **2015**, 44, 11269-11273.

[20] Carlucci, L., Ciani, G., Proserpio, D.M., and Sironi, A., *Angew. Chem. Int. Ed.*, **1995**, 34, 1895-1898.

[21] Kleywegt, G.J. and Jones, T.A., *Acta Crystallogr. Sect. D-Biol. Crystallogr.*, **1994**, 50, 178-185.

[22] Sanders, J.K.M., Bampos, N., Clyde-Watson, Z., Darling, S.L., Hawley, J.C., Kim, H.-J., Mak, C.C., and Webb, S.J., *Axial coordination chemistry of metalloporphyrins*, in *The Porphyrin Handbook*, K.M. Kadish, K.M. Smith, and R. Guilard, Editors. 2000, Academic Press: London, UK. p. 1-48.

[23] Kadish, K.M., Bottomley, L.A., and Beroiz, D., *Inorg. Chem.*, **1978**, 17, 1124-1129.

[24] Piguet, C., *J. Chem. Educ.*, **1997**, 74, 815.

[25] Heitmann, G., Schütt, C., and Herges, R., *Eur. J. Inorg. Chem.*, **2016**, 2016, 3817-3823.

[26] Bruns, C.J. and Stoddart, J.F., *The nature of the mechanical bond: from molecules to machines*. 2017, New Jersey: John Wiley & Sons, Inc.

[27] Dominguez, Z., Dang, H., Strouse, M.J., and Garcia-Garibay, M.A., *J. Am. Chem. Soc.*, **2002**, 124, 2398-2399.

[28] Day, A.I., Blanch, R.J., Arnold, A.P., Lorenzo, S., Lewis, G.R., and Dance, I., *Angew. Chem. Int. Ed.*, **2002**, 41, 275-277.

[29] Spek, A.L., *Acta Crystallogr. Sect C*, **2015**, 71, 9-18.

[30] Spek, A.L., *Acta Crystallogr. Sect. D*, **2009**, 65, 148-155.

[31] Bricogne, G., Blanc, E., Brandle, M., Flensburg, C., Keller, P., Paciorek, W., Roversi, P., Sharff, A., Smart, O.S., Vonrhein, C., and Womack, T.O., BUSTER 2.11.12 ed., Global Phasing Ltd., Cambridge, United Kingdom, 2011.

[32] Smart, O.S. and Womack, T.O., GRADE Web Server, Global Phasing Ltd., 2014.

Chapter 6

Integrative self-sorting to express a steroid-binding, heteroleptic triangular prism

6.1 Advantages of heteroleptic structures

Natural products are generally enantiopure with a low-symmetry structure. A cage designed to bind an asymmetric guest should ideally have a low-symmetry cavity, or else rely on site-specific interactions between host and guest molecules to enforce binding.[1,2] Homoleptic capsules often generate highly symmetric voids; heteroleptic cages, on the other hand, often have less symmetric cavities due to the incorporation of two or more different ligand symmetries and/or sizes.[3-5]

A prime advantage of heteroleptic architectures is that their cavities are enclosed by more than one type of surface (*i.e.*, more than one ligand). It was thus hypothesised that heteroleptic architectures may provide a route towards generating systems whereby either multiple internal binding events, or combined internal/external binding events, could be modulated, based on the differential interactions of guests with the different ligand surfaces of the cage. In particular, it was predicted that employing units capable of structural adaptation may lead to 'breathable' structures, wherein internal binding would cause a significant structural distortion that resulted in modular binding around the periphery of the cage. It was proposed that, in complement to the procedure discussed in Chapter Four, cavities able to alter their size and shape in response to guest binding events would provide a new route to the modulation of binding cooperativity.

6.2 Investigations into the sorting of polydentate, polytopic systems

Four supramolecular assemblies, each of a distinct shape, can be assembled by employing either threefold- or fourfold-symmetric subcomponents (**6A** and **6B**, respectively) with either 2-formylpyridine or 2-formylphenanthroline, and Co^{II}. The generation of tetrahedral $Co^{II}_4L_4$, octahedral $Co^{II}_6L_4$, cubic $Co^{II}_8L_6$ and cuboctahedral $Co^{II}_{12}L_6$ assemblies (**6.1-6.4**, respectively[6-9]) can thus be achieved by careful consideration of the topicity and denticity of ligand chelation vectors (Figure 6.1).

In light of the distinct geometries produced by these assembly reactions, systems wherein both bidentate and tridentate ligands were formed simultaneously – that is, wherein both 2-formylpyridine and 2-formylphenanthroline were employed with either threefold- or fourfold-symmetric amine subcomponents – were explored. When a single amine subcomponent (**6A** or **6B**) was mixed with both 2-formylphenanthroline and 2-formylpyridine in the presence of Co^{II} salts, the individual ligands self-recognised, generating two distinct shapes: employing triamine **6A** produced homoleptic **6.1** and **6.2**; using tetramine **6B** yielded homoleptic **6.3** and **6.4** as the exclusive products in CH_3CN by both ESI-MS and ^{1}H NMR spectroscopy (Figure 6.2).

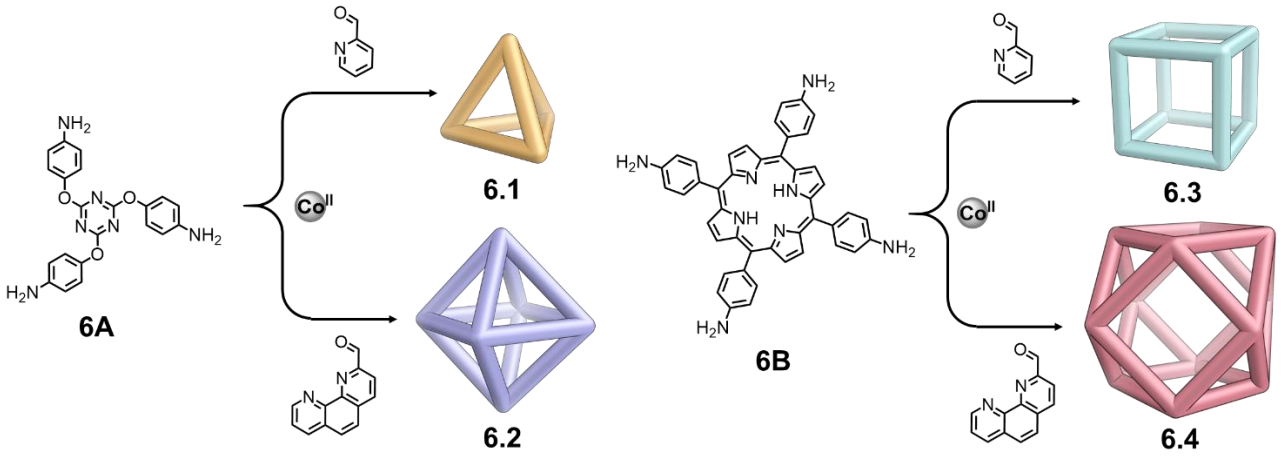

Figure 6.1 | Four different architectures can be synthesised by using a single amine subcomponent (**6A** or **6B**), a single aldehyde subcomponent (2-formylpyridine or 2-formylphenantholine) and Co^{II}: $Co^{II}_4L_4$ tetrahedron **6.1**, $Co^{II}_6L_4$ octahedron **6.2**, $Co^{II}_8L_6$ cube **6.3** and $Co^{II}_{12}L_6$ cuboctahedron **6.4**.

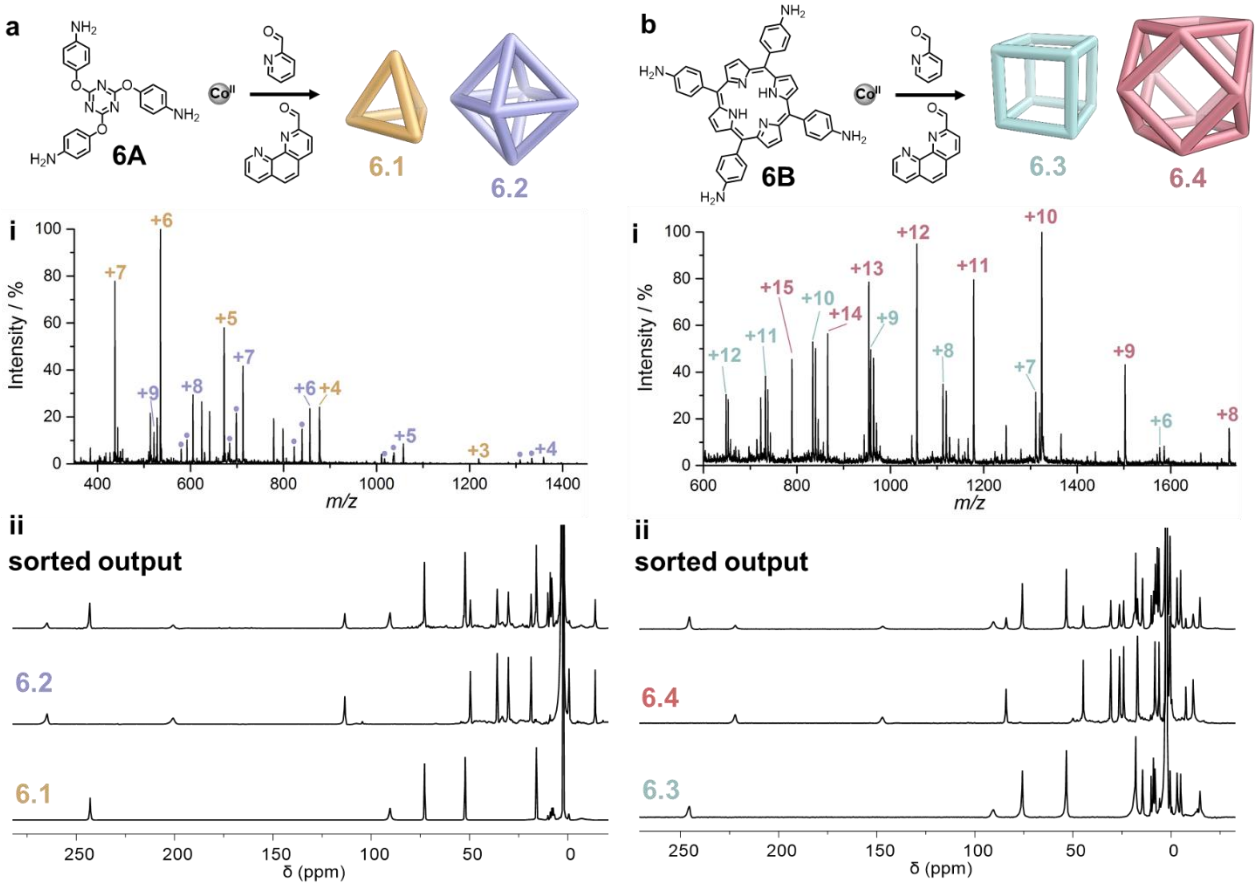

Figure 6.2 | Narcissistic self-sorting was observed when two different aldehyde subcomponents were both employed with either **a**, **6A** or **b**, **6B** during self-assembly, as observed by (i) ESI-MS and (ii) wide sweep ^{1}H NMR spectroscopy (400 MHz, 298 K, CD_3CN). Purple circles in **ai** show anion exchange of OTf^- for ClO_4^-.

6.3 *Generating heteroleptic structures*

Markedly different behaviour was observed when only a single aldehyde subcomponent was used with both amine subcomponents (**6A** and **6B**) and Co^{II}. When triamine and tetramine subcomponents were combined with 2-formylpyridine in a 1:1 mixture of DMF:MeCN, only the tetrahedron and cube were observed; however, when pure MeCN was used as the reaction solvent, a third product corresponding to a heteroleptic $Co^{II}\mathbf{L}^{6A}{}_2\mathbf{L}^{6B}{}_3$ assembly was also observed by ESI-MS (Figure 6.3). This solvent dependence may be attributed to the higher solubility (and better stability) of porphyrin-derived cubes in DMF as compared to CH_3CN.[8]

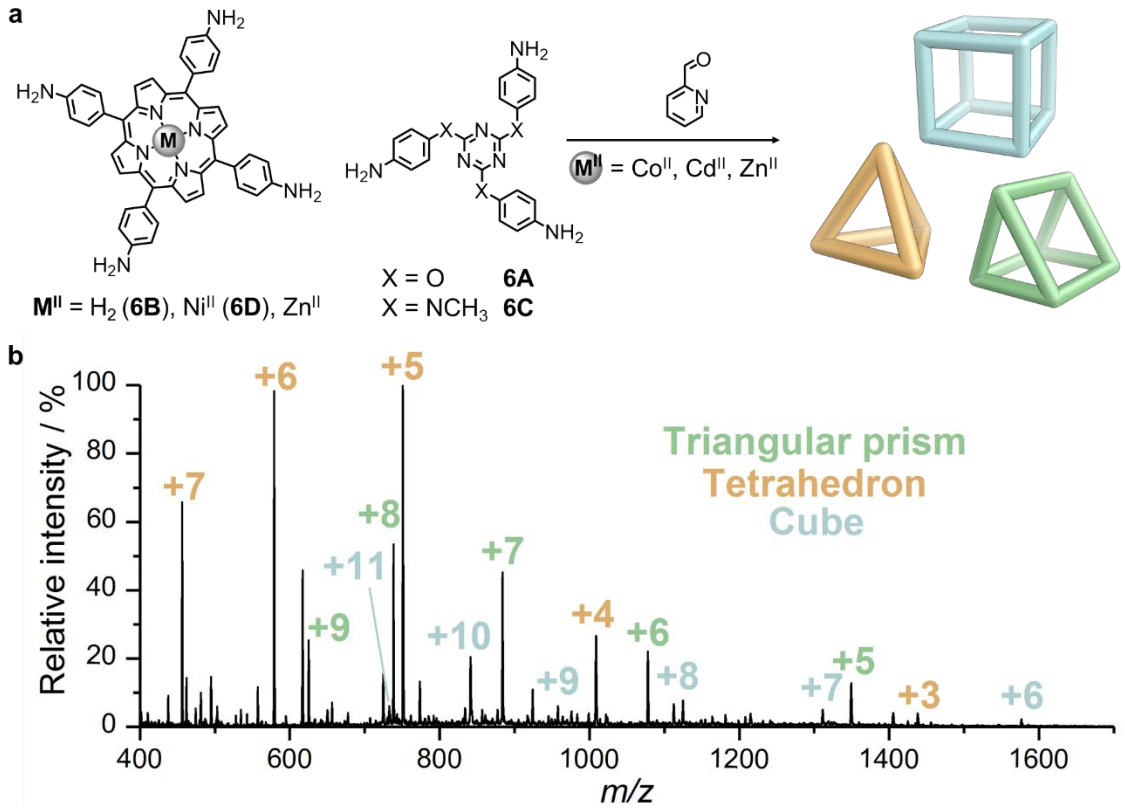

Figure 6.3 | **a**, Product mixtures showed either only the homoleptic produces, or mixtures of homoleptic and heteroleptic products, when three- and four-fold symmetric ligands were combined in the presence of 2-formylpyridine and octahedrally-directing metal ions. **b**, ESI mass spectra of the product mixture obtained when **6A**, **6B**, 2-formylpyridine and Co^{II} were employed during self-assembly in MeCN.

Employing **6C** in place of **6A** in the assembly process was observed to generate a similar distribution of species at 70 ºC. The slow diffusion of diethyl ether into a solution of this mixture generated single crystals of $Co^{II}\mathbf{L}^{6C}{}_2\mathbf{L}^{6B}{}_3$ assembly **6.5**, a heteroleptic complex with the morphology of a triangular prism (Figure 6.4). The structure consists of three porphyrin units, forming the square faces of the prism, and two triamine units, which cap the triangular ends of the structure. The ability for the arms of $\mathbf{L}^{6B}$ and $\mathbf{L}^{6C}$ to span similar metal-metal distances appears to enable this geometry. Each Co^{II} corner has *facial* stereochemistry, and all six metal centres are either all-Δ or all-Λ, rendering the structure chiral, with non-crystallographic D_3 symmetry.

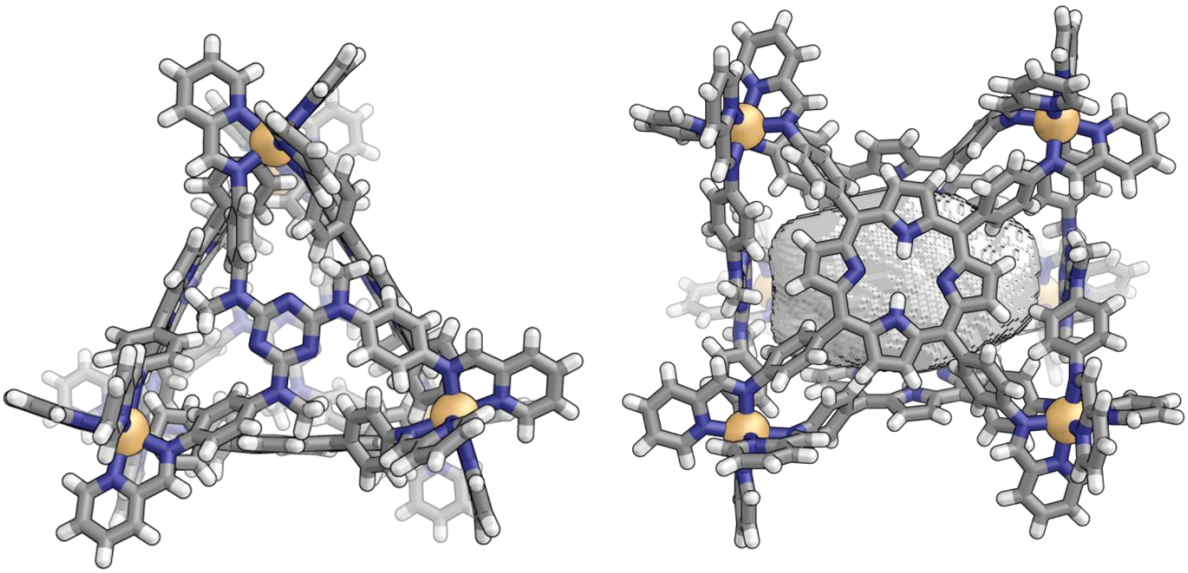

Figure 6.4 | X-ray crystal structure of **6.5**, viewed perpendicular to the threefold (left) and fourfold (right) ligands. Void space inside the structure is displayed as a grey solid (Co – orange, C – grey, N – blue, H – white).

Having confirmed the geometry of the heteroleptic species generated by the reaction of three- and fourfold-symmetric components, experiments were undertaken to improve its abundance in solution by modulating its system components: using different metal vertices, or employing either **6A** or geometric congener **6C**, and either Ni^{II}-, Zn^{II}- or H_2-centered derivatives of **6B**. ESI-MS consistently confirmed the presence of the triangular prism in solution, along with the presence of tetrahedra and cubes, even when the ^{1}H NMR spectra of these assemblies were broad (Figure 6.3a).

In only one instance could the triangular prism be produced as the unique species. When **6C**, Ni-centred porphyrin **6D** and Zn^{II} subcomponents were heated at 70 ºC for 16 h, triangular prism **6.8** was observed as the sole product. During optimisation, it was observed that the generation of the homo- *vs.* the hetero-leptic products of this reaction was temperature dependent; heating the same reaction mixture at 50 ºC produced an ^{1}H NMR spectrum wherein all three products (tetrahedron **6.6**, cube **6.7** and triangular prism **6.8**) were observed. At low temperatures, the homoleptic products were favoured; at high temperatures, the heteroleptic product was favoured (Figure 6.5).

A Van't Hoff analysis of the equilibrium between the heteroleptic and homoleptic structures indicated that the generation of the triangular prism was an entropically favourable process, wherein $\Delta H = +68 \pm 7$ kJ mol^{-1} and $\Delta S = +0.24 \pm 0.02$ kJ mol^{-1} (Figure 6.6). Subsequent crystallographic investigations revealed that the Ni^{II} porphyrins in **6.8** could exist in two bent conformations.[10] As Ni^{II} porphyrin units exist exclusively in a flat conformation within **6.7**,[8] the higher degree of conformational freedom in **6.8** as compared to **6.7** renders the triangular prism entropically favourable. This entropically-driven process defines a new mode of heteroleptic self-assembly: while the number of components and bonds broken/formed remain the same in both directions of the

equilibrium, the conformational freedom of the ligands in **6.8** provides an entropic driving force for its assembly. The differential solvation characteristics of the cavities may also contribute to this entropic driving force.

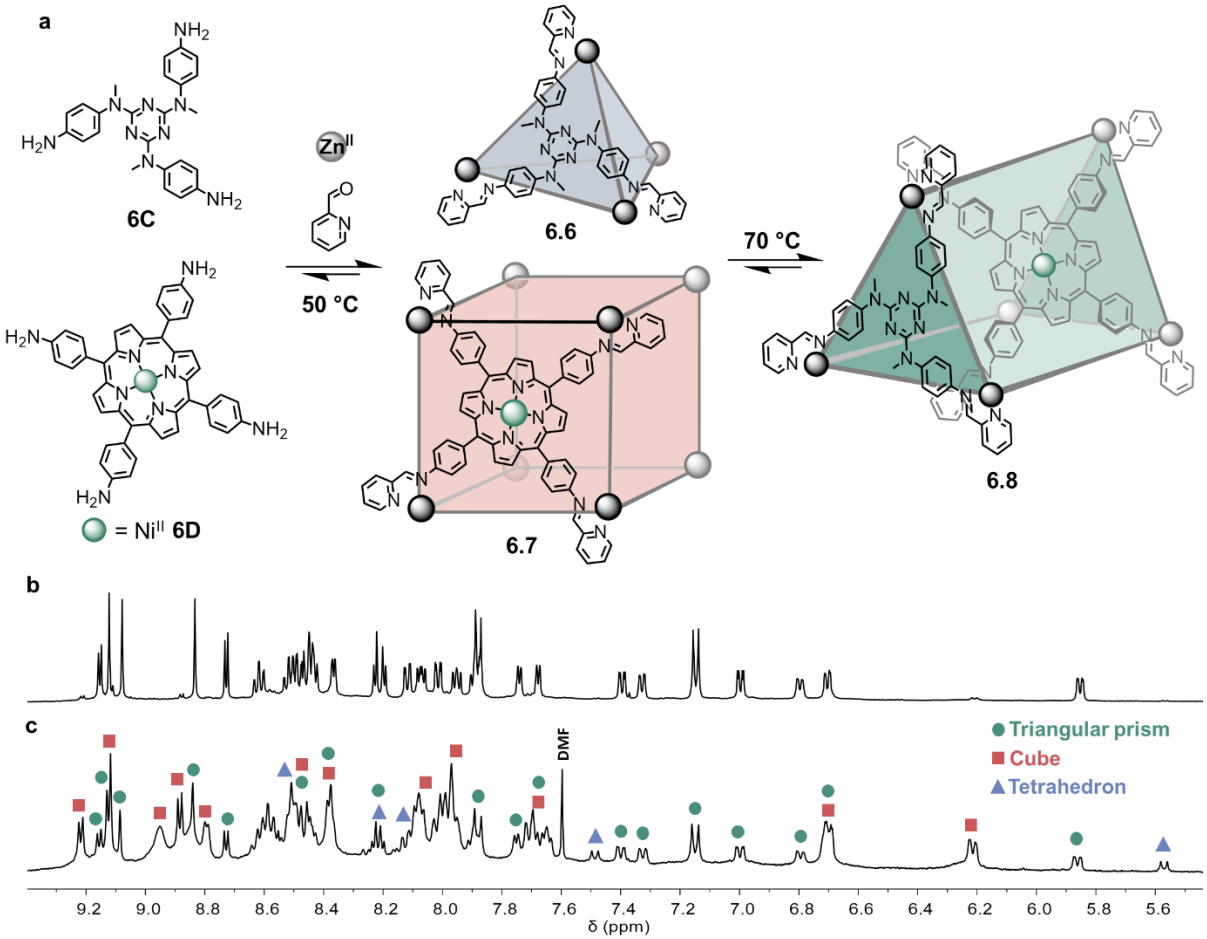

Figure 6.5 | a, The reaction of **6C**, **6D**, 2-formylpyridine and Zn^{II} subcomponents at 50 °C led to the formation of **6.6**, **6.7** and **6.8** (spectrum **c**). When this mixture was heated at 70 °C for a further 16 h, **6.8** was observed as the unique product (spectrum **b**).

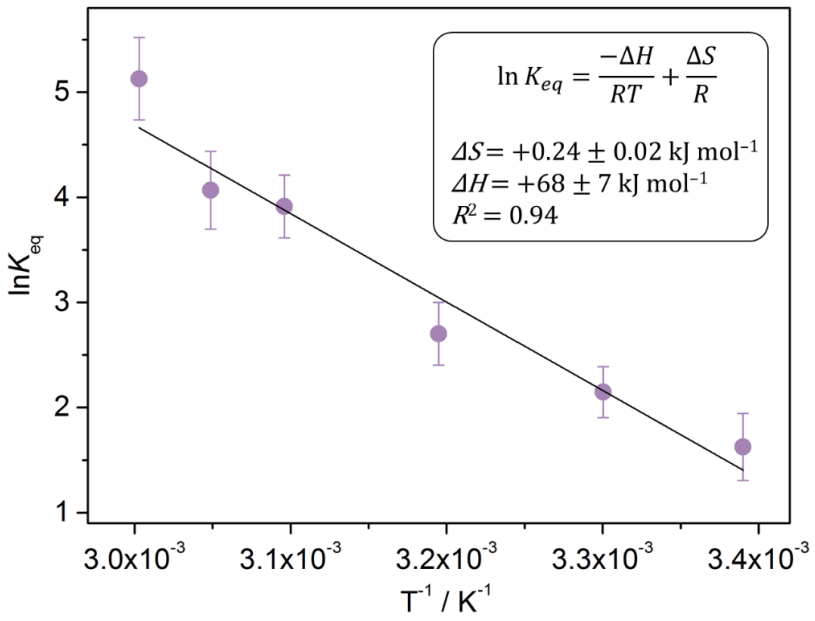

Figure 6.6 | Van't Hoff analysis of the equilibrium generating triangular prism **6.8**.

The ^{1}H NMR spectrum of **6.8** indicated slow rotation of the porphyrin phenylene protons with twofold desymmetrisation of the porphyrin unit, consistent with the approximate D_3 symmetry of the triangular prism. Several ^{1}H–^{1}H NOE correlations could also be identified between the three- and fourfold symmetric ligands, highlighting the proximity between triangular and square faces of the prism (Figure 6.7a). Specifically, correlations between the methyl protons of $\mathbf{L^{6C}}$ and the phenyl, β-pyrrolic and imine protons of one arm of $\mathbf{L^{6D}}$ were identified. This is consistent with twofold desymmetrisation of the square ligand face, in which one set of environments is proximal to $\mathbf{L^{6C}}$, while the other set of environments is proximal to itself (red and green atoms, respectively, in Figure 6.7b). Slow diffusion of Et_2O into a solution of **6.8** in MeCN yielded crystals suitable for X-ray diffraction studies, which confirmed the proposed solution-state configuration (Figure 6.7b).

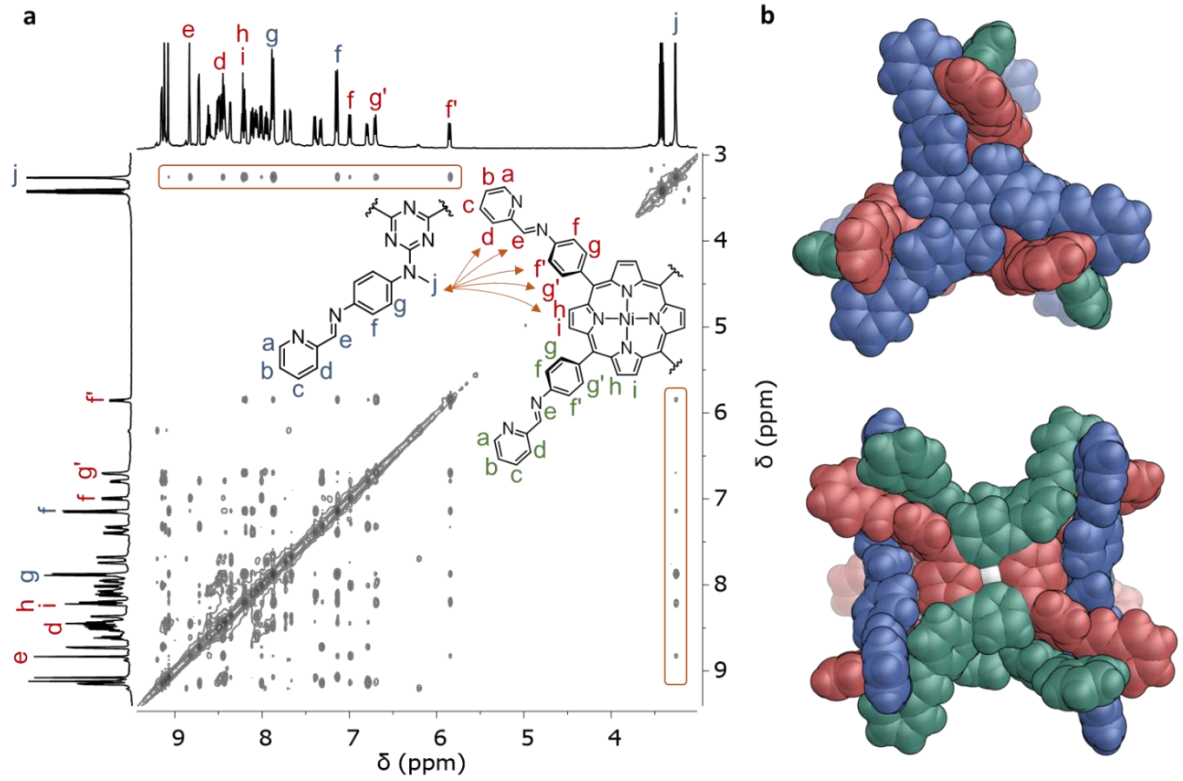

Figure 6.7 | a, ^{1}H-^{1}H NOESY NMR spectrum (500 MHz, 298 K, CD_3CN) of **6.8**, with important NOE correlations between ligands highlighted with orange rectangles and arrows. **b**, Two views of the crystal structure of **6.8**, with each unique ligand environment highlighted in a different colour, rotated 90° with respect to each other.

6.4 Guest binding investigations with 6.8

6.4.1 Anionic guests

Non-cooperative binding of two carborate anions was observed in the cavity of **6.8** by ^{1}H NMR titration, where $K_1 = (242 \pm 2)$ M^{-1} (Figure 6.8a&b). Binding was observed in fast exchange with the host on the NMR timescale, with the most significant proton shifts observed for the porphyrin and imine protons of **6.8**. The $CoC_4B_{18}H_{22}^-$ (cobalticarborane) anion was observed to bind in slow

exchange ($K_a > 10^4$ M^{-1}) with **6.8**, with distinct changes in the ^{11}B spectrum of the guest observed upon binding (Figure 6.8c&d). Full saturation of the host was observed after the addition of 2 equivalents of guest.

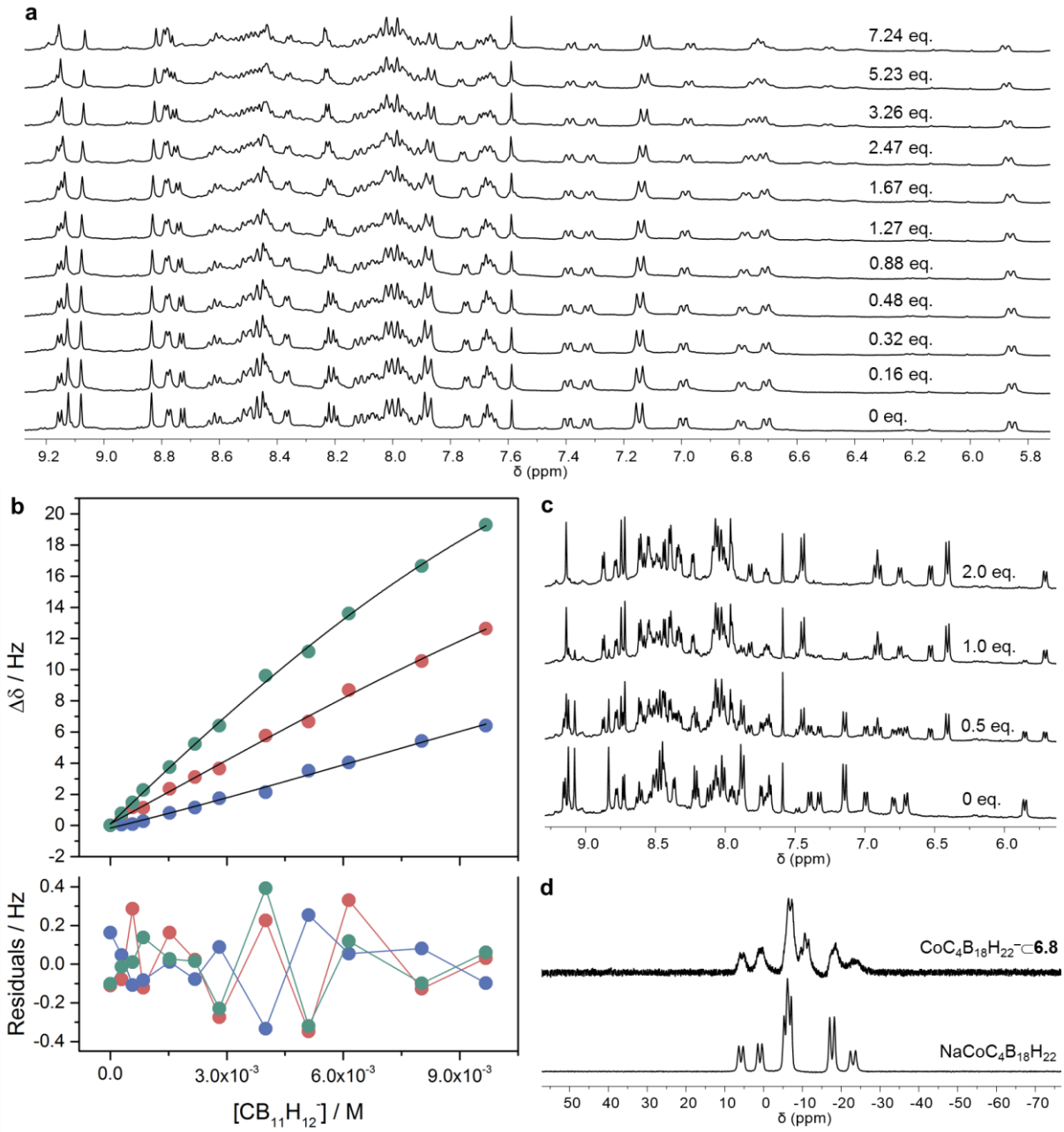

Figure 6.8 | **a**, ^1H NMR titration (400 MHz, 298 K, CD_3CN) of $CsCB_{11}H_{12}$ into **6.8**, marked with the number of anion equivalents added. **b**, Titration data fitted to a non-cooperative 1:2 model (top) and the residuals from the fit (bottom). **c**, ^1H NMR titration (400 MHz, 298 K, CD_3CN) of $NaCoC_4B_{18}H_{12}$ into **6.8**, marked with the number of anion equivalents added. **d**, ^{11}B NMR (128 MHz, 298 K, CD_3CN) of free $CoC_4B_{18}H_{12}^-$ compared to $CoC_4B_{18}H_{12}^-$ bound within **6.8**.

A solid state structure of cobalticarborane bound within **6.8** suggested that the encapsulation of this guest led to a bulging of the structure around the porphyrin components: as a free cage, the porphyrins are concave; they are convex upon binding cobalticarborane (Figure 6.9). The binding of this guest leads to a 37% increase in the cavity volume of **6.8** (from 415 to 567 $Å^3$).

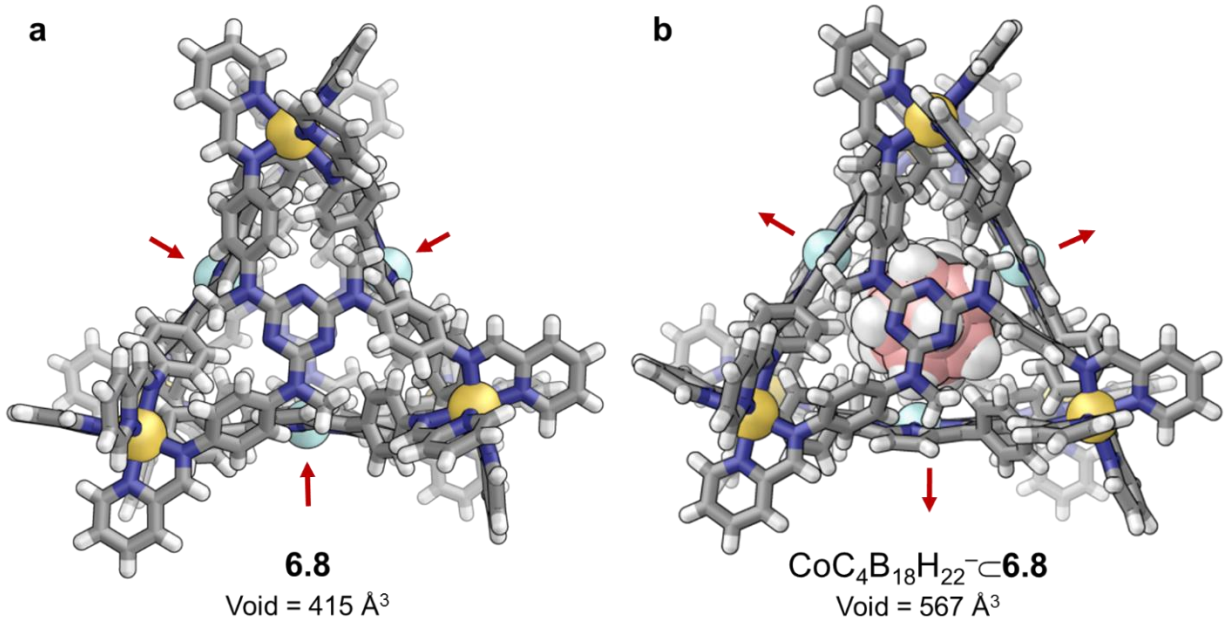

Figure 6.9 | X-ray crystal structures of **a**, **6.8** and **b**, $CoC_4B_{18}H_{22}^-$⊂**6.8** viewed down the C_3 axis of the cage. Red arrows indicate the directional bend of the porphyrin: in **6.8** the ligands point inwards (concave), whereas they bend outwards (convex) upon binding $CoC_4B_{18}H_{22}^-$ in the solid state. (Zn – yellow, Ni – cyan, C – grey, N – blue, B – pink, H – white).

The binding of the cobalticarborane anion within the cavity of the triangular prism was sufficiently strong to act as a template to generate congeners of **6.8**. Heating subcomponents **6A**, **6D**, 2-formylpyridine and $Zn(NTf_2)_2$ at 70 °C for 24 h generated spectra consistent with the formation of both homoleptic products (*i.e.*, the tetrahedron and cube, Figure 6.10a). When cobalticarborane was added and the mixture heated at 70 °C for a further 24 h, the triangular prism **6.9** was obtained in 93% yield (Figure 6.10b). This derivate of the triangular prism could not be formed cleanly by heating its subcomponents alone; the templating anion was necessary to cleanly generate **6.9**.

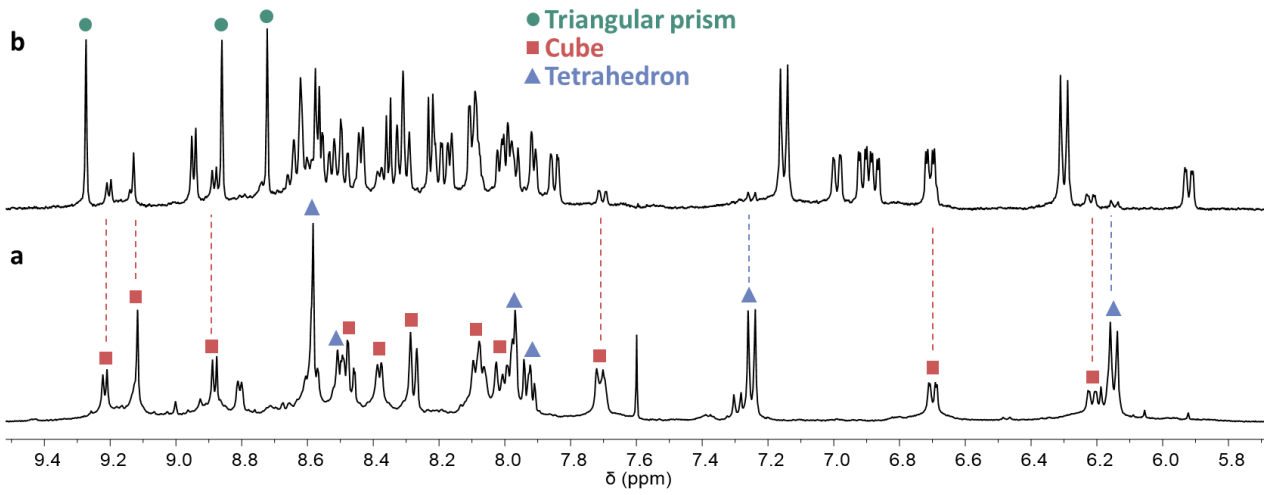

Figure 6.10 | **a**, Only the homoleptic products are synthesised from the reaction of subcomponents **6A**, **6D**, 2-formylpyridine and $Zn(NTf_2)_2$. **b**, When $NaCoC_4B_{18}H_{22}$ is added, the triangular prism is templated in 93% yield. Blue triangles mark the tetrahedron, red cubes mark the cube and green circles note the three unique imine environments of the triangular prism.

6.4.2 Natural product/drug guests

Further exploration of the guest-binding abilities of **6.8** revealed a propensity to bind non-centrosymmetric natural products, steroids and drugs (Figure 6.11). A series of steroids – estrogens, androgens, corticoids, progestogens and synthetic drug analogues – were observed to bind in slow exchange on the NMR timescale, with the proton environments of the guest shifted upfield to the range –1 to –6 ppm (Figure 6.13). In all cases, desymmetrisation of the cage proton environments was observed. Splitting of the methyl protons of $\mathbf{L}^{\mathbf{6C}}$ is furthermore consistent with restricted rotation of the steroids within the cavity of **6.8**, suggesting that guests are constrained within **6.8**. Decreasing the temperature to 233 K resolved further details in some instances, although it generally led to spectral broadening. In all cases, ESI mass spectra were consistent with the encapsulation of a single guest (Figure 6.12).

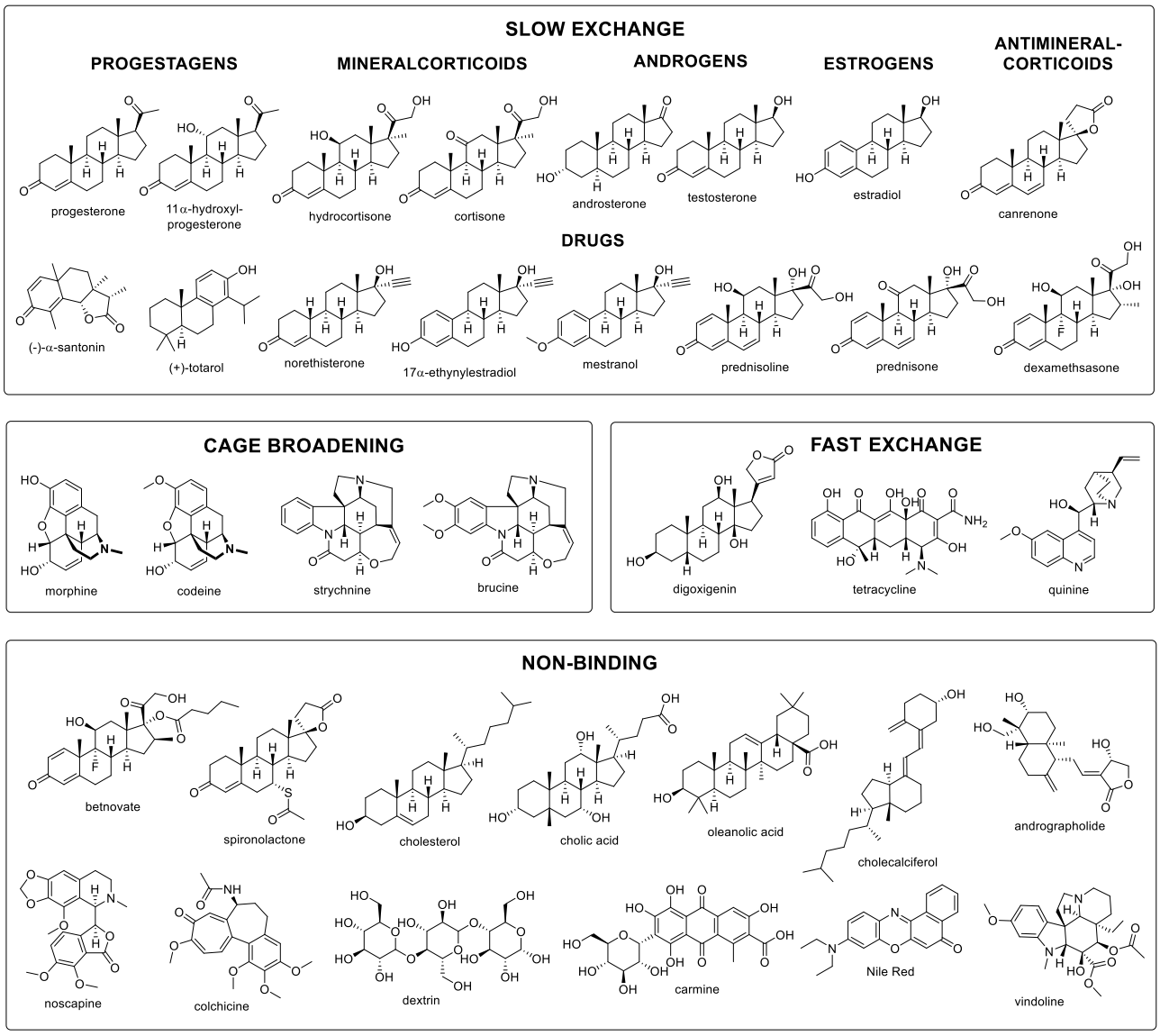

Figure 6.11 | Natural product and drug guests observed to bind to **6.8**, and those for which no binding was observed.

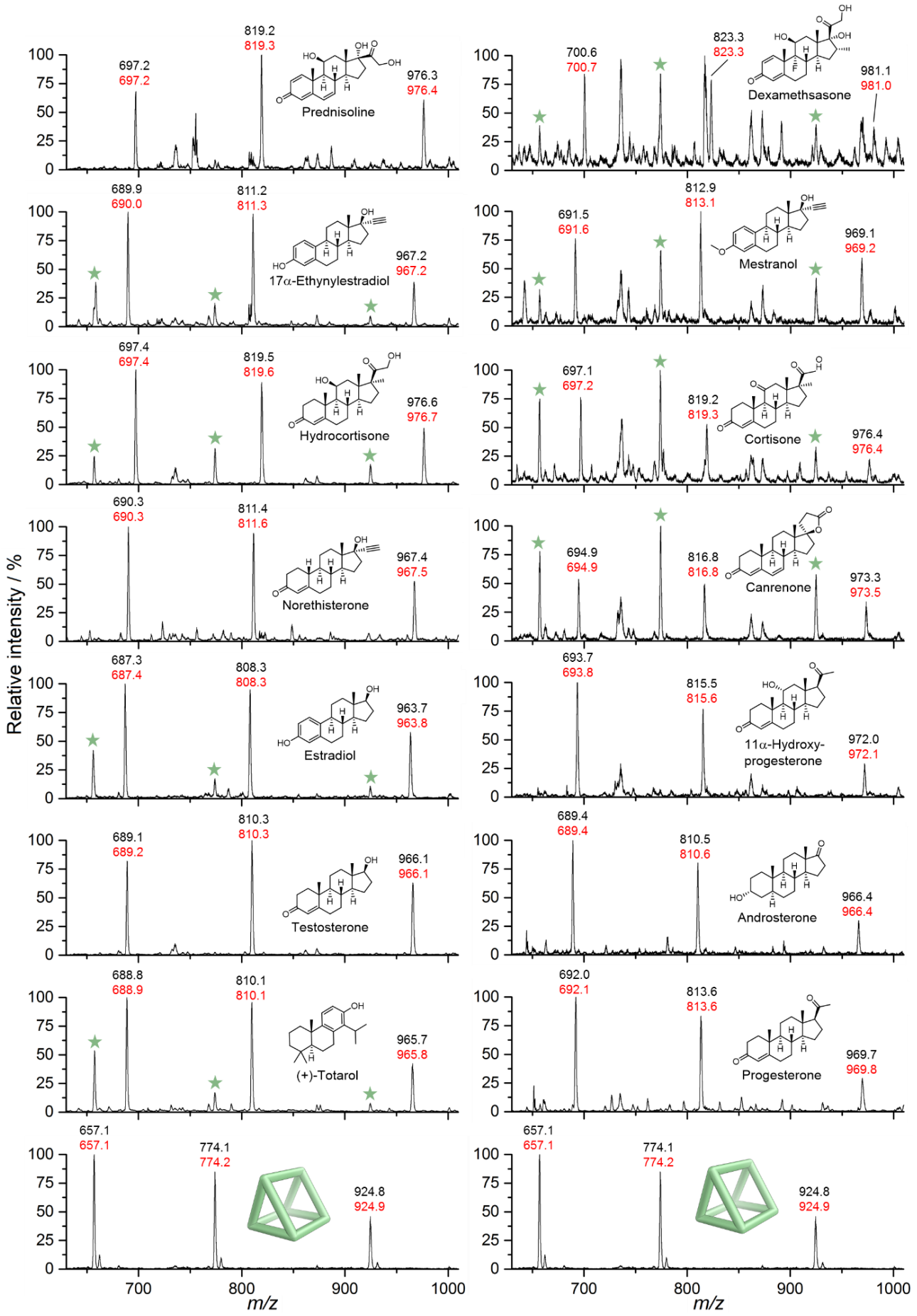

Figure 6.12 | ESI mass spectra of free cage **6.8** (bottom spectra), compared to the ESI mass spectra of steroids inside **6.8**. Red numbers are calculated *m/z* values; black numbers are measured data; green stars correspond to free cage signals.

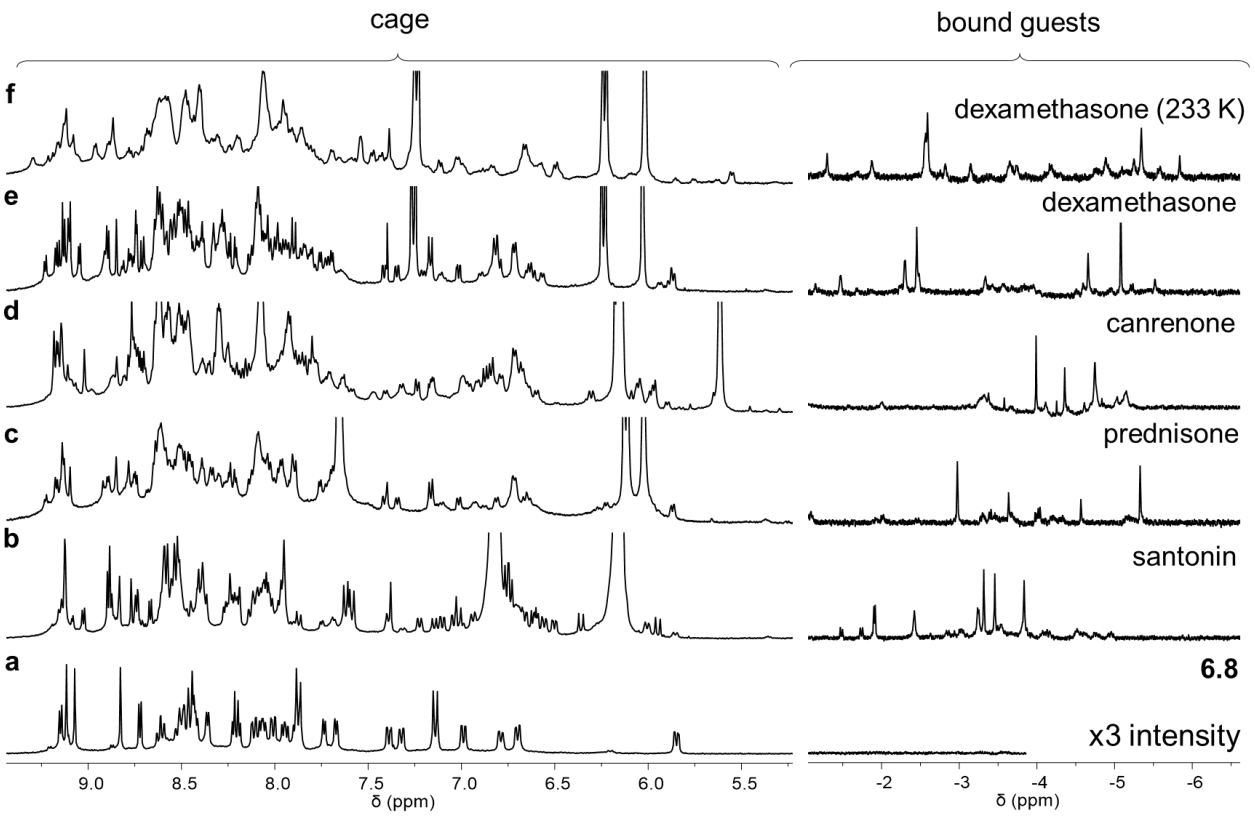

Figure 6.13 | Representative ^{1}H NMR spectra (500 MHz, 298 K, CD_3CN) of steroid and drug guests bound within **6.8**: **a**, free cage; **b**, santonin⊂**6.8**; **c**, prednisone⊂**6.8**; **d**, canrenone⊂**6.8**; **e**, dexamethasone⊂**6.8**; **f**, dexamethasone⊂**6.8** at 233 K. Cage peaks were observed to desymmetrise over the range 5.5–9.5 ppm; encapsulated guest peaks were observed in the range –1 to –6 ppm.

Opiate drugs like codeine and morphine, along with natural products such as strychnine and brucine, were also observed to bind in **6.8**, although an excess of guest was often necessary for full saturation of the cavity. The NMR spectra of these host-guest species were broad, and no signals corresponding to the encapsulated guest could be accurately assigned (Figure 6.14); however, a crystal structure of strychnine within the cavity of **6.8** was obtained (Figure 6.15a). To accommodate the guest, two porphyrin faces remain concave, while the other becomes convex in the solid state. This stands in contrast to the binding of ovoid guests more accurately matched to the symmetry of the cavity of **6.8** (like cobalticarborane), where all porphyrin faces are convex (Figure 6.9b).

A crystal structure displaying similar host features was obtained for encapsulated testosterone (Figure 6.15b). As with strychnine⊂**6.8**, testosterone⊂**6.8** crystallised in the centrosymmetric space group P1, despite containing a non-centrosymmetric steroid guest. The presence of the guest was unambiguously evidenced in the electron density map of the crystal, which displayed a distorted rectangle of electron density inside the cage, representing a series of disordered configurations of testosterone within the cavity. As a result of this disorder, both strychnine and testosterone were modelled as rigid bodies, disordered over two or three locations, respectively. Both the all-Δ and all-Λ

enantiomers of **6.8** are present in the crystal structures of testosterone⊂**6.8** and strychnine⊂**6.8**, suggesting that enantiopure guests do not lead to chiral induction of the host. No solution could be obtained in P1, or in any other chiral space group.

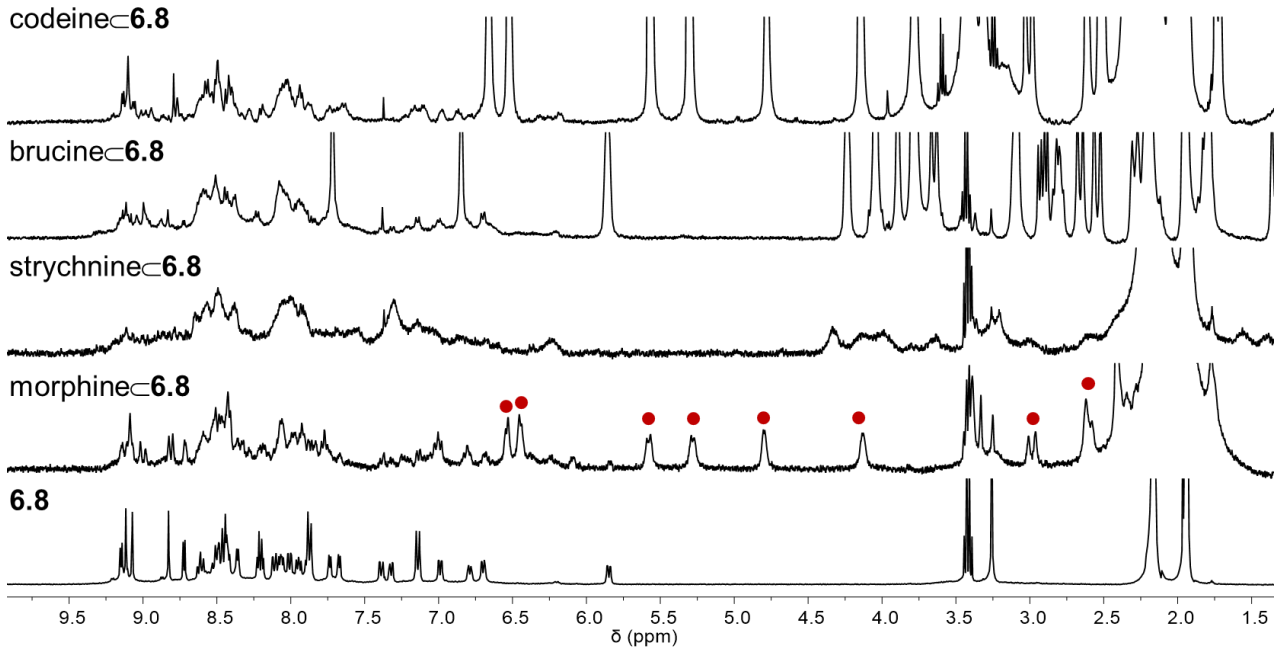

Figure 6.14 | ^{1}H NMR spectra (400 MHz, 298 K, CD_3CN) of **6.8** (bottom spectra) compared to four host-guest complexes containing morphine, strychnine, brucine and codeine. Red circles mark free morphine.

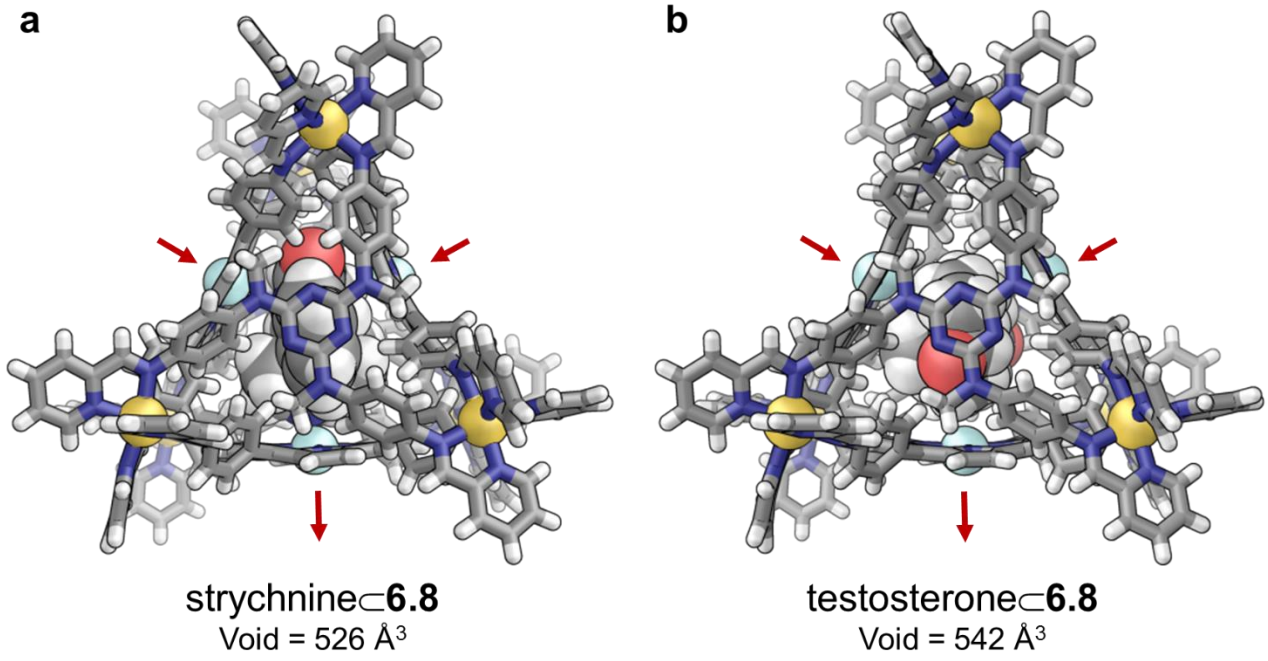

Figure 6.15 | X-ray crystal structures of **a**, strychnine⊂**6.8** and **b**, testosterone⊂**6.8**. Arrows indicate the direction of the porphyrin bend observed in the solid state. Only one location of the guest is shown in both cases (Zn – yellow, Ni – cyan, C – grey, N – blue, O – red, H – white).

The crystallography is consistent with the solution-state evidence, which indicates that the guest experiences configurational freedom along one axis, and no rotation about the other, within **6.8** (Figure 6.16). The ^{1}H NMR spectrum of testosterone⊂**6.8** displayed four signals corresponding to the methyl protons of $\mathbf{L}^{\mathbf{6C}}$, each of equal integration (Figure 6.16b). The methyl protons of testosterone were furthermore each observed to split into two signals, also of equal integration (Figure 6.16d). The NMR spectra thus suggest that testosterone does not act as a chiral inductor within **6.8**, echoing the solid state structures; both all-Δ and all-Λ structures exist in equal concentration, and the guest is rotating rapidly about its longer axis on the NMR timescale. This maintains the threefold symmetry of either end-capping C_3 ligand, but causes each $\mathbf{L}^{\mathbf{6C}}$ ligand of the cage to have a different magnetic environment (Figure 6.16c). Testosterone⊂**6.8** is thus C_3-symmetric, whereas **6.8** was D_3-symmetric.

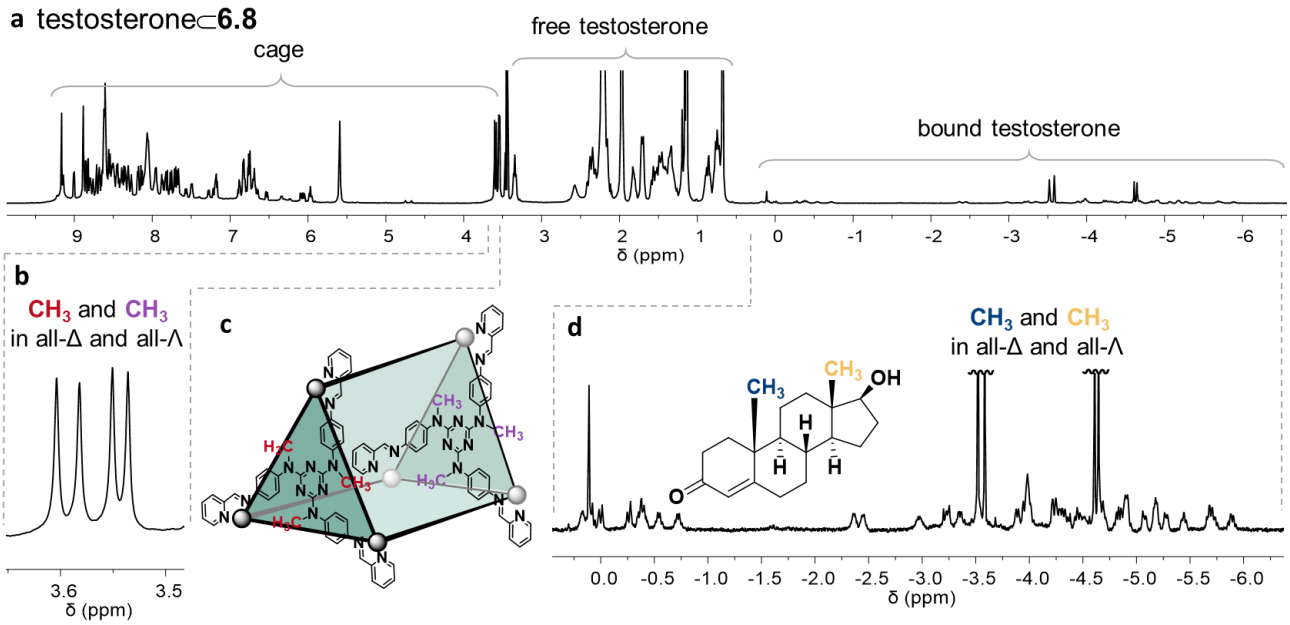

Figure 6.16 | a, ^{1}H NMR spectrum (500 MHz, 298 K, CD_3CN) of testosterone⊂**6.8**, showing regions for signals corresponding to the cage, free testosterone and bound testosterone. **b**, Close-up of the methyl protons on $\mathbf{L}^{\mathbf{6C}}$, showing two unique environments, corresponding to the front and back ligands in the two enantiomers of the cage framework. **c**, Showing the desymmetrisation of **6.8** upon testosterone binding, where the back and front ligands have different chemical environments. **d**, The presence of both cage enantiomers was supported by the splitting of signals corresponding to testosterone within **6.8**, wherein the steroid creates a diastereotopic host-guest pair with the two cage enantiomers.

A clear size limitation for binding within **6.8** is evident – canrenone and dexamethasone represent the size limit for encapsulation, with the slightly larger digoxigenin observed to bind in fast exchange on the NMR timescale (Figure 6.17b). Steroids with axial substitutions (e.g. spironolactone) or long alkyl chains (e.g. cholesterol) furthermore do not provide a good steric fit within **6.8**, leading to no observable binding. Both tetracycline and quinine were observed to bind to **6.8** in fast exchange on the NMR timescale (Figure 6.17c–f). Splitting of the guest protons into two signals of equal intensity suggested that no chiral amplification was observed upon binding these guests; tetracycline acts as a chiral shift agent, discriminating between the all-Δ and all-Λ enantiomers of **6.8** (Figure 6.17d).

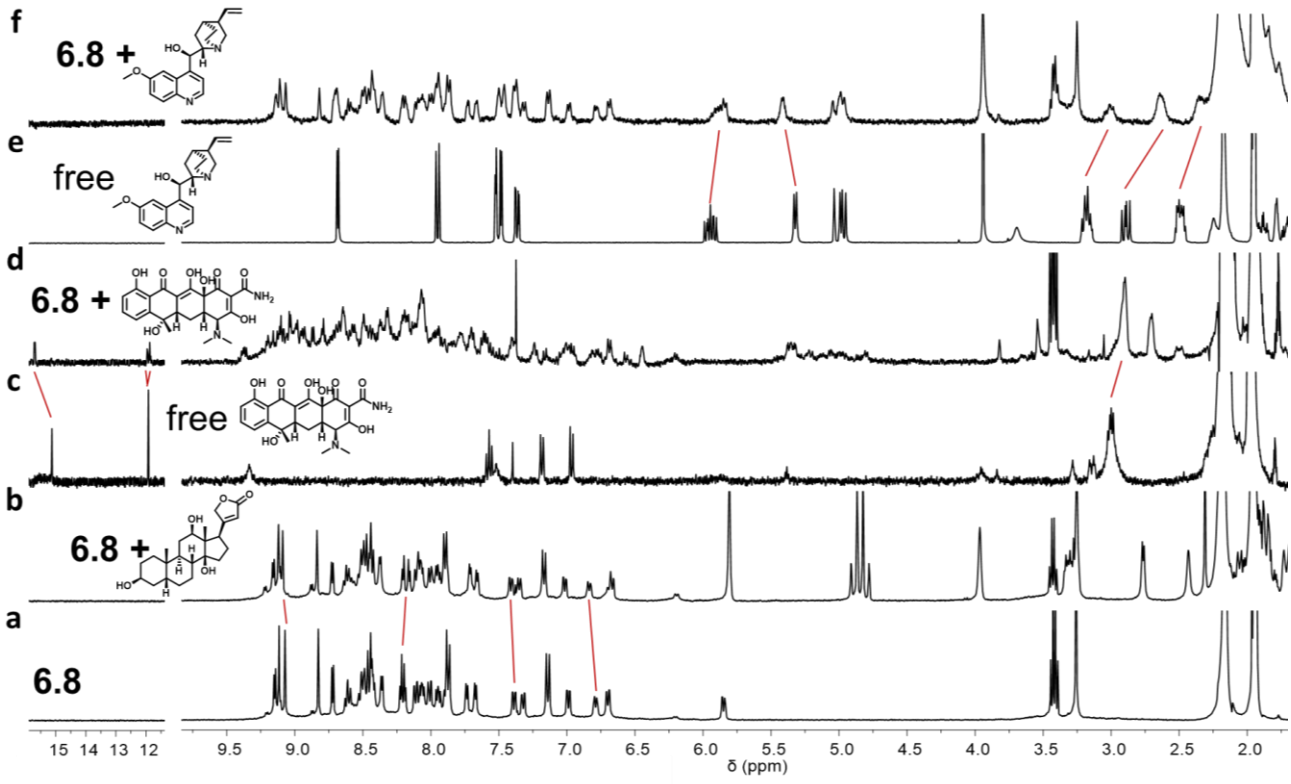

Figure 6.17 | a, ^{1}H NMR spectra (500 MHz, 298 K, CD_3CN) of fast-exchanging guests with **6.8**. **a**, Free cage. The addition of **b**, dioxigenin, **d**, tetracycline or **f**, quinine to **6.8** led to shifts in the protons of both host and guest, consistent with fast exchange binding. Red lines mark the signal shifts for the addition of digoxigenin (**a&b**), tetracycline (**c&d**) and quinine (**e&f**).

Table 6.1 | Binding constants for guests within **6.8**, measured by ^{1}H NMR spectroscopy (500 MHz, 298 K, CD_3CN).

Guest	K_a **(M^{-1})**
Testosterone	$>10^4$[a]
Androsterone	$>10^4$[a]
Progesterone	$(3.9 \pm 0.3) \times 10^4$
Norethisterone	$(1.9 \pm 0.1) \times 10^4$
11α-Progesterone	$(9 \pm 1) \times 10^3$
Prednisolone	$(6.7 \pm 0.9) \times 10^3$
Hydrocortisone	$(4.5 \pm 0.5) \times 10^3$
17α-Ethynylestradiol	$(3.6 \pm 0.4) \times 10^3$
(+)-Totarol	$(3.4 \pm 0.2) \times 10^3$
Dexamethasone	$(1.28 \pm 0.08) \times 10^3$
Prednisone	$(7.2 \pm 0.3) \times 10^2$
Mestranol	$(6.5 \pm 0.4) \times 10^2$
Cortisone	$(2.3 \pm 0.6) \times 10^2$
(–)-α-Santonin	$(1.1 \pm 0.1) \times 10^2$
Estradiol	-[b]
Canrenone	-[c]

[a] Full saturation of the host was observed upon the addition of one equivalent of guest. [b] Guest was poorly soluble in CH_3CN. [c] Significant signal overlap prevented accurate binding constant determination.

Binding constants for guests in slow exchange with host **6.8** were measured by ^{1}H NMR spectroscopy and are displayed in Table 6.1. The binding hierarchy with **6.8** suggests that androgens and progestogens are the strongest binding guests. With increased steric bulk around the termini of the molecules, or increased structural rigidity of the backbone, the binding affinity of steroids (and their derivatives) within **6.8** generally decreases.

6.5 Potential allosteric binding sites

Decreasing the ionisation voltage from 30 to 7 eV during the ESI mass spectrometry of testosterone⊂**6.8** resolved several steroid guests associated with **6.8** in the gas phase (Figure 6.18). It was furthermore observed by ^{1}H NMR that while a series of bound guest signals were identified in slow exchange with the host on the NMR timescale, guest signals corresponding to fast exchange binding on the NMR timescale (*i.e.* shifts in the free guest signals relative to their unbound states) were also observed (Figure 6.19). This data suggests that, along with internal binding, host **6.8** may have peripheral sites for binding steroids. Importantly, UV-Vis titrations could not be fit to either a 1:1 or 1:2 host:guest binding model, indicating the possibility of higher binding stoichiometries in solution. Subsequent experiments by dynamic light scattering (DLS) and ^{1}H NOESY NMR spectroscopy did not reveal any significant change in size, or NOE correlations between host and fast-exchanging guest. Current investigations are looking at sequential binding experiments, wherein a weak-binding guest is added to testosterone⊂**6.8**. Shifts in guest signals after already binding testosterone internally may confirm the hypothesised peripheral interaction.

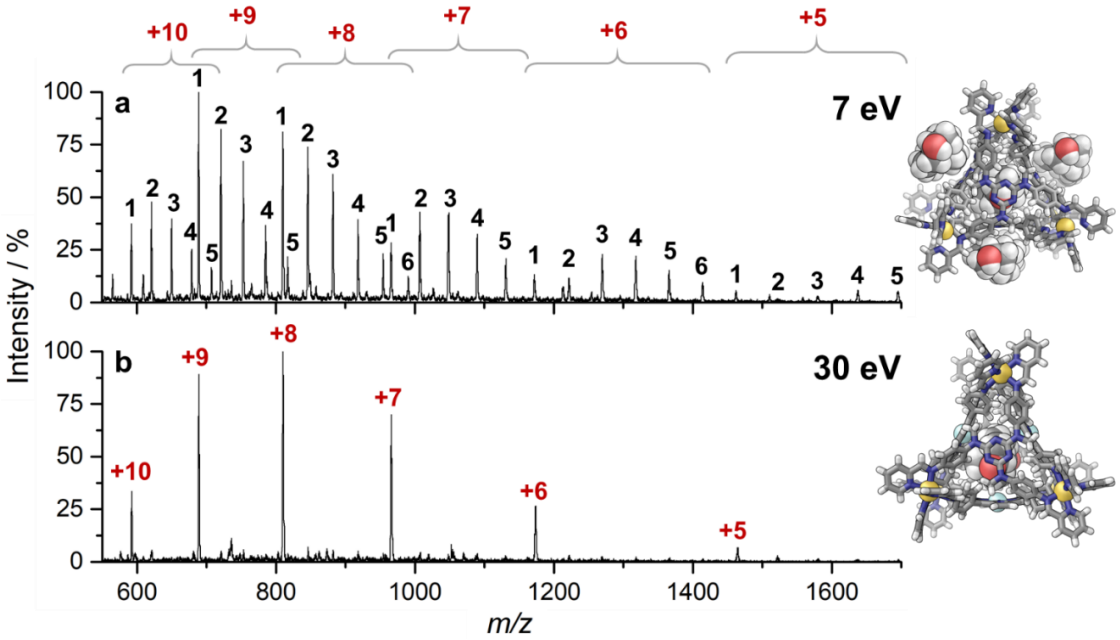

Figure 6.18 | ESI mass spectra of testosterone⊂**6.8** at **a**, low cone voltage, wherein species corresponding to **6.8**·(testosterone)$_x$ were observed (number of steroids associated with **6.8** are shown in black). **b**, At high cone voltage, only testosterone⊂**6.8** was observed.

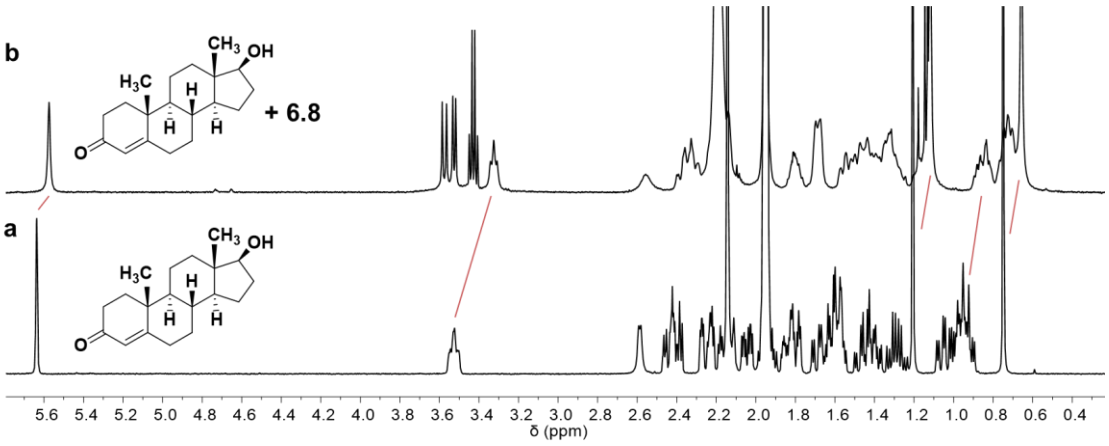

Figure 6.19 | ^{1}H NMR spectra (500 MHz, 298 K, CD_3CN) comparing **a**, free testosterone to **b**, testosterone with **6.8**. Red lines trace the signals of testosterone associated with the cage in fast exchange, which are observed to shift *ca*. 0.3 ppm relative to their free values. Many signals at 0.6–2.7 ppm were also observed to broaden.

6.6 Sorting systems of polydentate, polytopic ligands

Having shown that heteroleptic structures could be generated by employing different subcomponents with different topicities, it was hypothesised that more complex systems of subcomponents may lead to different sorting behaviour. When all five components (**6A**, **6B**, Co^{II}, 2-formylpyridine and 2-formylphenanthroline) were combined in a single pot during assembly (wherein an equimolar ratio of **6.1**:**6.2**:**6.3**:**6.4** cages was expected), **6.3** was not observed; the cube, cuboctahedron and tetrahedron were observed to form by both ^{1}H NMR (Figure 6.20) and ESI-MS.

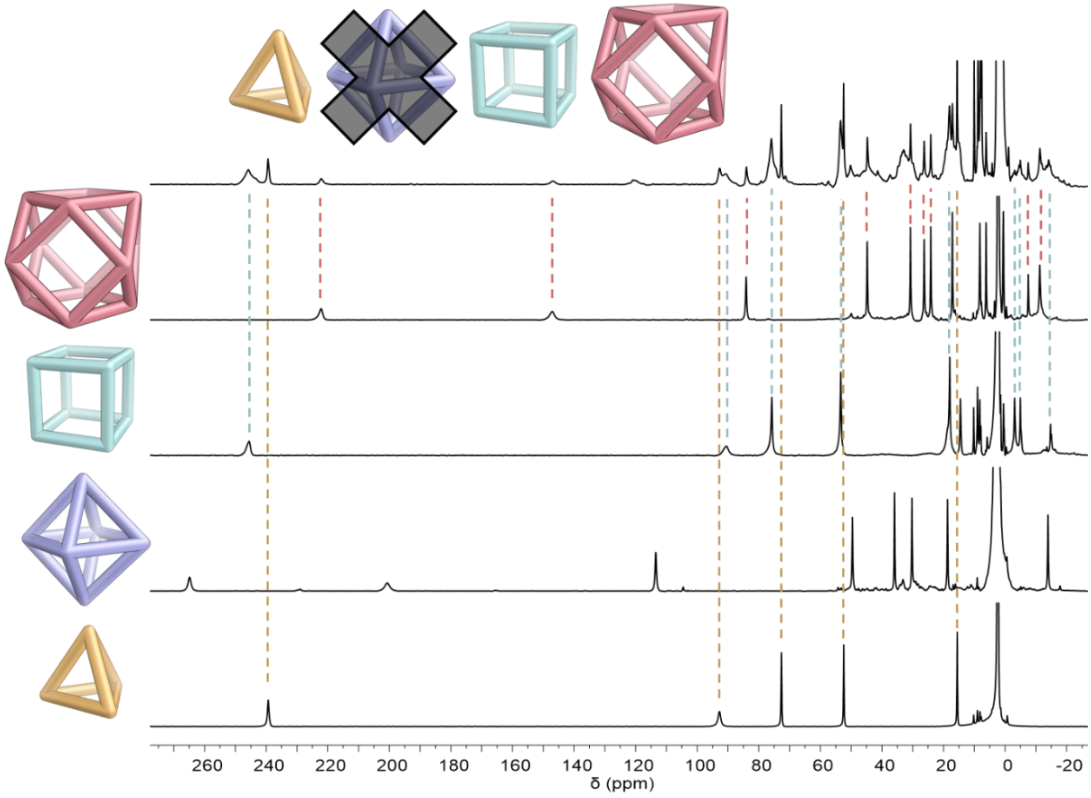

Figure 6.20 | ^{1}H NMR spectra (400 MHz, 298 K, CD_3CN) of each separate cage compound (bottom four spectra) compared to the sorting mixture generated when all five subcomponents were heated together (topmost spectrum).

The observed output of cages can be rationalised on the basis of limiting reagents and entropy. Assuming that each imine condensation is energetically equivalent, the enthalpic cost of forming the complexes will increase with size (cuboctahedron > cube > octahedron > tetrahedron), assuming that enthalpic effects associated with strain are negligible. Considering entropy, complexes with the smallest number of subcomponents will be favoured. As the smallest and most thermodynamically-favoured structure, tetrahedron **6.1** should theoretically be the most stable. Thus, the equilibration of the tetrahedron should determine the remaining components available for subsequent assembly.

Routes describing the potential assembly pathways of the system are depicted in Figure 6.21. Full sequestration of subcomponent **6A** by the tetrahedron results in no remaining threefold subcomponent, such that the octahedron has no amine subcomponent to form. Two potential paths then diverge from this initial step: either the cube is formed from the remaining 2-formylpyridine, leaving only the components to form the cuboctahedron behind; or the cuboctahedron is formed from the remaining 2-formylphenanthroline, leaving only the cube subcomponents remaining. The final assembly step involves the remaining subcomponents assembling into the cuboctahedron or cube, depending on the previous step. ^{1}H NMR signal integration of the sorted mixture indicated that the cube was more abundant than the cuboctahedron, suggesting that the cube assembles in preference to the cuboctahedron, in line with its thermodynamic hierarchy of formation noted previously.

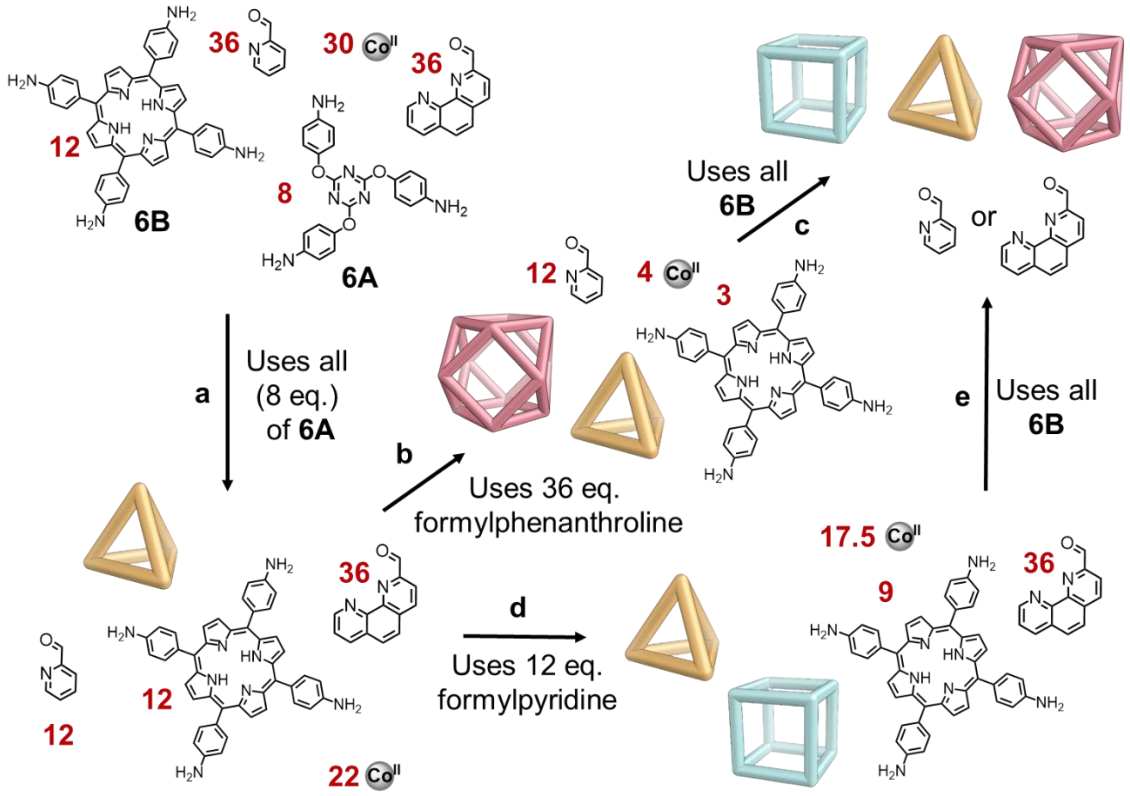

Figure 6.21 | An outline of the proposed sorting pathway undertaken when all five subcomponents were combined simultaneously during assembly. **a**, If the tetrahedron forms first, all of **6A** is sequestered. Two paths to further assembly then emerge: **b&c**, the cuboctahedron is preferred over the cube or **d&e**, the cube is preferred over the cuboctahedron. Both paths lead to a situation in which only the tetrahedron, cube and cuboctahedron are observed.

This hypothesis is supported by the rate of formation of individual cages, measured using UV-Vis spectroscopy. As the kinetics of formation of these structures is complex, UV-Vis spectra of aliquots taken at specific time intervals during synthesis at 60 °C were measured for each individual cage assembly (each synthesised at 1 mM concentration); a plateau in the intensity of the absorbance marked completion of the reaction and complete formation of cage, which was then verified by ^{1}H NMR spectroscopy (Figure 6.22).

The tetrahedron was observed to form within 10 minutes. This stands in contrast to the cube, octahedron and cuboctahedron, which required between 3-6 hours to form (Figure 6.22). Generally, structures involving more subcomponents took longer to assemble. The sequestration of 2-formylpyridine by the tetrahedron thus leads to a cascade reaction that forms the largest structure in preference to the second smallest one. No evidence of the triangular prism was observed by either ESI-MS or NMR during the reaction of all five subcomponents. This may be attributed to the sequestration of the porphyrin subcomponent by the 2-formylphenanthroline.

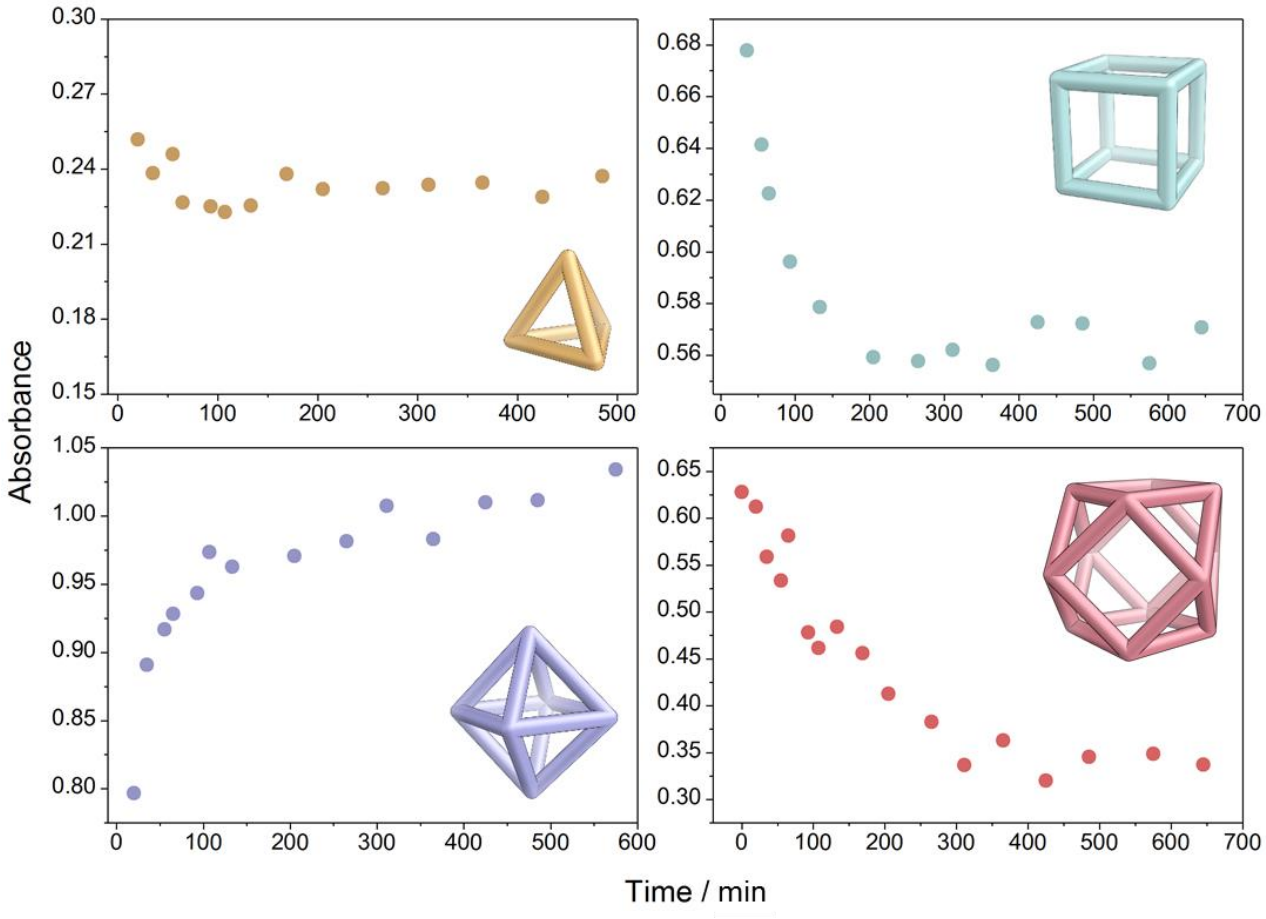

Figure 6.22 | Plots showing the rate of formation of each homoleptic architecture, monitored by UV-Vis spectroscopy, following the UV bands of **6.1** (346 nm) and **6.3** (370 nm), and the porphyrin Soret band for **6.2** (411 nm) and **6.4** (420 nm).

Furthermore, when 2-formylphenanthroline, **6A**, **6B** and Co^{II} were combined in isolation, no discrete products were observed by ESI-MS. Several imine resonances were observed by ^{1}H NMR spectroscopy, most likely corresponding to a dynamic library of fragments and intermediary species. The poor mutual sorting of octahedron **6.2** and cuboctahedron **6.4** may also contribute to the lack of observation of the former species in the five-component sorting experiment.

6.7 Conclusions and future work

Interactions between components of different, but complementary, geometries can lead to complex sorting behaviour – homoleptic or heteroleptic products could each be selectively amplified by altering temperature and/or subcomponent denticity, and using templates. Heteroleptic face-capped triangular prisms can be used to bind a range of steroids, natural products, large anions and drug molecules. The cage adapts in different ways to bind each of these guests: in the absence to guests, the square faces of the cage are concave; in binding cobalticarborate, all the faces become convex; in binding steroids, two faces remain concave, while one becomes convex. The ability for this capsule to adapt the volume of its cavity in response to guest stimuli means that it can bind a range of guest shapes, lengths, and sizes with great versatility.

Future work could focus on the development of triangular prisms as a broader class of structure type, and the development of a broader range of heteroleptic architectures by subcomponent self-assembly. Another tack could involve the investigation of even more complex sorting systems, wherein the generation of twofold-symmetric subcomponents could be employed to generate structures with antiprism topology. The generation of these heteroleptic species could lead to more desymmetrised cavities which, in turn, may bind an even broader range of asymmetric guests.

6.8 Experimental section

6.8.1 Synthesis and characterisation of 6.1

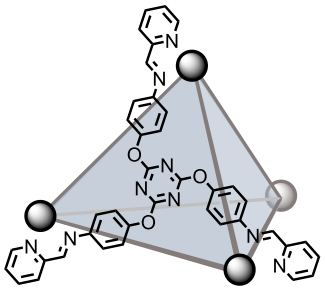

The synthesis of **6.1** was adapted from a literature procedure.[6] Subcomponent **6A** (2.00 mg, 4.96×10^{-6} mol, 4 equiv), 2-formylpyridine (1.42 µL, 1.49×10^{-5} mol, 12 equiv) and either $Co(NTf_2)_2 \cdot 6H_2O$ (3.61 mg, 4.96×10^{-6} mol, 4 equiv) or $Co(OTf)_2$ (1.77 mg, 4.96×10^{-6} mol, 4 equiv) were combined in CD_3CN (0.6 mL) in a sealed NMR tube. The mixture was heated at 60 °C for 16 h. Spectra were recorded upon cooling to room temperature. **^{1}H NMR** (400 MHz, 298 K, CD_3CN) of **6.1**$(NTf_2)_8$: δ 239.3, 92.8, 72.6, 52.4, 15.5 ppm. **^{1}H NMR** (400 MHz, 298 K, CD_3CN) of **6.1**$(OTf)_8$: δ 243.0, 90.5, 72.9, 52.2, 16.0, –6.7, –60.3 ppm. *Note:* The reported Fe^{II} cage was observed to bind OTf^-.[6] **LR-ESI-MS** [charge, calculated for **6.1**$(OTf)_8$]: *m/z* = 877.4 [**6.1**$(OTf)_4^{4+}$, 877.7], 672.1 [**6.1**$(OTf)_3^{5+}$, 672.3], 535.3 [**6.1**$(OTf)_2^{6+}$, 535.4], 437.4 [**6.1**$(OTf)_4^{7+}$, 437.7]. **HR-ESI-MS**: *m/z* calculated for [**6.1**$(NTf_2)_5]^{3+}$ = 1438.0721; observed = 1438.0615.

6.8.2 Synthesis and characterisation of 6.3

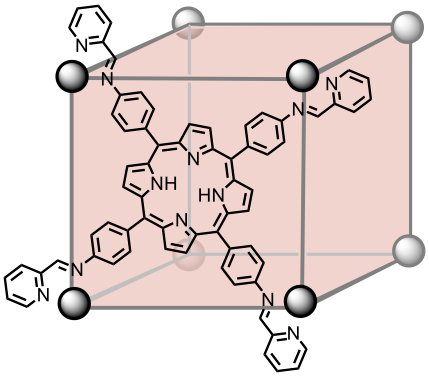

The synthesis of **6.3** was adapted from a literature procedure.[8] Subcomponent **6A** (2.20 mg, 3.18×10^{-6} mol, 6 equiv), 2-formylpyridine (1.20 µL, 1.27×10^{-5} mol, 24 equiv) and $Co(NTf_2)_2 \cdot 6H_2O$ (3.09 mg, 4.25×10^{-6} mol, 8 equiv) were combined in CD_3CN (0.6 mL) in a sealed NMR tube. The mixture was heated at 60 °C for 16 h. **^{1}H NMR** (400 MHz, 298 K, CD_3CN): δ 245.5, 90.5, 75.8, 53.3, 18.0, 14.5, –3.1, –4.9, –14.7, –64.6 ppm. **LR-ESI-MS** [charge, calculated for **6.3**$(NTf_2)_{16}$]: *m/z* = 1576.7 [**6.3**$(NTf_2)_{10}^{6+}$, 1576.7], 1311.2 [**6.3**$(NTf_2)_9^{7+}$, 1311.4], 1112.3 [**6.3**$(NTf_2)_8^{8+}$, 1112.5], 957.7 [**6.3**$(NTf_2)_7^{9+}$, 957.7], 833.9 [**6.3**$(NTf_2)_6^{10+}$, 833.9], 732.5 [**6.3**$(NTf_2)_5^{11+}$, 732.7], 648.1 [**6.3**$(NTf_2)_4^{12+}$, 648.3]. **HR-ESI-MS** *m/z* calculated for [**6.3**$(NTf_2)_8]^{8+}$ = 1112.4632; observed = 1112.4627.

6.8.3 Sorting experiments - same triamine, different aldehydes

Subcomponent **6A** or **6B** (9.6×10^{-6} mol, 8 equiv), 2-formylpyridine (1.4×10^{-5} mol, 12 equiv), 2-formylphenanthroline (1.4×10^{-5} mol, 12 equiv) and $Co(OTf)_2$ (1.2×10^{-5} mol, 10 equiv) were combined in CD_3CN (0.6 mL) in a sealed NMR tube. The mixture was heated at 60 °C for 16 h and cooled to room temperature, furnishing a mixture of homo- and heteroleptic products.

6.8.4 Synthesis and characterisation of 6.8

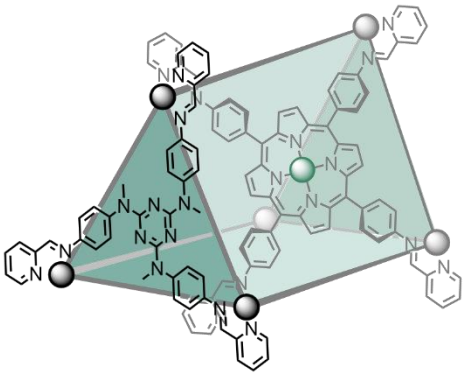

Triamine **6C** (6.40 mg, 1.45×10^{-5} mol, 2 equiv), tetramine **6D** (15.9 mg, 2.17×10^{-5} mol, 3 equiv), 2-formylpyridine (12.5 µL, 1.30×10^{-4} mol, 18 equiv) and $Zn(NTf_2)_2.6H_2O$ (31.8 mg, 4.35×10^{-5} mol, 6 equiv) were combined in CH_3CN (8 mL) and heated at 70 °C overnight. Upon cooling, Et_2O (30 mL) was added and the mixture was shaken vigorously in a centrifuge tube. The mixture was centrifuged, the supernatant decanted, and the solid washed with Et_2O (2 × 20 mL). The residue was dried under vacuum to yield a dark red powder (57.5 mg, 6.82×10^{-6} mol, 94%). **^{1}H NMR** (500 MHz, CD_3CN, 298 K): δ 9.15 (d, J = 4.9 Hz, 6H), 9.12 (s, 6H), 9.08 (s, 6H), 8.83 (s, 6H), 8.73 (d, J = 4.9 Hz, 6H), 8.62 (td, J = 7.8, 1.6 Hz, 6H), 8.54 – 8.47 (m, 12H), 8.47 – 8.41 (m, 18H), 8.37 (dd, J = 4.9, 1.7 Hz, 6H), 8.23 (d, J = 5.1 Hz, 6H), 8.20 (d, J = 5.1 Hz, 6H), 8.12 (dd, J = 8.2, 2.0 Hz, 6H), 8.07 (ddd, J = 8.1, 4.9, 1.3 Hz, 6H), 8.01 (dd, J = 8.0, 2.0 Hz, 6H), 7.95 (ddd, J = 7.5, 5.2, 1.3 Hz, 6H), 7.91 – 7.87 (m, 6H), 7.88 (d, J = 9.0 Hz, 12H), 7.74 (d, br, 6H), 7.68 (dd, J = 5.3, 1.4 Hz, 6H), 7.40 (dd, J = 8.1, 2.4 Hz, 6H), 7.33 (dd, J = 8.1, 2.0 Hz, 6H), 7.15 (d, J = 9.0 Hz, 12H), 7.00 (dd, J = 8.0, 2.4 Hz, 6H), 6.80 (dd, J = 8.1, 2.4 Hz, 6H), 6.70 (dd, J = 8.0, 2.1 Hz, 6H), 5.85 (dd, J = 7.9, 2.4 Hz, 6H), 3.26 (s, 18H) ppm. See Figure 6.23 for signal assignment. **^{13}C NMR** (126 MHz, 298 K, CD_3CN): δ 165.3, 164.4, 164.1, 149.8, 149.5, 149.2, 147.9, 147.0, 146.6, 146.5, 146.4, 144.1, 143.8, 143.5, 143.0, 142.6, 142.5, 140.3, 139.8, 137.3, 135.4, 134.2, 133.8, 131.7, 131.4, 131.3, 131.2, 131.1, 131.0, 130.9, 130.8, 130.8, 130.6, 126.2, 123.7, 122.0, 121.5, 121.1, 120.9, 120.7, 119.7, 119.2, 118.6, 36.5 ppm. **LR-ESI-MS** [charge fragment, calculated for **6.8**$(NTf_2)_{12}$]: *m/z* = 1406.9 [**6.8**$(NTf_2)_7^{5+}$, 1406.9], 1125.5 [**6.8**$(NTf_2)_6^{6+}$, 1125.7], 924.7 [**6.8**$(NTf_2)_5^{7+}$, 924.9], 774.0 [**6.8**$(NTf_2)_4^{8+}$, 774.2], 657.0 [**6.8**$(NTf_2)_3^{9+}$, 657.1], 563.3 [**6.8**$(NTf_2)_2^{10+}$, 563.4], 486.5 [**6.8**$(NTf_2)^{11+}$, 486.7]. **HR-ESI-MS** *m/z* calculated for [**6.8**$(NTf_2)_7]^{5+}$ = 1406.9212; observed = 1406.9226.

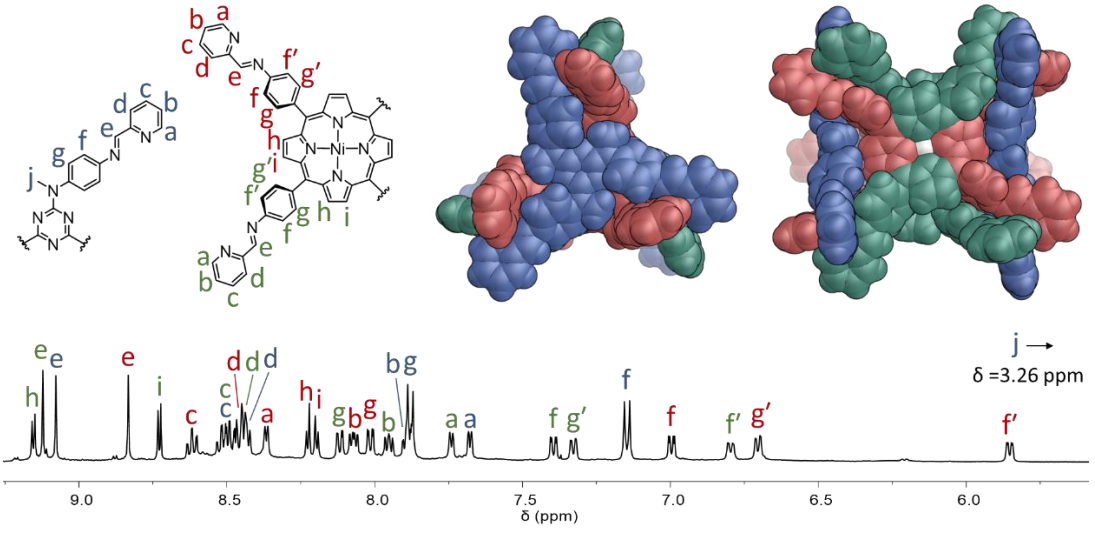

Figure 6.23 | Aromatic region of the ^{1}H NMR spectrum (500 MHz, 298 K, CD_3CN) of **6.8** with signal assignment.

6.8.5 Templation of 6.9 by cobalticarborane

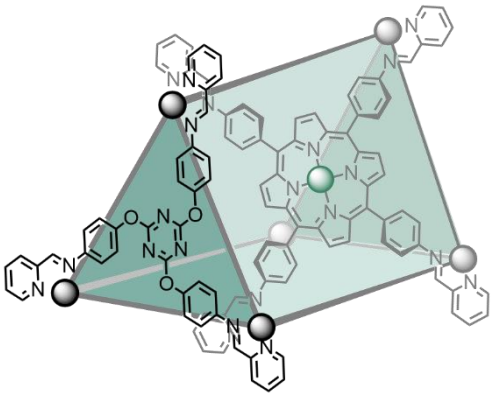

Triamine **6A** (0.73 mg, 1.82 × 10^{-6} mol, 2 equiv), tetramine **6D** (2.00 mg, 2.73 × 10^{-6} mol, 3 equiv), 2-formylpyridine (1.62 μL, 1.64 × 10^{-5} mol, 18 equiv), $Zn(NTf_2)_2$ (4.00 mg, 5.47 × 10^{-6} mol, 6 equiv) and sodium cobalticarborane (X, 1.50 mg, 4.33 × 10^{-6} mol, 5 equiv) were combined in CD_3CN (0.6 mL) in a sealed NMR tube. The mixture was heated at 70 °C for 16 h. Upon cooling to room temperature, Et_2O (*ca.* 10 mL) was added, precipitating a red solid. This mixture was centrifuged, the supernatant decanted, and the remaining solid dried over a N_2 stream to yield **6.9** as a red powder (7.48 mg, 8.72 × 10^{-7} mol, 93% based on proportion of **6.9**$(NTf_2)_7(X)_5$ present in the mixture by ^{1}H NMR integration). **^{1}H NMR** (400 MHz, 298 K, CD_3CN): δ 9.27 (s, 6H), 8.95 (d, J = 5.0 Hz, 6H), 8.86 (s, 6H), 8.72 (s, 6H), 8.66 – 8.47 (m, 24H), 8.44 (d, J = 5.1 Hz, 6H), 8.35 (d, J = 5.1 Hz, 6H), 8.34 – 8.28 (m, 12H), 8.23 (d, J = 5.1 Hz, 12H), 8.20 (dd, J = 8.1, 1.9 Hz, 6H), 8.17 (d, 4.3 Hz, 6H), 8.12 - 8.06 (m, 18H), 8.03 – 7.95 (m, 12H), 7.91 (d, J = 5.5 Hz, 6H), 7.85 (dd, J = 8.2, 2.0 Hz, 6H), 7.15 (d, J = 8.8 Hz, 12H), 6.99 (dd, J = 7.9, 2.3 Hz, 6H), 6.91 (dd, J = 8.0, 2.4 Hz, 6H), 6.88 (dd, J = 8.1, 2.4 Hz, 6H), 6.71 (dd, J = 8.0, 2.5 Hz, 6H), 6.30 (d, J = 8.8 Hz, 12H), 5.92 (dd, J = 7.9, 2.5 Hz, 6H) ppm. See Figure 6.24 for signal assignment. **LR-ESI-MS** [charge fragment, calculated for **6.9**$(NTf_2)_x(X)_{12-x}$]: *m/z* = 1434.9 [**6.9**$(NTf_2)_2(X)_5^{5+}$, 1434.9], 1426.0 [**6.9**$(NTf_2)_3(X)_4^{5+}$, 1426.2], 1417.2 [**6.9**$(NTf_2)_4(X)_3^{5+}$, 1417.4], 1408.7 [**6.9**$(NTf_2)_5(X)_2^{5+}$, 1408.7], 1399.6 [**6.9**$(NTf_2)_6(X)^{5+}$, 1400.0], 1149.0 [**6.9**$(NTf_2)(X)_5^{6+}$, 1149.0], 1141.8 [**6.9**$(NTf_2)_2(X)_4^{6+}$, 1141.8], 1134.5 [**6.9**$(NTf_2)_3(X)_3^{6+}$, 1134.5], 1127.2 [**6.9**$(NTf_2)_4(X)_2^{6+}$, 1127.2], 1119.9 [**6.9**$(NTf_2)_5(X)^{6+}$, 1120.0], 944.9 [**6.9**$(X)_5^{7+}$, 944.9], 938.6 [**6.9**$(NTf_2)(X)_4^{7+}$, 938.6], 932.4 [**6.9**$(NTf_2)_2(X)_3^{7+}$, 932.4], 926.1 [**6.9**$(NTf_2)_3(X)_2^{7+}$, 926.2], 919.9 [**6.9**$(NTf_2)_4(X)^{7+}$, 920.0], 786.3 [**6.9**$(X)_4^{8+}$, 786.3], 780.8 [**6.9**$(NTf_2)(X)_3^{8+}$, 780.8], 775.4 [**6.9**$(NTf_2)_2(X)_2^{8+}$, 775.4], 769.8 [**6.9**$(NTf_2)_3(X)^{8+}$, 770.0], 662.8 [**6.9**$(X)_3^{9+}$, 663.0], 658.0 [**6.9**$(NTf_2)(X)_2^{9+}$, 658.1], 653.3 [**6.9**$(NTf_2)_2(X)^{9+}$, 653.3]. Some peaks attributed to the cube could also be identified; see Figure 6.25. **HR-ESI-MS** *m/z* calculated for [**6.9**$(NTf_2)_5(X)_2]^{5+}$ = 1408.6241; observed = 1408.6234.

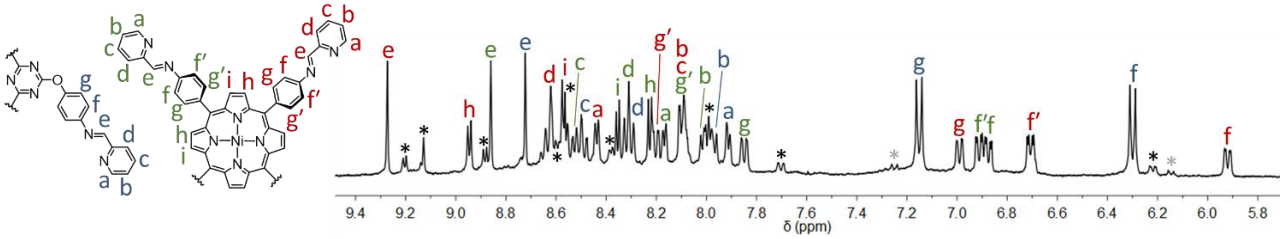

Figure 6.24 | Aromatic region of the ^{1}H NMR spectrum (500 MHz, 298 K, CD_3CN) of $CoC_4B_{18}H_{22}^-\subset$**6.8** with signal assignment. Black asterisks mark signals attributed to residual cube; grey asterisks mark signals attributed to residual tetrahedron.

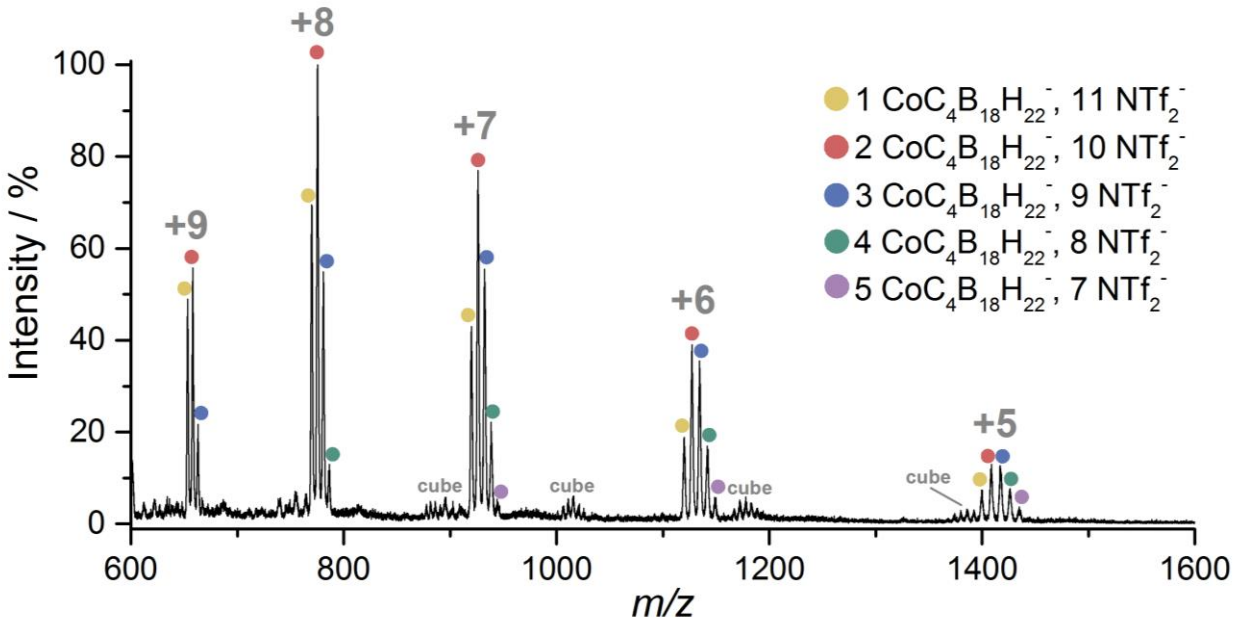

Figure 6.25 | ESI mass spectrum, of $CoC_4B_{18}H_{22}^-$⊂**6.8**, showing a distribution of charge fragments corresponding to **6.8**$(CoC_4B_{18}H_{22})_x(NTf_2)_{12-x}$.

6.8.6 Van't Hoff analysis of the triangular prism equilibrium

A small vial was charged with **6D** (4.00 mg, 5.47×10^{-5} mol, 3 equiv), **6C** (1.61 mg, 3.65×10^{-5} mol, 2 equiv), 2-formylpyridine (3.12 μL, 3.28×10^{-4} mol, 18 equiv), $Zn(NTf_2)_2 \cdot 6H_2O$ (8.00 mg, 1.09×10^{-4} mol, 6 equiv) and CD_3CN (3.0 mL). The mixture was sonicated until all starting materials dissolved (*ca.* 3 mins) and was then separated into six J-Young tubes, each with 0.5 mL of solution. Each NMR tube was heated at a specific temperature – either 295, 303, 313, 323, 328 or 333 K – for 72 h. Upon cooling to room temperature, a ^{1}H NMR spectrum was collected (Figure 6.26). No change in these spectra was observed after a further 72 h heating.

The equilibrium between the cube + tetrahedron and the triangular prism (*TP*) is described by the following equation

$$cube + tetrahedron \leftrightarrow 2\,TP$$

$$K_{eq} = \frac{[TP]^2}{[cube][tetrahedron]}$$

The ^{1}H NMR signals of the cube were often broad, preventing an accurate determination of their integration values. However, assuming all starting materials are consumed, [*cube*] = [*tetrahedron*] and thus the equation can be reduced to

$$K_{eq} = \frac{[TP]^2}{[tetrahedron]^2}$$

Integration of the tetrahedron protons relative to the triangular prism protons for each temperature state of the reaction thus provides K_{eq} for each value of temperature (T). A linear regression of these data was then undertaken using an integrated form of the Van't Hoff equation, where

$$\ln K_{eq} = \frac{-\Delta H}{RT} + \frac{\Delta S}{R}$$

where R is the ideal gas constant (8.314 J mol^{-1}), ΔH is the change in enthalpy and ΔS is the change in entropy.

Cooling a heated mixture was not observed to redistribute the equilibration of the mixture, suggesting that formation of the tetrahedron+cube mixture from the triangular prism is kinetically slow. Cooling each of the samples down to 233 K was not observed to alter the distribution of products observed at room temperature collection.

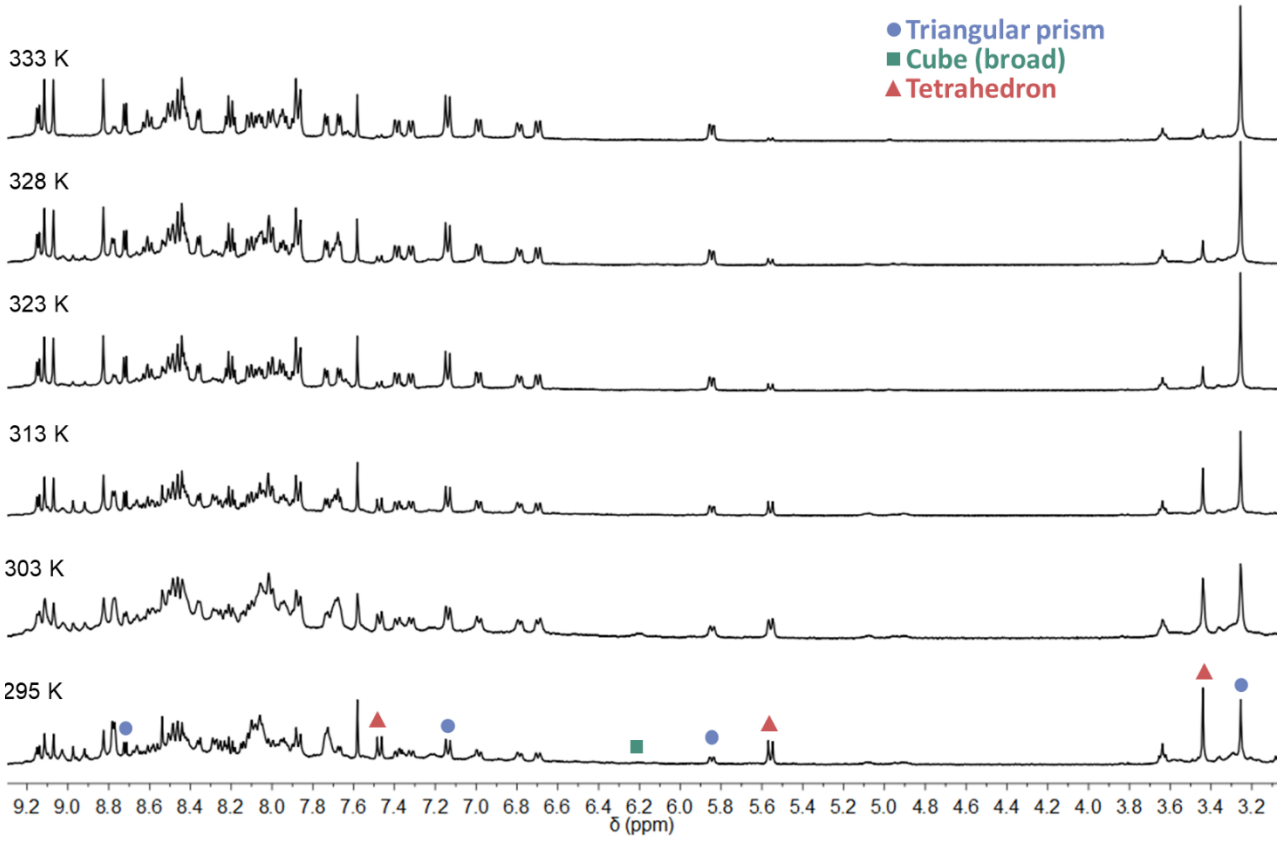

Figure 6.26 | ^{1}H NMR spectra (400 MHz, 298 K, CD_3CN) of the temperature-dependent synthesis of triangular prism **6.8**. Proton environments used in the Van't Hoff analysis are marked.

6.8.7 Crystallography

The crystals employed in this Chapter rapidly lost solvent after removal from the mother liquor and rapid handling prior to flash cooling in the cryostream was required to collect data. Due to the less than ideal resolution, bond lengths and angles within pairs of organic ligands were restrained to

be similar to each other (SAME) and thermal parameter restraints (SIMU, DELU) were applied to all non-metal atoms to facilitate anisotropic refinement. Ligand-based atoms that still displayed thermal parameters greater than 0.4 were further refined to approximate isotropic behaviour (ISOR). In all cases, the remaining anions present in the asymmetric unit could not be successfully assigned despite numerous attempts at modelling, including the use of rigid bodies. Consequently, the SQUEEZE[11] function of PLATON[12] was employed to remove the contribution of the electron density associated with these anions and the remaining highly disordered solvent molecules. The crystallographic data for this Chapter are available from the author upon request.

*6.8.7.1 Crystal structure of **6.5**·12NTf$_2$*

Formula $C_{312}H_{210}Co_6F_{72}N_{72}O_{48}S_{24}$, *M* 8226.53, Triclinic, *P*1– (#2), *a* 26.428(5), *b* 34.545(7), *c* 48.902(10) Å, α 79.82(3), β 85.36(3), γ 78.09(3)º, *V* 42951(16) Å^3, D_c 1.272 g cm^{-3}, *Z* 4, crystal size 0.180 by 0.100 by 0.090 mm, colour dark orange, habit block, temperature 100(2) Kelvin, λ(Synchrotron) 0.6889 Å, μ(Synchrotron) 0.400 mm^{-1}, *T*(SADABS)$_{min,max}$ 0.4759, 0.7440, $2\theta_{max}$ 33.48, *hkl* range –22 22, –28 28, –40 40, *N* 153699, N_{ind} 51890(R_{merge} 0.0934), N_{obs} 31579(I > 2σ(I)), N_{var} 7365, residuals* *R*1(*F*) 0.1698, *wR*2(F^2) 0.4249, GoF(all) 1.089, $\Delta\rho_{min,max}$ –0.521, 0.719 e$^-$ Å^{-3}. *$R1 = \Sigma||F_o| - |F_c||/\Sigma|F_o|$ for $F_o > 2\sigma(F_o)$; $wR2 = (\Sigma w(F_o^2 - F_c^2)^2/\Sigma(wF_c^2)^2)^{1/2}$ all reflections $w=1/[\sigma^2(F_o^2)+(0.1000P)^2+400.0000P]$ where $P=(F_o^2+2F_c^2)/3$

Specific refinement details

Crystals of **6.5·12NTf$_2$** were grown by slow diffusion of diethyl ether into a CD_3CN solution of **6.5**$(NTf_2)_{12}$. Despite the use of synchrotron radiation, few reflections at greater than 1.2 Å resolution were observed; nevertheless, the quality of the data is more than sufficient to establish the connectivity of the structure. The ellipsoids in the organic portion of the crystal are larger than ideal, reflective of the high thermal motion of atoms and resultant low intensity data. The asymmetric unit contained two whole triangular prisms.

The SQUEEZEd portion of the cell totals 5,137 electrons per unit cell, with a solvent accessible void volume of 20,013 Å^3 per unit cell. This equates to 1,284 electrons per structure, where $Z = 4$. This density accounts for the 8 unresolved NTf_2^- molecules per structure (8 × 137 e$^-$ = 1,096 e$^-$) and further unresolved solvent molecules (188 e$^-$).

*6.8.7.2 Crystal structure of 0.4$CoC_4B_{18}H_{22}$⊂**6.8**·8.725$CoC_4B_{18}H_{22}$·2.875$CB_{11}H_{12}$·0.5MeCN*

Formula $C_{318.77}H_{387.95}B_{152.68}Co_{6.72}N_{60.50}Ni_3Zn_6$, *M* 7682.19, Monoclinic, $P2_1/n$ (#14), *a* 43.5430(3), *b* 52.2987(3), *c* 47.2858(2) Å, β 111.67°, *V* 100071.6(10) Å^3, D_c 1.020 g cm^{-3}, *Z* 8, crystal size 0.080 by 0.080 by 0.040 mm, colour red, habit block, temperature 100(2) Kelvin, λ(Synchrotron) 0.6889 Å, μ(Synchrotron) 0.601 mm^{-1}, $T(\text{xia2})_{\text{min,max}}$ 0.9537, 1.0, $2\theta_{\text{max}}$ 36.50, *hkl* range –39 39, –47 46, –42 42, *N* 380358, N_{ind} 78703(R_{merge} 0.0576), N_{obs} 44404(I >2σ(I)), N_{var} 10820, residuals* *R*1(*F*) 0.1424, *wR*2(F^2) 0.4081, GoF(all) 1.093, $\Delta\rho_{\text{min,max}}$ –1.035, 2.554 e$^-$ Å^{-3}. *$R1 = \Sigma||F_o| - |F_c||/\Sigma|F_o|$ for $F_o > 2\sigma(F_o)$; $wR2 = (\Sigma w(F_o^2 - F_c^2)^2/\Sigma wF_c^2)^2)^{1/2}$ all reflections $w=1/[\sigma^2(F_o^2)+(0.2000P)^2+400.0000P]$ where $P=(F_o^2+2F_c^2)/3$

Specific refinement details

Crystals of 0.4$CoC_4B_{18}H_{22}$⊂**6.8**·8.725$CoC_4B_{18}H_{22}$·2.875$CB_{11}H_{12}$·0.5MeCN were grown by slow diffusion of diethyl ether into a CD_3CN solution of **6.8**$(NTf_2)_{12}$ containing excess $NaCoC_4B_{18}H_{22}$ and $CsCB_{11}H_{12}$. Despite the use of synchrotron radiation, few reflections at greater than 1.1 Å resolution were observed; nevertheless, the quality of the data is more than sufficient to establish the connectivity of the structure.

The anions present in the structure displayed a significant amount of disorder and thermal motion. As a result, all anion occupancies were allowed to freely refine, and were fixed to the closest 0.05 at the end of the structure refinement. The asymmetric unit contained two triangular prisms, each with a molecule of cobalticarborane bound inside (the occupancies of both bound anions refined as 0.4). In total, the asymmetric unit contains 13.45 molecules of $CoC_4B_{18}H_{22}^-$ and 5.75 molecules of $CB_{11}H_{12}^-$. Several of these anions were modelled as disordered over two or three positions. In two instances, $CoC_4B_{18}H_{22}^-$ and $CB_{11}H_{12}^-$ were modelled as disordered on top of each other. $CoC_4B_{18}H_{22}^-$ and $CB_{11}H_{12}^-$ were differentiated by the presence of high electron density peaks between carborate moieties, indicative of the presence of Co.

The carborate and cobalticarborate anions showed a significant amount of thermal motion. The SAME command was applied to five cobalticarborate anions to approximate icosahedral symmetry and realistically model these anions; all other anions were modelled as rigid groups. Given the 12-fold-symmetric disorder of the carbon atom in $CB_{11}H_{12}^-$, and the 5-fold symmetric disorder of the carbon atoms in $CoC_4B_{18}H_{22}^-$, all organic atoms in these anions were assigned as boron; there was no indication that any of the atoms were carbon outright.

The SQUEEZEd portion of the cell totals 6,105 electrons per unit cell, with a solvent accessible void volume of 23,186 Å^3 per unit cell. This equates to 763 electrons per structure, where *Z* = 8. This

density accounts for 2.4 unresolved $CoC_4B_{18}H_{22}^-$ anions per structure (164 e^- each, 394 e^- total) and further unresolved solvent molecules (369 e^-).

*6.8.7.3 Crystal structure of strychnine⊂**6.8**·12NTf₂*

Formula $C_{333}H_{226}F_{72}N_{74}Ni_3O_{50}S_{21}Zn_6$, *M* 8673.47, Triclinic, *P*1– (#2), *a* 24.5314(7), *b* 27.4382(6), *c* 31.7765(8) Å, α 78.027(2), β 78.100(2), γ 83.972(2)°, *V* 20430.4(9) $Å^3$, D_c 1.410 g cm^{-3}, *Z* 2, crystal size 0.300 by 0.100 by 0.040 mm, colour red, habit needle, temperature 100(2) Kelvin, λ(Synchrotron) 0.6889 Å, μ(Synchrotron) 0.634 mm^{-1}, $T(xia2)_{min,max}$ 0.9810, 1.0, $2\theta_{max}$ 42.52, *hkl* range –25 25, –27 28, –32 33, *N* 113889, N_{ind} 48160(R_{merge} 0.0989), N_{obs} 32363(I>2σ(I)), N_{var} 4325, residuals* *R*1(*F*) 0.2085, *wR*2(F^2) 0.4736, GoF(all) 1.033, $\Delta\rho_{min,max}$ –1.058, 3.513 e^- $Å^{-3}$. *$R1 = \Sigma||F_o| - |F_c||/\Sigma|F_o|$ for $F_o > 2\sigma(F_o)$; $wR2 = (\Sigma w(F_o^2 - F_c^2)^2/\Sigma wF_c^2)^2)^{1/2}$ all reflections w=1/[$\sigma^2(F_o^2)$+(0.1000P)^2+500.0000P] where P=(F_o^2+2F_c^2)/3

Specific refinement details

Crystals of strychnine⊂**6.8**·12NTf_2 were grown by slow diffusion of diethyl ether into a CD_3CN solution of **6.8**$(NTf_2)_{12}$ containing excess strychnine. Despite the use of synchrotron radiation, few reflections at greater than 0.95 Å resolution were observed; nevertheless, the quality of the data is more than sufficient to establish the connectivity of the structure.

It is unusual that a structure with an enantiomerically pure component would crystallise in a centrosymmetric space group, although this has been hypothesised by the crystallographic community.[13] No solution for the structure in *P*1, or any other chiral space group, was found. The diffraction capabilities of these crystals were poor, necessitating high levels of irradiation to collect high-angle data, leading to significant crystal decomposition by the end of the experiment. To obtain sufficient data completeness in a triclinic crystal system, several less-than-ideal images were integrated into the data and, despite numerous attempts at integration with resolution limits and frame omissions, the integration remains less than ideal. As such, the discussion of this structure in this thesis is limited to the effect of guest binding on the morphology of the cage scaffold, and not the particular characteristics of the guest within.

The presence of strychnine inside the cage was unambiguously identified by the electron density map, which showed a tube of amorphous electron density (that could not be successfully modelled as disordered anions or solvent molecules). Owing to its significant disorder and thermal motion, the strychnine present inside **6.8** was modelled as disordered over two positions employing rigid group

restraints. A third disordered component could be introduced, but it did not significantly reduce the ellipsoids or residuals of the structure, and was thus omitted.

The SQUEEZEd portion of the cell totals 2,620 electrons per unit cell, with a solvent accessible void volume of 6,908 $Å^3$ per unit cell. This equates to 1,310 electrons per structure, where $Z = 2$. This density accounts for 6 unresolved NTf_2^- anions per structure (6 × 137 e^- = 822 e^- total) and further unresolved solvent molecules (488 e^-).

*6.8.7.4 Crystal structure of testosterone⊂**6.8**·12NTf₂·2MeCN*

Formula $C_{335}H_{239}F_{72}N_{74}Ni_3O_{50}S_{24}Zn_6$, *M* 8806.78, Triclinic, *P*1– (#2), *a* 24.6285(15), *b* 27.660(2), *c* 31.783(3) Å, α 78.088(7), β 78.308(6), γ 84.065(6)º, *V* 20703(3) $Å^3$, D_c 1.413 g cm^{-3}, *Z* 2, crystal size 0.100 by 0.080 by 0.040 mm, colour block, habit dark red, temperature 100(2) Kelvin, λ(Synchrotron) 0.6889 Å, μ(Synchrotron) 0.700 mm^{-1}, $T(\text{xia2})_{\text{min,max}}$ 0.9832, 1.0, $2\theta_{\text{max}}$ 42.41, *hkl* range –25 25, –29 28, –32 32, *N* 73857, N_{ind} 43976(R_{merge} 0.0626), N_{obs} 30221(I > 2s(I)), N_{var} 4943, residuals* *R*1(*F*) 0.1731, *wR*2(F^2) 0.4350, GoF(all) 0.969, $\Delta\rho_{\text{min,max}}$ –1.065, 3.911 e^- $Å^{-3}$. *$R1 = \Sigma||F_o| - |F_c||/\Sigma|F_o|$ for $F_o > 2\sigma(F_o)$; $wR2 = (\Sigma w(F_o^2 - F_c^2)^2/\Sigma wF_c^2)^2)^{1/2}$ all reflections w=1/[$\sigma^2(F_o^2)$+(0.2000P)^2+400.0000P] where P=(F_o^2+2F_c^2)/3

Specific refinement details

Crystals of testosterone⊂**6.8**·12NTf_2·2MeCN were grown by slow diffusion of diethyl ether into a CD_3CN solution of **6.8**$(NTf_2)_{12}$ containing excess testosterone. Despite the use of synchrotron radiation, few reflections at greater than 0.95 Å resolution were observed; nevertheless, the quality of the data is more than sufficient to establish the connectivity of the structure.

As with strychnine⊂**6.8**·12NTf_2, testosterone⊂**6.8**·12NTf_2·2MeCN crystallised in a centrosymmetric space group. No solution for the structure in *P*1, or any other chiral space group, was found. The diffraction capabilities of these crystals were poor, necessitating high levels of irradiation to collect high-angle data, leading to significant crystal decomposition by the end of the experiment. To obtain sufficient data completeness in a triclinic crystal system, several less-than-ideal images were integrated into the data and, despite numerous attempts at integration with resolution limits and frame omissions, the integration remains less than ideal and the completeness of the data is low. As such, the discussion of this structure in this thesis is limited to the effect of guest binding on the morphology of the cage scaffold, and not the particular characteristics of the guest within.

The presence of testosterone inside the cage was unambiguously identified by the electron density map, which showed a tube of amorphous electron density (that could not be successfully modelled as disordered anions or solvent molecules). Owing to its significant disorder and thermal motion, the testosterone present inside **6.8** was modelled as disordered over three positions employing rigid group restraints. A series of short intermolecular H–H contacts between the cage and encapsulated guest result, owing to the significant disorder of the guest. Two ligand arms were further modelled as disordered over two sites.

The SQUEEZEd portion of the cell totals 2,009 electrons per unit cell, with a solvent accessible void volume of 5,591 $Å^3$ per unit cell. This equates to 1,005 electrons per structure, where $Z = 2$. This density accounts for 5 unresolved NTf_2^- anions per structure ($5 \times 137\ e^- = 685\ e^-$ total) and further unresolved solvent molecules (320 e^-).

6.9 References

[1] Mazik, M., Cavga, H., and Jones, P.G., *J. Am. Chem. Soc.*, **2005**, 127, 9045-9052.

[2] Ke, C., Destecroix, H., Crump, M.P., and Davis, A.P., *Nat. Chem.*, **2012**, 4, 718.

[3] Bloch, W.M., Holstein, J.J., Hiller, W., and Clever, G.H., *Angew. Chem. Int. Ed.*, **2017**, 56, 8285-8289.

[4] Argent, S.P., Adams, H., Riis-Johannessen, T., Jeffery, J.C., Harding, L.P., and Ward, M.D., *J. Am. Chem. Soc.*, **2006**, 128, 72-73.

[5] Preston, D., Barnsley, J.E., Gordon, K.C., and Crowley, J.D., *J. Am. Chem. Soc.*, **2016**, 138, 10578-10585.

[6] Ferguson, A., Staniland, R.W., Fitchett, C.M., Squire, M.A., Williamson, B.E., and Kruger, P.E., *Dalton Trans.*, **2014**, 43, 14550-14553.

[7] Rizzuto, F.J., Kieffer, M., and Nitschke, J.R., *Chem. Sci.*, **2018**, 9, 1925-1930.

[8] Meng, W., Breiner, B., Rissanen, K., Thoburn, J.D., Clegg, J.K., and Nitschke, J.R., *Angew. Chem. Int. Ed.*, **2011**, 50, 3479-3483.

[9] Rizzuto, F.J. and Nitschke, J.R., *Nat. Chem.*, **2017**, 9, 903-908.

[10] Wood, D.M., Meng, W., Ronson, T.K., Stefankiewicz, A.R., Sanders, J.K.M., and Nitschke, J.R., *Angew. Chem. Int. Ed.*, **2015**, 54, 3988-3992.

[11] Spek, A.L., *Acta Crystallogr. Sect C*, **2015**, 71, 9-18.

[12] Spek, A.L., *Acta Crystallogr. Sect. D*, **2009**, 65, 148-155.

[13] Flack, H.D. and Bernardinelli, G., *Cryst. Eng.*, **2003**, 6, 213-223.

Chapter 7

Tuning the redox properties of fullerene clusters within a metal-organic tetrahedron

7.1 Fullerenes and fullerene hosts

Fullerene C_{60} has a multi-electron accepting ability that results from its high-symmetry, conjugated structure.[1-3] This has led to the integration of fullerenes into photovoltaic devices[4,5] such as bulk-heterojunction solar cells,[6,7] and their application in artificial photosynthesis, and energy capture and storage.[8] The arrangement of fullerenes within these devices impacts their optoelectronic properties,[9] generating interest in new methods of rational control over fullerene organisation.[10,11]

A substantial body of research has thus been directed towards designing receptor molecules that can bind fullerenes in solution,[12] often with the aim of separating the different carbon allotropes from fullerene soot.[13-16] Both metal-organic[17-19] and purely covalent hosts[20-26] have been investigated, with aromatic stacking interactions between the host and the fullerene guest being used in many cases to drive binding.[27,28] Most such structures have been designed to bind a single fullerene; few examples of supramolecular hosts that can accommodate multiple fullerenes have been reported.[20,29,30] The aggregation of fullerenes has been investigated from a kinetic[31] and geometric[32] perspective, but rarely with a view towards controlling the electrical properties of fullerene clusters. A host that binds multiple fullerenes in proximity would be desirable, owing to the useful electronic properties predicted for fullerene clusters.[33,34]

This Chapter[35] focuses on a new method of preparing multi-fullerene host-guest complexes, where up to four molecules of fullerene C_{60} are brought together within reported $Fe^{II}_4L_6$ tetrahedral capsule **7.1**[36] (Figure 7.1). The structure of the host-guest complexes, including the number of fullerenes encapsulated per host, was observed to depend on the solvent employed when the fullerene guest was introduced. The structures of the complexes were elucidated using NMR spectroscopy, mass spectrometry, and single-crystal X-ray diffraction, by Dr Daniel Wood and Dr Tanya Ronson. Subsequent electrochemical and spectroscopic studies on these adducts revealed electronic communication between components within the assemblies, allowing for the electron-acceptor properties of encapsulated fullerene clusters to be tuned depending on the mode of encapsulation.

7.2 Background

Previous investigations by Dr Daniel Wood revealed that **7.1** bound up to 3 molecules of C_{60} per host in $MeNO_2$ (Figure 7.1). The choice of solvent influenced the outcome; conducting a similar experiment in MeCN yielded the smaller $Fe^{II}_3L_4$ species $C_{60}\subset$**7.2**, a congener of the configuration observed previously with C_{70}[36], as the major product (Figure 7.1b). The less-coordinating solvent disfavoured the formation of $C_{60}\subset$**7.2**, which requires two solvent molecules to coordinate to the apical Fe^{II} ion, thereby promoting the formation of $(C_{60})_{1\text{-}3}\subset$**7.1** in $MeNO_2$. Confirmation of the

encapsulation of three molecules of C_{60} within **7.1** was obtained by single crystal X-ray diffraction analysis. Three molecules of C_{60} protrude from the faces of **7.1**, leaving one empty face, lending the host-guest complex approximate C_3 symmetry.

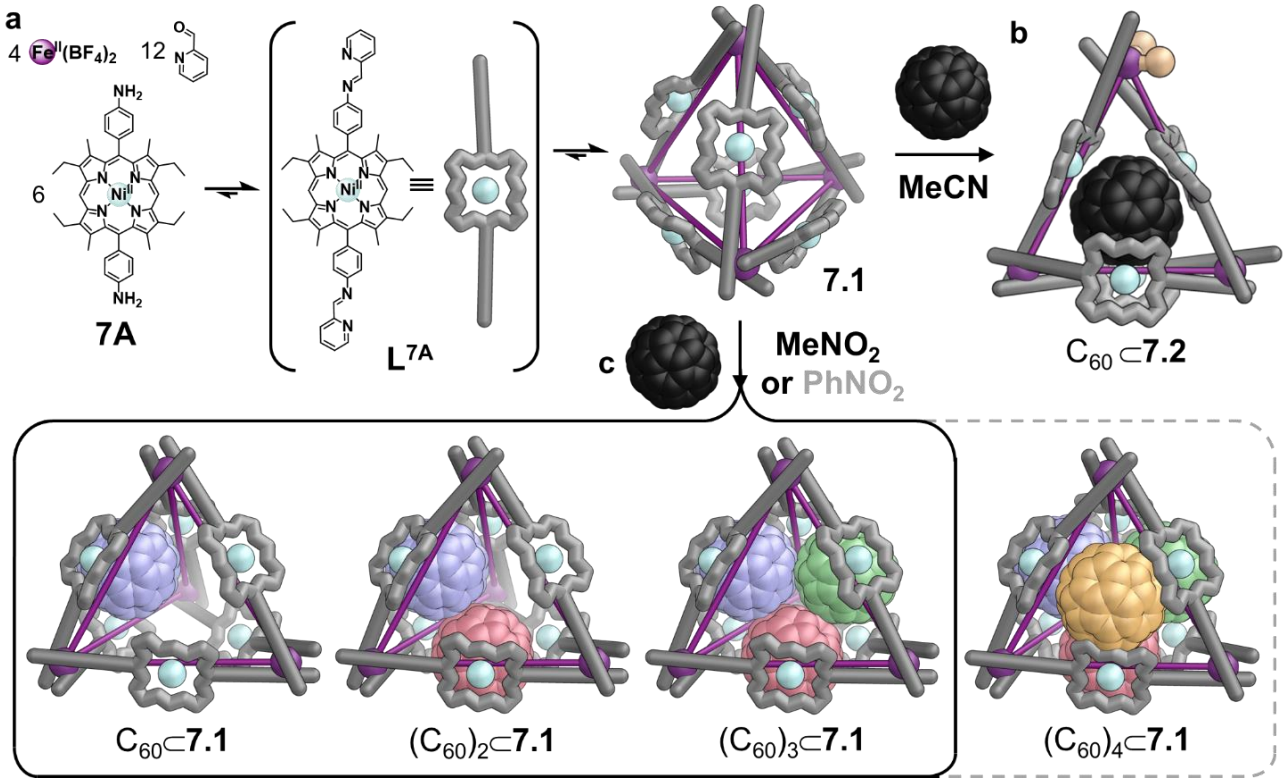

Figure 7.1 | **a**, Synthesis of reported **7.1**. **b**, Upon addition of C_{60} to **7.1** in MeCN, C_{60}⊂**7.2** was generated. **c**, In $MeNO_2$, adducts $(C_{60})_{1\text{-}3}$⊂**7.1** were observed; in $PhNO_2$, the fully occupied host-guest complex $(C_{60})_4$⊂**7.1** also formed. Purple lines between Fe^{II} centres illustrate the tetrahedral host framework.

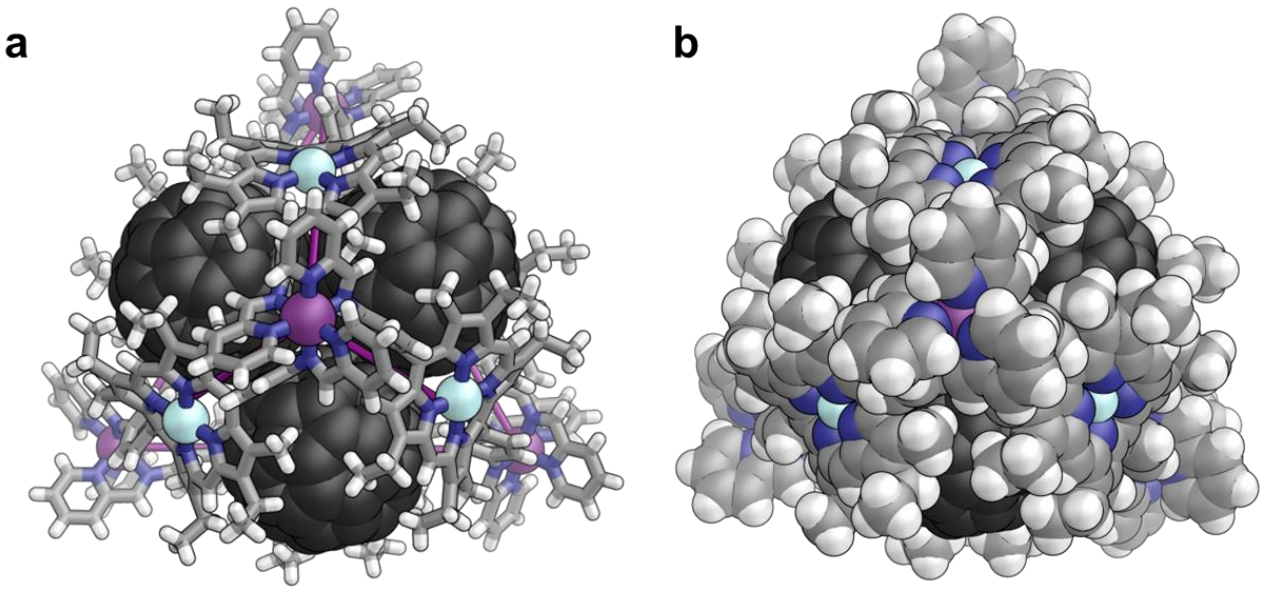

Figure 7.2 | Crystal structure of $(C_{60})_3$⊂**7.1** down the C_3 axis of the complex. Connections between the Fe^{II} centres (purple lines) are included in **a** to highlight the tetrahedral framework and the saddled conformation of the porphyrins. Counterions, disorder and solvent molecules have been omitted for clarity (C – grey, N – blue, Fe – purple, H – white, Ni – cyan, C_{60} – black).

7.3 Investigations into higher binding stoichiometries

Despite the presence of a fourth fullerene-sized pocket, no evidence for the inclusion of four C_{60} guests was observed in $MeNO_2$. When C_{60} (10 equiv) was added to a $PhNO_2$ solution of **7.1**, however, all four adducts $(C_{60})_{1\text{-}4}\subset$**7.1** were observed by ESI-MS (Figure 7.3b). The triply- and quadruply-occupied hosts were observed to be more abundant than the singly- or doubly-occupied cages by ESI-MS. The ^{1}H NMR spectra of $(C_{60})_{1\text{-}4}\subset$**7.1** in d_5-$PhNO_2$ retained the symmetry of the free cage **7.1**, with the most pronounced changes in chemical shifts observed for the porphyrin protons and imine signals of **7.1** following fullerene binding (Figure 7.3a). A single, broad ^{13}C signal corresponding to encapsulated C_{60} was likewise observed in d_5-$PhNO_2$ (Figure 7.3c). It was inferred that the increased solubility of C_{60} in $PhNO_2$ as compared to $MeNO_2$[37] promoted the formation of $(C_{60})_4\subset$**7.1** by increasing the amount of fullerene present in solution, thus favouring the tetra-adduct by mass action. ESI mass spectra of $(C_{60})_{1\text{-}4}\subset$**7.1** dissolved in $MeNO_2$ showed the consistent presence of peaks attributed to $(C_{60})_4\subset$**7.1**; re-equilibration to the $(C_{60})_{1\text{-}3}$ adducts was not observed over the course of 24 hours. Both $(C_{60})_{1\text{-}3}\subset$**7.1** and $(C_{60})_4\subset$**7.1** were likewise stable in MeCN for up to 8 hours, after which ESI-MS signals attributed to $C_{60}\subset$**7.2** could be identified.

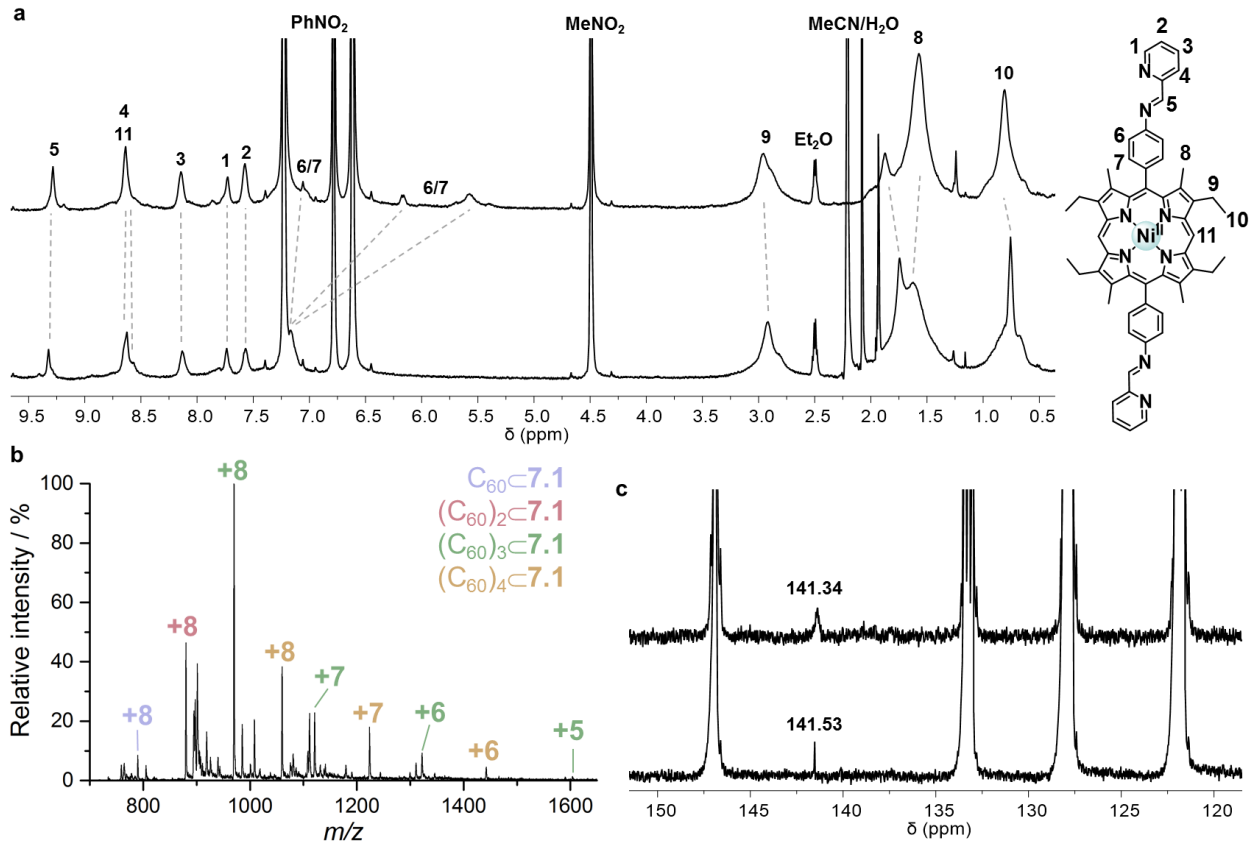

Figure 7.3 | Spectra of $(C_{60})_{1\text{-}4}\subset$**7.1**. **a**, ^{1}H NMR spectra (500 MHz, 298 K, d_5-$PhNO_2$) of $(C_{60})_{1\text{-}4}\subset$**7.1** (top) compared to **7.1** (bottom). **b**, ESI mass spectrum of $(C_{60})_{1\text{-}4}\subset$**7.1**. **c**, ^{13}C NMR spectra (126 MHz, 298 K, d_5-$PhNO_2$) of free C_{60} (bottom) compared to $(C_{60})_{1\text{-}4}\subset$**7.1** (top).

Crystallisation from solutions of $(C_{60})_{1\text{-}4}\subset$**7.1** in $PhNO_2$ provided X-ray quality crystals of $C_{60}\subset$**7.1** (structure solved by Dr Tanya Ronson), wherein a single fullerene was observed within capsule **7.1** (Figure 7.4). Rather than binding centrally, the single C_{60} was observed within a single facial pocket of **7.1** defined by three porphyrin moieties, in a similar manner to the binding observed in $(C_{60})_3\subset$**7.1**. This observation suggests that the binding configuration observed in $(C_{60})_3\subset$**7.1** is not due to steric crowding of the fullerenes. Although each window of the cage provides favourable aromatic interactions for binding C_{60}, comparatively, the central cavity does not. The broad ^{1}H NMR signals of these mixtures were not observed to coalesce into those corresponding to individual adducts over the range 235–320 K in CD_3CN (Figure 7.5).

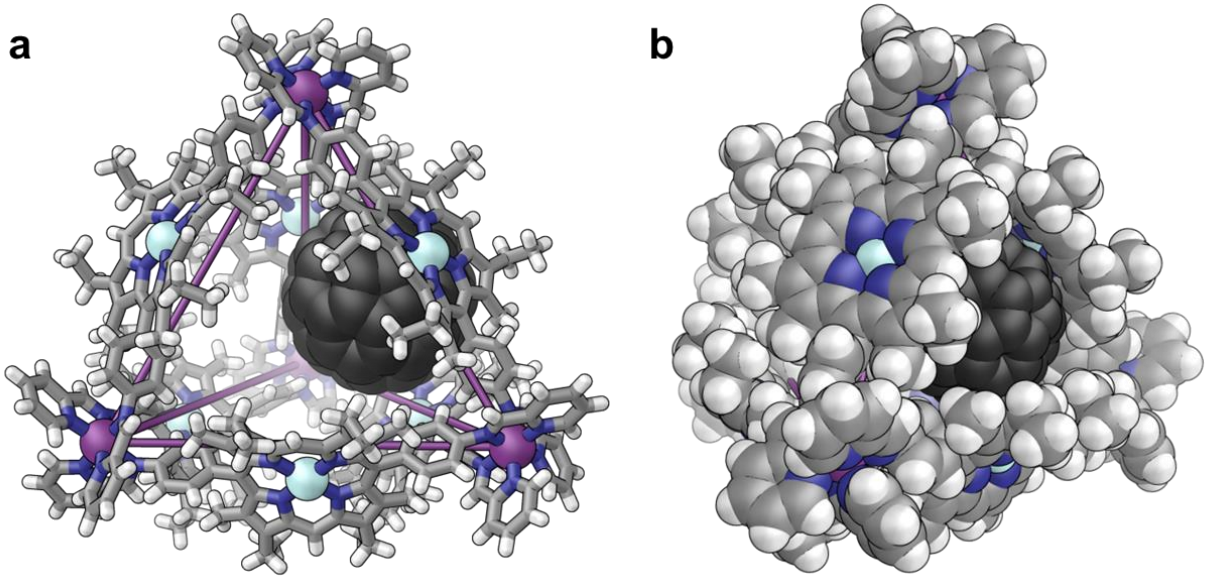

Figure 7.4 | Crystal structure of $C_{60}\subset$**7.1**, viewed **a**, through a window and **b**, adjacent to an edge of the complex, showing the off-centre binding of C_{60} within **7.1**.

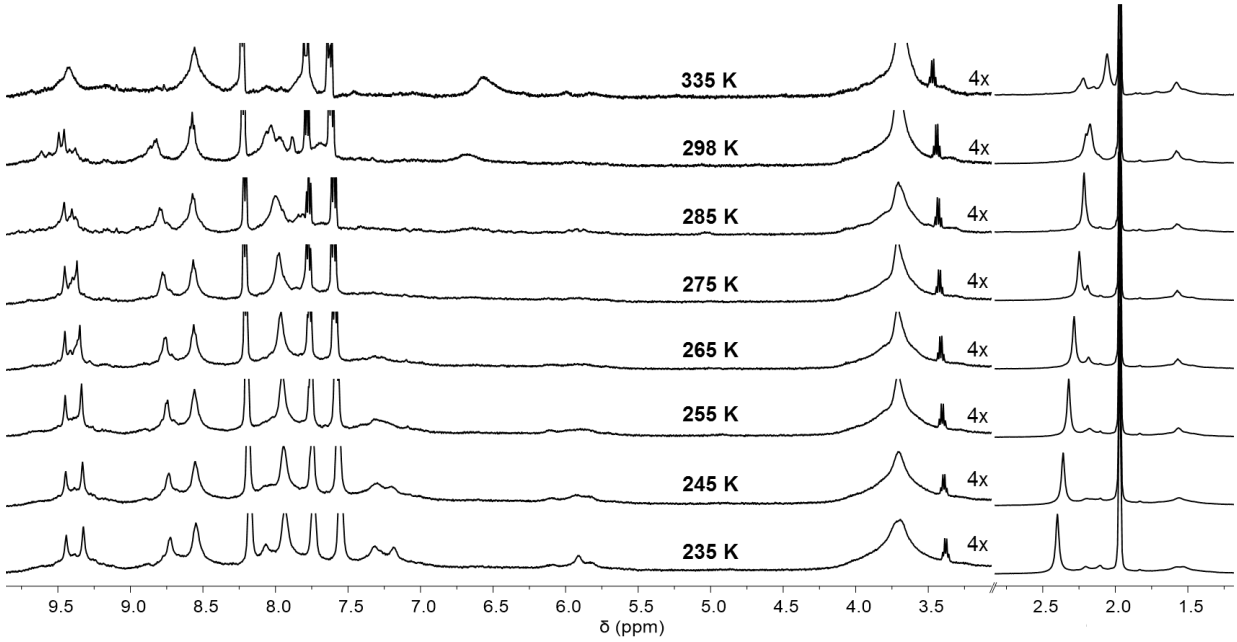

Figure 7.5 | Variable temperature ^{1}H NMR spectra (500 MHz, CD_3CN) of $(C_{60})_{1\text{-}4}\subset$**7.1**.

The Ni-porphyrins adopted a bent conformation in the crystal structure of **7.1**, with an N_{imine}-Ni-N_{imine} angle of 150.2°.[36] In $(C_{60})_3$⊂**7.1** the porphyrins were observed to adopt a more linear arrangement, with the average bend reduced to 157°. In C_{60}⊂**7.1**, the Ni-porphyrins enclosing the fullerene are more linear (161.8°) than those that do not (154.0°). Linearisation of the porphyrin units around the C_{60} guests appears to aid binding; this hinge-like porphyrin flexibility appears to be a key feature enabling the binding of up to four fullerene guests.

7.4 Cooperativity of fullerene binding

The binding of fullerenes within **7.1** in $PhNO_2$ was monitored by UV-Vis spectroscopy titration (Figure 7.6a). The graded hyperbolic shape of the binding isotherm suggested that fullerenes bind to **7.1** in an anti-cooperative manner (Figure 7.6b). Indeed, sigmoidal residuals and high fitting covariances were observed when these titration data were fitted to non-cooperative models. A better fit was obtained to a 1:2 host:guest isotherm, where $K_1 = (3.0 \pm 0.3) \times 10^5$ M^{-1} and $K_2 = (1.6 \pm 0.1) \times 10^4$ M^{-1} (Figure 7.6b).[38] It is hypothesised that the third and fourth binding events are not strong enough to be observed at the μM concentrations required for UV-Vis titration.

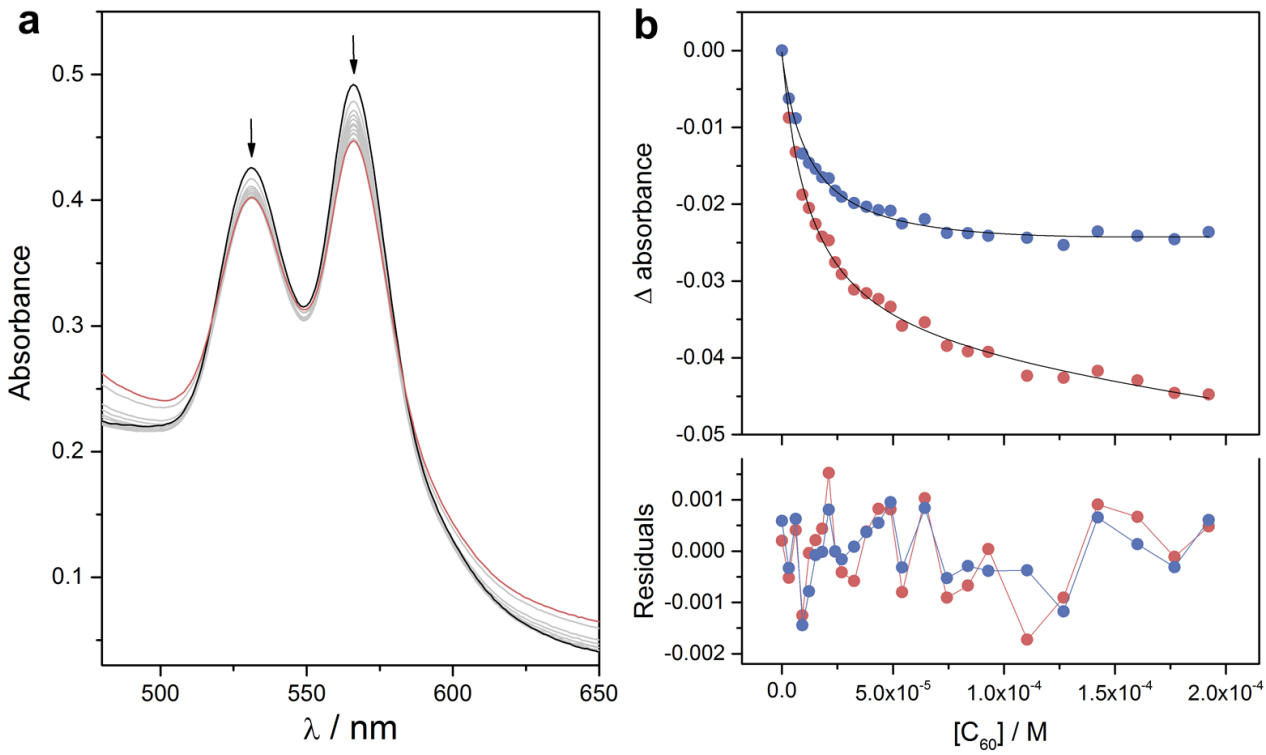

Figure 7.6 | **a**, UV-Vis titration of C_{60} into **7.1** in $PhNO_2$. The absorbance of C_{60} has been subtracted in each spectrum. The black trace is the spectrum of the initial solution (0 equiv C_{60}) and the red trace is the final spectrum (35 equiv C_{60}), with arrows showing the direction of spectral progression. **b**, Titration data fit to a 1:2 cooperative model (top) and the residuals from the fit (bottom). Low errors and a covariance an order of magnitude lower than that observed for the non-cooperative model were observed.

Host **7.1** contains four potential binding sites, necessitating the application of statistical factors to account for the binding microstates.[39] Here, $K_1 = 4k$, $K_2 = 3/2k$, $K_3 = 2/3k$ and $K_4 = 1/4k$. The ratio of K_2/K_1 is thus described as

$$\frac{K_2}{K_1} = \frac{\frac{3}{2}k}{4k} = \frac{3}{8}$$

and the cooperativity parameter α is described as

$$a = \frac{8K_2}{3K_1}$$

where $\alpha > 1$ is positive cooperativity and $\alpha < 1$ is negative cooperativity for the first two binding events. The value of the cooperativity parameter was calculated to be $\alpha = 0.14$, confirming the anticooperative binding of fullerenes within **7.1**.

The observation of anticooperative binding of fullerenes within **7.1** is consistent with the incomplete saturation of binding sites observed by ESI-MS (Figure 7.3b), which suggested progressively weaker fullerene binding events within **7.1**. Examination of the structures of $C_{60}\subset$**7.1** and $(C_{60})_3\subset$**7.1** suggests that the porphyrins maximise contact with the C_{60} guests by rotating towards them, thus pivoting away from adjacent pockets. This twisting of the porphyrins may result in the observed anticooperative binding in adjacent pockets.

7.5 Electrochemical investigations

It was hypothesised that the proximity of porphyrin and fullerene units in $(C_{60})_{1\text{-}4}\subset$**7.1** would facilitate electronic communication between the encapsulated guests as well as between the guests and host. To investigate the electrochemical effect of holding multiple fullerene guests in proximity, cyclic voltammetry (CV) experiments were carried out on **7.1** and its host-guest complexes over the range –2.5 to +1.0 V *vs.* Fc/Fc^+. CV was also conducted on $Fe^{II}{}_3L_4$ assembly **7.2**, which contains a single molecule of C_{60}, to facilitate the comparison between singly- and multiply-occupied fullerene hosts.

Two reductions and one broad oxidation were observed for **7.1** in 0.1 M nBu$_4$NPF$_6$/CH$_3$CN electrolyte at a scan rate of 500 mV s^{-1} (Figure 7.7). The single reduction wave at –1.73 V *vs*. Fc/Fc^+ and the broad oxidation wave at 0.17 V *vs.* Fc/Fc^+, both irreversible, are attributed to the porphyrin moieties,[40] while the reversible reduction at $E_{1/2} = –2.09$ V is attributed to a redox process localised on the pyridyl-imines coordinated to Fe^{II}.[41] The $Fe^{II}\rightarrow Fe^{III}$ oxidation process at the corners of the

cage occurs at the edge of the potential window for MeCN. CVs swept to potentials >+2 V showed a collapse of all redox waves, indicative of degradation of the complex upon oxidation to Fe^{III}. Lowering the scan rate from 500 to 100 and then 25 mV s^{-1} resolved the broad porphyrin-cantered oxidation process into three distinct redox waves (Figure 7.7b&c). This rate-dependent behaviour may be attributed either to electrical communication between porphyrin units in **7.1**, or to different responses from the distinct diastereomers observed (having *T*, S_4 and C_3 symmetries)[42] in solution.

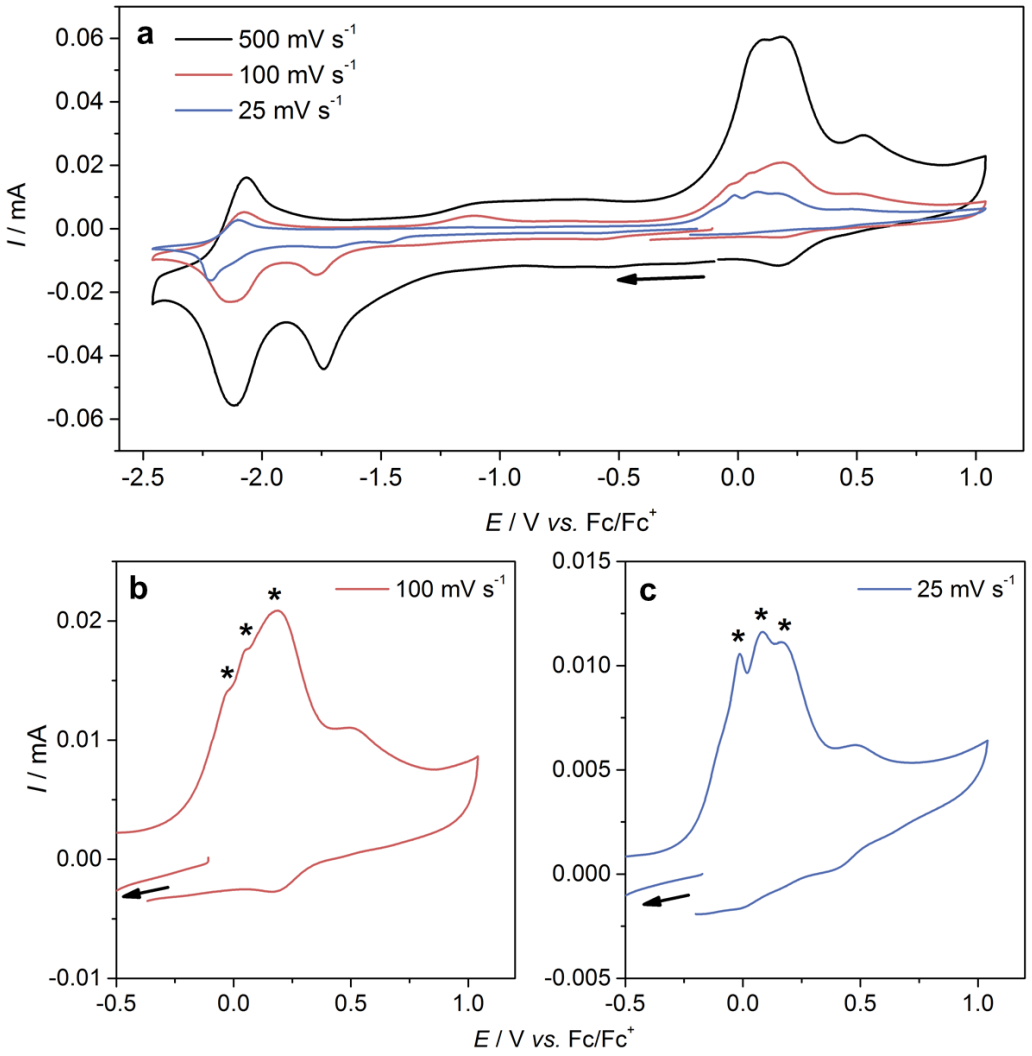

Figure 7.7 | **a**, CVs of **7.1** in 0.1 M nBu$_4$NPF$_6$/CH$_3$CN electrolyte at 500, 100 and 25 mV s^{-1}, indicating distinct electronic environments of the porphyrin units in **7.1**. Close-ups of anodic sweeps at **a**, 100 and **b**, 25 mV s^{-1}, showing three distinct waves, consistent with electrical communication between porphyrin units during oxidation. Arrows indicate the direction of the forward scan. The reversible wave at $E_{1/2}$ = +0.40 V is attributed to free Fe^{II} oxidation.

In 0.1 M nBu$_4$NPF$_6$/MeCN electrolyte, C$_{60}$⊂**7.2** displayed a broad, irreversible reduction wave at low potential, which may be attributed to overlapping reductions of C$_{60}$ (Figure 7.8). More definitive electrochemical data were obtained in a 1:4 DMF:MeCN medium containing 0.1 M nBu$_4$NPF$_6$. At high scan rates (200–500 mV s^{-1}), three processes corresponding to the reduction of C$_{60}$ inside the cavity were observed over the range –0.8 to –1.5 V (Figure 7.9). In addition, four

processes corresponding to cage **7.2** were observed: two reductions, attributed to the porphyrin cores and pyridyl-imine motifs, and two oxidations, one irreversible wave attributed to the porphyrins and one reversible process corresponding to the oxidation of the bis-chelated Fe^{II} apex.

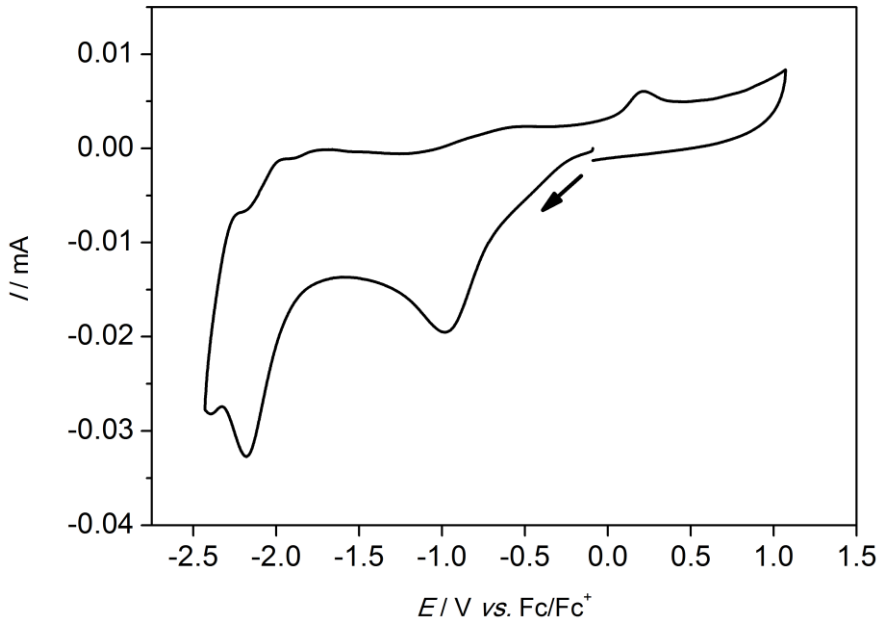

Figure 7.8 | CV of C_{60}⊂**7.2** in 0.1 M nBu$_4$NPF$_6$/CH$_3$CN electrolyte at 100 mV s^{-1}. The arrow indicates the direction of the forward scan. Fullerene reduction is observed as a single broad reduction band.

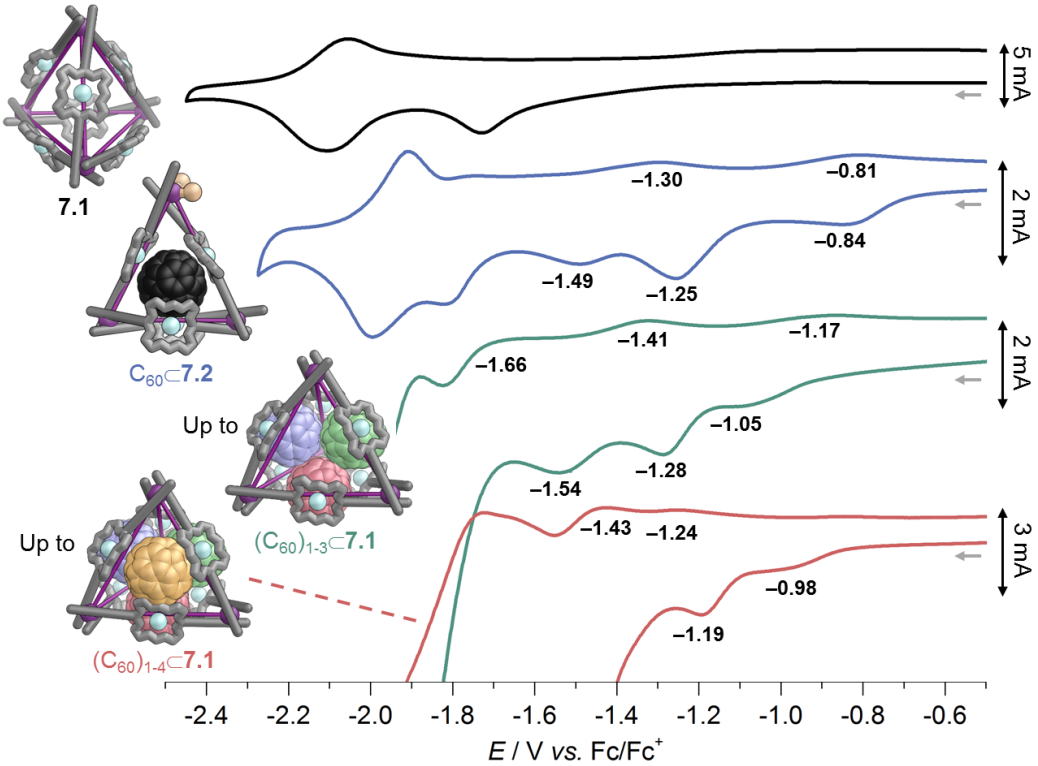

Figure 7.9 | CVs of the various assemblies. Measurements on **7.1** (black trace), $(C_{60})_{1\text{-}4}$⊂**7.1** (bottom red trace) and $(C_{60})_{1\text{-}3}$⊂**7.1** (2nd from the bottom, green trace) were conducted in nBu$_4$NPF$_6$/CH$_3$CN electrolyte, while C_{60}⊂**7.2** (2nd from the top, blue trace) was studied in nBu$_4$NPF$_6$/(1:4 DMF:CH$_3$CN) electrolyte. The reduction potentials of processes assigned to the bound fullerenes are labelled. Processes past –1.8 V are attributed to the cage framework. Grey arrows indicate the direction of the forward scan. The CV of **7.1** (top black trace) was carried out at a scan rate of 500 mV s^{-1}; all others were collected at 200 mV s^{-1}.

Several processes attributed to the bound fullerenes could be identified in the CVs of $(C_{60})_{1\text{-}3}\subset$**7.1** and $(C_{60})_{1\text{-}4}\subset$**7.1** (Figure 7.9). These occurred at –1.05, –1.28 and –1.54 V in $(C_{60})_{1\text{-}3}\subset$**7.1**, and at –0.98 and –1.19 V in $(C_{60})_{1\text{-}4}\subset$**7.1**, in 0.1 M *n*$Bu_4NPF_6$/MeCN electrolyte. In both cases, the reductions of the porphyrin and pyridyl-imine motifs occurred in the range –1.7 to –2.1 V, and often overlapped. Multiple oxidation processes attributed to the porphyrin moieties were observed in both host-guest adducts, consistent with the multiple distinct electronic environments of the ligands in these fullerene-occupied tetrahedra (Figure 7.9).

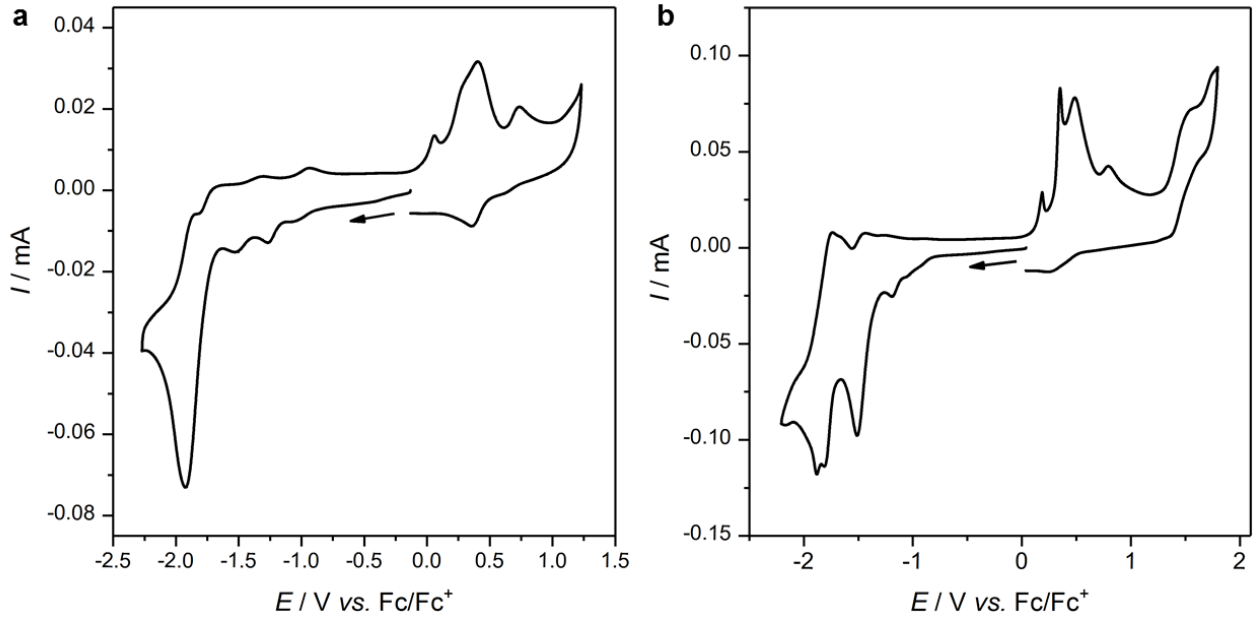

Figure 7.10 | Full CVs of **a**, $(C_{60})_{1\text{-}3}\subset$**7.1** and **b**, $(C_{60})_{1\text{-}4}\subset$**7.1** in 0.1 M *n*$Bu_4NPF_6$/$CH_3CN$ electrolyte at 200 mV s^{-1}. The arrow indicates the direction of the forward scan. The reduction process associated with the small portion of residual $PhNO_2$ (identified in the NMR spectrum) occurs underneath the wave at –1.5 V in **b**.

The first and second reduction potentials of unbound C_{60} are known to be solvent-dependent, generally occurring in the ranges –0.7 to –1.0 and –1.2 to –1.5 V *vs.* Fc/Fc^+, respectively.[43] The fullerene reductions observed for $C_{60}\subset$**7.2** fall within these ranges, however, the reduction potential of the fullerenes bound in **7.1** are cathodically shifted by *ca.* 0.1–0.4 V compared to those bound in **7.2 (**Figure 7.9). Furthermore, the fullerene redox waves in $(C_{60})_{1\text{-}4}\subset$**7.1** are anodically shifted compared to those observed for $(C_{60})_{1\text{-}3}\subset$**7.1**. The presence of more fullerenes in the cavity of **7.1** thus makes fullerene reduction easier. This observation is consistent with theoretical calculations, which predict that fullerene clusters may generate 'super atoms', wherein the first electron affinity of the van der Waals cluster increases in larger C_{60} aggregates.[34]

Comparison between the UV-Vis spectra of **7.1**, its fullerene adducts, and $C_{60}\subset$**7.2** revealed that the inclusion of fullerenes in all cases resulted in a bathochromic shift of the Soret (*ca.* +6 nm) and

Q (*ca.* +4 nm) bands of the porphyrin units (Figure 7.11), as observed in other porphyrin-fullerene assemblies.[44] In both host-guest spectra, Fe^{II}(pyridylimine)$_3$ MLCT bands overlapped with the porphyrin Q-bands. Broad bands in the range 700–900 nm for C_{60}⊂**7.2** and 600–750 nm for $(C_{60})_{1\text{-}4}$⊂**7.1** are attributed to ground state porphyrin-to-fullerene charge transfer (CT) interactions.[45,46]

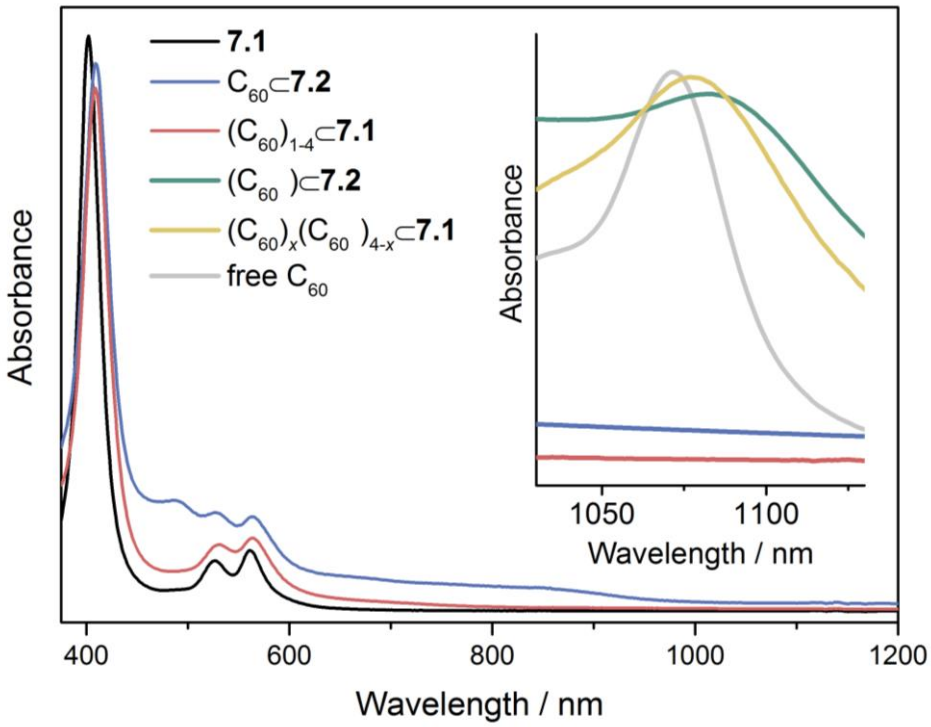

Figure 7.11 | UV-Vis spectra comparing the three species in MeCN. Inset displays the spectrum of free $C_{60}^{\bullet-}$ compared to the spectral signatures of $C_{60}^{\bullet-}$ bound in **7.1** and **7.2**, generated by chemical reduction with Cp_2Co.

7.6 Studies of C_{60} radicals inside assemblies

Chemical generation of $C_{60}^{\bullet-}$ within the cavities of **7.1** and **7.2** occurred following the addition of Cp_2Co (a $1e^-$ reductant, –1.3 V *vs.* Fc/Fc^+, *ca.* 1 equiv per fullerene) to a MeCN solution of $(C_{60})_{1\text{-}4}$⊂**7.1** or C_{60}⊂**7.2**. In both cases, near-IR absorptions were observed corresponding to encapsulated $C_{60}^{\bullet-}$ at 1078 and 1083 nm for **7.1** and **7.2**, respectively (inset, Figure 7.11). To compare against the value of free $C_{60}^{\bullet-}$, Cp_2Co was titrated into a solid sample of C_{60} in MeCN. Upon the dissolution of a substantial portion of $C_{60}^{\bullet-}$, the solution was filtered, and the titration continued, enabling differentiation between the spectral bands of free $C_{60}^{\bullet-}$ and C_{60}^{2-} (Figure 7.12).

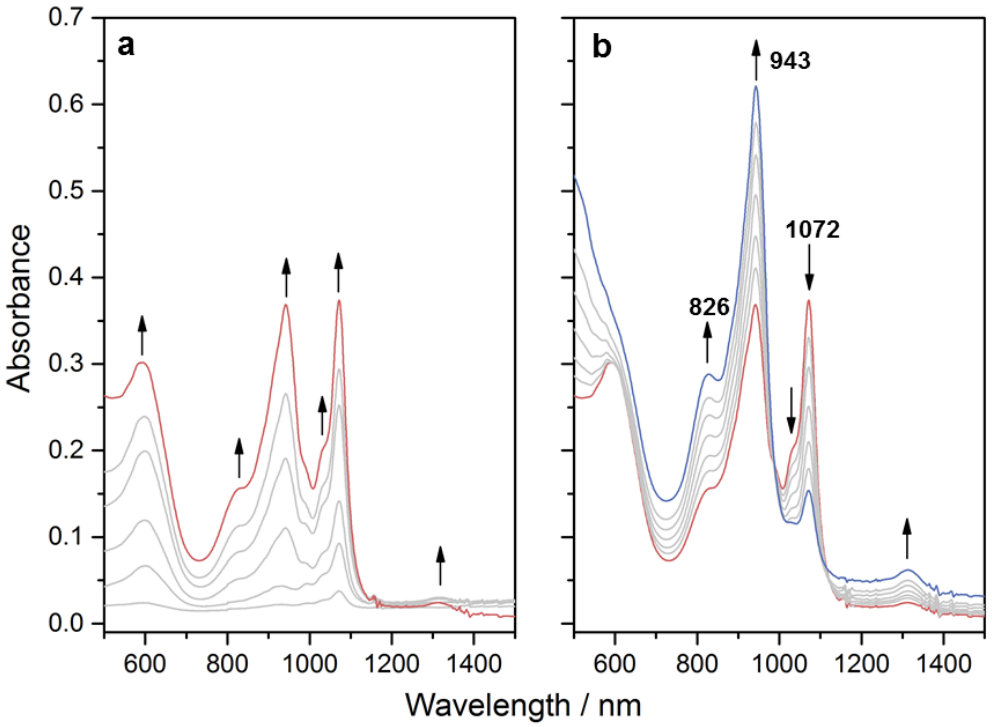

Figure 7.12 | **a**, The titration of Cp_2Co in MeCN to a solid sample of C_{60} dispersed in MeCN led to the evolution of NIR bands corresponding to anions of C_{60}, which were observed to dissolve in MeCN upon *ex-situ* generation. **b**, After filtering the remaining solid, the continued titration of Cp_2Co in MeCN to the mixture of fullerene anions in MeCN (red spectrum) resulted in an increase of higher energy NIR bands at 943 and 826 nm (attributed to C_{60}^{2-}), concomitant with a decrease in lower energy bands at 1072 and 1033 nm (attributed to $C_{60}^{\bullet-}$). The persistence of an isosbestic point indicated conversion of one species to another without decomposition.

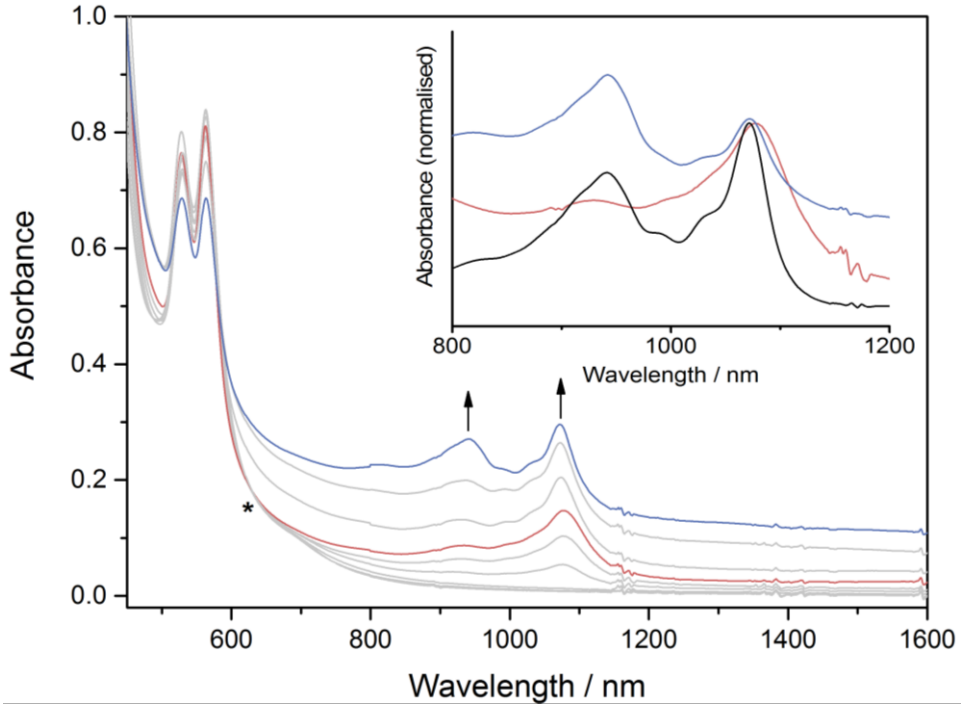

Figure 7.13 | The generation of $(C_{60}^{\bullet-})_x(C_{60})_{4-x}\subset$**7.1** was achieved by the addition of Cp_2Co to a solution of $(C_{60})_{1\text{-}4}\subset$**7.1** in MeCN. The inset highlights two important stages in the reduction, wherein a band is observed after the addition of 2 equiv. of Cp_2Co (red line). This is distinct in broadness and shift compared to the spectrum of C_{60} anions in MeCN alone (black line). During the addition of up to 5 equiv of Cp_2Co (blue line), this band was observed to slowly shift to a wavelength consistent with free $C_{60}^{\bullet-}$ (black line); the appearance of bands corresponding to free C_{60}^{2-} were also observed. It is proposed that the accessibility of C_{60}^{2-} within the assembly increases the charge repulsion between fullerene units, leading to expulsion from the cage.

The transitions of reduced fullerenes inside **7.1** and **7.2** were distinct in both linewidth and wavelength from the absorptions of unbound $C_{60}^{\bullet-}$ at 1072 nm or C_{60}^{2-} at 943 nm (Figure 7.12). The addition of further Cp_2Co led to a shift in these bands to wavelengths corresponding to unbound $C_{60}^{\bullet-}$ and C_{60}^{2-}, concurrent with the deterioration of isosbestic points, suggesting that fullerene anions were released into solution upon degradation of the host-guest complexes (Figure 7.13). *In-situ* spectroelectrochemical investigations on both host-guest complexes revealed no indication of reversibility for these processes, reflecting the limited reversibility observed by CV. CVs scanned over multiple cycles showed distinct differences, consistent with a change in host-guest occupancy and morphology upon the accessibility of C_{60}^{2-} (Figure 7.14).

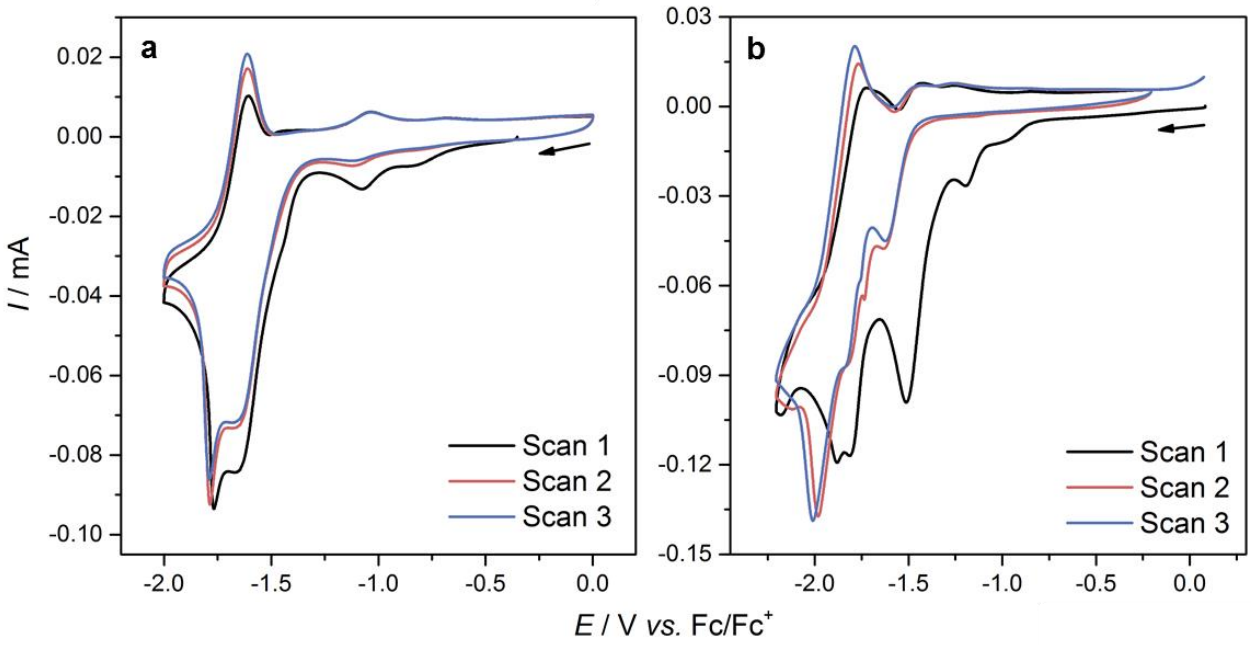

Figure 7.14 | CVs of **a**, $(C_{60})_{1\text{-}3}\subset$**7.1** and **b**, $(C_{60})_{1\text{-}4}\subset$**7.1** in 0.1 M nBu$_4NPF_6$/CH$_3$CN electrolyte at 200 mV s^{-1} over 3 sequential scan cycles. Notable in the voltammograms are the relaxation of redox waves attributed to the bound fullerenes by the second scan, suggesting that the guests are no longer bound in the cage after the first scan. The redox processes associated with the porphyrins/pyridylimines also shift cathodically following the first scan in **b**, resembling that of the free cage. The arrow indicates the direction of the forward scan.

7.7 Conclusions and future work

The encapsulation of multiple fullerenes in well-defined pockets within **7.1** was thus observed to tune the electron affinity of neutral C_{60} and lower the HOMO–LUMO gap of an encapsulated $C_{60}^{\bullet-}$ radical. When larger fullerene clusters were encapsulated in **7.1**, they became easier to reduce, confirming theoretical predictions that larger C_{60} van der Waals oligomers act as better electron traps.[34] This new, non-covalent mechanism of electronic tuning of fullerene reduction potentials may be of use in some of the myriad applications of fullerenes as electron acceptors, for example in the field of photovoltaics.[47]

While a wealth of coordination cages capable of binding multiple guests have been investigated, in few instances have the electrochemical consequences of molecular clustering been explored. Further investigation of the electronic changes to bound guests within hosts may provide information about the ways in which electronic communication between components can be engineered. For instance, the binding of guests in well-defined positions within a cage (such that the symmetry of that cage is broken), may lead to communication between ligand arms, or between the guest and localised regions of the cage. Exploring these ideas further could lead to the integration of host-guest systems into functional electronic or optical devices.

7.8 Experimental section

7.8.1 Synthesis and characterisation of host-guest species $(C_{60})_{1\text{-}4}$⊂7.1

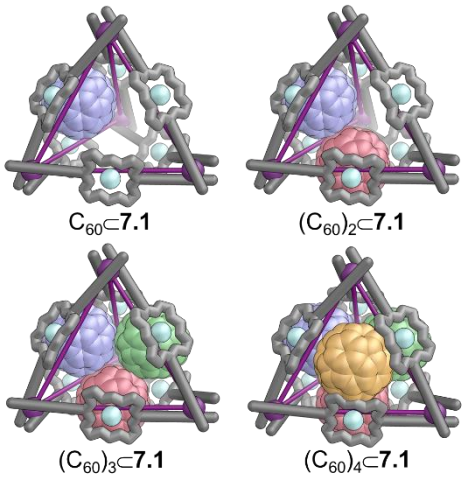

A sample of **7.1**$(BF_4)_8$ (6.0 mg, 0.96 µmol) was dissolved in nitrobenzene (1 mL). C_{60} (15 mg, 20.9 µmol) was added. The mixture was sonicated for five minutes then stirred at room temperature for 24 h. The sample was added dropwise to Et_2O and filtered through Celite. The solid residue was dissolved in $MeNO_2$ or MeCN, centrifuged to remove unbound C_{60}, and the supernatant decanted. The solution was dried to yield $(C_{60})_{1\text{-}4}$⊂**7.1**. **^{1}H NMR** (500 MHz, 298 K, d_5-$PhNO_2$): δ 9.29 (12H), 8.65 (24H), 8.14 (12H), 7.73 (12H), 7.57 (12H), 7.06 (24H), 5.58 (24H), 3.3 – 2.8 (br, 48H), 2.0 – 1.7 (br, 72H), 1.0 – 0.6 (br, 72H) ppm. All signals were broad; for spectral assignment see Figure 7.3a. **^{13}C NMR** (125 MHz, 298 K, d_5-$PhNO_2$): δ 175.3, 155.5, 141.3 (broad, C_{60}), 140.1, 130.8, 130.1, 95.4, 19.6 – 18.0, 17.8 – 15.3, 16.8 – 13.7 ppm. Reported ^{13}C signals for the cage are only those that could be identified from the ^{1}H–^{13}C HSQC spectrum. **LR-ESI-MS** [charge, calculated for $(C_{60})_x$⊂**7.1**$(BF_4)_8$]: *m/z* = 1604.1 [$(C_{60})_3$⊂**7.1**$(BF_4)_3^{5+}$, 1604.1], 1442.5 [$(C_{60})_4$⊂**7.1**$(BF_4)_2^{6+}$, 1442.4], 1322.1 [$(C_{60})_3$⊂**7.1**$(BF_4)_2^{6+}$, 1322.3], 1223.3 [$(C_{60})_4$⊂**7.1**$(BF_4)^{7+}$, 1223.9], 1121.0 [$(C_{60})_3$⊂**7.1**$(BF_4)^{7+}$, 1121.0], 1060.0 [$(C_{60})_4$⊂**7.1**$^{8+}$, 1060.1], 970.0 [$(C_{60})_3$⊂**7.1**$^{8+}$, 970.0], 880.0 [$(C_{60})_2$⊂**7.1**$^{8+}$, 880.0], 789.7 [C_{60}⊂**7.1**$^{8+}$, 789.8]. **HR-ESI-MS:** *m/z* calculated for C_{60}⊂**7.1**$^{8+}$ = 789.7439, found = 789.7435; *m/z* calculated for $(C_{60})_2$⊂**7.1**$^{8+}$ *m/z* = 879.8692, found = 879.8697; *m/z* calculated for $(C_{60})_3$⊂**7.1**$^{8+}$ = 969.8694, found = 969.8685; *m/z* calculated for $(C_{60})_4$⊂**7.1**$(BF_4)^{7+}$ = 1223.8489, found = 1223.8503. Note: samples of $(C_{60})_{1\text{-}4}$⊂**7.1** formed in $PhNO_2$ showed no sign of redistribution to the 1–3 adduct by ESI-MS after 8 hours standing at RT in CH_3CN. This suggests stability of the respective host-guest occupancies over the course of the electrochemical and spectroscopic experiments.

7.8.2 Cyclic voltammetry

Solution state cyclic voltammetry (CV) was performed using a BioLogic SP-150 potentiostat with ferrocene (Fc) as an internal reference. Measurements were conducted under an Ar atmosphere using a conventional three-electrode cell: a glassy carbon working electrode, a Pt wire auxiliary electrode, and a Ag/Ag^+ quasi-reference electrode. A 0.1 M $n$$Bu_4NPF_6$/$CH_2Cl_2$, /$CH_3CN$ or /(1:4 DMF:CH_3CN) electrolyte was used, with scan rates in the range 25–1000 mV s^{-1}. The ^{1}H NMR

spectrum of C_{60}⊂**7.2** in a 1:4 d_7-DMF:CD_3CN solution indicated stability in this solvent mixture over the course of the electrochemical experiments.

7.8.3 Procedure for UV-Vis titration

A solution of host (5.65×10^{-6} M) in $PhNO_2$ (2.00 mL) in a UV-Vis cuvette was titrated with a solution of the same concentration of host (5.65×10^{-6} M) and excess C_{60} guest (6.24×10^{-4} M) in $PhNO_2$, such that the concentration of the host remained constant with each addition of guest. Upon each addition, the solution was manually stirred for 2 min before acquiring the UV-Vis spectrum.

Fullerenes absorb strongly in the visible region. To counter the absorption of free fullerenes during the titration, a 'blank' titration was conducted with a solution of guest (6.24×10^{-4} M) in $PhNO_2$ into a UV-Vis cuvette with $PhNO_2$ (2.00 mL). This enabled the absorption spectra of the free fullerene to be subtracted from the original titration data. The validity of this method was supported by the presence of stable isosbestic points after subtraction of the individual fullerene spectra, furthermore indicating stability of the complex over the course of the titration.

Binding isotherms for the titrations were calculated using BINDFIT.[48] As $PhNO_2$ displays strong absorption >450 nm, only the two Q bands could be used in the fitting processes. The equations used for these analyses are available in the review by Thordarson.[38] The covariance of the fit (variance of the residuals divided by the variance in the data), along with the appearance of fitting residuals and error values, were used to qualify the appropriateness of each model, following the methods outlined by Thordarson and others.[49]

7.8.4 Procedure for the generation of C_{60} radicals

It was hypothesised that the unique electronic environment surrounding the fullerene guests in **7.1** and **7.2**, along with the different reduction behaviour observed by CV, would alter the optical properties of their corresponding anions.

Firstly, the generation of free $C_{60}^{\bullet-}$ or C_{60}^{2-} in MeCN was attempted; neutral C_{60} is insoluble in MeCN, precluding spectroelectrochemistry in this solvent. Neither $MeNO_2$ nor $PhNO_2$ could be used due to their low reduction potential windows. C_{60} is furthermore highly solvatochromic, necessitating that the comparison of bound $C_{60}^{\bullet-}$ and C_{60}^{2-} to the free anions be in the same solvent – MeCN was the only orthogonal choice.

To a solid sample of C_{60} in a UV-Vis cuvette was thus added dried and degassed MeCN. The cuvette was sealed under N_2, and remained under N_2 throughout the experiment. An initial blank

spectrum revealed no peaks in the visible or NIR region. Aliquots of a concentrated solution of Cp_2Co in dry and degassed MeCN were added to the cuvette containing C_{60}. Spectra were collected with increasing concentration of Cp_2Co until no insoluble fullerene was observed by eye. The steady evolution of a range of NIR and visible bands was observed (Figure 7.12a).

To determine which bands corresponded to $C_{60}^{\bullet-}$ or C_{60}^{2-}, the solution was firstly filtered to remove any insoluble neutral C_{60}. The titration of Cp_2Co into this solution was then continued. A steady increase in higher energy NIR bands at 943 and 826 nm was observed, concomitant with a decrease in lower energy bands at 1072 and 1033 nm (Figure 7.12b). Persistent isosbestic points were observed throughout the titration, indicating conversion of one species to another without degradation. This spectral progression may be attributed to the conversion of $C_{60}^{\bullet-}$ to C_{60}^{2-}, as higher redox states of C_{60} lie outside the potential window of Cp_2Co in MeCN (–1.3 V *vs.* Fc/Fc^+).[50] NIR bands corresponding to both anions in MeCN were thus assigned as: $C_{60}^{\bullet-}$ = 943 and 826 nm; C_{60}^{2-} = 1072 and 1033 nm.

These values correspond well to the electrogenerated fullerene anions reported by Kato *et al.* at 1073 and 930 nm for $C_{60}^{\bullet-}$, and at 950 and 840 nm for C_{60}^{2-} in nBu$_4$NClO$_4$/CH_2Cl_2 electrolyte,[51] lending confidence to the assignment of these charged states of C_{60} in MeCN. Thus, a yardstick for the bands of unbound C_{60} anions was achieved, providing comparison for the ex-*situ* generation of these anions in **7.1** and **7.2**.

7.8.5 Generation of $C_{60}^{\bullet-}$ in $(C_{60})_{1\text{-}4}$⊂7.1 and C_{60}⊂7.2

A sample of Cp_2Co in dried and degassed MeCN was titrated into a sample of either $(C_{60})_{1\text{-}4}$⊂**7.1** or C_{60}⊂**7.2** in dried and degassed MeCN. Spectral changes occurring in the visible and NIR region were monitored by UV-Vis spectroscopy. NIR bands were compared against those of the 'free' anions in MeCN, described above.

λ_{max} of $C_{60}^{\bullet-}$ in $(C_{60}^{\bullet-})_x(C_{60})_y$⊂**7.1** (where $(x + y) \leq 4$): 1078 nm

λ_{max} of $C_{60}^{\bullet-}$ in $(C_{60}^{\cdot-})$⊂**7.2**: 1083 nm

7.8.6 Crystal structure of C_{60}⊂7.1·8BF_4·6.5$PhNO_2$

Formula $C_{435}H_{344.50}B_8F_{32}Fe_4N_{54.50}Ni_6O_{13}$, M 7813.27, Trigonal, space group $R\bar{3}$ (#167), a 38.8188(8), b 38.8188(8), c 111.372(3) Å, γ 120°, V 145342(7) Å^3, D_c 1.071 g cm^{-3}, Z 12, crystal size 0.015 by 0.010 by 0.010 mm, colour dark brown, habit block, temperature 100(2) Kelvin, λ(Synchrotron) 0.6889 Å, μ(Synchrotron) 0.377 mm^{-1}, T(SADABS)$_{min,max}$ 0.5653, 0.7441, $2\theta_{max}$

33.36, *hkl* range –32 32, –32 32, –92 92, *N* 316681, N_{ind} 9789(R_{merge} 0.0856), N_{obs} 8028(I > 2σ(I)), N_{var} 1302, residuals* *R*1(*F*) 0.1424, *wR*2(F^2) 0.3879, GoF(all) 1.148, $\Delta\rho_{min,max}$ –0.397, 0.658 e^- $Å^{-3}$, CCDC 1549079. $^*R1 = \Sigma||F_o| - |F_c||/\Sigma|F_o|$ for $F_o > 2\sigma(F_o)$; $wR2 = (\Sigma w(F_o^2 - F_c^2)^2/\Sigma(wF_c^2)^2)^{1/2}$ all reflections $w=1/[\sigma^2(F_o^2)+(0.2000P)^2+1500.0000P]$ where $P=(F_o^2+2F_c^2)/3$

Specific refinement details

X-ray quality crystals of $C_{60}\subset$**7.1**$\cdot 8BF_4\cdot 6.5PhNO_2$ were grown by vapour diffusion of diethyl ether into a nitrobenzene solution of $(C_{60})_{1\text{-}4}\subset$**7.1**. The crystals employed proved to be weakly diffracting and rapidly suffered solvent loss. Rapid (<1 min) handling prior to flash cooling in the cryostream was required to collect data. Despite these measures and the use of synchrotron radiation, few reflections at greater than 1.2 Å resolution were observed. Despite these limitations the data is more than sufficient to establish the connectivity of the structure. The asymmetric unit contains one third of a $Fe^{II}_4L_6$ tetrahedron and C_{60} guest. There is a significant amount of thermal motion in the extremities of the molecule and extensive thermal parameter and bond length restraints were required to facilitate realistic modelling of the organic parts of the structure. The bond lengths and angles within the two crystallographically unique organic ligands were restrained to be similar to each other and some additional bond length restraints were applied to achieve a reasonable model.

Three of the porphyrin ethyl substituents were modelled as disordered over two locations and several more show evidence of thermal motion resulting from the presence of dynamic disorder in these groups. Consequently, there are a number of close contacts between symmetry-generated and/or disordered methyl groups. One nitrobenzene solvent molecule was modelled as disordered over two locations and all nitrobenzenes were modelled with isotropic thermal parameters and substantial bond length restraints.

The positioning of the C_{60} molecule was established unequivocally from the electron density map. This C_{60} molecule is rotationally disordered around a threefold axis and behaves as a shell of electron density, similar to disorder seen in other fullerene structures.[52-54] To facilitate realistic modelling a rigid-body constraint of a well-defined C_{60} was used and the C_{60} was refined with isotropic thermal parameters. The thermal parameters of the C_{60} atoms remain higher than ideal, possibly indicative of further unresolved disorder.

Only one tetrafluoroborate lattice site (per asymmetric unit) could be located. This tetrafluoroborate anion was modelled as disordered over three locations with a number of bond length and thermal parameter restraints. The remaining anions (five per tetrahedron) and additional solvent molecules within the lattice were significantly disordered and despite numerous attempts at

modelling, including with rigid bodies, no satisfactory model for the electron-density associated with them could be found. Therefore, the SQUEEZE[55] function of PLATON[56] was employed to remove the contribution of the electron density associated with the anions and disordered solvent from the model, which resulted in more satisfactory residuals. The crystallography in this project was performed by Dr Tanya Ronson.

7.9 References

[1] Chaur, M.N., Melin, F., Ortiz, A.L., and Echegoyen, L., *Angew. Chem. Int. Ed.*, **2009**, 48, 7514-7538.

[2] Echegoyen, L. and Echegoyen, L.E., *Acc. Chem. Res.*, **1998**, 4842, 593-601.

[3] Reed, C.A. and Bolskar, R.D., *Chem. Rev.*, **2000**, 100, 1075-1120.

[4] Clarke, T.M. and Durrant, J.R., *Chem. Rev.*, **2010**, 110, 6736-6767.

[5] Günes, S., Neugebauer, H., and Sariciftci, N.S., *Chem. Rev.*, **2007**, 107, 1324-1338.

[6] Facchetti, A., *Chem. Mater.*, **2011**, 23, 733-758.

[7] Cambarau, W., Fritze, U.F., Viterisi, A., Palomares, E., and von Delius, M., *Chem. Commun.*, **2015**, 51, 1128-1130.

[8] Tachibana, Y., Vayssieres, L., and Durrant, J.R., *Nat. Photon.*, **2012**, 6, 511-518.

[9] Barnes, J.C., Dale, E.J., Prokofjevs, A., Narayanan, A., Gibbs-Hall, I.C., Juríček, M., Stern, C.L., Sarjeant, A.A., Botros, Y.Y., Stupp, S.I., and Stoddart, J.F., *J. Am. Chem. Soc.*, **2015**, 137, 2392-2399.

[10] Liao, X.-X., Wang, T., Wang, J., Zheng, J.-C., Wang, C., and Yam, V.W.-W., *ACS Appl. Mater. Interfaces*, **2013**, 5, 9579-9584.

[11] Neti, V.S.P.K., Saha, M.L., Yan, X., Zhou, Z., and Stang, P.J., *Organometallics*, **2015**, 34, 4813-4815.

[12] Suzuki, K., Takao, K., Sato, S., and Fujita, M., *J. Am. Chem. Soc.*, **2010**, 132, 2544-2545.

[13] Garcia-Simon, C., Garcia-Borras, M., Gomez, L., Parella, T., Osuna, S., Juanhuix, J., Imaz, I., Maspoch, D., Costas, M., and Ribas, X., *Nat. Commun.*, **2014**, 5, 5557.

[14] Boyd, P.D.W. and Reed, C.A., *Acc. Chem. Res.*, **2005**, 38, 235-242.

[15] Canevet, D., Pérez, E.M., and Martín, N., *Angew. Chem. Int. Ed.*, **2011**, 50, 9248-9259.

[16] Shoji, Y., Tashiro, K., and Aida, T., *J. Am. Chem. Soc.*, **2004**, 126, 6570-6571.

[17] Kishi, N., Akita, M., and Yoshizawa, M., *Angew. Chem. Int. Ed.*, **2014**, 53, 3604-3607.

[18] Nakamura, T., Ube, H., Miyake, R., and Shionoya, M., *J. Am. Chem. Soc.*, **2013**, 135, 18790-18793.

[19] Garcia-Simon, C., Costas, M., and Ribas, X., *Chem. Soc. Rev.*, **2016**, 45, 40-62.

[20] Kang, B., Totten, R.K., Weston, M.H., Hupp, J.T., and Nguyen, S.T., *Dalton Trans.*, **2012**, 41, 12156-12162.

[21] Tashiro, K. and Aida, T., *Chem. Soc. Rev.*, **2007**, 36, 189-197.

[22] Stefankiewicz, A.R., Tamanini, E., Pantoş, G.D., and Sanders, J.K.M., *Angew. Chem. Int. Ed.*, **2011**, 50, 5725-5728.

[23] Davis, C.M., Lim, J.M., Larsen, K.R., Kim, D.S., Sung, Y.M., Lyons, D.M., Lynch, V.M., Nielsen, K.a., Jeppesen, J.O., Kim, D., Park, J.S., and Sessler, J.L., *J. Am. Chem. Soc.*, **2014**, 136, 10410-10417.

[24] Gil-Ramírez, G., Karlen, S.D., Shundo, A., Porfyrakis, K., Ito, Y., Briggs, G.A.D., Morton, J.J.L., and Anderson, H.L., *Org. Lett.*, **2010**, 12, 3544-3547.

[25] Maggini, L., Fustos, M.-E., Chamberlain, T.W., Cebrian, C., Natali, M., Pietraszkiewicz, M., Pietraszkiewicz, O., Szekely, E., Kamaras, K., De Cola, L., Khlobystov, A.N., and Bonifazi, D., *Nanoscale*, **2014**, 6, 2887-2894.

[26] Moreira, L., Calbo, J., Illescas, B.M., Aragó, J., Nierengarten, I., Delavaux-Nicot, B., Ortí, E., Martín, N., and Nierengarten, J.-F., *Angew. Chem. Int. Ed.*, **2015**, 54, 1255-1260.

[27] Sygula, A., Fronczek, F.R., Sygula, R., Rabideau, P.W., and Olmstead, M.M., *J. Am. Chem. Soc.*, **2007**, 129, 3842-3843.

[28] Tanaka, T. and Osuka, A., *Chem. Soc. Rev.*, **2015**, 44, 943-969.

[29] Mahata, K., Frischmann, P.D., and Würthner, F., *J. Am. Chem. Soc.*, **2013**, 135, 15656-15661.

[30] Rizzuto, F.J. and Nitschke, J.R., *Nat. Chem.*, **2017**, 9, 903-908.

[31] Prylutskyy, Y.I., Buchelnikov, A.S., Voronin, D.P., Kostjukov, V.V., Ritter, U., Parkinson, J.A., and Evstigneev, M.P., *Phys. Chem. Chem. Phys.*, **2013**, 15, 9351-9360.

[32] Montero-Alejo, A.L., Menendez-Proupin, E., Fuentes, M.E., Delgado, A., Montforts, F.P., Montero-Cabrera, L.A., and Garcia de la Vega, J.M., *Phys. Chem. Chem. Phys.*, **2012**, 14, 13058-13066.

[33] Hou, W.-C. and Huang, S.-H., *J. Hazardous Mater.*, **2017**, 322, 310-317.

[34] Shubina, T.E., Sharapa, D.I., Schubert, C., Zahn, D., Halik, M., Keller, P.A., Pyne, S.G., Jennepalli, S., Guldi, D.M., and Clark, T., *J. Am. Chem. Soc.*, **2014**, 136, 10890-10893.

[35] Rizzuto, F.J., Wood, D.M., Ronson, T.K., and Nitschke, J.R., *J. Am. Chem. Soc.*, **2017**, 139, 11008-11011.

[36] Wood, D.M., Meng, W., Ronson, T.K., Stefankiewicz, A.R., Sanders, J.K.M., and Nitschke, J.R., *Angew. Chem. Int. Ed.*, **2015**, 54, 3988-3992.

[37] Marcus, Y., Smith, A.L., Korobov, M.V., Mirakyan, A.L., Avramenko, N.V., and Stukalin, E.B., *J. Phys. Chem.*, **2001**, 105, 2499-2506.

[38] Thordarson, P., *Chem. Soc. Rev.*, **2011**, 40, 1305-1323.

[39] Zarra, S., Smulders, M.M.J., Lefebvre, Q., Clegg, J.K., and Nitschke, J.R., *Angew. Chem. Int. Ed.*, **2012**, 51, 6882-6885.

[40] Kadish, K.M., Smith, K.M., and Guilard, R., *The Porphyrin Handbook: Database of redox potentials and binding constants*. 1999: Academic Press.

[41] Roth, H.G., Romero, N.A., and Nicewicz, D.A., *Synlett*, **2016**, 27, 714-723.

[42] Beissel, T., Powers, R.E., Parac, T.N., and Raymond, K.N., *J. Am. Chem. Soc.*, **1999**, 121, 4200-4206.

[43] Hirsch, A. and Brettreich, M., *Fullerenes: Chemistry and Reactions*. 2006, Weinheim: John Wiley & Sons.

[44] Sun, D., Tham, F.S., Reed, C.A., Chaker, L., and Boyd, P.D.W., *J. Am. Chem. Soc.*, **2002**, 124, 6604-6612.

[45] Hosseini, A., Taylor, S., Accorsi, G., Armaroli, N., Reed, C.A., and Boyd, P.D.W., *J. Am. Chem. Soc.*, **2006**, 128, 15903-15913.

[46] Armaroli, N., Marconi, G., Echegoyen, L., Bourgeois, J.-P., and Diederich, F., *Chem. – Eur. J.*, **2000**, 6, 1629-1645.

[47] Li, C.-Z., Yip, H.-L., and Jen, A.K.Y., *J. Mater. Chem. B*, **2012**, 22, 4161-4177.

[48] Samanta, D., Mukherjee, S., Patil, Y.P., and Mukherjee, P.S., *Chem. – Eur. J.*, **2012**, 18, 12322-12329.

[49] Brynn Hibbert, D. and Thordarson, P., *Chem. Commun.*, **2016**, 52, 12792-12805.

[50] Connelly, N.G. and Geiger, W.E., *Chem. Rev.*, **1996**, 96, 877-910.

[51] Kato, T., *Laser Chem.*, **1994**, 14, 155-160.

[52] Hardie, M.J., Torrens, R., and Raston, C.L., *Chem. Commun.*, **2003**, 1854-1855.

[53] Makha, M., Hardie, M.J., and Raston, C.L., *Chem. Commun.*, **2002**, 1446-1447.

[54] Bi, Y., Liao, W., Wang, X., Wang, X., and Zhang, H., *Dalton Trans.*, **2011**, 40, 1849-1851.

[55] van der Sluis, P. and Spek, A.L., *Acta Cryst.*, **1990**, A46, 194-201.

[56] Spek, A.L., *PLATON: A Multipurpose Crystallographic Tool*. 2008, Utrecht University: Utrecht, The Netherlands.

Chapter 8

Final remarks

Metal-organic cages that can bind multiple guests in more than one mode or location enable systems of interacting molecules to express complex and varied functions. In particular, the translation of the principles behind biological allostery into supramolecular chemistry has enabled the generation of distinct chemical systems that are able to recognise and respond to homo- and hetero-tropic guest binding events. This thesis has explored the potential for different modes of allosteric binding to lead to new functions for host-guest chemistry: beyond binding regulation, new modes of templation, molecular stabilisation and electronic perturbations have been detailed.

Chapters Three and Four were concerned with generating new structure types – octahedra and cuboctahedra – by employing 2-formylphenanthroline during subcomponent self-assembly. These architectures contain both a well-defined central void, along with multiple aperture environments; each of these unique spaces could bind guests. While no significant allosteric regulation effects were observed in the octahedra investigated, the strong peripheral association of guests to these structures enabled a new form of templation to be developed, wherein the preorganisation of apertures, and not the central void, drives structural generation. In larger cuboctahedral structures, the all-or-nothing cooperative binding of two guests stabilised a unique cage stereoisomer. Different isomers of the assembly showed different cooperativity characteristics in binding pairs of icosahedral guests around their periphery: in one case, positive cooperativity was promoted from a system initially displaying anticooperative binding, while in another all binding affinities were enhanced by an order of magnitude, and in a third the binding events were only minimally perturbed. The system could interconvert between three diastereomers – with D_4-, *O*- or S_4-point symmetry – under different temperature and template stimuli.

Similar cuboctahedral receptors were used in Chapter Five to stabilise coordination complexes and interlocked molecules within synthetic cavities. Different polypyridyl guests caused different degrees of symmetry breaking within the capsule, each segregating the cavity space in different ways. Multiple guests could be sequentially layered within these architectures, which were capable of binding heterotopic guest configurations in new stoichiometries and locations. Unique coordination complexes, none of which were observed outside the confines of the cage environment, were observed inside, many of which displayed altered electronic characteristics.

The ability for heteroleptic architectures to engender diverse host-guest interactions was studied in Chapter Six. The architectures generated by the integrative self-sorting of three- and fourfold symmetric ligand components were able to adapt their structure to bind guests. This led to binding interactions with a range of anions, steroids, drugs and natural products at both the internal and external cage sites: over 20 different enantiopure guests could be bound.

Chapter Seven explored the electronic effects of hosting multiple guests in proximity. Electrical communication between guests, and between host and guests, were uncovered. Larger clusters of molecules were observed to lead to more delocalised electronic density and easier electrochemical reduction of guests. Radicals bound within these cage frameworks showed altered optical properties depending on the mode of encapsulation.

Combined, these chapters have investigated atypical encapsulation phenomena in central cavities, peripheral apertures and external recognition sites. Focus in the literature to date has largely been placed on developing coordination cages with closed-off cavities; however, biological recognition processes rarely occur in the direct centre of a structure. This thesis shows that developing coordination cages with well-defined external and/or peripheral environments can be as important as generating cages with closed-off central voids.